In Situ Imaging of Heterogeneous Catalysts from the Micrometer to the Nanometer Scale

Zur Erlangung des akademischen Grades eines

DOKTORS DER NATURWISSENSCHAFTEN

(Dr. rer. nat.)

von der KIT-Fakultät für Chemie und Biowissenschaften

des Karlsruher Instituts für Technologie (KIT)

genehmigte

DISSERTATION

von

M. Sc. Sina Baier

aus

Fulda

KIT-Dekan: Prof. Dr. Willem Klopper

Referent: Prof. Dr. Jan-Dierk Grunwaldt

Korreferent: Prof. Dr. Christian G. Schroer

Tag der mündlichen Prüfung: 22.07.2016

Für Matze

Denk immer nur an die Meile,
die gerade vor dir liegt,
dann kannst du es schaffen.
aus Dänemark

Preface and Acknowledgements

This thesis is based on the work carried out between December 2012 and May 2016 at the Institute for Chemical Technology and Polymer Chemistry at the Karlsruhe Institute of Technology (KIT). ETEM studies and some preparation has been carried out at the Center for Electron Nanoscopy of the Technical University of Denmark (DTU) from September to October 2016.

In the following, I would like to thank a lot of people who have helped me in the context of this work. This work would not exist without the help of several collaborators, scientific discussions or the personal encouragement I encountered.

First, I would particularly like to thank Prof. Dr. Jan-Dierk Grunwaldt for supervising this work and providing the interesting and microscopy based topic. I am grateful for the possibility to spend two months at the Technical University of Denmark and to attend international conferences. I am thankful for the freedom in research and for the opportunity to work and cooperate with several research groups, which I really appreciated.

I would also like to thank Prof. Dr. Christian G. Schroer for agreeing to be the second examiner of this thesis, for his advice in discussions and for his optimistic attitude during beamtimes.

I am very thankful, that I had the possibility to work in close collaboration with Dr. Amélie Rochet, who supervised me at the beginning of my PhD, who joined many beamtimes and who also corrected parts of this thesis. I thank her furthermore for her confidence in me, for her positive attitude, for her structured way of working and for encouraging me, even when she had already left KIT.

I also owe many many thanks to Ass. Prof. Dr. Christian D. Damsgaard who supervised me during my stay at DTU, helped me with testing the *in situ* cell, explained the use of several microscopes, advised me concerning all scientific or "Denmark-related" questions, joined during beamtimes and supported me during the whole time of my PhD. Thank you very much for always taking time, for being positive and encouraging me.

I would also like to thank Prof. Dr. Jakob B. Wagner at DTU for enabling and supervising my stay at DTU and for very constructive discussions during paper writing. During my stay at DTU I also got lots of help and support from Dr. Zoltan Balogh at the FIB, Dr. Takeshi Kasama for sample preparation, and Cristiano Spiga, who helped me with the TEM.

I am grateful for the collaboration with Dr. Arne Wittstock from the University of Bremen, who I could always discuss with, who helped me a lot during trying to understand the behavior of nanoporous gold and who always motivated and supported me. I would also like to thank him and Junjie Shi for preparing the nanoporous gold samples I used in this work.

Abstract

The function and efficiency of a catalyst is influenced by its design on several length scales. Therefore the characterization of catalysts on all length scales is required to understand the underlying processes and to improve the catalyst function. Additionally, by the combination of several characterization techniques on the same system, complementary information can be obtained. Since catalytic processes are dynamic processes, the characterization has to be performed during the reaction processes under *in situ* conditions. For this purpose, dedicated cells which allow *in situ* studies have to be developed. Besides different spectroscopic or scattering techniques, imaging techniques may be used to study the catalysts. However, *in situ* studies are often complicated due to constraints on *in situ* cells. Hard X-rays are well suited for catalyst characterization under *in situ* conditions and may be used for both spatially resolved measurements and imaging studies. Hard X-ray microscopy, particularly X-ray ptychography, is therefore a promising characterization tool in heterogeneous catalysis.

Catalyst characterization on the micrometer to the nanometer scale requires different approaches covering different length scales. While the micrometer scale can be well covered by a variety of spatially resolved measurements, the nanometer scale can only be probed indirectly by scattering or spectroscopic techniques, or directly by electron microscopy. However, while the latter exhibits constraints for *in situ* measurements, hard X-ray microscopy is regarded as a promising tool for bridging the gap between studies on the nanoscale under model conditions and studies on the micrometer scale under more realistic conditions. In this work, tools for evaluation of the micrometer and the nanometer scale should be improved and developed. This includes the testing and improvement of a gas phase microreactor suited for correlative characterization techniques on the micrometer scale, as well as the development of a complementary X-ray microscopy and electron microscopy approach for the nanometer scale, based on special *in situ* ptychography cells.

To study the micrometer scale of catalysts, several characterization techniques can be applied in a spatially resolved manner. Among them are X-ray spectroscopy and X-ray diffraction techniques, IR thermography or Raman spectroscopy. In this work, a silicon-based gas phase microreactor, which allows the correlative application of these techniques, was developed and optimized. Among other qualities, the microreactor enables rapid heating and cooling rates due to its design, which makes it an ideal tool for studying transient reaction conditions. In the context of this work, the reactor design, optimization and first applications are described. The reactor design, originally composed of silicon and glass, was developed to minimize temperature variations across the length of the catalytic bed. Additionally, a reactor completely composed of silicon was built, which allows for high temperature application. It was proven

that XAS spectra and XRD patterns free from distortions could be acquired with both microre-actors, and that IR thermography and Raman spectroscopy could be performed. The reactor was applied to study the ignition and extinction process of the catalytic partial oxidation of methane over noble metal catalysts, which show pronounced gradients in oxidation state and tempera-ture. Both the evolution of hot spots as well as the appearance of a gradient in oxidation state could be observed in the microreactor, while the reaction process was monitored by on-line mass spectrometry. These results were in line with those obtained previously in conventional capillary reactors, which clearly showed the applicability of the gas phase microreactor for spa-tially resolved *in situ* studies.

Next to this *in situ* study, the potential of the reactor for the application during transient reaction conditions was shown on the example of the simulation of a realistic driving cycle. This re-quires fast heating and cooling rates, which are extremely difficult to obtain using conventional *in situ* cells. During the simulation of the driving cycle, the selective catalytic reduction of nitrogen oxides over copper zeolites was followed by *operando* quick X-ray absorption spec-troscopy. By probing the gas composition and the catalyst during the simulation of the driving cycle, it could be shown that changes in the gas composition as well as in the coordination geometry of the catalyst followed the fast heating and cooling profiles. These first measure-ments revealed the unique possibilities of this gas phase microreactor for the application during transient reaction conditions, which will open the door for future studies during transient con-ditions.

To bridge the gap between *in situ* microscopy on the micrometer and the nanometer scale, hard X-ray ptychography can be applied. In this work, dedicated *in situ* cells for hard X-ray ptycho-graphy were evaluated, developed and applied on different catalysts. Furthermore, a hierarchi-cal imaging approach was presented, based on a complementary study of the same catalysts by electron microscopy and ptychography. In this work, both a cell developed at DTU and a cell developed at KIT were introduced. The DTU-cell was intensively studied and its applicability for *in situ* ptychography was demonstrated. Experiences gained from these measurements were used to optimize the design of the KIT-cell, which is still in preliminary testing phase. In the context of this work, for the first time, a unique spatial resolution of 20 nm was obtained for *in situ* hard X-ray ptychography, which is by a factor of 5 to 10 better than the best resolution reported for *in situ* ptychography so far. Additionally, *in situ* ptychography was combined with infrared thermography, for simultaneous temperature mapping. Furthermore, the unique possi-bility to perform complementary EM and X-ray microscopy on the same sample was exploited in this work. This allows studying samples on different length scales, covering different pres-sure ranges and sample thicknesses.

In this work, the thermal annealing of nanoporous gold based catalysts was studied under dif-ferent atmospheres and pressures. It was found that the behavior under annealing conditions

strongly depends on the gas atmosphere. Contrarily to a reported coarsening behavior, a material loss or migration was observed at high temperatures under vacuum conditions, while a coarsening behavior was found in oxygen atmosphere under reduced pressure or in O_2/N_2 atmosphere at ambient pressure. Strikingly, under O_2/He atmosphere at ambient pressure, a material loss or migration, similar to the one observed under vacuum conditions, was found. These results highlight that in addition to coarsening caused by surface diffusion, other mechanisms might be present. These can be related to similar discussions for the growth mechanisms of nanoparticles, like Ostwald ripening or coalescence. Pure nanoporous gold and ceria stabilized nanoporous gold catalysts were studied and both showed a similar annealing behavior. Ceria however was shown to stabilize the sample as expected, which was demonstrated by the onset of changes at higher temperatures.

As a second example, a core-shell catalyst for direct production of dimethyl ether was studied during redox treatment. In particular, the stability of the core-shell interface was studied during reductive activation and subsequent reoxidation of the copper containing core material. The complementary character of *in situ* ptychography and electron microscopy was exploited by studying a thin section of the core-shell interface under model conditions by environmental transmission electron microscopy and electron energy loss spectroscopy. A thicker section was studied under realistic conditions during *in situ* ptychography and by complementary secondary electron microscopy and energy dispersive X-ray spectroscopy. The complementary approach revealed that the core-shell interface remains unchanged up to 250 °C, although changes on the nanometer scale occur, caused by rearrangement of the copper containing particles during redox treatment. At 350 °C, microscopic changes occurred, affecting both the core and the shell of the particle, but the overall core-shell interface remained stable, which is crucial for the bifunctional behavior of the catalyst.

In conclusion, the importance of correlative spatially resolved characterization techniques and hierarchical imaging approaches is presented. The new gas phase microreactor is proven to be applicable for *in situ* studies and the potential for application under transient reaction conditions is highlighted. Furthermore, the potential of a hierarchical imaging approach is presented by complementary electron microscopy and hard X-ray ptychography. First *in situ* ptychography measurements with a unique resolution are presented, exploiting the benefits of the complementary nature of both microscopy techniques. Studying the thermal annealing of nanoporous gold, the importance for *in situ* measurements under realistic conditions is underlined, while the hierarchical approach is proven to be useful for hierarchically structured catalysts. The developed cells will help to perform more detailed studies on both spatially resolved characterization on the micro scale, as well as on the nano scale in future. In addition, the knowledge obtained throughout this work will help to further improve correlative characterization techniques.

Kurzfassung

Die Funktion und Effizienz von Katalysatoren wird durch ihre Struktur auf verschiedenen Längenskalen beeinflusst. Daher wird eine Charakterisierung der Katalysatoren auf allen Längenskalen benötigt, um die der Katalyse zu Grunde liegenden Prozesse zu verstehen und zu optimieren. Auf Grund der Dynamik von Katalysatoren muss die Charakterisierung möglichst unter Reaktionsbedingungen, d. h. *in situ*, erfolgen, was die Entwicklung spezieller *in situ*-Zellen notwendig macht. Neben verschiedenen Streu- und Spektroskopiemethoden können auch bildgebende Verfahren zur Untersuchung der Katalysatoren verwendet werden. Insbesondere letztere sind jedoch nicht uneingeschränkt kompatibel mit *in situ*-Methoden, welches die Entwicklung von *in situ*-Zellen erschwert. Harte Röntgenstrahlung ist jedoch gut für die *in situ*-Charakterisierung von Katalysatoren geeignet und räumlich aufgelöste Messungen sowie Röntgenmikroskopie mittels harter Röntgenstrahlung, insbesondere die sogenannte „Ptychographie", stellen vielversprechende Methoden zur *in situ*-Charakterisierung dar.

Um unterschiedliche Längenskalen zu untersuchen, werden verschiedene Ansätze zur Studie der Mikrometer- und Nanometerskala benötigt. Die Mikrometerskala kann beispielsweise gut mittels vieler räumlich aufgelöster Methoden untersucht werden, während die Nanometerskala nur indirekt, mittels spektroskopischer Verfahren, oder direkt, mittels Elektronenmikroskopie, untersucht werden kann. Im Gegensatz zur Elektronenmikroskopie, die nur eingeschränkt zur *in situ*-Charakterisierung verwendet werden kann, wird die Röntgenmikroskopie mittels harter Röntgenstrahlung als zukunftsweisende Mikroskopiemethode angesehen, um die hochauflösende Bildgebung unter Modellbedingungen mit den niedriger auflösenden Techniken unter realistischeren Bedingungen zu verknüpfen.

Das Ziel dieser Arbeit war die Entwicklung und Verbesserung von *in situ*-Messmethoden, die räumlich aufgelöste hierarchische Untersuchungen von katalytischen Reaktionen unter realistischen Bedingungen erlauben. Hierzu wurden einerseits spezielle *in situ*-Zellen für komplementäre Röntgen- und Elektronenmikroskopie entwickelt und erfolgreich an Modellsystemen getestet. Andererseits wurde auch ein Gasphasenmikroreaktor, der für korrelative Charakterisierungsmethoden auf der Mikrometerskala geeignet ist, erprobt und weiter verbessert.

Zur Untersuchung von Katalysatoren auf Mikrometerskala können verschiedene räumlich aufgelöste Charakterisierungsmethoden verwendet werden, wie Röntgenspektroskopie und Diffraktion, Infrarot Thermographie oder Raman Spektroskopie. In dieser Arbeit wird ein auf Silizium basierender Gasphasenmikroreaktor vorgestellt, der die korrelative Verwendung der genannten Techniken ermöglicht, sowie seine Anwendung und Verbesserung diskutiert. Da dieser Reaktor hohe Heiz- und Abkühlraten ermöglicht, ist er besonders zur Untersuchung von transienten Zuständen geeignet .

Im Zuge dieser Arbeit wurde die Geometrie des Heizers des ursprünglich aus Silizium und Borosilikatglas bestehenden Reaktors optimiert, sodass entlang des Katalysatorbetts eine homogenere Temperaturverteilung erhalten wurde. Weiterhin wurde ein komplett aus Silizium bestehender Reaktor entwickelt, der die Anwendung bei höheren Temperaturen erlaubt. Verzerrungsfreie Röntgenabsorptionsspektren und Diffraktogramme wurden für beide Reaktoren demonstriert. Weiterhin ermöglichen beide Reaktoren die Durchführung von Infrarot Thermographie, sowie Raman Spektroskopie an dem Silizum-Glas-Reaktor. Der Gasphasenmikroreaktor wurde neben den reinen Erprobung auch zur Untersuchung der Zündung und Beendigung der katalytischen partiellen Oxidation von Methan mit Hilfe von Edelmetallkatalysatoren untersucht. Während der Reaktion treten zudem charakteristische Temperatur- und Oxidationszustandsgradienten auf, die mit Hilfe des neuen Mikroreaktors nachgewiesen wurden. Auf Grund der parallelen Gasanalytik mittels on-line Massenspektrometrie wurden die Ergebnisse ebenfalls mit der katalytischen Reaktion korreliert. Die so erhaltenen Ergebnisse sind vergleichbar zu den literaturbekannten Ergebnissen an konventionellen Reaktoren, welches die Anwendbarkeit des Mikroreaktors für räumlich aufgelöste Studien zeigt.

Des Weiteren wurde das Potential dieses Reaktors an Hand der Untersuchung von instationären Zuständen während der Simulation eines Fahrtzyklus untersucht, welcher durch die Nachahmung schneller Geschwindigkeitswechsel hohe Heiz- und Abkühlraten benötigt und daher nicht mit Hilfe konventioneller *in situ*-Zellen durchgeführt werden kann. An Hand von schneller Röntgenabsorptionsspektroskopie wurde die selektive katalytische Reduktion von Stickoxiden mittels Kupfer-Zeolith-Katalysatoren während eines solchen Zyklus analysiert. Die Zusammensetzung des Abgases wurde dabei parallel zu der räumlichen Struktur des Kupferkatalysators in Abhängigkeit der Temperatur ebenfalls gemessen. Durch die Veränderungen der Gaszusammensetzung und die Änderungen in der Koordinationsgeometrie des Kupfers konnte gezeigt werden, dass der Reaktor zur Untersuchung solcher transienter Reaktionsbedingungen geeignet ist. Diese Ergebnisse untermauern daher das Potential dieses Reaktors für weitere Studien von instationären Zuständen.

Um mikroskopische *in situ*-Methoden auf Mikrometer- und Nanometerskala miteinander zu verbinden, eignet sich Röntgenptychographie mittels harter Röntgenstrahlung. Die Entwicklung, Anwendung und Bewertung von *in situ*-Zellen wird in dieser Arbeit beleuchtet, sowie ein hierarchischer Ansatz zur Kombination von Elektronenmikroskopie und Röntgenmikroskopie an der selben Probe vorgestellt.

In dieser Arbeit werden zwei Zellen präsentiert. Eine Zelle wurde in enger Kooperation mit der Technischen Universität Dänemarks (DTU) entwickelt, dort hergestellt und schließlich im Zuge dieser Arbeit intensiv verwendet. Die zweite Zelle wurde am KIT hergestellt und in Hinblick auf die beobachteten Herausforderungen bei der anderen Zelle optimiert. Diese Zelle besitzt das Potential für zukünftige Anwendungen, konnte jedoch bisher nur im Rahmen erster

Tests verwendet werden. Im Rahmen dieser Arbeit wurden mit Hilfe von *in situ*-Ptychographie bisher einzigartige hohe räumliche Auflösungen von 20 nm bei 385 °C erhalten, die um den Faktor 5 bis 10 besser sind, als bisher literaturbekannte Auflösungen. Weiterhin wurde zum ersten Mal *in situ*-Ptychographie mit räumlich aufgelöster Infrarot Thermographie kombiniert. Die in dieser Arbeit präsentierten *in situ*-Zellen ermöglichen ebenfalls einen komplementären Charakterisierungsansatz von Elektronenmikrospie in Kombination mit Röntgenmikroskopie, welcher im Zuge der Arbeit am Beispiel der Stabilitätsuntersuchung während der thermischen Behandlung von nanoporösem Gold und von bifunktionalen Kern-Schale-Katalysatoren gezeigt wurde.

Katalysatoren basierend auf nanoporösem Gold wurden unter verschiedenen Gasatmosphären und unterschiedlichen Drücken während der thermischen Behandlung mittels komplementärer Elektronenmikroskopie und Ptychographie untersucht. Dabei konnte eine starke Abhängigkeit des Verhaltens von der Gasatmosphäre beobachtet werden. Im Gegensatz zu literaturbekannten Vergröberungen konnte unter Vakuum bei hohen Temperaturen ebenfalls ein Materialverlust oder eine Umlagerung beobachtet werden. Unter reiner Sauerstoffatmosphäre und reduziertem Druck, sowie in synthetischer Luft bei Raumdruck, wurde jedoch eine Vergröberung beobachtet. Erstaunlicherweise konnte diese jedoch nicht unter 20 % Sauerstoff in Helium bei Raumdruck beobachtet werden und stattdessen wurde ein ähnlicher Materialverlust oder Transport wie unter Vakuum erhalten. Die Ergebnisse weisen daher auf zusätzliche Vergröberungsmechanismen hin, die nicht mit der literaturbekannten Oberflächendiffusion beschrieben werden können. Diese können jedoch auf die diskutierten Wachstumsmechanismen für Nanopartikelwachstum, Koaleszenz und Ostwald Reifung, übertragen werden. Weiterhin zeigten beide untersuchten Katalysatoren, reines nanoporöses Gold und Ceroxid stabilisiertes nanoporöses Gold, vergleichbares Verhalten, jedoch konnte eine gewisse thermische Stabilisierung durch Ceroxid erreicht werden.

Als weiteres Katalysatorsystem wurde ein Kern-Schale-Katalysator, der zur direkten Produktion von Dimethylether verwendet wird, untersucht. Das Kernmaterial katalysiert hierbei die Reaktion von Synthesegas zu Methanol, welches anschließend mit Hilfe des Schalenmaterials zu Dimethylether umgesetzt wird. Für das bifunktionale Verhalten des hierarchisch aufgebauten Kern-Schale-Katalysators ist die Stabilität der Kern-Schale-Grenzfläche signifikant, sodass diese unter Redoxbedingungen untersucht wurde. Als Modellkonditionen wurde die zur Aktivierung des Katalysators verwendete Reduktion der sich im Kern befindenden Kupferpartikel, sowie deren Reoxidation untersucht. Um die komplementären Methoden Elektronenmikroskopie und *in situ*-Ptychographie bestmöglich auszunutzen, wurde ein Dünnschnitt der Kern-Schale-Grenzfläche mittels *in situ*-Transmissionselektronenmikroskopie und Elektronenenergieverlustspektroskopie untersucht. Weiterhin wurde eine dickere Schicht unter realistischen Bedingungen mittels *in situ*-Ptychographie und komplementärer Röntgenfluores-

zenzspektroskopie sowie *ex situ*-Rasterelektronenmikroskopie untersucht. Dieser kombinierte Ansatz zeigte, dass die Grenzfläche bis zu Temperaturen von 250 ° unverändert bleibt, obwohl die Kupfernanopartikel im Kern ihre Größe auf der 10 nm Skala verändern, wie durch Elektronenmikroskopie nachgewiesen werden konnte. Bei weiterer Erwärmung auf 350 °C wurden signifikante Veränderungen im Kern und in der Schale auf Mikrometerskala beobachtet, die jedoch nicht die Struktur der Grenzfläche beeinflussten und somit auf eine hohe Stabilität des Kern-Schale-Katalysators hindeuten.

Zusammenfassend wurde in dieser Arbeit die Bedeutung von komplementären, räumlich aufgelösten Charakterisierungsmethoden, sowie die Wichtigkeit von hierarchischen Untersuchungen präsentiert. Die Ergebnisse zeigen, dass der neu entwickelte Gasphasenmikroreaktor die Anwendung von korrelativen *in situ*-Studien erlaubt und ein hohes Potential für die Untersuchung von instationären Zuständen besitzt. Zur Untersuchung der Nanometerskala wurde das Potential von hierarchischen Abbildungsverfahren mittels komplementärer Elektronenmikroskopie und Röntgenptychographie diskutiert. Erste *in situ*-Röntgenptychographiemessungen mit einer bisher einzigartigen Auflösung wurden präsentiert, sowie die Vorteile der komplementären Herangehensweise beleuchtet. Die Ergebnisse der korrelativen Untersuchungen des Verhaltens von nanoporösem Gold bei Erhitzen unterstrichen die Bedeutung von *in situ*-Messungen unter realistischen Bedingungen, während der hierarchische Charakterisierungsansatz von Elektronenmikroskopie in Kombination mit Röntgenmikroskopie am Beispiel der Stabilitätsuntersuchung von Kern-Schale-Katalysatoren gezeigt wurde.

Die in dieser Arbeit entwickelten Zellen werden somit helfen in zukünftigen Messungen sowohl räumlich aufgelöste Informationen auf Mikroskala als auch auf Nanoskala zu erhalten. Zusätzlich kann das in dieser Arbeit erlangte Wissen zur weiteren Kombination komplementärer Charakterisierungstechniken verwendet werden.

Contents

Part I

Introduction and Methods

1 Introduction

More then 90% of daily chemical products undergo at least one catalytic step during their production [1], which demands optimization of the catalysts due to economical reasons. Furthermore, the development and improvement of catalysts is of interest for academic research, but especially with respect to the application of renewable energy sources or efficient exhaust gas aftertreatment systems, also for society.

For catalyst optimization, a multi-scale approach is of great importance, which can be realized through multi-scale characterization [2], multi-scale modeling [3] and multi-scale design [4, 5] of catalysts. Thereby, on each length scale different processes dominate and influence the overall efficiency of the catalyst. In the following section, the different length scales, which are shown schematically in Fig. 1.1, will be shortly discussed.
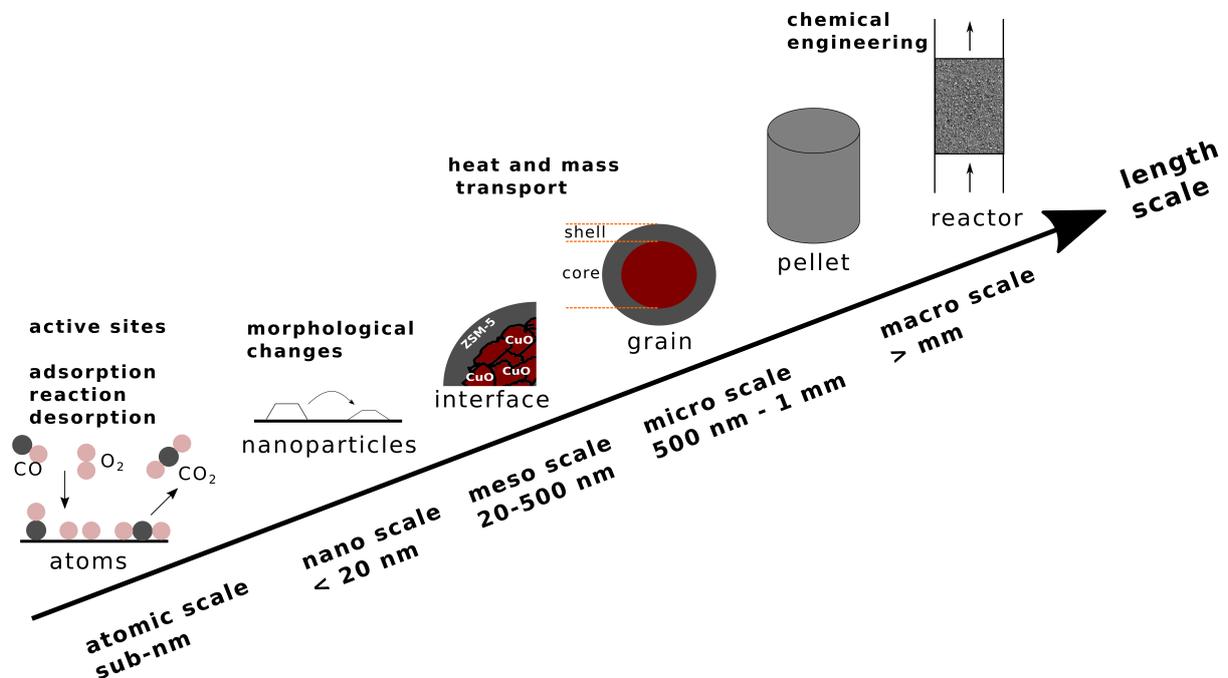
Figure 1.1: Schematic representation of the multi-scale approach used for modeling, characterization and design of catalysts. From the left to right the atomic, nano, meso, micro and macro scale are shown together with typical processes and anchor points for optimization on the different length scales.

Especially for industrial large scale applications, solid heterogeneous catalysts are predominantly used. The so called "product design" addresses the question of how to fabricate a catalyst with a certain microstructure, so that it can be used in industrial applications [6]. The origin of the catalytic activity however is on the atomic scale, since the reaction happens on the active sites on the surface as shown in Fig. 1.1. Due to the large dimensions in the meter range, tons of catalysts are required and the catalyst itself is filled inside industrial plants as a catalytically active material on heterogeneous support materials. These "catalyst bodies" have a certain shape and geometry, *e. g.* extrudates. A pelletized catalyst and a reactor with a catalyst

bed are schematically shown in Fig. 1.1 and represent the macro scale. On this length scale, a chemical engineering approach is required, evaluating different carrier designs or pre-shapings of catalyst bodies. These carriers are usually in the size range from mm to cm, which is referred to as the "macro" scale. The carriers and catalyst bodies are designed in such a way that optimal heat and mass flow is obtained, for which reactor modeling can be used to further optimize the catalytic reaction [3]. For exhaust gas aftertreatment systems for example, honeycomb shaped carriers allow optimal flow and heat transfer, as well as minimized pressure drops [2, 3].

Despite the importance of the catalyst design on the macro scale, the micro scale and even below is equally important. Since the porosity of the material becomes relevant at this length scale [7], heat and mass transport are also influenced by the catalyst design on the micro ($<$ mm) and meso (20 to 500 nm) scale. Therefore, also on these length scales, modeling approaches can be used to optimize the catalyst [8]. The catalyst efficiency can *e. g.* be tuned by introducing different pore sizes [5, 9] or developing hierarchically structured bifunctional catalysts [10, 11]. In particular, the development of bifunctional core-shell structured catalysts recently gained lots of interest [12, 13]. Such a core-shell catalyst is therefore depicted schematically in Fig. 1.1 to represent the micro scale. In such bifunctional core-shell catalysts, two catalysts with different functionalities are combined. By this combination synergistic effects can be exploited due to the hierarchic order of active sites. For example, a bifunctional catalyst for direct dimethyl ether (DME) production can be applied by encapsulating a methanol forming core with an acidic shell for direct methanol dehydration to DME. By this approach, not only the micro scale, *i. e.* the overall design of the core-shell catalyst, influences the catalytic efficiency, but also the design on the meso scale, *e. g.* if the interface between the core and the shell is well connected. This is also depicted in Fig. 1.1.

Although, catalyst design from the meso to the macro scale mostly optimizes transport processes, the interaction of catalysts with gas species is not influenced by this length scale, albeit this is the most important process for catalytic reactions. Instead, the catalytic reaction itself takes place on the atomic scale (sub- nm) on the surface of the catalyst, as shown schematically in Fig. 1.1. By the strength of the interaction, which influences the adsorption and desorption processes of gaseous reaction species, the kinetics of the reaction can be controlled. Therefore, tuning the catalyst surface on the atomic scale can be used to optimize the catalytic efficiency [2]. Furthermore, the nano scale of the catalysts (sub-nm to 20 nm) also has an effect on the catalytic activity, since it also influences the surface of the catalyst which is exposed to the gas atmosphere. A typical example showing the importance of the nano scale is that the size and shape of the metal nanoparticles matters [14, 15]. For example, oxidation reactions catalyzed by gold nanoparticles show a high dependence on particle size of gold nanoparticles, which on one hand highlights the demand for size controlled preparation methods, but on the other hand shows the need to prevent the particles from sintering [14, 16, 17]. Another example showing

the importance of the nano scale is that under different gas atmospheres, restructuring of the catalysts on the nano scale can be observed, which directly influences the surface of the active materials [18].

From the previous examples it becomes clear that all length scales are important for catalyst development and improvement. However, for optimization of the catalysts, independent from the length scale on which the optimization should be performed, knowledge of the underlying processes is required. To cover all length scales from the atomic scale to the macro scale [2, 19–21], the combination of various characterization methods, as well as the application of hierarchical approaches [2, 22–24] on the same system is required. Such a hierarchical approach on the same system is depicted schematically in Fig. 1.2 for the one step production of DME over a $CuO/ZnO/Al_2O_3$@ZSM–5 catalyst. It is shown that for the production of DME, the macro scale has to be considered by optimizing different reactors [13, 25], but the reaction can also be influenced by optimizing the micro scale by the development of bifunctional core-shell catalysts, which are structured on both the micro and meso scale [26, 27]. Finally, the reaction itself depends on both nano scale effects including particle size, and atomic scale effects. The latter have a decisive influence on surface reaction rates and process activation energies and depend *e. g.* on the oxidation state, number of active sites and the surface coordination of the active species [28–30].

macro (> mm)   micro (< mm)   meso (20 – 500 nm)   nano (< 20 nm)
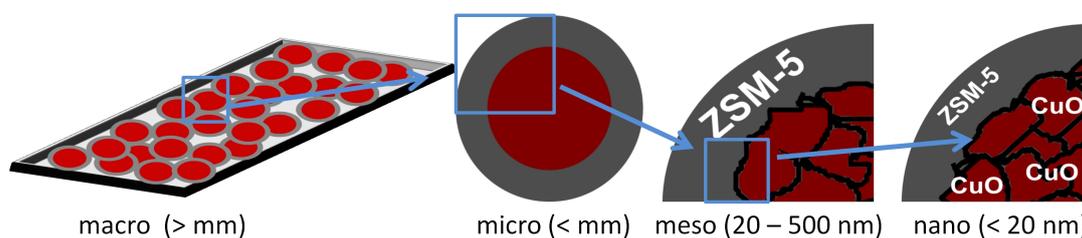
Figure 1.2: Schematic overview on the different length scales needed for optimization of heterogeneous catalysts on the example of dimethyl ether production. The macro scale requiring optimization on reactor design, the micro scale implying development of core-shell catalysts, the meso scale showing the structured catalyst and the nano scale depicting the active metal particles, are shown.

Since all mentioned processes – from heat transfer on the macro and micro scale, to rearragement on the nano scale and surface reactions on the atomic scale – occur under reaction conditions, knowledge has to be gained in a controlled environment or under reaction conditions [31–36]. For example, studying nobel metal based catalysts for the Catalytic Partial Oxidation (CPO) of methane before and after the reaction shows oxidized metal species, whereas under catalytic application reduced species are observed [37, 38]. Therefore, the conduction of *in situ* studies, which means under controlled atmospheres, pressures and temperatures, is a prerequisite for understanding the underlying processes of catalytic reactions. Preferably, even so-called *operando* studies, *i. e.* studies performed under realistic process conditions with direct analysis of the working catalyst by activity measurements, should be performed [31, 39].

Last but not least, the dynamics of catalytic systems have to be considered as well, introducing the importance of the time scale in addition to the length scale. For example, catalysts can show dynamic restructuring processes [18], oscillating oxidation state changes [40] or sintering and deactivation processes [15, 41]. This requires *in situ* studies not only on different length scales, but also on different time scales, ranging from the sub-s regime during reaction processes, to minutes or even months for deactivation processes [2].

1.1 *In Situ* Characterization of Heterogeneous Catalysts

In situ characterization of heterogeneous catalysts is a prerequisite for understanding catalytic reaction processes, since the catalyst structure itself depends on the environment [18, 40]. In addition, transport effects can only be studied during the catalytic process. Since heterogeneous catalysts are usually in the solid state, basically all characterization techniques used for solid materials, including spectroscopic, scattering or microscopic methods, can be used as characterization methods. However, *in situ* measurements constrain some techniques, *e. g.* those requiring ultra high vacuum conditions. Especially, *operando* techniques even need simultaneous analysis of the gas and/or liquid phase, so that catalytic activity can be determined. Therefore, *in situ* or *operando* measurements have to be performed inside special cells providing the reaction environment [42] and facilitating on-line product analysis at the same time. Some useful characterization techniques for probing catalysts at different length scales are summarized in Fig. 1.3. Apart from probing the catalyst itself, measurements on the gas phase have to be carried out, which are not implemented in Fig. 1.3.

To follow the catalytic process during gas phase reactions, Mass Spectrometry (MS), Infrared (IR) spectroscopy or Gas Chromatography (GC) are often used to characterize the products downstream from the catalyst bed. In parallel, the solid catalyst can be probed with radiation, like Ultra Violet (UV) or visible (vis) light, electrons or X-rays. Due to the measurements inside special cells, the radiation has to penetrate through the cell material, which results in some constraints. For visible light, measurements using glass cells are possible applying for example Raman scattering [43, 44] or UV-vis spectroscopy [45, 46]. IR spectroscopy and thermography can for example be performed using reactors made of sapphire [40] or using setups with special windows *e. g.* reactors applied for Diffuse Reflectance Infrared Fourier Transform Spectroscopy (DRIFTS) [47]. The small penetration depth of electrons however does not allow simple *in situ* measurements and it is rather difficult to penetrate through reactors [48, 49]. Electron microscopy (EM) can therefore only be applied using very thin window materials, like $1.2\,\mu m$ thick silicon nitride membranes [50], or applying differential pumping systems implemented in the microscopes [15, 18, 51].
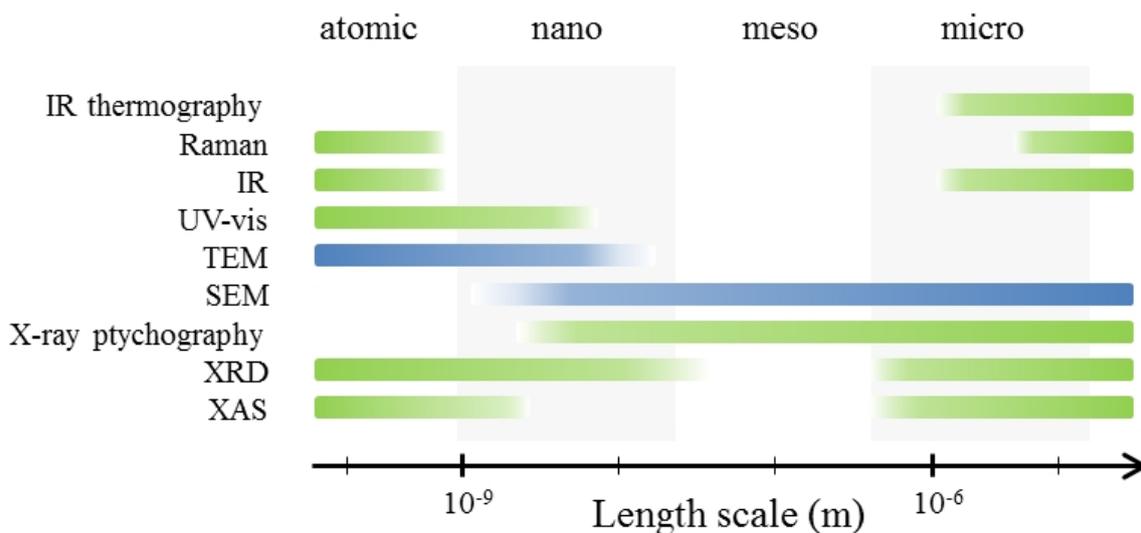
Figure 1.3: Some typical characterization techniques used to study heterogeneous catalysts at different length scales. Green: Highly compatible with *in situ* studies, blue: limited for *in situ* studies. The atomic scale can be well probed by spectroscopic techniques and Transmission Electron Microscopy (TEM), while starting from the micro scale, spatially resolved techniques based on spectrsocopic or diffractive measurements can be applied. The nano scale and meso scale are usually probed by TEM and Scanning Electron Microscopy (SEM). These however suffer from the low penetration depth of electrons and the high interaction with matter, therefore, the relatively new technique X-ray ptychography is a promising method for *in situ* studies on this length scale. IR: Infrared (spectroscopy), Raman: Raman spectroscopy, UV-vis: Ultraviolet and visible light spectroscopy, XRD: X-Ray Diffraction, XAS: X-ray Absorption Spectroscopy.

Contrarily to electrons, X-rays have a higher penetration depth and show lower interaction with the probed material. Therefore, they are suited very well for *in situ* measurements [19, 36, 52–54]. Especially hard X-rays (E>5 keV) allow an easy design of dedicated *in situ* cells [2, 49], while soft X-rays usually require vacuum environments and thin window materials. The development of synchrotron radiation sources facilitates X-ray based techniques by providing a tunable energy range, which is required for X-ray absorption techniques. Additionally, also a high photon flux allows faster measurements, *e. g.* for time resolved spectroscopy, diffraction or imaging experiments. Within the application of synchrotron radiation based methods, especially scattering methods and spectroscopy are well established, but also direct imaging techniques are becoming more and more important. As already mentioned, complementary knowledge needs to be obtained by a combination of various techniques, *e. g.* X-ray Absorption Spectroscopy (XAS) and X-Ray Diffraction (XRD) [52, 55–57]. Thereby, XAS allows the local coordination geometry and oxidation state of a catalyst to be studied, independently of the crystallographic state (crystalline/amorphous). In contrast, XRD enables probing of the long range order of a crystalline material, *i. e.* the crystallographic phase. In addition to the combination of different spectroscopic or scattering techniques, the combination of imaging techniques with chemical contrast by spectroscopy [21, 58, 59] is of special interest as it also offers spatial information on the catalyst.

1.1.1 *In situ* Imaging of Heterogeneous Catalysts on the Micrometer Scale

The micro scale plays an important role for the product design of heterogeneous catalysts, *e. g.* for optimization of heat, flow and mass transport properties [3]. For example, gradients in concentration, temperature, or oxidation state of the catalyst can be observed in the working state of the catalyst and their understanding can help to identify critical parameters for product design [2, 19, 60]. Therefore, these gradients have to be studied in the gas phase [61, 62], as well as on the solid phase [2]. To detect such gradients, spatially resolved characterization techniques have to be used, *e. g.* spatially resolved MS [61, 63, 64] or laser-induced fluorescence [65] enabling studying the gas phase, IR thermography [66–68] allowing studies of temperature gradients or spectroscopic techniques allowing studying structural gradients within the catalyst. Among the most common spectroscopic techniques are UV-vis and Raman spectroscopy [45, 46, 69, 70], IR spectromicroscopy [70, 71] or X-ray based techniques [2, 49, 53]. Since each of them has its unique advantages and disadvantages, a combination of several of them, preferably all applied simultaneously, is highly desirable to be able to correlate individual results [40, 72]. Therefore suitable reactors are required which can be used for several methods. Such reactors do no only have to be suitable for the dedicated methods, but have to be compact enough to be used at a beamline. For example, reactors fitting the requirements are microreactors, which also show intrinsic advantages such as a high heat and mass transfer [57, 73]. The application of microreactors is further discussed in section 3.

In the following section, the importance of such gradients will be highlighted for the example of the CPO methane over noble metal catalysts, which can be applied to produce synthesis gas (syngas, CO and H_2) as described by Eq. 1.1 [74].

$$CH_4 + \frac{1}{2}O_2 \longrightarrow CO + 2H_2 \quad \Delta_f H^\circ_{298} = -36 \, kJ/mol \tag{1.1}$$
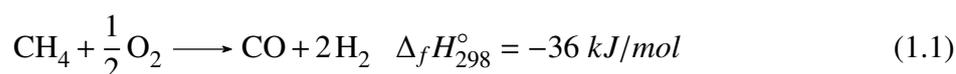
Spatially resolved MS of Rh/γ-Al$_2$O$_3$ and Pd-Rh/γ-Al$_2$O$_3$ catalysts revealed gradients in gaseous product evolution along the catalyst structure [63, 64]. An explanation for these gradients is a consecutive reaction pathway, assuming a combustion of methane (Eq. 1.2) followed by reforming processes (Eq. 1.3 and 1.4). This consecutive pathway could also explain the temperature gradients observed along the catalyst bed. These gradients studied by IR thermography show a higher temperature in the area of total combustion which is in line with the high exothermicity of the reaction [72, 75, 76].

$$CH_4 + 2\,O_2 \longrightarrow CO_2 + 2\,H_2O \quad \Delta_f H^\circ_{298} = -803\ kJ/mol \tag{1.2}$$

$$CH_4 + H_2O \longrightarrow CO + 3\,H_2 \quad \Delta_f H^\circ_{298} = -206\ kJ/mol \tag{1.3}$$

$$CH_4 + CO_2 \longrightarrow 2\,CO + 2\,H_2 \quad \Delta_f H^\circ_{298} = -247\ kJ/mol \tag{1.4}$$
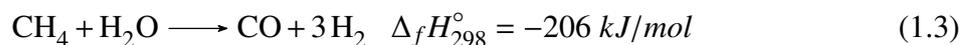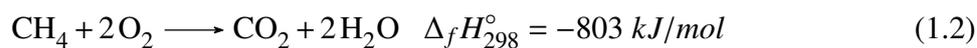
This example of the CPO of methane shows that the study of gradients in reactors or catalyst beds can be used to obtain knowledge on the reaction process. Apart from gradients in temperature and concentration, also gradients on the catalyst structure itself, *i. e.* in oxidation state, can be studied. For the CPO of methane, these are discussed in the following paragraph. However, to study gradients on the catalyst structure itself, dedicated techniques probing the catalyst structure on the atomic scale have to be used. By a combination of such approaches different length scales from the atomic scale to the reactor scale can be probed. The obtained knowledge can then be correlated to draw further conclusions on the underlying processes, which at the end helps to optimize the catalyst overall efficiency.

Synchrotron Radiation Based Techniques   Due to the high penetration depth of X-rays, X-ray based techniques are widely applied for *in situ* observation of catalysts, *i. e.* by X-Ray Absorption Spectroscopy (XAS) [33], X-Ray Diffraction (XRD) [77, 78] or X-ray Fluorescence (XRF) [21, 22], which provide complementary structural information and elemental distribution. These spectroscopic techniques can be used to study the atomic scale of the catalysts, due to the interaction of the radiation with the catalyst material. However, spatially resolved measurements allow furthermore probing the micro scale.

Gradients in oxidation state, for example, can be detected by spatially resolved XAS by probing the area of interest with a focused X-ray beam [72, 79], which requires dedicated micro-probe beamlines. Additionally, a resonant full-field imaging approach, in which the full catalyst bed is probed at once [72, 80, 81], can be applied. In this case, a spatially sensitive detector, *e. g.* a CCD camera, is used. The advantage of such an approach is that the whole area of interest can be probed at the same time, which allows faster acquisition [82].

Referring back to the example of the CPO of methane, the complementarity of different techniques could for example be used to study the ignition of the CPO of methane in more detail. Here, the combination of spatially resolved XAS and IR thermography revealed that gradients in temperature and oxidation state were visible along the catalytic bed even before a detectable formation of syngas [83, 84]. In particular, before ignition of the reaction, a hotspot could be observed at the end of the catalytic bed. Additionally, it was found that the end of the catalyst bed was reduced, while the front was still oxidized when the hotspot was further shifted to the beginning of the catalyst bed after ignition. The combination with on-line MS further allowed

to conclude that the reduction started at the end of the catalytic bed when the reaction ignited, *i. e.* when H_2 was detected. Such complementary techniques allowed additional information of the ignition process of the reaction to be obtained. In particular, it was suggested that the high temperature reached by combustion of CH_4 caused a self-reduction of the catalyst, which itself led to the ignition of the CPO and to a formation of syngas [72].

Next to the CPO of methane, such gradients were also found in the Selective Catalytic Reduction (SCR) of NO_x by NH_3 *via* Cu-zeolites [85] or in the CO_2 capture-reduction [86]. Even oscillating behavior, *i. e.* time dependent occurrence of gradients, has been observed for the CO oxidation using Pt catalysts [40]. However, it has to be noted that these studies only reveal 2D information, although 3D catalysts and reactors are monitored. Therefore, it is important to further develop the possibilities for 3D measurements, *i. e.* tomography.

Tomography   Tomographic studies can be obtained by recording 2D projection images while rotating the sample. For each rotation angle, such 2D images are acquired and further processed into 3D "images". By this approach, full 3D information on both the exterior and the interior of the catalyst can be obtained non-destructively [87]. This allows the measurement of realistic catalysts without further preparation. Ideally, this is then further combined with *in situ* studies during catalytic processes.

Yet, catalytic *in situ* studies are rare and the image acquisition under *in situ* or *operando* conditions is challenging, as a high stability and precision of the setup is required. Nevertheless, Price *et al.* [88] recently demonstrated an *in situ* μ–XRD/XRF-Computed Tomogragphy (CT) study, even in liquid phase. A single catalyst grain was studied during standard conditions for the hydrogenation of nitrobenzene. By this *in situ* study it could be shown that the active state of the Mo-promoted Pt/C catalyst is the reduced Pt state and that it is homogeneously distributed on the carbon support surface. Especially the latter finding could only be obtained non-invasively by *in situ* X-ray studies, revealing the high importance of such *in situ* 3D approaches. However, apart from *in situ* studies during catalytic reaction, the study of the formation of catalysts is equally important for further catalyst development and Jacques *et al.* [78] studied the evolution of the formation of Nickel impregnated γ-Al_2O_3 catalyst bodies by *in situ* XRD-CT. Despite these examples, such *in situ* studies were hardly applied yet and *quasi-in situ* studies and *ex situ* studies are more widely used [89–91].

1.1.2 *In situ* Imaging of Heterogeneous Catalysts on the Nanometer Scale

Electron Microscopy   For imaging approaches on the nano and atomic scale Transmission Electron Microscopy (TEM) is usually applied, as it offers imaging of a sample with atomic resolution. However, as already mentioned, the low penetration depth of electrons is critical for *in situ* measurements. Currently, there are two approaches for *in situ* TEM imaging, both summarized by the term "Environmental TEM" (ETEM) [48]. One approach applies closed cells and can also be used for atmospheric pressures [50, 92], while the other one uses differentially pumped microscopes [93–95], which restricts the studies to an environment with reduced pressure.

The development of ETEM offered completely new insights into the dynamic behavior of catalysts. For example, with ETEM a model methanol catalyst was studied under different gas atmospheres on atomic scale and a rearrangement of Cu nanoparticles supported on ZnO was observed. ETEM revealed that the Cu particles reversibly change their shape when varying the gas atmospheres. In particular, a pronounced flattening of the nanoparticles could be observed in a syngas environment, in comparison to the "rounder" shape in pure H_2 or H_2/H_2O atmosphere. This behavior on the nanoscale is depicted schematically in Fig. 1.1 and is supported by earlier complementary *in situ* spectroscopic studies [30]. Additionally, by a study from Holse *et al.* [29] the redox behavior of a similar model methanol catalyst was studied. The study was combined with non-spatially resolved XPS analysis, revealing similar results for both studies. Under reducing atmosphere, a shrinkage of the CuO particles was observed, which was caused by the phase change to metallic Cu. Furthermore, it was shown that the Cu particles were partly covered by ZnO nanocrystals, which is considered to be critical for catalytic activity, as also Behrens *et al.* stated [28]. The Cu/ZnO system has also been used to show the applicability of the closed cell approach which has the advantage of allowing measurements under ambient pressure. It was shown, that Cu nanocrystals could be studied with a resolution of 0.18 nm at 500 °C under ambient pressure in a H_2 atmosphere [50]. These realistic conditions were achieved by using micrometer sized flow channels and thin SiN_x windows, which can also be applied for liquid environments [96].

These examples show that ETEM offers a unique high resolution, enabling measurements on the influence of molecules on the atomic scale [97]. Among other studies, it also allows studying the oxidation of soot [98], the formation of carbon nanotubes [99] or sintering of nanoparticles in different atmospheres. The latter can reveal information about the growth mechanisms of nanoparticles, like particle migration and coalescence or Ostwald ripening *via* the formation of mobile species or adatom movement [15, 41]. Such understanding of the underlying mechanisms can then be further used to optimize the catalysts with respect to their thermal stability. However, despite such strong benefits, a drawback of ETEM is the strong interaction of the

electron beam with the gas molecules, leading to ionization of the gas molecules which can influence or damage the probed sample system [51, 100, 101]. Furthermore, due to the small field of view, it is hard to obtain statistic information and as the electrons have to penetrate through the sample, only very thin specimens can be probed.

X-ray Microscopy   Complementary to TEM, X-ray microscopy offers spatially resolved information on the micro and meso scale while profiting from a higher penetration depth [2, 82, 102–104]. This enables studies under more realistic conditions (*e. g.* liquids or corrosive gases) and potentially more easily sample preparation. Furthermore, tomographic studies can be performed easier and a variety of different contrast mechanisms can be applied, *e. g.* X-ray scattering or absorption. A short overview of the characteristics of both methods, transmission electron microscopy and X-ray microscopy, is given in Tab. 1.1.

As for the micrometer scale one can distinguish between full-field and scanning techniques. The former one is more suited for dynamic processes due to the faster acquisition. For hard X-ray full-field microscopy, resolutions in the tens of nanometers have been reached [105]. For example, Kiss *et al.* [106] studied the oxidation of Ni powder *in situ* by resonant full-field microscopy, obtaining a resolution of 55 nm. Especially in the soft X-ray regime, Scanning Transmission X-ray Microscopy (STXM) has been used [32, 107, 108]. As the samples are scanned under a focused beam, a variety of imaging contrasts can be applied [32]. Focusing optics such as Kirkpatrick Baez mirrors [109, 110], Fresnel zone plates [111, 112], refractive X-ray lenses [113–115] and waveguides [116] are used for such techniques and the resolution depends on the size of the beam. For STXM applying soft X-rays (200 to 2000 eV), a spatial resolution down to 15 nm was obtained [108, 117]. However, the shorter penetration depth of soft X-rays can cause problems and complicates the *in situ* cell design as well as studies at atmospheric pressure [24, 107]. Nevertheless, de Smit *et al.* [108] studied an iron-based Fischer–Tropsch catalyst *in situ* during reduction and under reaction conditions. A similar cell to the one applied in the closed cell ETEM approach was used to study the catalyst under ambient pressure at 250 and 350 °C. Under these conditions, a spatial resolution around 15 nm was achieved and chemical contrast was further gained by varying the energy.

Nevertheless, hard X-rays are more feasible with respect to *in situ* measurements, and nowadays focusing possibilities for hard X-rays allow to focus the beam down to approximately 50 to 80 nm conveniently [118], while recently, a focused X-ray beam down to 8 nm was obtained [119]. However, when conventional X-ray microscopes are used, the image is magnified by an objective lens behind the object, which could suffer from abberations.

Table 1.1: Characteristics for transmission electron microscopy and X-ray microscopy. SAED: Selected Angle Energy Diffraction, HAADF: High Angle Annular Dark Field, EELS: Electron Energy Loss Spectroscopy, EDX: Energy Dispersive X-ray spectroscopy, XRF: X-Ray Fluorescence, XRD: X-Ray Diffraction, XAS: X-ray Absorption Spectroscopy, WAXS/SAXS: Wide/Small Angle X-ray Scattering, CDI: Coherent Diffraction Imaging.

Transmission Electron Microscopy	X-ray microscopy
atomic resolution (less than 1 Å)	resolution down to the nano scale (5 to 10 nm)
model samples	realistic samples
thin specimens	thicker specimens
combination with SAED, HAADF	combination with XRF, XRD, XAS
combination with EELS, EDX	combination with WAXS, SAXS, CDI
small gas volumes	big gas volumes, high penetration depth
	high energy resolution
	easier tomographic measurements

Therefore, promising techniques for high-resolution imaging are based on the interaction of coherent radiation available by synchrotron radiation sources with the probed samples [82, 120]. This Coherent Diffraction Imaging (CDI) allows for "lensless" imaging without an objective lens. It is based on recording far-field diffraction patterns and applying iterative reconstruction algorithms to obtain real space reconstructions of the probed object [82, 121].

In contrast to the full-field method, scanning coherent X-ray diffraction imaging, which is also called X-ray ptychography [122–125], uses a focused X-ray beam and the samples are scanned through the coherent beam. By iterative reconstruction algorithms, real space images can be obtained from the far-field diffraction patterns [126, 127]. Ptychography can also be combined with resonant image acquisition, which offers the possibility to obtain chemical contrast [58, 128, 129] in addition to high resolution imaging. So far, for hard X-ray ptychography resolutions below 10 nm were recently demonstrated during *ex situ* application [130, 131], while for soft X-ray ptychography, a resolution of 5 nm was achieved [129]. Regardless of the resolution, however one of the constraints for ptychography results from the scanning and reconstruction procedure. It requires the sample to remain stable and unchanged during image acquisition, which complicates the application for *in situ* studies. Only recently, *in situ* measurements could be performed [132–136], which will be further discussed in section 9.

1.2 Motivation for Hierarchical Imaging and Aim of the Thesis

As outlined in the previous sections, catalytic reactions can be tuned on all length scales from the atomic to the reactor scale. Relevant processes like the kinetics of a reaction (atomic scale) or transport processes (meso to macro scale) occur on all these length scales and each of them influences the overall kinetics of a reaction. Therefore, it is important to study heterogeneous catalysts on different length scales and with a variety of complementary techniques, ideally simultaneously.

On the one hand, the atomic and nano scale can be studied very well by TEM under model conditions, while spectroscopic techniques like XAS can be used to probe this length scale under realistic conditions. On the other hand, the micro and macro scale can be covered by spatially resolved spectroscopic techniques under realistic conditions like XAS, IR or Raman spectroscopy. However, also on these length scales, it is still challenging to combine different characterization techniques on the same sample. Similarly, it is a challenge to probe the nano and meso scale, since either model conditions like in SEM have to be applied, or, for studies under realistic conditions, common techniques are missing. This is also depicted in Fig. 1.2. Here, one promising technique is X-ray ptychography, which allows imaging on the meso scale under realistic conditions. Therefore, *in situ* ptychography is regarded as a promising tool to bridge imaging under model conditions on the nano scale with imaging under more realistic conditions on the micro scale.

Especially, when hierarchically designed catalysts are used, the application of different techniques is required to cover all length scales. Among others, such hierarchically designed catalyst materials can be found in bifunctional catalysts [137–139], catalysts for fluidized bed reactors [22, 140, 141], bifunctional core-shell catalysts for direct DME synthesis [13, 142], or bifunctional encapsulated Fischer-Tropsch catalysts [4, 143]. In all these examples, the structure and stability of the catalyst is critically related to the function. Therefore, the study of materials at various length scales under *in situ* conditions, is expected to become more important in the near future and dedicated techniques bridging different length scales have to be developed.

Aim of the Thesis   With this work, new strategies for hierarchically performed imaging of catalysts and complementary characterization on the same sample will be evaluated. For this purpose, two different approaches were examined:

- The application and optimization of a gas phase microreactor for complementary *in situ* characterization techniques on the micrometer scale, which was tested on the example of the CPO of methane and the selective catalytic reduction of NO_x by NH_3.

- The application and development of *in situ* cells for hard X-ray ptychography for *in situ* imaging on the meso scale, which allow complementary electron microscopy on the nano scale. Tests were performed on the annealing of nanoporous gold and during redox treatment of a core-shell catalyst.

The first section of the work (part II) is dedicated to the improvement and application of a gas phase microreactor, which allows the combination of several characterization techniques: XAS, XRD, Raman spectroscopy, IR thermography and on-line gas analysis. Due to the intrinsic advantages of microreactors, which will be further discussed in section 3, it allows fast heating and cooling processes. This makes the microreactor *e. g.* a perfect tool for studying transient conditions, like in the simulation of exhaust gas catalysts under realistic model driving cycle conditions. Due to its design, the reactor can be used for 2D imaging approaches and will help to understand processes on the micro and meso scale, *e. g.* heat and mass transport.

The second section of the work (part III) is dedicated to X-ray microscopy, in particular hard X-ray ptychography and its application during *in situ* studies on the meso and nano scale. It covers the application of a cell developed for complementary *in situ* ptychography and electron microscopy. Furthermore, the recent design of an optimized *in situ* cell manufactured for *in situ* ptychography is reported. By complementary *in situ* ptychography and electron microscopy, the annealing of nanoporous gold (np-Au) under different gas atmospheres was studied (section 11). Furthermore, ETEM and *in situ* ptychography were applied for studying the stability of bifunctional core-shell catalysts for direct synthesis of dimethyl ether (section 12). Both studies take advantage of the complementary character of electron microscopy and ptychography and highlight the importance of such combined methods to cover different length scales and pressure regimes.

2 Methods

The aim of this chapter is to give a brief overview on the characterization techniques employed throughout this work. Technical details on the performed experiments are discussed in the related sections of the thesis. At first, the principles of electron microscopy and X-ray radiation based techniques are discussed. Subsequently, general characterization techniques are described, such as mass spectrometry, IR thermography and Raman spectroscopy. For more details on the topic the reader is referred to the references given throughout the individual paragraphs.

2.1 Electron Microscopy (EM)

Electron microscopy uses electrons to probe the sample and is divided into transmission techniques and scanning techniques. For both techniques, the electrons are emitted by an electron gun, which is composed of a vacuum tube and the electron emitter itself. The electrons are commonly emitted by thermionic emission from a *e. g.* heated tungsten filament. By application of a potential between the filament, used as a cathode, and another anode, the emitted electrons are accelerated in the direction of the anode and can be focused and/or redirected by electromagnetic lenses. Besides thermionic emission electron guns, field emission guns are applied as well. For these guns, the emitter exhibits a very small tip and is placed in a high electrical field, which leads to a very focused emission of electrons [144]. Dependent on the technique, the so formed electrons are either tightly focused and scanned over the sample, or widened up to a large spot size with which the whole area is illuminated at once. In contrast to other microscopic techniques, EM is of particular interest since it enables higher spatial resolutions than any other microscopic technique, even down to the atomic level.

2.1.1 Scanning Electron Microscopy (SEM)

In Scanning Electron Microscopy (SEM), an electron beam with an energy of usually 5-20 kV is focused and raster scanned across the sample. Usually, the detector is placed above the sample, so that either Secondary Electrons (SEs) or Backscattered Electrons (BSEs) are detected. SEs are the electrons which were created by inelastic scattering events within the sample and commonly exhibit energies up to 50 eV. Due to the low energy, only those released from the top few nanometers of the sample can be detected. Therefore, SE contrast predominantly leads to information about the topology of the sample [145]. In contrast, BSEs are the ones which

were almost directly scattered back by the sample and thus still possess (almost) the initial acceleration energy. As the backscattering coefficient is very sensitive to the atomic number of the probed element, BSE contrast is useful to map the composition of the probed sample [146]. In the present work, SEM was used in SE contrast to pre-study the structure of the Au nanoparticles and np-Au samples used for *in situ* ptychography and to obtain complementary SEM images (*c. f.* section 10.2 and 11). For the $CuO/ZnO/Al_2O_3$-ZSM-5 catalyst, BSE contrast is applied before and after *in situ* ptychography studies to obtain a stronger chemical contrast between the core and the shell area (*c. f.* section 12).

Energy Dispersive X-ray Spectroscopy (EDX)   Besides BSEs, also X-rays and so-called Auger electrons can be used to study the composition of the probed material. They are generated by inelastic scattering processes of the incident electrons with inner shell electrons of the probed atoms. Measuring the energy of the emitted X-rays or the kinetic energy of the Auger electrons enables identifying the location of the respective energy levels. Since these discretized levels are characteristic for each atom, the results can be used to identify the probed material. Here, EDX is used to track the Cu areas $CuO/ZnO/Al_2O_3$-ZSM-5 catalyst prior to and after *in situ* ptychography.

2.1.2 Focused Ion Beam (FIB) Micromanipulation

For Focused Ion Beam (FIB) micromanipulation a dual beam FIB/SEM is used, which is equipped with an electron beam and an ion beam (usually Ga). The focused ion beam can be used, dependent on the chosen beam parameters, to ablate material or to generate SEs for SE imaging purposes. In addition to the two beam emitters, the microscope is also equipped with a micromanipulator, a small needle which is used to transfer specimens, and gas insertion system, which enables insertion of *e. g.* volatile Pt species for position and size controlled material deposition *via* reduction. For sample preparation, *e. g.* TEM lamella preparation, a FIB/SEM can be used to cut the sample and to transfer it *via* the manipulator, *e. g.* onto a TEM grid. The sample can be fixed on the manipulator by material deposition (of *e. g.* platinum) across the interface (*e. g.* lamella/TEM-grid interface) [147]. Besides micromanipulation, FIB/SEM dual beam microscopes can also be used for depth resolved imaging, by imaging and consecutive surface ablation, which can be used for tomographic studies [148].

In this work, FIB was used to prepare samples, mostly for *in situ* ptychography or TEM studies. The samples are cut and transferred onto special TEM heating chips (*c. f.* section 11.2.1.1 and 12.2.1).

2.1.3 Transmission Electron Microscopy (TEM)

Instead of measuring the electrons which are sent back from the sample, in TEM the electrons transmitted through the sample are detected. Though this technique requires delicate sample preparation, due to the low penetration depth of electrons, it is intensively used since it offers the highest spatial resolution, down to the atomic level. In this work, TEM is used to probe the nano scale of np-Au based catalysts and core-shell catalysts.

In a transmission electron microscope, the sample is commonly probed with a widened high energetic electron beam with a typical kinetic energy of 200 or 300 kV. Either the unscattered (Bright Field (BF) mode) or scattered (Dark Field (DF) mode) electrons can be used for the image construction. While during BF imaging, the thicker/denser material appears darker, in DF imaging it is the other way around [144]. Furthermore, high resolution images can be acquired by TEM as well, allowing sub-nm resolution and *i. e.* imaging of crystal planes or atom columns [18, 149]. In addition, the electron beam can also be tightly focused and raster scanned across the sample. In this mode, called scanning TEM (STEM), the contrast depends strongly on the scattering coefficient of the probed material. Therefore, High Angle Annular Dark Field (HAADF) detectors are used and materials of low atomic number appear darker, while those with a high atomic number are brighter. Due to this strong contrast, it is often applied for supported catalysts [149]. Some microscopes are furthermore equipped with special detectors for spectroscopic measurements, like for EDX or Electron Energy Loss Spectroscopy (EELS). In this work, TEM imaging is used as a complementary microscopy technique to X-ray ptychography and applied in section III.

Electron Energy Loss Spectroscopy (EELS) Besides the amount of transmitted electrons, also their kinetic energy which can be reduced due to inelastic scattering events can be measured. Since such an energy loss is characteristic for the electronic configuration of the probed material, it can be used to study composition as well as the oxidation states [150]. In this work, EELS is used to probe the oxidation state of Cu particles inside the $CuO/ZnO/Al_2O_3$-ZSM-5 catalyst qualitatively (*c. f.* section 12) and to study the composition of weak residues observed after annealing of np-Au samples (*c. f.* section 11.3.2.3).

Environmental Transmission Electron Microscopy (ETEM) Electrons strongly interact with matter and thus have a short penetration depth. Therefore, EM is usually performed under vacuum conditions. However, to reach more realistic conditions, special environmental TEMs (ETEMs) have been developed. In these microscopes, gases can be introduced close to the sample. Due to the short penetration depth, however, these microscopes are still limited to low

pressure (mbar regime, obtained by differential pumping within the electron column) conditions. [94, 95]. Another approach for the introduction of gas environments is to use special closed cells, which have thin windows and allow working under atmospheric pressure [50].

In the present work, ETEM in a differentially pumped microscope was used to study the redox behaviour of a $CuO/ZnO/Al_2O_3$-ZSM-5 core-shell catalyst (*c. f.* section 11.2.3) and the annealing of np-Au *in situ* to obtain complementary information to *in situ* ptychography at atmospheric pressure (*c. f.* section 11.3.2.2).

2.2 X-ray Based Techniques

2.2.1 Generation of X-rays – Synchrotron Radiation

For laboratory applications, X-rays are created by bombardment of metal targets with electrons, which leads to an emission of "bremsstrahlung" and the characteristic X-ray lines of the target. However, the corresponding brilliance, which describes the quality of the X-ray beam in terms of intensity, degree of divergence, source area and spectral distribution, of such X-ray tubes is low compared to X-rays produced by synchrotron radiation sources [151]. Synchrotron radiation, especially that from modern third or fourth generation synchrotron radiation sources, exhibits a high brilliance and high degree of coherent radiation. In synchrotron radiation sources, electrons or positrons are circulated inside storage rings, in which bending magnets are used to keep the electrons in a closed orbit while synchrotron radiation is emitted. The emitted intensity can be further increased, which is important for imaging techniques, by insertion devices such as undulators or wigglers, which are used to generate alternating magnetic fields resulting in an oscillating electron path [151, 152].

2.2.2 X-ray Absorption Spectroscopy (XAS)

XAS can be used to probe the local environment of an atom, like the coordination state and geometry, the neighboring atoms or the oxidation state of the probed atom. In the present work, it is used to determine the oxidation state of Pt/γ-Al_2O_3 catalysts applied in the gas phase microreactor (*c. f.* section 5.3 and 6.2).

In XAS, the absorption of the probed material in dependence of the energy of the incident X-ray beam, is determined. Therefore, X-ray sources with a tunable energy, like synchrotron radiation sources are required. Due to the photoelectric effect, parts of the incident intensity are absorbed and the atoms are excited by the X-rays. This can be measured either directly by determining the

X-ray intensity before and after the sample or indirectly by recording the fluorescence radiation which is emitted during the relaxation process of the excited atoms. By application of Beer's law, it can further be related to the absorption coefficient. Once the incident energy is high enough to excite an inner shell electron from the atom, a strong absorption is recorded in the absorption spectrum. When the emitted electron interacts with neighboring atoms, it can be back-scattered and interact with the probed atom, which results in oscillations of the absorption spectrum, the so called "fine structure". The region of the absorption spectrum around the absorption edge is called "X-ray Absorption Near Edge Structure" (XANES) and mostly used to determine the oxidation state or the symmetry of the coordination sphere of the absorber atom. The "Extended X-ray Absorption Fine Structure" (EXAFS) however, is caused by the single back-scattering events of the electron with the neighboring atoms and can be used to determine the coordination number or the bond distances to neigboring atoms [153]. A fast acquisition of XAFS measurements in the sub-s regime is useful for probing transient reaction conditions. This so-called "QEXAFS" can be *e. g.* obtained by periodically oscillating double crystal monochromators [154]. In this work, it was used to relate the fast temperature changes during driving cycle simulation to changes in the catalyst (*c. f.* section 7.2).

2.2.3 X-ray Diffraction (XRD)

XRD is used to probe the long range order of materials and is therefore a technique primarily used for studying crystalline materials. It can be used to determine the crystallographic phases of a material, which was applied for Pt/γ-Al_2O_3 catalysts in this work (*c. f.* section 5.1 and 6.2). XRD is based on the scattering of X-rays on the periodically ordered crystal planes of the probed material. According to Bragg's law, constructive interference is only obtained at certain scattering angles, while at all other angles the scattered radiation interferes destructively. Therefore, at a fixed energy, reflexes can only be observed at certain scattering angles in the diffraction pattern, which can be used to identify the crystallographic phase [1].

2.2.4 X-ray Microscopy

X-ray microscopy allows probing structures in the intermediate range between that probed by electron microscopy or by optical microscopy. X-ray microscopes can be divided into full-field microscopes or scanning microscopes.

Full-Field Imaging   Full-field imaging, also referred to as "radiography", means that the object is probed by a parallel beam which has the size of the field of view. In this work, radiography was used to image the gas-phase microreactor (*c. f.* Fig. 4.3).

Similar to an optical microscope, the image is magnified by an objective lens, which is usually a Fresnel zone plate [24, 105]. The image is detected by a position sensitive detector and different magnifications can be obtained, dependent on the distance between the objective lens and the detector [151]. Differences in the absorption coefficient of the different probed materials create the image contrast. Moreover, full-field microscopy can be combined with resonant imaging as well, when the energy is tuned around an absorption edge [24].

Scanning Transmission X-ray Microscopy (STXM)   In contrast to full-field techniques, for STXM approaches, the X-ray beam is focused by focusing optics [109, 110, 116] like Fresnel Zone Plates [111, 112] or refractive X-ray lenses [113–115], while the sample is raster scanned through the focused beam. This technique benefits from a high spatial resolution, limited by the spot size of the focused beam, and has the advantage that various contrasts, such as XRF, XRD and XAS contrast can be applied [24]. Since the image is built up pixel-by-pixel, it requires considerable longer acquisition times than full-field approaches. In this work, STXM is only applied by using scanning coherent X-ray diffraction imaging, the so-called "X-ray ptychography".

Coherent X-ray Diffraction Imaging (CDI) and X-ray Ptychography   CDI uses the partially coherent nature of X-rays obtained by synchrotron radiation. A small sample is illuminated with a large parallel beam and the far-field diffraction patterns are recorded. Since only the intensity can be measured, the phase information cannot be recorded directly, which requires dedicated "phase retrieval" algorithms to reconstruct the real-space image. Although the obtained resolution for CDI is high, this technique requires prior knowledge on the probed sample due to the complex image reconstruction [120].

X-ray ptychography is a scanning technique and uses a focused, coherent beam, through which the sample is rastered. Like for CDI, also here the far-field diffraction patterns are recorded. The spot size of the beam may vary from tens of nanometers to the micrometer range and a simultaneous recording of XRF contrast is possible, which can be used for complementary XRF-STXM. By recording diffraction patterns of overlapping steps, image reconstruction is facilitated in comparison to the full-field CDI, by the so called "over sampling". This makes hard X-ray ptychography the ideal candidate for high-resolution X-ray imaging, also for samples whose properties are relatively unknown.

The iterative phase retrieval algorithm, which is used to retrieve the phase, constantly Fourier transforms data from real space to reciprocal space and *vice versa*. For example, the estimated amplitude is obtained from the measured intensity by extracting the square root of it. This amplitude is then multiplied by a guessed phase factor and inversely Fourier transformed to result in an estimated electron density in real space. Real space constraints like "being positive and real" are then applied which are used to obtain a new electron density, which is subsequently Fourier transformed into an updated amplitude function. This can then be further optimized and the cycle can be continued until the errors are significantly reduced [151]. In this work, hard X-ray ptychography is used to obtain complementary high-resolution images to EM. The potential of hard X-ray *in situ* ptychography is highlighted in this work and discussed in section III.

2.3 General Characterization Techniques

2.3.1 Mass Spectrometry (MS)

The mass of a chemical compound is a very characteristic quantity which makes MS a useful tool to identify the composition of an unknown substance. In this work, on-line MS is used to monitor the composition of gaseous products in the reactor outlet (*e. g.* in section 6.2), which could be used for determination of the catalytic activity. In contrast to conventional MS, also spatially resolved MS could be performed, implying that the gas composition at different positions within the reactor is determined. This was not performed in this work, although it would reveal additional information during the study of gradients in reactors.

In a mass spectrometer, the gaseous sample becomes initially ionized before it is routed into the actual the mass analyzer. The latter consists of an electrical field in which the ions are deflected differently, depending on their mass m and charge z, which leads to a separation of the ions dependent on the m/z ratio [155]. Commonly, time-of-flight or quadrupole analyzers are used. In quadrupole MS, which was used in this work, the ions are accelerated before they pass the quadrupole. The electrodes opposite to each other are on the same potential, respectively, while a high frequency alternating current is applied on the electrodes next to each other. By varying the frequency, stable trajectories are obtained for different m/z ratios, which is used for mass separation. Afterwards, the amount of unblocked ions is measured by a detector like a Faraday cup or an electron multiplier [156].

2.3.2 Infrared (IR) Thermography

IR thermography is a useful tool to measure the temperature of an object since it is a contact-free measurement technique, enables high-speed data acquisition and features high spatial resolutions. In this work it is used to evaluate the temperature homogeneity of the gas phase micro-reactor and the *in situ* ptychography cells (*c. f.* section 4.1.2 and 11.3.2.1), or to study thermal gradients occurring during the CPO of methane (*c. f.* section 6.3).

As described by Planck's law, every body generates electromagnetic radiation whose intensity and spectral profile depends on its temperature. In IR thermography, this radiation, which commonly lies in the infrared regime of the electromagnetic spectrum (0.7 to 20 µm), is detected and used to identify the temperature of the studied object [157]. For this mainly two characteristics of the spectrum are monitored: the overall intensity, which increases with increasing temperature (described by the Stefan-Boltzmann law); and the wavelength at which the highest power is radiated (described by Wien's displacement law). While the generated electromagentic radiation is well described by Planck's law, the emitted radiation which is actually detected, is also influenced by the effectiveness of the object to emit radiation, commonly described by the so-called emissivity ϵ [157]. It is dependent on the probed wavelength and temperature of the material [158]. Therefore, prior to the actual measurement, the system must be calibrated (either experimentally or by using literature values for ϵ) to achieve an accurate temperature identification.

2.3.3 Raman spectroscopy

In Raman spectroscopy the characteristic vibrational bands of the probed sample are identified by using inelastic scattering of light with the probed substance. In this process, the scattering causes a shift of the photon energy by the amount of the respective vibrational excitation (*e. g.* a photon). Therefore, detection of this so-called Raman shift enables measuring the vibrational bands such that is is well suited to identify specific bonds within materials. For this, a monochromatic, high-intensity laser is used to probe the sample and the wavelength of the scattered light is measured [159].

In this work, it is used to distinguish between the Pt–Cl and the Pt–O bond in H_2PtCl_6 and PtO_2, respectively. Furthermore, Raman spectroscopy was also applied for imaging. For this, Raman spectra were recorded in a spatially resolved manner and the characteristic Raman bands were used as a contrast for construction of the image (*c. f.* section 5.2).

Part II

Complementary Characterization Techniques on the Micrometer Scale – Gas Phase Microreactor

3 Introduction –
Applications of Microreactors

The term "microreactor" denoted in former times tubular reactors with a diameter in the millimeter range [160]. Nowadays, the term is used for reactors exhibiting at least one dimension in the micrometer range which were build by microfabrication [161, 162]. The small dimensions come with some disadvantages like plugging, a difficult loading of the catalyst or small and fragile fittings, but offer numerous benefits [162–165]. Most advantages are based on the high surface to volume ratio, which microreactors exhibit due to their small dimensions [163]. Along with a fast mass transfer and narrow residence time distributions [164], in particular a fast heat transfer is regarded as very beneficial for microreactor applications in chemical processes, *e. g.* in the simulation for driving cycles (*c. f.* section 7.1). Those benefits also imply a precise and fast control of reaction parameters such as temperature, pressure and concentration, but nontheless, the small dimensions also minimize danger from exothermic reactions or toxic chemicals as only small amounts of reagents are used and the formation of hotspots is reduced due to the efficient heat transfer [166]. This does not only reduce costs and safety requirements, but makes microreactors also attractive for high-throughput applications, for testing and characterization of novel catalysts [167]. Last but not least, microreactors can also be used in industrial processes by running several microreactors in parallel, which on the one hand minimizes time and costs for up-scaling process development [160], and on the other hand reduces safety precautions.

Recently, the application of microreactors in chemical processes increased with utilization in catalysis [163, 168–171], biochemistry [172] or organic and polymer chemistry [173]. In heterogeneous catalysis, spectroscopic studies have been performed using microreactors [166, 174–178]. Additional benefit can be gained by the rapid heating and cooling possibilities. This also allows testing during transient changes of reaction parameters like gas and temperature or during modulation excitation spectroscopy experiments [179, 180]. Many studies were performed on capillaries with diameters in the mm range [55, 56, 181, 182]. With respect to *in situ* spectroscopy, additional benefit can be gained from the flat surfaces of the microreactor channel, which leads to reduced reflection from the surfaces and therefore improved data quality [42]. Another advantage using microreactors for *in situ* spectroscopic studies is that complementary techniques can be easily combined using the same reactor, e. g. IR spectroscopy [176] and thermography [40, 72], Raman spectroscopy [170], UV vis spectroscopy [183], X-ray diffraction [57], X-ray scattering [184, 185] and X-ray absorption spectroscopy [37, 175]. Moreover, spatially resolved measurements can be performed on the micrometer scale [49]. However, the use of microreactors requires considerations on sufficient detector sensitivity to follow the catalytic reaction despite the small amount of catalyst, on pressure drops caused by plugging or on more

difficult packing of the catalyst leading to bypassing of reactants.

Microreactors are often fabricated with lithographic methods and typically fabricated from silicon (Si) [163, 186], due to its high thermal stability, heat conductivity, mechanical robustness and chemical inertness. Processes for integrating additional functional structures like optical elements [187, 188], heaters and temperature sensors [169, 189] are well known and established. With respect to *in situ* spectroscopy, especially the mechanical robustness [190] enables fabrication of very thin windows. Furthermore, the rather low atomic number of Si goes along with moderate X-ray absorption. Although fabrication from Be or diamond would show even lower absorption, these materials are potentially poisonous or expensive, respectively. Therefore, Si is an ideal candidate for *in situ* cells used for X-ray studies. Such Si-based microreactors were already used as analytical *in situ* cells [174, 183, 191–193], for applications in gas sensors [194] or in CO oxidation [195].

In the following section, a silicon-based microreactor developed within a framework with the University Dresden, Göttingen, Bochum and DESY (Helmholtz Virtual Institute) and a BMBF- (Bundesministerium für Bildung und Forschung – engl. Federal Ministry of Education and Research)-funded project for development of user infrastructure for X-ray microscopy, is presented. The microreactor reported herein was manufactured by the company GeSiM GmbH (Großerkmannsdorf, Germany), and is based on the first generation developed and described by G. Hofmann [196]. The reactor and the majority of the presented results in this part are already published (Baier *et al.* [197] and Doronkin *et al.* [198]). Most of the work related to the improved design, *ex situ* and *in situ* application for the CPO of methane was performed in close collaboration with Dr. Amélie Rochet.

4 Gas Phase Microreactor, Sample Preparation and Spectroscopic Techniques

In the following section, a silicon-based gas phase microreactor which allows the combination of several techniques, such as XRD, XAS, IR thermography and Raman spectroscopy, is described. This reactor is beneficial for the application in *in situ* studies (*c. f.* section 1.1) and can be used to study the micro scale of catalysts as highlighted in section 1.1.1. Its design, fabrication and improvement with respect to heating in comparison to an earlier design is described. Additionally, the sample preparation and experimental techniques used for studies with this microreactor are presented in sections 4.2 and 4.3.

4.1 Design of the Gas Phase Microreactor

The microreactor is formed by a layer by layer design based on silicon. A channel is etched into the structure, in which the powder catalyst can be filled as a packed bed. Furthermore, a heater and a temperature sensor are located on the microreactor, allowing the reactor to be heated. The channel is located inside a silicon layer on which the heater and sensor are manufactured; another layer of either Si ("Si-Si microreactor", see section 4.1.2.1) or borosilicate glass ("Si-glass microreactor") is used to close the channel. The schematic representation of the microreactor and its layered structure is shown in Fig. 4.1. Detailed information on the single elements is given in section 4.1.1.
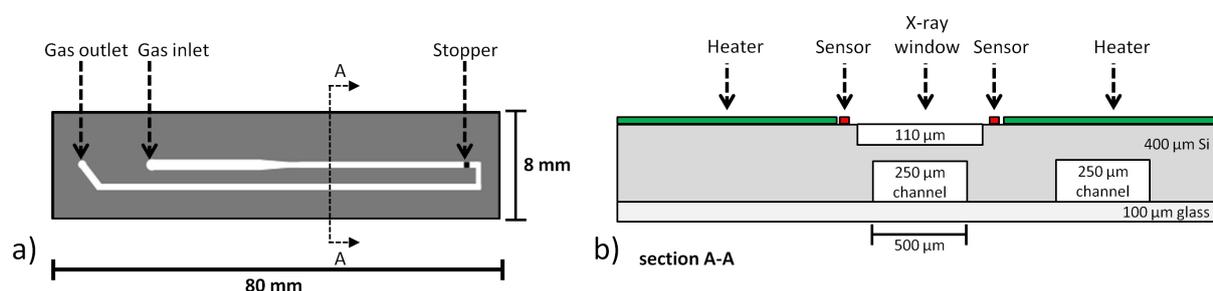
Figure 4.1: a) Schematic representation of a silicon-glass microreactor showing the U-shaped channel geometry from the glass side. The gas inlet and outlet as well as the stopper are depicted. b) Schematic representation of a section A-A as a side view. The channel dimensions, the thinned down area for the X-ray window, as well as the heater (green) and temperature sensor (red) are visualized.

The microreactor is used within a custom-built setup designed by GeSiM GmbH (Großerkmannsdorf, Germany) enabling electrical and gas connection, which is depicted in Fig. 4.2. For experiments, the whole setup composed of three parts is used:

- the microreactor itself, composed of a channel in which the powder catalyst is filled as a packed bed, a heater and a temperature sensor,

- the support for electrical connection used for heating and temperature sensing as well as for the gas connection,

- an external temperature controller (Eurotherm 2216e controlled by a LabVIEW based script) and gas feed system with mass flow controllers (Bronkhorst).
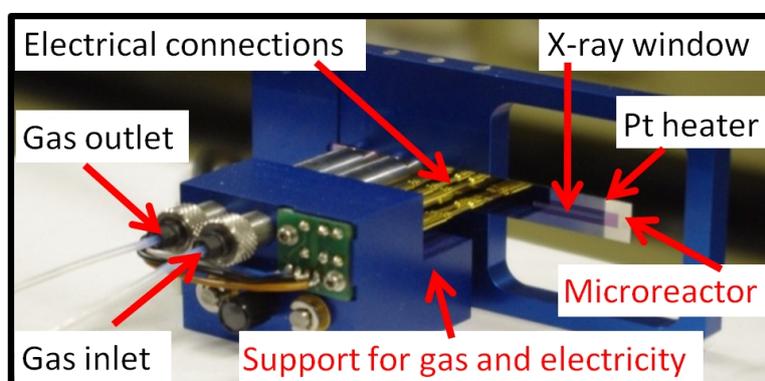
Figure 4.2: Photograph of the microreactor setup showing the microreactor positioned in the blue support part which is used for electrical and gas connection. Reprinted from [197] with the permission of AIP Publishing.

4.1.1 Fabrication and Details

The channel in the Si layer was formed by etching techniques and lithography on a 4" Si wafer and a positive resist was used for a double side optical lithography followed by deep reactive-ion etching (DRIE). Eventually, the channel was closed by anodic bonding using borosilicate glass (Borofloat glass, Schott AG Jena) [199], or silicon fusion bonding [200] for the Si-glass and Si-Si version (*c. f.* section 4.1.2.1) respectively. A channel of $500\,\mu m \times 250\,\mu m$ (width $\times$ depth) was etched inside the $400\,\mu m$ silicon layer, like in the first generation. The dimensions and positions of holes for the gas inlet (diameter $1.5\,\mu m$) and outlet (diameter $0.8\,\mu m$) were kept the same as well. Prior to mounting the microreactor into the support, the catalyst has to be filled into the channel through the inlet hole, which is also used to feed the reactants. For easier filling of the powder catalyst, the channel dimensions are broader close to the inlet hole ($1500\,\mu m \times 250\,\mu m$, width $\times$ depth) and decrease gradually to reach $500\,\mu m$ width after $10\,mm$. When the reactor is mounted in the support, O-rings which are pressed between the reactor and

the support, enable a tight connection between the reactor and the gas fed through the support. As the reactor is especially designed to be suitable with XAS experiments, the Si material was thinned down to a thickness of 40 μm, as depicted in Fig. 4.1, to improve the transmission of X-rays through the reactor. This area is referred to as an "X-ray window" and can *e. g.* improve the transmission. For example, around the Pt L_3 edge at 11.56 keV by a factor of 1.7. To define the end of the catalyst bed at the end of the X-ray window and to act as a trap for particles, a so called "stopper" was built by pillars of Si with spacings of 35-40 μm. The stopper region is represented in Fig. 4.3a by an optical micrograph showing the grain size of a sieve fraction of 100-200 μm catalyst grains with respect to the channel and stopper dimensions. Furthermore, a radiograph recorded at 11.56 keV in bright field contrast is shown in Fig. 4.3b. Thicker areas are stronger absorbing and appear darker (like the stopper inside the channel or the Pt sensor around the channel), while thinner areas like the channel and X-ray window show higher transmission and appear brighter. The spacing of the pillars from the stopper constrain the grain size used for this microreactor, but to avoid pressure drops due to plugging with too small particles, sieve fractions of 100-200 μm are recommended.
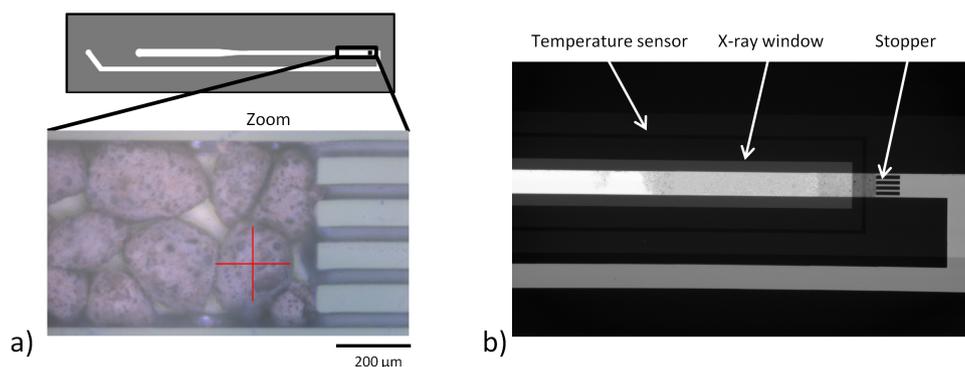
Figure 4.3: a) Scheme of the microreactor and optical micrograph of the stopper region in the channel showing catalyst grains filled into the microreactor. b) Radiograph of the channel region recorded at 11.56 keV in bright field contrast. Stronger absorbing areas (Pt heater, Pt temperature sensor, stopper) appear darker then thinner areas (channel and X-ray window).

4.1.2 Improved Heating Capabilities of the Microreactor

The microreactor is heated by an electrical current (Joule heating) through the Pt heating layer (*c. f.* Fig. 4.4). Accurate temperature control is achieved by a proportional-integrative-derivative (PID) controller which either uses an on-chip Pt sensing layer, or an externally glued Pt 100 element, as a resistive thermometer and adjusts the current flow accordingly. A 10 to 15 nm thick titanium adhesion layer was used between the silicon layer and the approximately 400 μm thick Pt heating layer, deposited by physical vapor deposition with a 4" magnetron. For improved electrical contact with the support, a 250 nm thick gold layer was added on top of the Pt layer.

The first generation of microreactors, described by G. Hofmann [196], had a simple heater design of a rectangular shaped (44 mm × 25 mm) layer around the X-ray window, which covered almost the whole microreactor area. However, a very pronounced temperature gradient could be observed (140 °C along the X-ray window [197]), which was also present along the catalytic bed. This gradient was caused by the good thermal contact at the mounting point, where the reactor temperature remained at almost room temperature. Since for controlled chemical reaction parameters a uniform temperature along the catalyst bed is required, the heating geometry was optimized for the second generation of microreactors. The difference between the first and second heater design is visualized in Fig. 4.4, showing a more efficient heating towards the beginning of the catalyst bed.
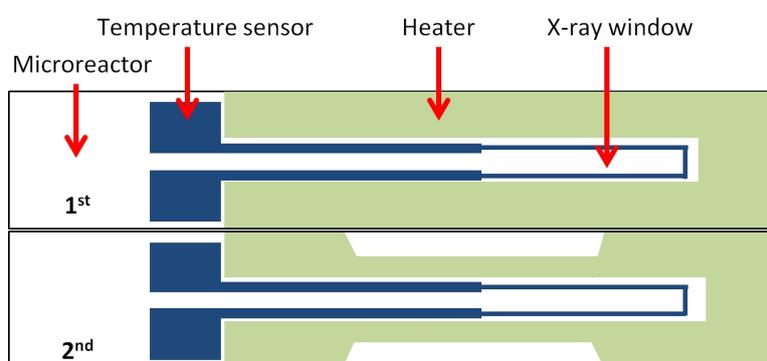
Figure 4.4: Top: Schematic representation of the two different heater designs of the first (1st) and second (2nd) heater design with the heater area represented in green and the sensor shown in blue.

The temperature homogeneity could be improved by the second heater design, which is depicted in Fig. 4.5. Different line profiles along the reactor width and length (*c. f.* Fig. 4.5b and c, respectively) are shown for different temperatures. Fig. 4.5a shows an IR thermogram of the reactor for a sensor temperature of 410 °C with respect to the positions of the line profiles. Fig. 4.5b highlights the temperature uniformity within the 250 µm wide channel, while Fig. 4.5c indicates that the gradient along the reactor length is still present, even within the X-ray window. A gradient of 50 °C could be detected at a sensor temperature of 400 °C within the complete X-ray window, which resulted in an improved temperature homogeneity by a factor of 2.8 compared to the first generation. Nevertheless, for the first 8 mm of the X-ray window, the temperature is homogeneous. For a typical catalytic bed length of 4-5 mm, gradients due to heating of the reactor can be neglected (compare ref. [197]).

To use the internal temperature sensor, calibration curves determining the resistance of the sensor with respect to the temperature have to be acquired. However, it has been shown that the temperature determined by the internal sensor differs a lot from the temperature determined with an external thermocouple attached at the first 5 mm on the X-ray window. This is shown in Fig. 4.6a and can be explained by the temperature gradient along the X-ray window. The tem-

perature sensor with its dimensions of 33.5 mm × 80 μm × 200 nm (length × width × thickness) is located around the whole X-ray window. This implies that the resistance measured on the temperature sensor corresponds to an averaged temperature around the whole X-ray window. Therefore to use the microreactors of the second generation, an external Pt 100 element was used as a temperature sensor. For future experiments, a third generation of microreactors was developed. The temperature sensor dimensions were adapted in such a way that the sensor was only located around the first 5 mm of the X-ray window, sensing just around the catalytic bed length so that the internal sensor could be used again.
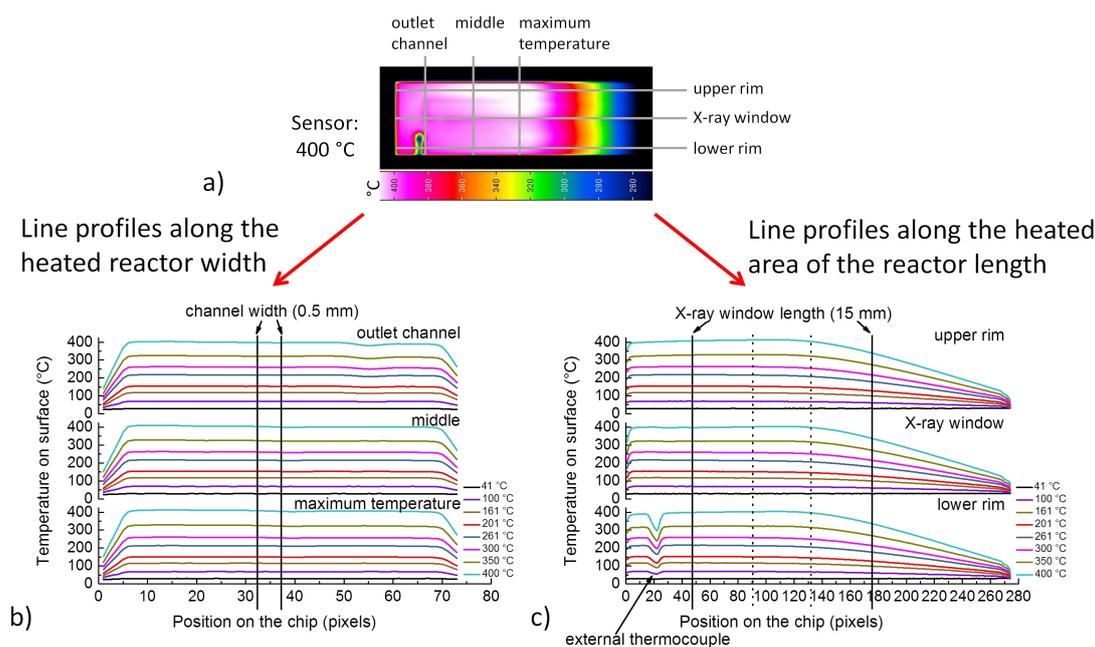
Figure 4.5: a) IR thermogram of the second generation of microreactors with the improved heater design. An external thermocouple was placed at the bottom of the microreactor. Several line profiles along the reactor are depicted for different temperatures measured by the internal temperature sensor. The positions for the profiles are marked in the IR thermogram. b) Line profiles along the reactor width showing the homogeneous temperature profile along the reactor bed. c) Line profiles along the reactor length reveal a gradient in this direction. Within the 15 mm long X-ray window, the gradient could be improved compared to the first generation and the temperature is homogeneous for the first 8 mm.

Besides the difference between the temperature measurement with the internal sensor and with an external thermocouple, it is also evident in Fig. 4.6a that the temperature measured by the external sensor decreases with time. This effect only happens during the first high temperature treatment of the reactors, after which the heating layer also looks different by visual inspection and which is shown in Fig. 4.6b by optical micrographs of a fresh (not heated before) and a used (after heating) reactor. The color change from dark to bright material after heating can also be seen by differences in the SEM images from different areas, as depicted in Fig. 4.6c and d. Fig. 4.6c shows an SEM image of the dark regions in SE contrast, whereas Fig. 4.6d shows one of the bright regions. Apart from irregularities in the surface structure, which are visible in

both images by darker areas, it becomes obvious that the surface seems rougher and particles are located on the brighter heating area in Fig. 4.6d, compared to the relatively planar and homogeneous surface depicted in Fig. 4.6c. The formation of particles and restructuring of the heater layer was also shown by SEM images after heating treatment of a typical microreactor, suggesting that the Pt heating layer ages and Pt particles sinter during use. To circumvent irregularities during application of the microreactors, a "conditioning" of the reactors prior to use and even prior to sensor calibration is required. Once the reactors were treated at the highest temperature used, they remain stable and show reproducible behavior as presented in Fig. 4.6a.
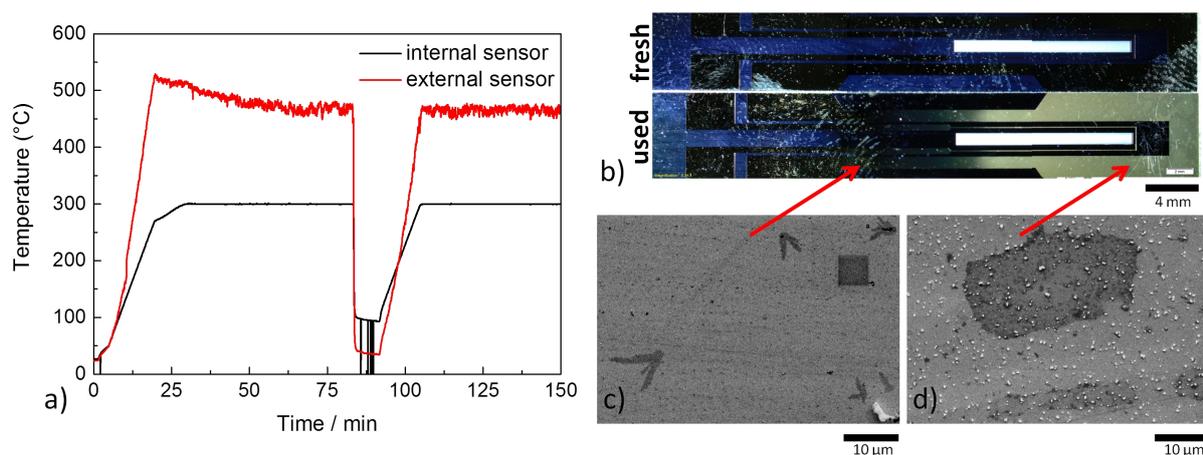
Figure 4.6: a) The temperatures measured by the internal temperature sensor (black) and an external thermocouple (red) are plotted *vs.* time showing a remarkable difference between the two sensors as well as a temperature decrease of the externally measured temperature with time. The setpoint was set to 300 °C for the heating. b) Optical micrographs of a fresh and a used microreactor revealing a color change after heating the reactors, c) SEM image in SE contrast of a dark area of a heated microreactor exhibiting a relatively homogeneous Pt surface, while d) shows a SEM image in SE contrast of a bright area of a heated microreactor and gives evidence to an irregular surface with the formation of particles on the surface.

4.1.2.1 High Temperature Application – Si-Si Microreactor

The second generation of microreactors was not only motivated by reaching an improved temperature homogeneity of the reactor, but also by gaining improved temperature stability. Using the Si-glass microreactor at T>500 °C, the borosilicate glass reaches the glass point at 525 °C [201] and undergoes structural changes. This not only influences the stability of the reactor as the reactor can start to leak, but it also influences spectroscopic data quality, as diffraction signals changing with time become visible. This is depicted in Fig. 4.7, where QEXAFS spectra of a Pt/γ-Al$_2$O$_3$ sample heated at T>500 °C are shown at different times. Diffraction signals, unstable over time, appear additionally to the XAS signal.
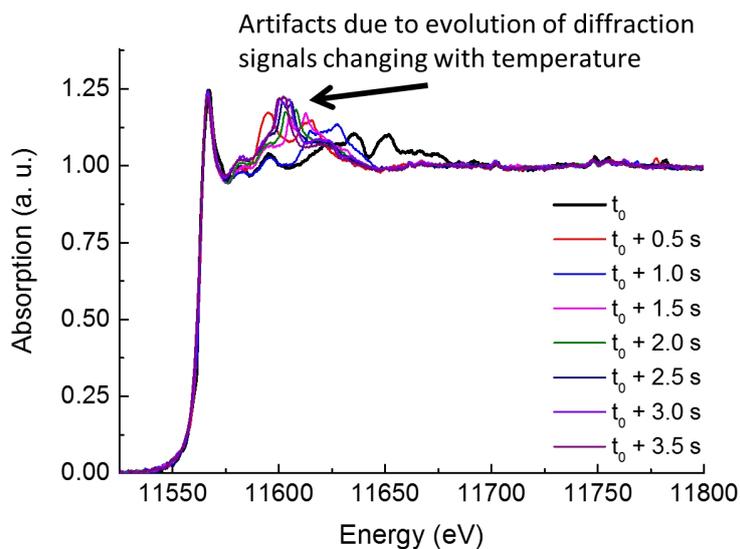
Figure 4.7: Pt L_3 XAS spectra of a Pt/γ-Al$_2$O$_3$ catalyst recorded at T>500 °C in a Si-glass microreactor. The original spectrum before the evolution of diffraction signals is shown in black, whereas the spectra influenced by the diffraction signals caused by restructuring of the Si-glass microreactor are depicted multicolored. This demonstrates, that the temperature of this microreactor should be limited to 500 °C.

In order to use the microreactor for high temperature applications, a purely Si-based design was implemented. Whereas this version has the benefit of use at higher temperatures than the Si-glass version without undergoing structural transitions, it suffers from opaqueness for visible light. The catalytic bed length however can be visualized by probing the reactor with IR radiation or with X-rays. Although the application of quartz glass would have prevented the problems caused by opaqueness, it could not be used due to the different thermal expansion coefficients between Si (2.45·10^{-6} °C^{-1}) and quartz (0.5·10^{-6} °C^{-1}) [202]. Therefore, the reactor was completely fabricated from Si, allowing use at temperatures higher than 500 °C.

This gas phase microreactor completely composed of Si was successfully applied for transient studies during the simulation of a driving cycle, described in section 7.1, however, this reaction did not require temperatures above 500 °C.

4.2 Sample Preparation and Reaction Conditions

The presented microreactor was tested for the Catalytic Partial Oxidation (CPO) of methane over Pt/γ-Al$_2$O$_3$ catalysts and for the Selective Catalytic Reduction (SCR) of nitrogen oxides using Cu zeolite catalysts. Therefore, dedicated catalysts were prepared. Catalyst preparation and reaction conditions are described in the following part.

4.2.1 Catalytic Partial Oxidation of Methane - Catalyst Preparation and Reaction Conditions

The 4 wt.% Pt/γ-Al$_2$O$_3$ sample used in this work was prepared by Sabrina Conrad by incipient wetness impregnation of γ-Al$_2$O$_3$ with an aqueous solution of H$_2$PtCl$_6$ (hexachloroplatinic acid). After drying at 70 °C, the sample was calcined for 2 h at 500 °C before it was reduced for 5 h at 400 °C under 5 % H$_2$/He [203]. TEM images revealed a Pt metal particle size around 1.5 nm resulting in a dispersion of 63% [47]. A sieve fraction of 100-200 μm powder catalyst was loaded inside the reactor channel to result in a 4.5 mm long catalyst bed.

The CPO was carried out from Room Temperature (RT) up to 450 °C in steps of 5 °C in a premixed gas mixture of 6 %CH$_4$/3 %O$_2$/He with a total flow of 2.6 ml/min provided by mass flow controllers (Bronkhorst). The mass spectrometer signals for H$_2$, H$_2$O, CO$_2$, O$_2$ and CH$_4$ were monitored. Additionally, for proof of concept measurements, a 20 wt. % Pt/γ-Al$_2$O$_3$, a 20 wt. % Pt/γ-Al$_2$O$_3$ and an each 2.5 wt. % Pd,Rh/γ-Al$_2$O$_3$ sample were prepared similarly by incipient wetness impregnation.

4.2.2 Selective Catalytic Reduction of NO$_x$ during Simulation of the New European Driving Cycle – Catalyst Preparation and Reaction Conditions

Catalyst Preparation   A Cu-ZSM-5 zeolite sample was prepared by aqueous ion-exchange of NH$_4$-ZSM-5 zeolite (Si/Al ratio=11, Clariant) by Dr. Dmitry Doronkin. A 0.05 M Cu(II)acetate (Merck) solution was stirred with 5 g of the zeolite at 20 °C for 24 h. After separation of the solid by filtering, it was washed with 1 L of de-ionized water and dried at 80 °C over night. The calcination was carried out at 500 °C for 4 h. From XAS, the estimated Cu concentration was 2.9 wt.% [198]. A sieve fraction of 100-200 μm powder catalyst was loaded inside the reactor channel resulting in a 4-5 mm long catalyst bed.

Reaction Conditions   For driving cycle simulations, a gas feed containing 1000 ppm NO, 1000 ppm NH_3, 5 % O_2 and H_2O in He (GHSV $1 \cdot 10^6$ h^{-1}, 10 ml/min total flow) was provided by mass flow controllers (Bronkhorst). The mass spectrometer signals for N_2, NO, NO_2, N_2O and NH_3 were monitored. The temperature cycles were based on [204] and required heating ramps up to 300 °C/min.

4.3 Experimental Techniques

The microreactor presented in this chapter was developed to allow complementary characterization techniques, especially X-ray based techniques, and other spectroscopic methods. In the following, experimental details on the methods used for testing the applicability of the microreactor, namely XRD, XAS, radiography, Raman spectroscopy, IR thermography and MS, are given.

4.3.1 Temperature Measurements by IR Thermography

IR thermography was used to track the temperature along the microreactor: for evaluation of the microreactor design and for tracking temperature gradients or hot spots occurring during chemical reaction. The temperature was recorded from the Si-side of the reactor using an IR camera (VarioCam® HD 1024×768 mobile, InfraTec) which recorded the emitted thermal (infrared,7.5-13 µm optical wavelength) radiation from the sample. For evaluation of the temperature homogeneity, images were taken with a frequency of 1 Hz, whereas for the CPO, a frequency of 6 Hz was applied. The software IRBIS® 3 plus was afterwards used for thermography evaluation.

4.3.2 Raman Spectroscopy

For *ex situ* evaluation as a proof of principle study, a set of differently pre-treated model catalysts containing 20 wt.% Pt/γ-Al_2O_3 (prepared by Dr. Amélie Rochet by incipient wetness impregnation, drying and calcination at 150 °C and 500 °C, respectively) and pure γ-Al_2O_3 were filled as stacked parts into the Si-glass microreactor (*c. f.* section 4.1). An area of 4063.4 µm × 678.9 µm was probed by Raman spectroscopy with an inVia Raman microscope (Renishaw) at 532 nm. A step size of 9.7 µm and an exposure time of 10 s per sprectrum were used for one scan. To distinguish the different parts and to match the Raman spectra with the white light image, a direct classical least squares component analysis was used by Renishaw and overlaid with the white light image.

4.3.3 On-line Mass Spectrometry

An on-line MS (THERMO$^{\text{STAR}}$™ Pfeiffer) was directly connected to the gas outlet of the micro-reactor and used for product composition analysis during the CPO of methane. During selective catalytic reduction of NO_x under transient conditions, a Hiden Analytical QGA mass spectrometer provided by SLS was used, which was connected to the outlet of the microreactor by a T-piece.

4.3.4 Measurements with Synchrotron Radiation

4.3.4.1 Catalytic Partial Oxidation of Methane

XRD   The XRD measurements were performed at the SUL-X beamline at ANKA (Karslruhe, Germany) at an energy of 16 keV with an acquisition time of 20 s. A CCD detector was placed 85 mm behind the sample and a focused X-ray beam with a size of $100 \times 100\,\mu m^2$ was used. Data evaluation was performed using the FIT2D software [205] and a LaB_6 sample for calibration. Parameters used as reaction conditions are given in section 4.2.1.

XAS   XAS measurements with a focused beam were performed around the Pt L_3 edge directly after the XRD scans. Using the microreactor with a 250 μm channel depth, only a small edge jump was expected and XAS measurements were performed in fluorescence mode with a 7 element Si(Li) fluorescence detector (Graham Scientific Instruments) up to 16 Å^{-1} and an acquisition time of 13 min per spectrum. Parameters used as reaction conditions are given in section 4.2.1.

To compare the quality of XAS data recorded with conventional reactors, *e. g.* capillary reactors [56, 181], XAS of a 2.5 wt.% Pt-2.5 wt.% Pd/γ-Al_2O_3 sample (prepared by incipient wetness impregnation of γ-Al_2O_3 with an aqueous solution of $Rh(NO_3)_3$ and $Pd(NO_3)_3$, dried at 70 °C and calcined for 2 h at 700 °C) was recorded in the microreactor and in a capillary reactor. Measurements were performed at the SuperXAS beamline [154] at SLS, Switzerland, using the microreactor or a quartz capillary reactor (outer diameter 1 mm, inner diameter 980 μm, Hilgenberg). XAS spectra were recorded in fluorescence geometry for the microreactor and in transmission geometry for the capillary reactor [206].

XAS data analysis was performed with the Athena graphical interface [207] and normalization was performed using the flattening algorithm in the default energy range used by Athena. Linear combination fitting (LCF) was used from -40 – 120 eV around the Pt L_3 edge and the initial oxidized and the most reduced catalyst were used as standards.

Radiography   For radiography images, as depicted in Fig. 4.3, bright field contrast radiographs were recorded at the TOPO-TOMO beamline at ANKA [208] using a PCO.4000 CCD detector coupled to a YAG:Ce scintillator. Coupling to an optical system provided a magnification of 3.5 x [208]. A field of view of 10 mm × 6.7 mm (height × width) with an effective size of 2.5 μm was probed with a sample-detector distance of 1.9 cm and 2 s integration time.

4.3.4.2 Selective Catalytic Reduction of NO$_x$ during Rapid Heating and Cooling

XAS Measurements   *Operando* XAS measurements around the Cu *K* edge were carried out by Dr. Dmitry Doronkin, Dr. Federico Benzi and Dr. Thomas Sheppard at the SuperXAS beamline [154] at SLS, Switzerland. QEXAFS measurements were performed using a Si(111) channel cut monochromator operating at 10 Hz [154] while the spectra were collected in transmission mode using special ionization chambers for quick data acquisition [209]. The beginning of the catalyst bed was probed with a $100 \times 100\,\mu m^2$ focused X-ray beam. The recorded spectra were averaged, nomalized and treated by LCF analysis using the JAQ 2 software (by O. Müller, P. Becker and R. Frahm). The spectra at 50 °C and 350 °C under SCR conditions were used as references for for LCF, which was performed by Dr. Dmitry Doronkin. Parameters used as reaction conditions are given in section 4.2.2.

5 Suitability of the Gas Phase Microreactor for XRD, XAS and Raman Spectroscopy

This chapter describes *ex situ* measurements to evaluate the applicability of the reactor for the required measurement techniques. As the microreactor was especially developed for the use XAS and XRD measurements, the distortion free acquisition of the reactor is presented, as well as the applicability of the Si-glass reactor for Raman spectroscopy.

5.1 XRD Measurements

XRD is a useful method for determining the crystalline phases of a probed material [1]. For heterogeneous catalysis, the long range order of catalysts can be probed and information on the oxidation state as well as on preferred orientations can be gained additionally to the determination of the phase. To evaluate the application of the microreactor in XRD measurements, reference samples, the empty reactor and a model catalyst were measured *ex situ*. XRD patterns of reference samples, including the empty microreactor, are shown in Fig. 5.1. At first, a LaB$_6$ reference sample was measured inside a capillary (inner diameter 280 μm, outer diameter 300 μm, Hilgenberg; pattern shown as a black dashed line) and inside the reactor (pattern in red). The good agreement between both reactors with perfectly overlaying reflections highlights the applicabilty of the microreactor for XRD measurements. The observed background signal for the empty reactor channel (green pattern) is due to amorphous glass and silicon. Since it is relatively weak and broad from 3 ° to 20 ° (2θ), it does not significantly influence the signal quality. Moreover, the XRD pattern of the Pt heating layer is depicted in blue (Fig. 5.1), showing well-defined reflections which are characteristic for metallic Pt. While probing this layer in future experiments, the resulting pattern can be used for calibration instead of requiring other references.

Fig. 5.2 shows XRD patterns of the a pure γ-Al$_2$O$_3$ catalyst support and a reduced 5 wt.% Pt/γ-Al$_2$O$_3$ catalyst, which were acquired inside different microreactors. Additionally, the theoretically expected XRD pattern for bulk metallic Pt [210] is shown. Even though most of the reflections expected for Pt overlap with those of the pure support, the Pt (013) reflection at 38 ° (2θ) is clearly observable. This observation indicates big Pt crystallites, although only a Pt loading of 5 wt. % was used. However, also TEM revealed the appearance of big Pt particles. Nevertheless, the observation of the Pt (013) reflection at 38 ° (2θ) demonstrates that the microreactor can be applied for XRD measurements for real catalyst samples.
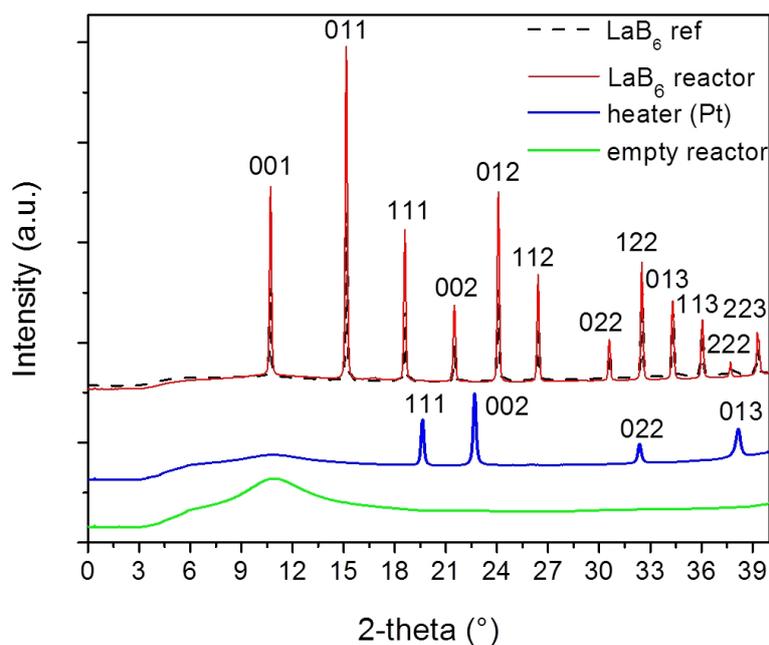
Figure 5.1: XRD patterns of the empty reactor recorded on the channel (green) and on the heater area (blue). LaB_6 XRD patterns recorded as a reference sample studied inside a reference capillary (black, dashed) and inside the microreactor (red). Reprinted from [197] with the permission of AIP Publishing.
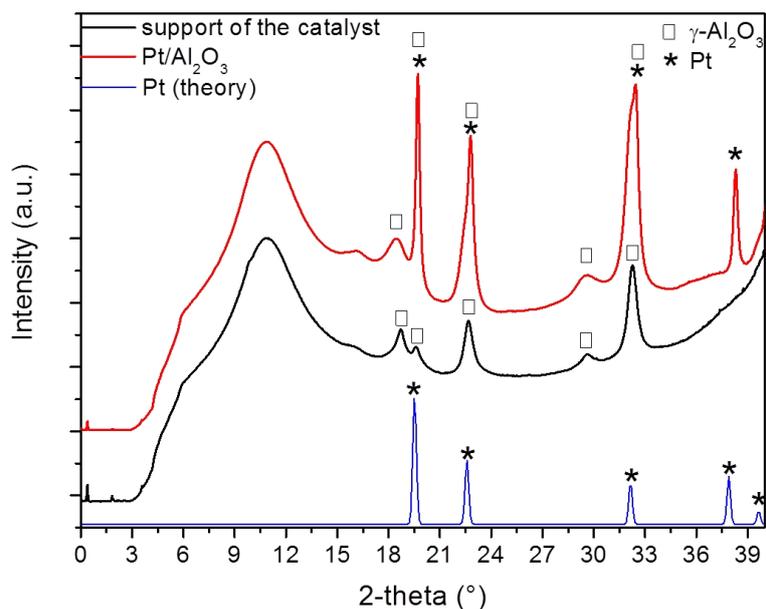
Figure 5.2: XRD patterns of a reduced 5 wt.% Pt/γ-Al_2O_3 catalyst (red) and a pure γ-Al_2O_3 catalyst (black) inside the microreactor. The theoretically expected reflections for metallic platinum are depicted in blue. Reprinted from [197] with the permission of AIP Publishing.

5.2 Raman Spectroscopy

Using Raman spectroscopy, the vibrational bands of materials are probed on changing the polarization of the material [159]. For heterogeneous catalysis, it is mostly used to probe the catalyst composition. For example, when probing a solid catalyst with hard X-rays during a reaction in which carbon can be formed on the catalyst, it can be helpful to probe the carbon, which cannot be probed with hard X-rays directly. Especially in this reactor, the flat window design is beneficial for Raman spectroscopy, since reflections due to bent surfaces are reduced [42].
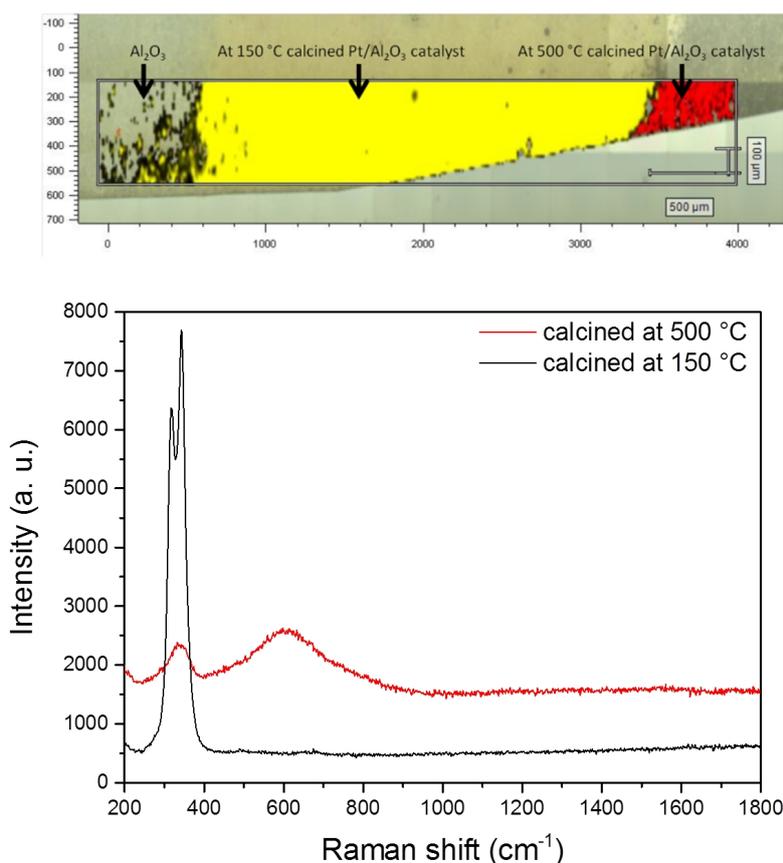
Figure 5.3: Top: White light image with overlaid Raman spectroscopy results for a stack of Pt/γ-Al$_2$O$_3$ samples which were calcined at different temperatures (150 °C depicted in yellow and 500 °C depicted in red) and a pure γ-Al$_2$O$_3$ sample (grey). Bottom: Selected Raman spectra of the catalysts calcined at 150 °C (black) and 500 °C (red). Reprinted from [197] with the permission of AIP Publishing.

As a proof of principle for Raman spectroscopy and microscopy within the Si-glass microreactors, a selected area of two 20 wt.% Pt/γ-Al$_2$O$_3$ samples, calcined at different temperatures, and a pure γ-Al$_2$O$_3$ sample was imaged by recording Raman spectra at different points within the area. The white light image was overlaid with the spectroscopic information in order to track the differences resolved by spectroscopy inside the image. Fig. 5.3 presents the white light image with the overlaid Raman spectroscopy results on top, as well as on the bottom selected Raman signals for the catalyst samples treated at 150 °C and 500 °C, respectively. The

results clearly show the differences between the pure support (grey) and the samples calcined at different temperatures (yellow: 150 °C, red: 500 °C), which are also obvious in the bottom part showing single Raman spectra. Bands at 319 cm^{-1} and 344 cm^{-1} were recorded for the catalyst calcined at 150 °C, whereas the one calcined at 500 °C shows a distinct band at 338 cm^{-1} and a very broad band at 600 cm^{-1}. The clear bands at 319 cm^{-1} and 344 cm^{-1} can be related to the catalyst precursor material H_2PtCl_6 [211], which can be attributed to an incomplete decomposition of the precursor at this low temperature. However, after calcination at 500 °C, the broad band at 600 cm^{-1} can be assigned to PtO_2 [212], which was formed after decomposition of the precursor. The band 338 cm^{-1} was observed for highly dispersed Pt/γ-Al_2O_3 catalysts previously [213, 214], which is expected for the produced Pt/γ-Al_2O_3 catalyst. Therefore, the performed Raman imaging clearly showed the applicability of the Si-glass microreactor for Raman spectroscopy and microscopy.

5.3 XAS Measurements

For comparison of the quality of the XAS data recorded in the new microreactor in comparison to conventional *in situ* cells such as quartz-based capillary reactors, measurements have been performed in both reactors. *Ex situ* measurements were acquired on a 2.5 wt.% Rh-2.5 wt.% Pd/γ-Al_2O_3 sample at the SuperXAS beamline at SLS [154] at the Pd and Rh *K* edges in transmission geometry for the sample inside the quartz capillary reactor and in fluorescence mode for the sample inside the silicon-based microreactor. Fig. 5.4 shows a comparison of the XANES spectra within the microreactor (black) and the capillary (red) of the Pd and the EXAFS spectrum of the Rh *K* edge, additionally for the Rh *K* edge the k^2-weighted χ(k) functions are depicted.

The data obtained for both edges within both reactor types show a good agreement without significant differences, which prompts to the conclusion that the microreactor can be used for XAS measurements while introducing hardly any artifacts in the spectra.
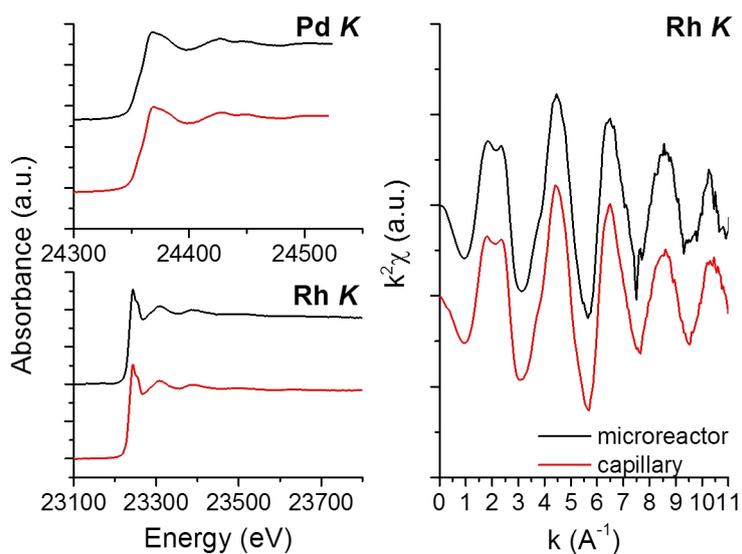
Figure 5.4: XAS spectra at the Rh and Pd K edges of a 2.5 wt.% Rh-2.5 wt.% Pd/γ-Al$_2$O$_3$ catalyst within the microreactor (black) and a capillary reactor (red). For the Pd K edge, XANES spectra are given, whereas for the Rh K edge, complete EXAFS spectra and the k^2-weighted χ(k) functions are shown. Reprinted from [197] with the permission of AIP Publishing.

6 Application of the Gas Phase Microreactor during the Catalytic Partial Oxidation of Methane

The CPO of methane exhibits pronounced gradients on the micrometer scale [37, 38, 72, 81, 83, 84, 215, 216] as already introduced in section 1.1.1. Therefore, it was chosen as a test reaction to evaluate the applicability of the gas phase microreactor for complementary spatially resolved studies. The application of *in situ* XAS, XRD, IR thermography and on-line MS are shown in this chapter. Gradients in oxidation state and temperature are correlated with catalytic activity and similar results as obtained in conventional capillary reactors were gained, showing the suitability of the gas phase microreactor for *in situ* studies.

6.1 Introduction to the Catalytic Partial Oxidation of Methane

The CPO of methane using noble metal catalysts to produce synthesis gas recently attracted a lot of attention [37, 83, 84, 217]. Methane is an important chemical feedstock and can be converted by CPO to synthesis gas (H_2 and CO), which can subsequently be transformed into alcohols or liquid hydrocarbons resulting in gas-to-liquid-processes. Furthermore, it is widely applied for solid oxide fuel cells. Improving on such processes usually demands a better understanding on the structure of the active sites of the catalyst, as already highlighted in section 1. For the CPO of methane during the ignition and extinction of the reaction, pronounced gradients in oxidation state and temperature have been found along the catalyst bed for different noble metals [37, 38, 72, 81, 83, 84, 215, 216]. Those can be related to a total combustion of methane in the first part of the catalyst bed and a subsequent reforming process [83, 217]. However, also a direct partial oxidation was suggested for the formation of synthesis gas [38]. The strongly exothermic total combustion with $\Delta_r H$= -803 kJ mol^{-1} [72], and the change to the less exothermic partial oxidation with $\Delta_r H$= -36 kJ mol^{-1} [72] result in non-isothermal conditions which might lead to special safety precautions in bigger reactors. Therefore the use of microreactors exhibiting a pronounced heat transfer is favorable for this reaction. In the following *in situ* studies, a 4 wt.% Pt/γ-Al$_2$O$_3$ catalyst was studied during CPO of methane to validate the use of the microreactor for *in situ* studies.

6.2 XAS and XRD during the CPO of Methane

The applicability of the microreactor for XAS spectra under *ex situ* conditions was already shwon in section 5.3. In the following, XAS spectra were recorded during reaction conditions of the CPO of methane. Representative XAS spectra of the catalyst during the first two cycles of the CPO are presented in Fig. 6.1.
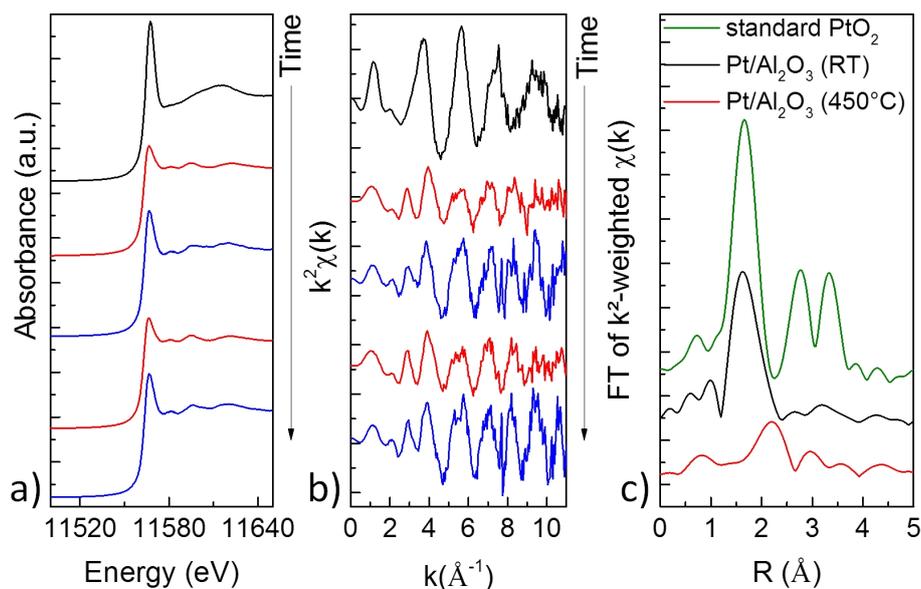
Figure 6.1: XAS spectra of the Pt L_3 edge during the first two cycles of the CPO of methane over a 4 wt.% Pt/γ-Al$_2$O$_3$ catalyst for the measurements at the end of the catalytic bed. The spectrum during heating up is represented in black, whereas the maximum temperature is shown in red and the cooling process is given in blue, a) shows the XANES spectra, b) the corresponding k^2-weighted χ(k) functions and c) the Fourier transforms of a PtO$_2$ reference and the initial catalyst at RT as well as at T=450 °C.

The XAS spectra during heating up (black), at maximum temperature (T=450 °C, red) and during cooling down (blue) are presented in Fig. 6.1a, whereas the corresponding k^2-weighted χ(k) functions are shown in Fig. 6.1b. On the right in 6.1c, the Fourier transforms (FT) of a PtO$_2$, the initial catalyst at RT and the catalyst at 450 °C are shown. As evident from the FT, the initial catalyst at RT exhibits a strong peak around 1.7 Å (without phase correction), which is also present in the PtO$_2$ reference and can be attributed to Pt–O. At higher R-values, no other backscattering peaks could be observed, which can be ascribed to small PtO$_2$ nanoparticles with a high dispersion. This goes along with the absence of XRD signals (see below, Fig. 6.2) and the small crystallite sizes gained from TEM analysis [47]. Under reaction conditions by applying a higher temperature, a change in the whiteline intensity can be observed (black spectra vs. red spectra in Fig. 6.2) with changes in the EXAFS functions (Fig.6.1b) as well. During cooling down (blue spectra), the whiteline intensity increases again. This observation can be explained by a change in oxidation state, reducing the oxide with increasing temperature and reoxidizing

metallic Pt with decreasing temperature. The reduction at high temperature can also be seen in the FT (Fig. 6.1c), revealing the disappearance of the signal at 1.7 Å with evolution of a signal at 2.2 Å (not corrected for phase-shift) attributed to the formation of Pt particles and a Pt neighbor, visible as first backscatterer in the Fourier transformed EXAFS spectrum.
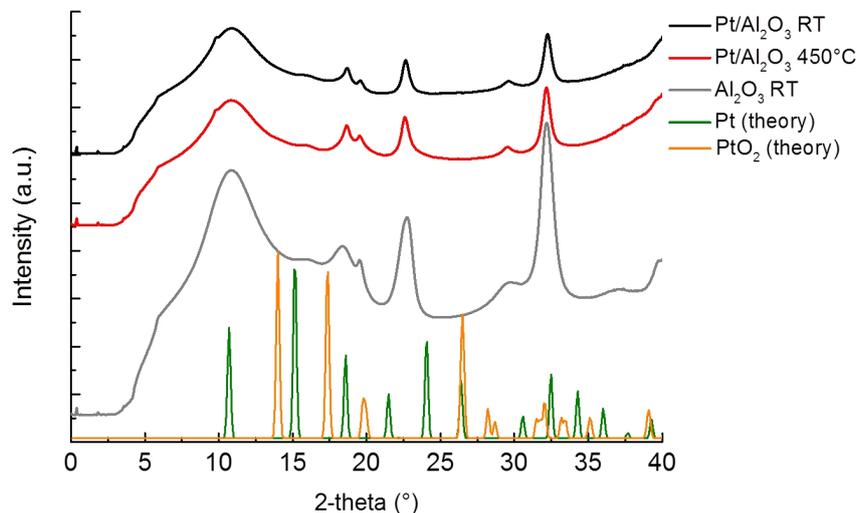
Figure 6.2: XRD patterns of the 4 wt.% Pt/γ-Al$_2$O$_3$ catalyst in the initial state at RT (black) and at maximum temperature during CPO (450 °C, red). Hardly any changes could be detected. Additionally, the XRD pattern of the catalyst support γ-Al$_2$O$_3$ (grey) is depicted together with the theoretically expected reflections for metallic Pt (green) and PtO$_2$.

Fig. 6.2 shows complementary XRD patterns of the catalyst in the initial state (black) and at the maximum temperature (red), similarly to these depicted in section 5.1. Additionally to XRD patterns of the catalyst at different temperatures, the γ-Al$_2$O$_3$ support inside the microreactor is depicted (grey) as well as the theoretically expected patterns for metallic Pt (green) [210] and PtO$_2$ (orange) [218]. For all conditions, no other reflections than the pure γ-Al$_2$O$_3$ support could be observed. If the particles had sintered, a Pt reflection at 38 ° (2θ) should have been observed (compare Fig. 5.2) showing that no significant sintering of the nanoparticles occurred. To correlate the catalytic activity and changes in oxidation state, the MS signals for the formation of H$_2$ and the consumption of O$_2$ are depicted together with the fraction of Pt species in Fig. 6.3. The fractions of Pt species were obtained by LCF of the XANES spectra for the beginning (closer to the gas inlet) and the end of the catalyst bed (closer to the gas outlet), respectively. Simultaneously to the detection of H$_2$, which indicates the ignition of the CPO, a reduction of the originally partly metallic and oxidic Pt catalyst species started at the end of the catalyst bed. At the beginning of the catalyst bed, such a reduction could only be observed at higher temperature. Then, the whole catalyst bed was completely reduced. When the temperature was decreased, the start of the catalyst bed was reoxidized at higher temperature than its end. These observations reveal that shortly after ignition and shortly before extinction, gradients over the catalytic bed can be observed, if the reactor is probed in a spatially resolved way.
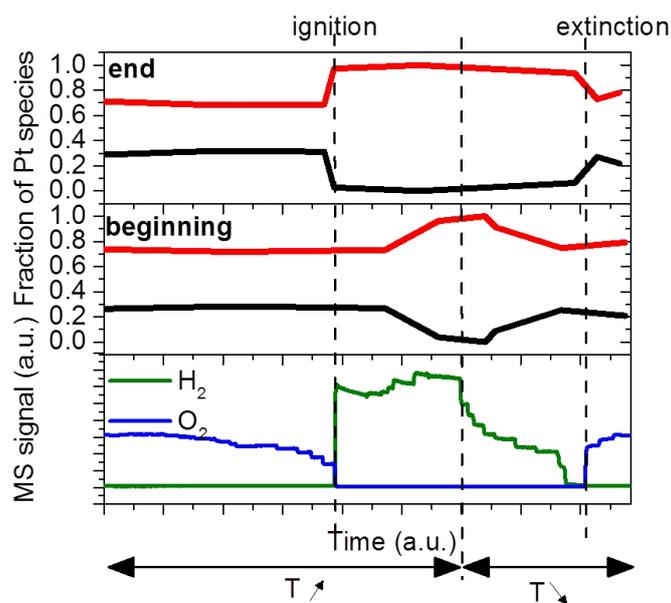
Figure 6.3: Top: Fraction of Pt species at the end and the beginning of the catalyst bed showing the reduced fraction in red, whereas the oxidic fraction is depicted in black. The fractions are obtained by LCF of the XANES spectra which were collected *in situ* during the CPO of a 4 wt.% Pt/γ-Al$_2$O$_3$ catalyst. Bottom: MS signals for H$_2$ and O$_2$, revealing the catalytic activity of the probed catalyst. The formation of H$_2$ can be correlated to the evolution of metallic Pt species at the end of the catalyst bed. Reprinted from [197] with the permission of AIP Publishing.

6.3 IR Thermography during the CPO of Methane

Recent studies showed that the gradient in oxidation state goes along with hotspot formation in the catalyst bed [72, 83]. Studying temperature gradients caused by a reaction requires the temperature obtained during heating to remain stable. This was proven in section 4.1.2, which allows the gas phase microreactor to be used to study temperature gradients within the CPO of methane.

To study the appearance of the hotspot within the microreactor, IR thermography was performed to evaluate the temperature distribution along the catalyst bed. Representative IR thermograms for the extinction and line profiles of the temperature along the catalytic bed for the ignition are shown in Fig. 6.4. During ignition, first a hot spot was observed at the end of the catalytic bed, which shifted to the beginning of the catalytic bed with increasing temperature. During extinction, the process occurred vice versa showing a shift from the beginning of the catalytic bed to the end of the catalytic bed. The hotspot detected within the microreactor, showed only a temperature difference of 2-3 °C, which is much lower compared to the one detected in conventional capillary reactors [72], although the general behavior of the hotspot movement was comparable [216]. Most reasonably, this difference in temperature can be explained by a higher thermal conductivity of the Si ($150\,W\,m\,K^{-1}$ [219]) compared to quartz glass ($1.4\,W\,m\,K^{-1}$ [220]), in addition to the high surface to volume ratio provided by the micoreactor leading to a faster heat exchange.
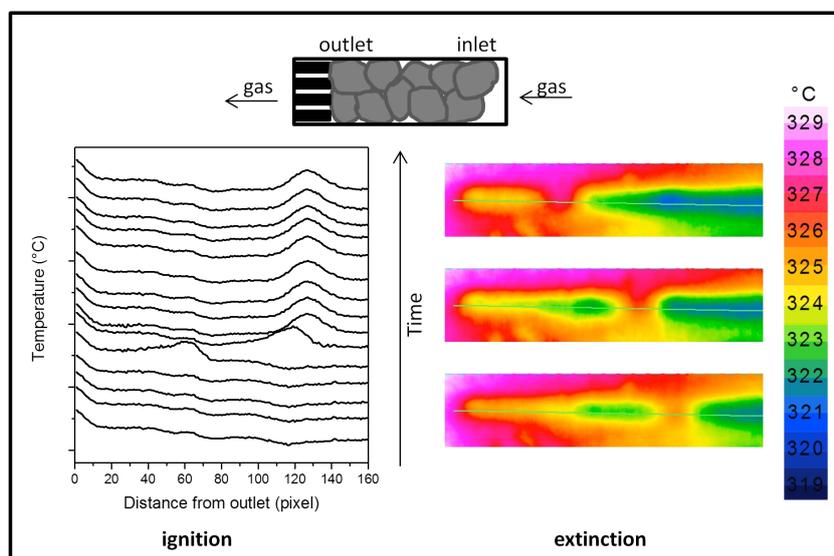
Figure 6.4: Left: Temperature profiles along the catalytic bed during the ignition of the CPO of a 4 wt.% Pt/γ-Al$_2$O$_3$ catalyst reavealing a hot spot moving from the end of the catalyst bed to the beginning with increasing temperature. Right: IR thermograms during the extinction of the reaction revealing a hot spot moving from the beginning of the catalyst bed to the end of the catalyst bed with decreasing temperature. Reprinted from [197] with the permission of AIP Publishing.

By correlation of the IR thermography data with MS and XAS data, it can be concluded that the hotspot follows the reduction front, which is also shifted from the end of the catalyst bed to the beginning when the temperature is increased after ignition. Therefore, it is assumed that the high temperature caused by the strongly exothermic total combustion of methane leads to a reduction of the catalyst. With increasing temperature, the hotspot shifts to the beginning of the catalyst and induces a reduction as well, which explains the movement of the hotspot and the reduction front during ignition and extinction of the CPO.

These results obtained during the CPO of methane show that the gas phase microreactor can be used to study reactions under *in situ* conditions. It allows applying a variety of characterization techniques like XAS, XRD, on-line MS and IR thermography and leads to similar results as obtained in conventional *in situ* cells, like quartz-based capillary reactors.

7 Application under Transient Conditions – Proof of Principle and Outlook

One of the key advantages of the presented gas phase microreactor are its fast heating and cooling capabilities. These enable studying catalysts under transient conditions, *i. e.* during the conduction of realistic driving cycles in exhaust gas aftertreatment. This chapter presents first *operando* QEXAFS measurements during the conduction of the New European Driving Cycle (NEDC). The already published measurements (*c. f.* ref. [198]) were performed on the selective catalytic reduction of NO_x over a Cu-ZSM-5 zeolite and serve as a proof of principle study for the application of the microreactor for studying transient reaction conditions.

7.1 Introduction to the Selective Catalytic Reduction of NO_x and Driving Cycles for Exhaust Gas Aftertreatment

The fast heat transfer and local heating provided by microreactors was already mentioned in section 3. It is especially promising for studying reactions in transient regimes, *e. g.* when fast heating or cooling is required. Therefore, it offers knowledge on reaction mechanisms during modulation excitation spectroscopy experiments [180]. Furthermore, it can be used to study realistic applications, including simulation of realistic driving cycles for exhaust gas aftertreatment systems [221]. Besides environmental motivations to reduce the amount of harmful exhaust emissions, the strict European legislation requires a continuous improvement of automotive catalysts. Among others, the emission of nitrogen oxides (NO_x) has to be reduced which is achieved by selective catalytic reduction (SCR) catalysts to convert NO_x to N_2. For this, ammonia (NH_3) is usually added to the reaction mixture and copper- or iron-based zeolite catalyst are applied. Although this approach is widely used, the exact mechanism is still under discussion [222, 223]. Laboratory experiments are often simplified, which is why realistic test conditions, so called "driving cycles" were developed for testing exhaust gas catalysts [221]. The New European Driving Cycle (NEDC) mimics a vehicle during driving by defining the vehicle speed. By definition of the speed, the catalyst application parameters, such as temperature, gas concentration or GHSV are characterized. However realistic driving behavior like fast braking or acceleration, implies fast temperature changes, which can hardly be simulated by conventional catalyst testing systems. By using specially developed bench test systems, the driving cycles can be simulated, but currently, no test benches compatible with *operando* spectroscopy were reported so far. Here, the benefit of fast heat transfer provided by microreactors can be used and the first application of the above described microreactors for application during

the simulation of a NEDC is shown. *Operando* studies of a working catalyst were gained by QEXAFS measurements, while the catalytic performance was determined. Measurements were carried out by Dr. Dmitry Doronkin, Dr. Federico Benzi and Dr. Thomas Sheppard [198].

7.2 Conduction of the New European Driving Cycle (NEDC) during *operando* NH_3-SCR

In Fig. 7.1, Cu XANES spectra are presented during different conditions. On the left, a model gas feed under steady conditions is used. Spectra were acquired under NO/He and NH_3/He, respectively to provide reference data for Cu^+ (in NH_3/He) and Cu^{2+} (in NO/He). On the right, spectra acquired during SCR feed (*c. f.* section 4.2.2) are presented for temperatures of 50 °C and 350 °C respectively. Those spectra differ significantly from those shown on the left. By monitoring the mass signals for the exhaust in parallel to the QEXAFS acquisition, it was shown that the catalyst was inactive at 50 °C, whereas it was active at 350 °C. By the different spectra recorded under model conditions and during realistic SCR feed, it becomes clear that the spectra during SCR feed cannot easily be explained by a pure change in oxidation state. In contrast, by comparison with XAS spectra recorded in a conventional capillary reactor [85], it can be assumed that the changes recorded during SCR feed, can be explained by a change in Cu coordination geometry instead. At low temperature, the Cu sites showed five ligands (black spectrum), whereas the active catalyst at 350 °C (blue spectrum) exhibits a coordination sphere with three ligands.

The pre-edge peak for NH_3–Cu^+ recorded under reducing atmosphere was only observed under SCR conditions during the first heating cycle and vanished for the other heating/cooling processes during simulation of the NEDC. This might be explained by mass transfer limitations due to the use of a large sieve fraction and possible channeling effects [181]. Additionally, water could be adsorbed on the zeolite and therefore compete with NH_3 [224]. Moreover the water could also be retained in the microreactor and compact the catalyst bed, since the channel outlet was not heated and reached only a temperature of 40 °C.
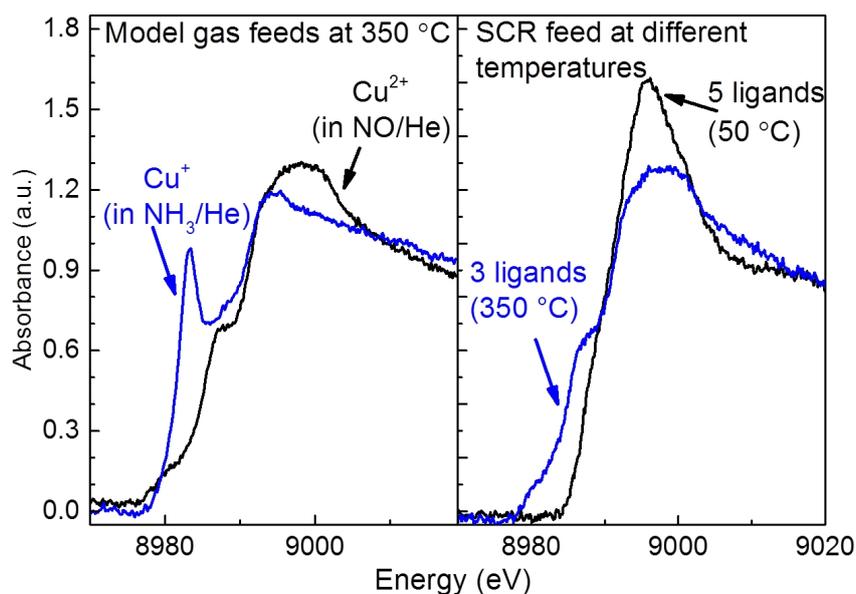
Figure 7.1: Left: XANES spectra of the Cu *K* edge of the catalyst under model gas feed (1000 ppm NH₃/He, blue; 1000 ppm NO/He, black) at 350 °C to determine the oxidation state. Right: XANES spectra during SCR feed at 50 °C (black) and 350 °C (blue).
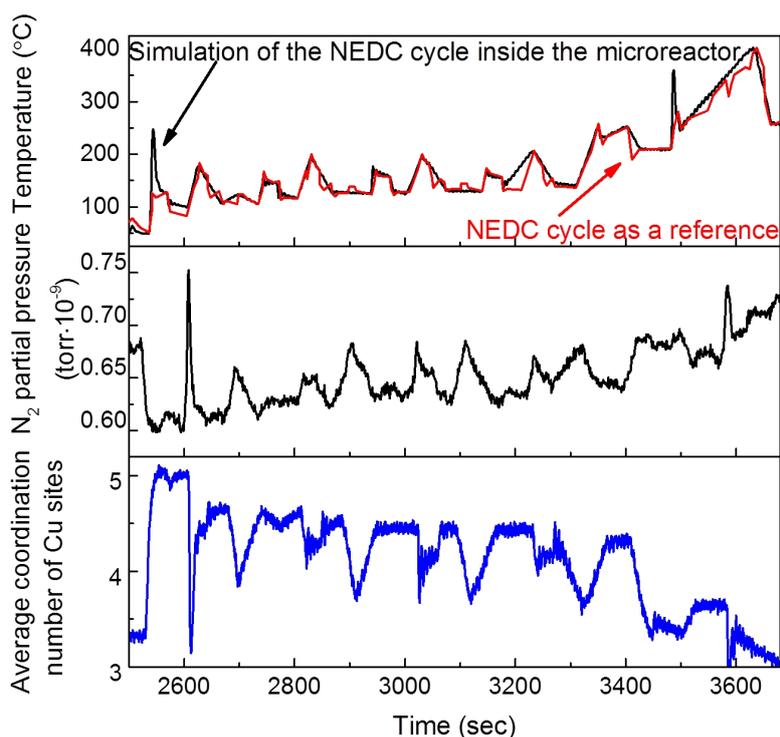
Figure 7.2: Top: Temperature profiles for simulation of the NEDC, black: simulated temperature profile [204], red: reference NEDC cycle. Middle: Presentation of the catalytic performance of the studied catalyst showing the MS signal for N₂, bottom: results gained by LCF showing the change from five to three fold Cu coordination spheres as a response of the temperature changes by simulation of the NEDC. The results clearly show the correlation of the catalytic performance and the coordination sphere variations as a result on the modulated temperature.

To show the applicability of the microreactor under transient regimes during the NEDC, LCF analysis was performed to unravel the changes in coordination sphere. The spectra shown in Fig. 7.1 under SCR feed conditions were used as references. Fig. 7.2 shows the results obtained by LCF (bottom), in parallel to the temperature profile applied for NEDC simulation (top) and the catalytic performance gained by MS analysis (middle). When the catalyst was heated, the N_2 signal increased, while the number of ligaments in the Cu coordination sphere decreased. The opposite behavior was detected during cooling and a comparison to other Cu-zeolite samples showed reproducible behavior. This distinct correlation of the MS and XAS signal to temperature changes applied by the simulated NEDC heating cycles clearly underlines the applicability of the microreactor during transient studies.

In future, the measurements can be further improved by implementation of an additional heating (T>100 °C) of the support of the microreactor and the outgoing gas lines to degrade water adsorption. Additionally, to optimize the catalyst packing, smaller sieve fractions of the catalysts can be used. Nevertheless, the obtained results present the first *operando* QEXAFS study during simulation of a NEDC and underline the applicability of the reactor for such studies. In fact, in a more recent study, also a Pt/γ-Al$_2$O$_3$ diesel oxidation catalyst was successfully studied for CO oxidation during the NEDC. The results show a strong variation of the oxidation state as a function of the conditions.

8 Conclusions and Outlook –
Gas Phase Microreactor

The design and application of a silicon-based gas phase microreactor applied in a modular setup were presented. The modular setup constructed by GeSim allows changing the reactor. The whole setup is now available for users at the P06 beamline of PETRA III. With respect to the design, the benefits of the second generation, like higher temperature stability and homogeneity, were highlighted. The possibility for performing correlative characterization techniques was demonstrated using spectroscopic and scattering techniques as well as on-line mass spectrometry for analyzing the gas composition.

In particular, the application of XAS and XRD revealed the artifact-free application of the reactor for both techniques. Furthermore, due to the modular setup, different microreactors based on pure Si and a Si-glass composition can be used, enabling additionally the use of Raman spectroscopy for the Si-glass reactor. Additionally to the spectroscopic techniques, the application of IR thermography was shown in parallel to on-line mass spectrometry. The reactor was used to study structures of catalysts during two different reactions. As a first example, the ignition and extinction of the CPO of methane was studied over a 4 wt.% Pt/γ-Al_2O_3 catalyst. Very similar behavior to previous measurements in conventional reactors, was observed, *i. e.* hotspot formation, gradients in oxidation state during CPO and changes of oxidation state during ignition and extinction. On the other hand, the application of the reactor under transient conditions was highlighted by showing first *operando* QEXAFS studies for the SCR of NO_x during measurements under the transient temperature regime of the New European Driving Cycle. This requires high cooling/heating rates, which can only be addressed with such microreactors and strong structural changes were observed by XAS.

Due to the unique heating and cooling capacities of this microreactor, further studies should be performed during transient reaction conditions in future. These can either be studies to unravel reaction mechanisms or application during modulation excitation spectroscopy. In addition, the capabilities of the reactor can be used for further studying exhaust gas catalysts during driving cycles to reduce air pollutants such as CO, NO_x or hydrocarbons. Therefore, further studies should include investigation of different SCR-catalysts or Diesel Oxidation Catalysts (DOC) during NEDC cycles. By the application of the microreactor in these studies, *in situ* characterization of the catalysts can be performed during realistic application, which has not been possible so far.

Furthermore, due to the modular setup, new microreactors can be developed, *e. g.* allowing for further spectroscopic studies like grazing incidence X-ray scattering [185]. Thereby it is important to note that only the chip has to be changed, while the support used for electrical and gas connection can be kept.

The present reactor can be further improved by elongating the X-ray window so that it covers the whole catalyst bed. Additionally, the temperature sensor should be shifted in position such that it is no longer placed on top of the catalyst bed, but next to it. This will enable precise measurements of the very end of the catalyst bed. Moreover, new materials for the microreactor could be investigated, such as aluminium oxynitride or graphite modifications. Last but not least, the small channel dimensions of the microreactor allow for the study of single grain effects, if a dedicated sieve fraction of catalyst grains is used. In particular, the microreactor is attractive for X-ray microscopy during the CPO of methane, either in full-field or scanning geometry. For example, it should be studied how the gradient moves with respect to the intergranular or intragranular structure of the catalyst, which will further help to understand the mechanism of the CPO including the role of heat and mass transport which are *e. g.* important for multi-scale modeling of the CPO.

Part III

Complementary X-ray Microscopy and Electron Microscopy

9 Introduction – *In Situ* X-ray Ptychography

Hard X-ray ptychography is regarded as a powerful microscopic tool for *in situ* catalyst investigations, as it allows high-resolution imaging of solids in gas or liquid phase (*c. f.* section 1.1.2). So far, spatial resolutions below 10 nm [130, 131] have been reported and the resolution will even be improved by high brilliance synchtrotron radiation sources like PETRA IV [225], MAX IV [226], SLS 2 [227] or Sirius [228]. By the use of hard X-rays the high penetration depth allows measurements inside special reactors as the reactor material and the sample can be penetrated by the radiation. Furthermore, the high penetration depth also facilitates non-destructive measurements. Hence, sample preparation is facilitated compared to EM. Complementary to EM, measurements can be conducted under realistic conditions requiring a gas flow and ambient or elevated pressure, which can hardly be reached in EM. Therefore, hard X-ray ptychography has the potential to bridge the gap between the atomic and the macro scale, which are commonly investigated under model conditions by ETEM or by conventional scanning X-ray microscopy techniques, respectively.

Until recently, technological challenges such as realization of small, light-weight *in situ* cells and the accessibility of this novel technique, have hindered the application of ptychography during *in situ* studies. Recently, *in situ* measurements have been carried out, *e. g.* studies on strain inside batteries *operando* [135], on crystal growth [136], on the densification during compression [134], or on lithium zirconate particles under gas atmosphere and high temperatures [132]. To use *in situ* ptychography, dedicated *in situ* cells have to be developed, which have to be small and light in weight, transparent for the radiation used and suitable for the desired application, *e. g.* heating [132, 229] or compression [134]. For heterogeneous gas phase catalysis, this implies compatibility with different gas atmospheres, ambient or elevated pressure (leak tight) and elevated temperature conditions (heating).

In this part of the thesis the design of two *in situ* cells which can be used for ptychography and complementary EM, and the application of one of the cells is presented. In the first part, the geometry of a cell designed in collaboration with Ass. Prof. Christian D. Damsgaard and co-workers (DTU) and built at DTU-CEN, is discussed. Subsequently, the proof of principle and application for catalytic materials will be presented. Results have been or will be published in parallel. As an outlook, a similar cell designed at KIT is presented, which offers different benefits, like smaller gas volume and a more compact sample environment for future experiments.

10 Design of an *In Situ* Cell for Ptychography and Proof of Principle Measurements

This chapter presents the design of an *in situ* cell which allows studying catalytic materials by complementary *in situ* hard X-ray ptychography and electron microscopy. It was developed in a joint collaboration between KIT and DTU and is based on commercial TEM heating chips. Additionally to the design, the first proof of principle measurements, which show the applicability of the cell for *in situ* hard X-ray ptychography and complementary electron microscopy, are presented on model samples.

10.1 Design of an *In Situ* Cell for Ptychography and Complementary Electron Microscopy

The developed cell is designed to enable measurements under a controlled gas atmosphere and at elevated temperature. To allow not only *in situ* ptychography, but also EM, the cell is based on a TEM heating chip (Protochips E-Chip^{TM}, Morrisville, USA), which is usually used for *in situ* heating inside the TEM [230, 231]. Joule heating by a current flow through a conductive, ceramic membrane (thickness approximately 120 nm Si and C) is used to reach elevated temperatures up to 1200 °C [232]. Electron transparent holes with an approximately 50 nm thick silicon nitride (Si_3N_4) film guarantee electron transparent areas, which are required for the application in TEM. The sample can be placed on these holes, which enables complementary TEM imaging, but for *in situ* ptychography or complementary SEM imaging, the sample can also be placed on the thicker parts (120 nm thick) of the ceramic membrane. An example of a chip is presented in Fig. 10.1. Fig. 10.1a shows a photograph with increasingly magnified positions of the sample area (from left to right: optical micrograph and SEM image), while Fig. 10.1b shows an example of SEM images of 50 nm Au nanoparticles deposited on one of the electron transparent holes (bright "ring" in the overview image of Fig. 10.1b) by drop-casting, *i. e.* placing a droplet of nanoparticle dispersion on the chip and evaporating the liquid.
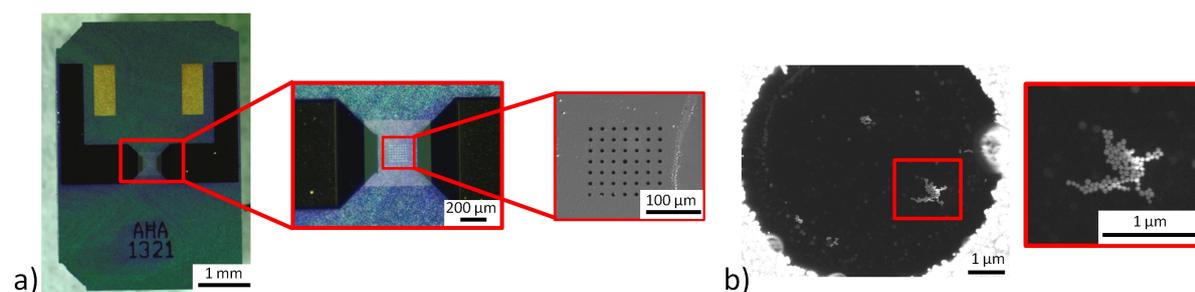
Figure 10.1: a): From left to right: Photograph of a Protochips E-Chip^{TM} showing the electrical contacts and the sample area in the center, optical micrograph and SEM image of the sample area. In the SEM image, the electron transparent holes, which are just covered by the approximately 50 nm thick Si_3N_4 film, appear black. b) SEM image of one of the electron transparent holes and an agglomeration of 50 nm Au nanoparticles deposited on the membrane by drop-casting of an aqueous dispersion.

The cell itself is constituted, as schematically presented in Fig. 10.2, by a steel body with X-ray transparent windows and a gas in- and outlet, respectively. The heating chip is placed inside the cell in between the windows. Mass flow controllers (Bronkhorst), controlled by a script based on NI LabVIEW 2013, are used to control the gas flow into the cell. A Keithley 6220 DC power supply is connected to the electrical contacts of the Protochips E-Chip^{TM} to facilitate heating. Although the temperature is related to the heating power, temperature determination is best to be performed by external IR thermography (*c. f.* section 2.3.2, section 11.3.2.1 and section 11.3.1.4), as the heating power to temperature relation differs slightly from chip to chip (approximately 50 °C). The Si_3N_4 membrane of the chip forms one window of the cell, whereas the other window to close the cell, is based on a 25 μm thick Kapton® foil. O-rings are used for leak tight connection between the cell body and the chip, which is placed on the bottom part of the cell with the sample facing inside. The gas connection is implemented by a central part, placed on top of the chip with an O-ring in between. The Kapton® foil is then added with another steel part to close the cell. Finally, a piece with spring contact probes is used to connect the electrodes of the chip with the power supply. Photographs of the cell are depicted in Fig. 10.3.
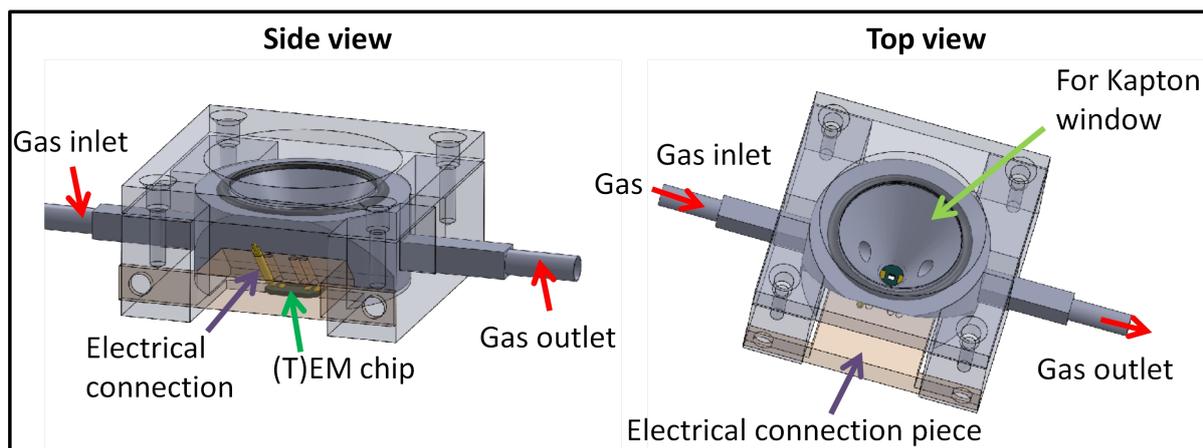
Figure 10.2: Schematic representation of the cell with a presentation of the side (left) and the top (right) view. The sample is placed on the TEM chip, which is used for heating. Additionally, it can be used outside the cell for complementary TEM and SEM measurements. When it is placed inside the cell, the sample can be kept under a desired gas flow.
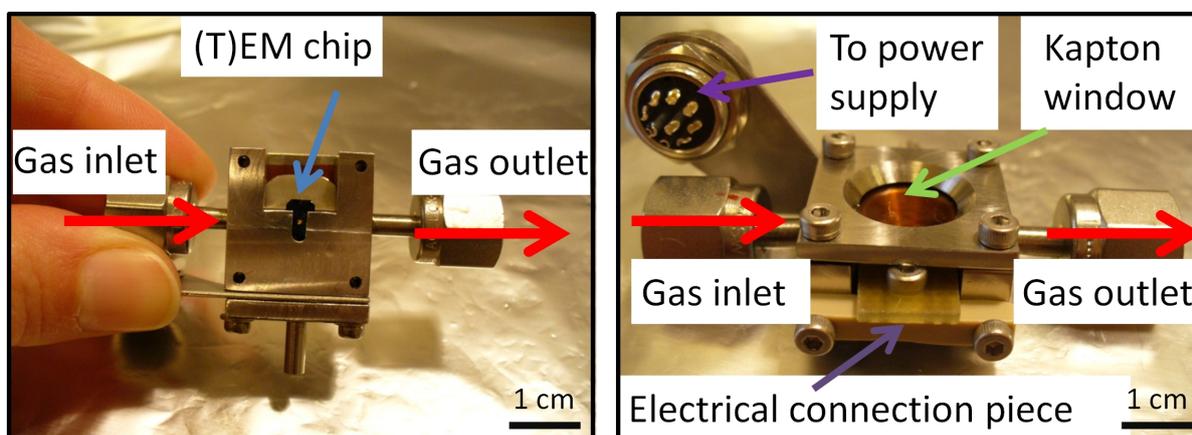
Figure 10.3: Photography of the *in situ* cell. Complementary to the schematic representation in Fig. 10.2, the bottom view is shown on the left, whereas the comparable side view is shown on the right.

10.2 Proof of Principle Measurements – Gold Colloids

To show the applicability of the newly developed cell, proof of principle measurements using model Au nanoparticles with a diameter of 50 nm, were carried out. First, *ex situ* SEM measurements before and after heating the colloids on the chip in the cell were performed to show the heating feasibility of the cell. Subsequently, thermal annealing of the nanoparticles was studied *in situ* with ptychography to demonstrate the applicability of the cell for *in situ* ptychography studies [229].

10.2.1 Experimental

10.2.1.1 Sample Preparation and Electron Microscopy

An aqueous dispersion of citrate stabilized colloidal Au nanoparticles (Sigma Aldrich) with a diameter of 50 nm was deposited on a Protochips E-Chip^{TM} by drop-casting of 30 μl, *i. e.* placing a droplet of nanoparticle dispersion on the chip, followed by drying in air for 30 min. For *ex situ* SEM analysis, a FEI Quanta 200 ESEM FEG located at DTU-CEN and operated at 20 keV with SE contrast, was used. First heating tests were conducted by heating the Au colloids on the Protochips E-Chip^{TM} for 1 h at 275 °C in air by using a hot plate. Afterwards, the heating capability of the cell was tested by heating a chip with nanoparticles at approximately 500 °C inside the *in situ* ptychography cell in a flow of synthetic air.

10.2.1.2 *In Situ* Ptychography

In situ ptychography was carried out at the nanofocus endstation of the beamline ID 13 at the European Synchrotron Radiation Facility (ESRF). During the experiment, the ring was operated in 7/8+1 mode (868 bunches, scheduled ring current 200 mA). The sample was mounted inside the cell, which was fixed on a kinematic mount. It was scanned through the focused beam, so that the beam first hit the sample on the "bottom" of the cell penetrating the Si_3N_4 window first. For beam focusing, nanofocusing lenses were used to provide an illumination with a FWHM spot size around 150 nm and a focus depth of roughly 100 μm. Far-field diffraction patterns were recorded at an energy of 14.9 keV monochromatized by a Si(111) channel cut monochromator. A Maxipix detector (pixel size: 55 μm) with a sample – detector distance of 2 m (q-range up to 0.27 nm^{-1}) was used for detection of the diffraction patterns. A step width of 50 nm was applied to scan an area of 2×2 μm and the signal at each single diffraction pattern was recorded over 0.03 s. By this, a signal of approximately 10^4 photons was gained for the most intense areas and one complete ptychogram was recorded within 10 – 15 min. For *in situ* annealing treatment, the sample was treated in synthetic air (20 % O_2/N_2) with a flow of 1 ml/min. For image reconstruction, an algorithm based on the (e)PIE algorithm presented by Maiden and Rodenburg [126] was used, which was carried out by Maria Scholz (DESY).

10.2.2 Results and Discussion

Feasibility of Heating Independent of the *in situ* ptychography, a series of *ex situ* studies was performed to study the behavior of the used model particles under thermal annealing. SEM images of the sample before and after heating are presented in Fig. 10.4. While Fig. 10.4a depicts the heating experiment by the hot plate on big agglomerations of colloid particles on the thick part (approximately 120 nm) of the membrane, Fig. 10.4b shows different agglomerations of the colloid particles located inside the electron transparent "holes" (approximately 50 nm) after heating with the *in situ* cell. Although only small agglomerations could be located, the size increase of the nanoparticles after the heating experiment clearly showed that heating was possible within the cell, which is crucial for the application for *in situ* ptychography.
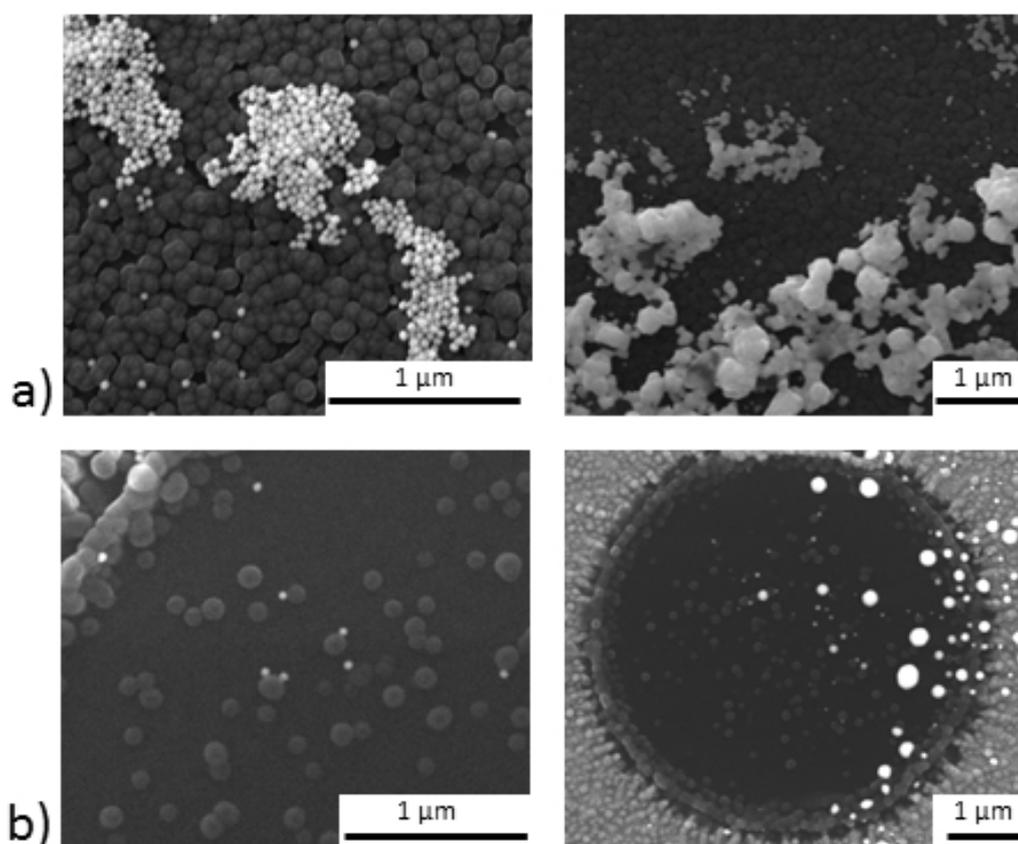
Figure 10.4: Model *ex situ* SEM images (SE contrast) performed before and after annealing of 50 nm Au nanoparticles. a) SEM images before (left) and after (right) thermal annealing using a hot plate at 275 °C for 1 h. SEM images were recorded on the approximately 120 nm thick membrane showing a big agglomeration of particles for both measurements. The size of the nanoparticles increased after annealing. b) SEM images before (left) and after (right) thermal annealing inside the *in situ* ptychography cell at approximately 500 °C for 1 h. SEM images were recorded on the thin approximately 50 nm thick membrane showing only single nanoparticles on the position probed before the annealing, whereas another position was probed after annealing showing the size increase of the nanoparticles.

Feasibility of *In Situ* Ptychography   To demonstrate the feasibility of *in situ* ptychography an agglomeration of the model samples was studied during *in situ* ptychography. By *ex situ* SEM before the treatment, an agglomeration of Au nanoparticles was identified and the same area was studied during *in situ* ptychography. Fig. 10.5a presents the SEM image before the annealing treatment, while Fig. 10.5b shows a phase contrast image derived by ptychographic reconstruction of the same structure without a gas flow, while Fig. 10.5c was recorded during a flow of 1 ml/min of synthetic air. The general shape of the structure is clearly visible. The resolution of the recording can be estimated to be around 100 nm, as the general shape is visible, but the single Au nanoparticles could not be resolved. Additionally, heating tests were performed for different annealing temperatures and the heating power is given together with an estimated temperature. An IR camera for temperature determination was not available during this experiment, so that the temperatures could only be correlated to IR thermography data obtained for different chips after the experiment. After the first annealing treatment at 180 mW (approximately 450 °C) for 45 min, a sintering of the structure could be observed, which is depicted in Fig. 10.5d. A ptychogram recorded after further heating for 25 min at 260 mW (approx. 600 °C) is depicted in Fig. 10.5e, revealing an even stronger sintering which resulted in a degradation of the original structure.

10.2.3 Conclusions

The presented study on the sintering of Au nanoparticles proves the applicability of the developed cell for hard X-ray *in situ* ptychography studies. The similarity of the SEM and the phase contrast images obtained by ptychography show that it is possible to track the same area by both techniques which is required for correlative imaging approaches. Furthermore, the proof of principle *in situ* ptychography measurements show that ptychography can be used to study model samples with a resolution around 100 nm, mainly limited by not optimized ptychographic data acquisition parameters. Improvements are required with respect to temperature measurement and the resolution obtained by hard X-ray ptychography. These aspects will be discussed together with the application of hard X-ray *in situ* ptychography in the next chapters.
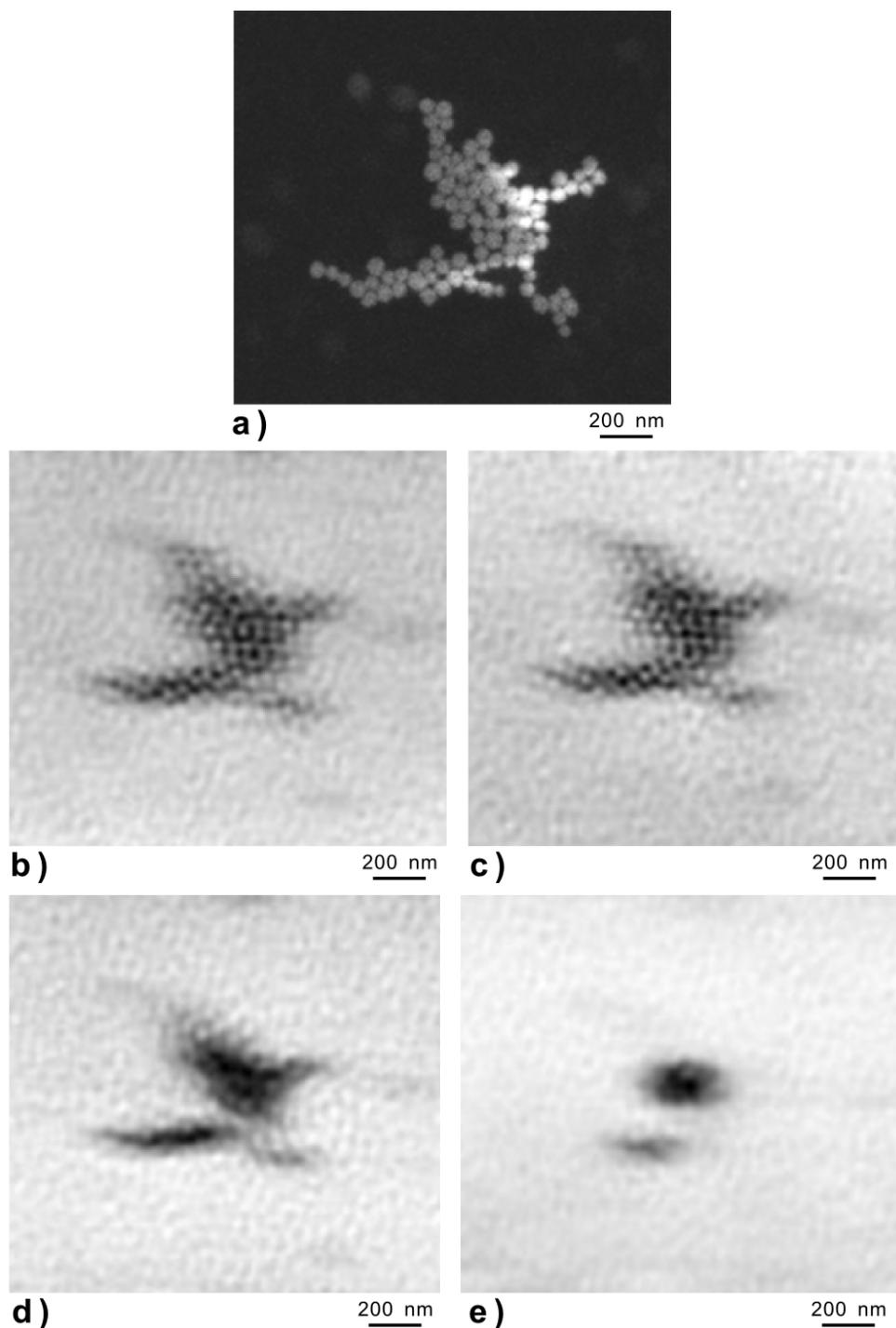
Figure 10.5: Proof of principle measurements on 50 nm colloidal Au particles deposited on a Si_3N_4 membrane. a) SEM image in SE contrast before the *in situ* ptychography measurement, b) phase contrast image of the same area in the ptychographic measurement without gas flow, c) phase contrast image of the same area in the ptychographic measurement with a flow of 1 ml/min of synthetic air, d) phase contrast image at RT after the first annealing for 45 min at 180 mW (approx. 450 °C), e) phase contrast image at RT after the second annealing for 25 min at 260 mW (approx. 600 °C). In d) a coarsening of the structure becomes visible, which is followed by degradation due to the high temperature in e). Reprinted from [229], reproduced with permission.

11 Thermal Annealing of Nanoporous Gold

A novel complementary approach of EM and *in situ* hard X-ray ptychography, based on the cell described in chapter 10.1, was used to study the thermally induced coarsening of np-Au under different atmospheres, pressures and after ceria deposition. *In situ* ptychography experiments were carried out at two different hard X-ray microscopes. The first study revealed a spatial resolution about 40 nm while the second experiment offered an improved resolution about 20 nm. In addition, the temperature was measured directly in the second case. The annealing of pure nanoporous gold and ceria stabilized nanoporous gold in different atmospheres showed that the atmosphere has a tremendous influence on the coarsening. The nanostructure of the samples was stable at high temperatures (approximately 800 °C) in vacuum, whereas pronounced changes and coarsening were observed at lower temperatures (approximately 300 °C) in O_2/N_2 and oxygen atmosphere. A layer of ceria on the nanoporous gold led to an improvement of the stability, but did not alleviate the influence of the gas atmosphere. Different behaviors were observed, such as coarsening and even material loss. It is suggested that additional mechanisms beyond surface diffusion need to be considered and studies aimed at more realistic conditions will be critical to understand the sintering behavior of catalysts under realistic conditions.

11.1 Introduction – Nanoporous Gold

Starting from the observation of catalytic activity of gold nanoparticles in the 1980's, gold was regarded as a promising material for heterogeneous catalysis. The most popular reaction is the CO oxidation using gold nanoparticles [16]. While originally mainly supported catalyst were used, unsupported skeletal gold has received strong interest in recent years [233]. A prominent example is nanoporous gold (np-Au), which exhibits a 3D sponge-like structure [234]. It can be obtained by dealloying of AgAu in nitric acid and used for catalytic applications [235–238], sensing [239, 240] or as a biomaterial interface [241]. Remaining small silver contents from the dealloying process [242], as well as the existence of kinks and steps on the ligaments, which are in the size range of tens of nanometers, support the catalytic activity [235]. The size of the ligaments influences the density of surface defects and therefore the reactivity and plays an important role for catalytic application [243]. The size can be controlled directly during dealloying [244], or by post-treatment like annealing [245–247]. Thermal annealing usually leads to a coarsening of the structures with an increased ligament and pore size [245, 248–250] and various studies have been performed to determine the effect of the heating power, *e. g.* during laser heating [246, 248], or the gas atmosphere [245, 251–253].

Mechanisms for Annealing   Up to now, the coarsening has mostly been studied by electron microscopy of samples studied *ex situ* after treatment in various atmospheres [245, 246, 253–255]. According to these studies, the observed coarsening is mainly explained by surface diffusion [245, 249, 253, 256] and recrystallization in the solid state was suggested to dominate over melting processes [257]. Complementary to surface diffusion based effects, especially for early states of coarsening and the corrosion process, Kolluri and Demkowicz [258] discussed volume diffusion by collapse of neighboring ligaments. For nanoporous palladium, Klein *et al.* [259] described surface diffusion driven mechanisms at lower temperatures, but bulk diffusion at higher temperatures. Stabilization of the structures to temperatures of several hundred degrees can be reached by deposition of solid metal oxides, like TiO_2 or CeO_2, allowing the catalyst to be used at even higher temperature processes like the water gas shift reaction [260]. However, a clear understanding of the mechanism is missing due to the lack of *in situ* studies.

Annealing of Np-Au in Different Atmospheres   Although gold is often considered as an inert material, a stabilization could also be tracked back to surface adsorbates [251]. In literature, there are different, sometimes contradictory studies about the influence of certain gas atmospheres on the annealing behavior. Recently, Kuwano-Nakatami *et al.* [252] found a different coarsening behavior of np-Au annealed in N_2 or O_2, than in Ar or vacuum. From varying activation energies dependent on the atmospheres, it was concluded that different mechanisms dominate. Lattice diffusion was suggested in vacuum or Ar atmosphere, while surface diffusion was suggested for O_2 or N_2 atmospheres. Also Sun *et al.* [253] did not observe pronounced coarsening behavior in vacuum, although the study was performed *ex situ* up to 600 °C in contrast to the one from Kuwano-Nakatami *et al.* [252], who studied the coarsening of np-Au in vacuum up to 400 °C by ETEM. In contrast to Kuwano-Nakatami *et al.* [252], Chen *et al.* [245] found a slight coarsening in Ar atmosphere at 400 °C and a pronounced coarsening at 600 °C. Additionally, the latter also reported a stabilization of the np-Au up to 600 °C, when using CO atmosphere and Biener *et al.* [251] reported on a stabilization by O_3 treatment, compared to the annealing in He atmosphere.

The influence of adsorbates, which interact with the gold surface, and the different observations of the coarsening behavior underline that further studies are required to understand the coarsening mechanisms. Partly, this is related to the fact that only now techniques to study the annealing under *in situ* conditions become available. Furthermore, complementary to the previous studies, measurements at higher temperatures have to be carried out. For *in situ* studies, this implies the use of dedicated sample holders, *e. g.* TEM heating chips [261], and techniques compatible with *in situ* application. Here, X-ray based techniques are especially promising [48]. In particular, *in situ* ptychography enables high-resolution imaging under realistic conditions. In the following, the annealing of np-Au and stabilized CeO_2/np-Au samples in different

gas atmospheres is presented. Measurements were performed during different *in situ* ptychography beamtimes and by (E)TEM. First, heating in 20 % O$_2$/N$_2$ was performed. The results are already published by Baier *et al.* [229]. Further studies were performed on the annealing of np-Au and CeO$_2$/np-Au samples in 20 % O$_2$/He and vacuum to unravel the influence of the annealing atmosphere and pressure [262].

11.2 Annealing 20 % O$_2$/N$_2$ – Proof of Principle

In chapter 10.2, the applicability of *in situ* ptychography was already shown using model samples. However, ptychographic data acquisition was not performed during heating so far. Here, the first real catalysts, np-Au and CeO$_2$/np-Au, were heated in 20 % O$_2$/N$_2$ and studied by *in situ* ptychography during annealing. The results presented in this section have been published (Baier *et al.*, ref. [229]).

11.2.1 Experimental

11.2.1.1 Sample Preparation and Electron Microscopy

All sample preparation steps, except the first one which was performed by Junjie Shi (University of Bremen) at Universitiy of Bremen, were carried out at KIT. Initially 100 nm thick np-Au films were obtained by dealloying of a AgAu alloy (American White Gold, 12 Karat, Noris Blattgold) with concentrated nitric acid (Sigma Aldrich p.a. $\geq$ 65%). After washing the sample carefully by floating on deionized water, the sample was transferred onto a copper TEM grid (100 mesh). For the CeO$_2$/np-Au sample, 10 µl of an ethanolic solution of cerium nitrate solution (Ce(NO$_3$)$_3$, 1 mol/l) were used to impregnate the np-Au sample on the TEM grid. After drying in air for 30 minutes, a calcination was performed at 250 °C for 2 h to form cerium oxide (CeO$_2$). Both as-prepared samples on the copper TEM grids were transferred to a FIB microscope to further process the samples.

Independently from the above described preparation, Al frames of L $\times$ W $\times$ H $\times$ = 60 $\times$ 60 $\times$ 13 µm^3 were fabricated by FIB milling. Those were used to stabilize the np-Au and CeO$_2$/np-Au sample. The frames were fixed on the np-Au and CeO$_2$/np-Au samples by platinum deposition on the outside of the frames. Afterwards, the stabilized samples were milled out and fixed by platinum deposition on different Protochips E-Chips$^{\text{TM}}$. FIB milling was performed by Dr. Torsten Scherer at the KNMF (located at the INT at KIT) using a Zeiss Auriga 60 or a FEI Strata dual beam FIB system. *Ex situ* SEM imaging was performed using the above mentioned FIB microscopes with a SE in-lens detector at 5 keV.

11.2.1.2 *In Situ* Ptychography

In situ ptychography was performed according to the procedure described in section 10.2.1.2. To improve the spatial resolution, a sample – detector distance of 2 m was used, covering a q-range up to $0.53\,nm^{-1}$. The reconstruction of the images was performed by Maria Scholz (DESY).

11.2.2 Results and Discussion

11.2.2.1 Thermal Annealing of np-Au in 20 % O_2/N_2

For the np-Au sample, a crack, which was formed artificially by FIB milling, was studied at different temperatures while a 3 ml/min flow of synthetic air was applied. The images obtained by *ex situ* SEM and *in situ* ptychography are shown in Fig. 11.1. A SEM image of the studied sample area, which was acquired under vacuum conditions prior to the thermal treatment, is presented in Fig. 11.1a. Afterwards, the sample was transferred to the X-ray microscope and studied by *in situ* ptychography. Again, like in section 10.2, the relation between the heating power and the temperature was estimated from a series of independent measurements where the temperature of a chip was monitored with IR thermography. The used heating powers and the estimated temperatures are summarized in Tab. 11.1.

In Fig. 11.1b, a ptychographic image of the same area, presented in Fig. 11.1a as an SEM image, is shown. The structure is clearly visible and matches accurately the one observed with SEM, as highlighted in Fig. 11.1h, where the SEM image was inverted, colorized and overlaid with the phase contrast image obtained by ptychography. As depicted in Fig. 11.1c, structures of 35 nm (the crack marked by the red arrow) could be visualized even at a temperature of approximately 60 °C. This demonstrates that in these measurements, a considerably higher resolution in comparison to the previous proof of principle measurements with the 50 nm Au particles has been obtained. This is most likely due to an improved experimental setup (see section 11.2.1.2 and section 10.2). However, the resolution at this temperature seems to be less than at RT, which could be related to slight thermal vibrations. A detailed calculation of the spatial resolution reached is given in section 11.2.2.3.

Table 11.1: Heating power and estimated temperature for the annealing treatment of np-Au with reference to the image panel.

heating power (mW)	estimated temperature (°C)	panel in Fig. 11.1
59	60	c)
130	250	d)
194	500	e)
270	> 600	f)
315	660	g)

After further heating to approx. 250 °C (Fig. 11.1d) obvious changes to the structure, marked by a red arrow, can be seen in the crack width. Upon further annealing (Fig. 11.1e-f), the appearance of areas with lower density and such with higher density can be observed, although the overall contrast seems to decrease. The changes in density are in agreement with the expected coarsening behavior for np-Au based samples [247, 254], as ligaments increase in size, while additionally pores become bigger. When the sample was heated further, the framework was destroyed (Fig. 11.1g) due to the melting of the Al frame used for stabilization. The melting of the Al frame could be confirmed by SEM imaging after the annealing treatment and the sample could not be retrieved again. From the performed experiment, it could be concluded that the coarsening for the studied np-Au sample started with small changes on the length scale of 10 nm at a temperature of approximately 250 °C, which is in agreement with previous studies [251] and became more distinct at higher temperatures.

11.2.2.2 Thermal Annealing of CeO$_2$/np-Au in 20 % O$_2$/N$_2$

In contrast to the pure np-Au sample where the measurements were performed close to an artificial crack from FIB milling, the measurements were performed close to a natural crack close to the border of the sample. The inverse catalyst CeO$_2$/np-Au showed similar results, which are depicted in Fig. 11.2. However, due to lower annealing temperatures and smaller temperature steps, fewer changes were observed for the CeO$_2$/np-Au sample in contrast to the np-Au sample. For comparison, the temperature when clearly visible changes occurred in Fig. 11.1c, was slightly higher than the highest temperature which was used for the study of CeO$_2$/np-Au. For annealing of CeO$_2$/np-Au, the applied heating power is depicted together with the estimated temperature and the panel of Fig. 11.2 in Tab. 11.2.

Table 11.2: Heating power and estimated temperature for the annealing treatment of CeO_2/np-Au with reference to the image panel.

heating power (mW)	estimated temperature (°C)	panel in Fig. 11.1
24	30	c)
65	60	d)
107	<250	e)

The changes observed during annealing were mainly located at the top of the studied sample, as marked by an arrow. A flattening of the structure could be found already at a heating power of 65 mW (approximately 60 °C), which is depicted in Fig. 11.2d. Upon further heating at 107 mW (< 250 °C) first contrast changes, most probably caused by density changes within the sample, indicated first coarsening. *Ex situ* SEM, which is given in Fig. 11.2f, also confirmed coarsening after the annealing.

To conclude, it was shown that both the pure np-Au and the stabilized CeO_2/np-Au showed a coarsening under 20 % O_2/N_2 atmosphere and first changes occurred at temperatures around 250 °C. The presented results further demonstrate that *in situ* ptychography is a promising tool to investigate the coarsening of np-Au based catalysts. So far, however, the obtained spatial resolution and the imaging contrast are not sufficient yet to draw conclusions on the underlying processes or on the precise temperature, when the coarsening started. The latter is partly due to the fact that the samples were placed on different E-Chips[TM] and the temperature could not be determined under *in situ* conditions. For further studies, the measurements were improved by preparing the two different samples on the same E-Chip[TM] and by using an IR thermography camera under *in situ* conditions to determine the temperature.
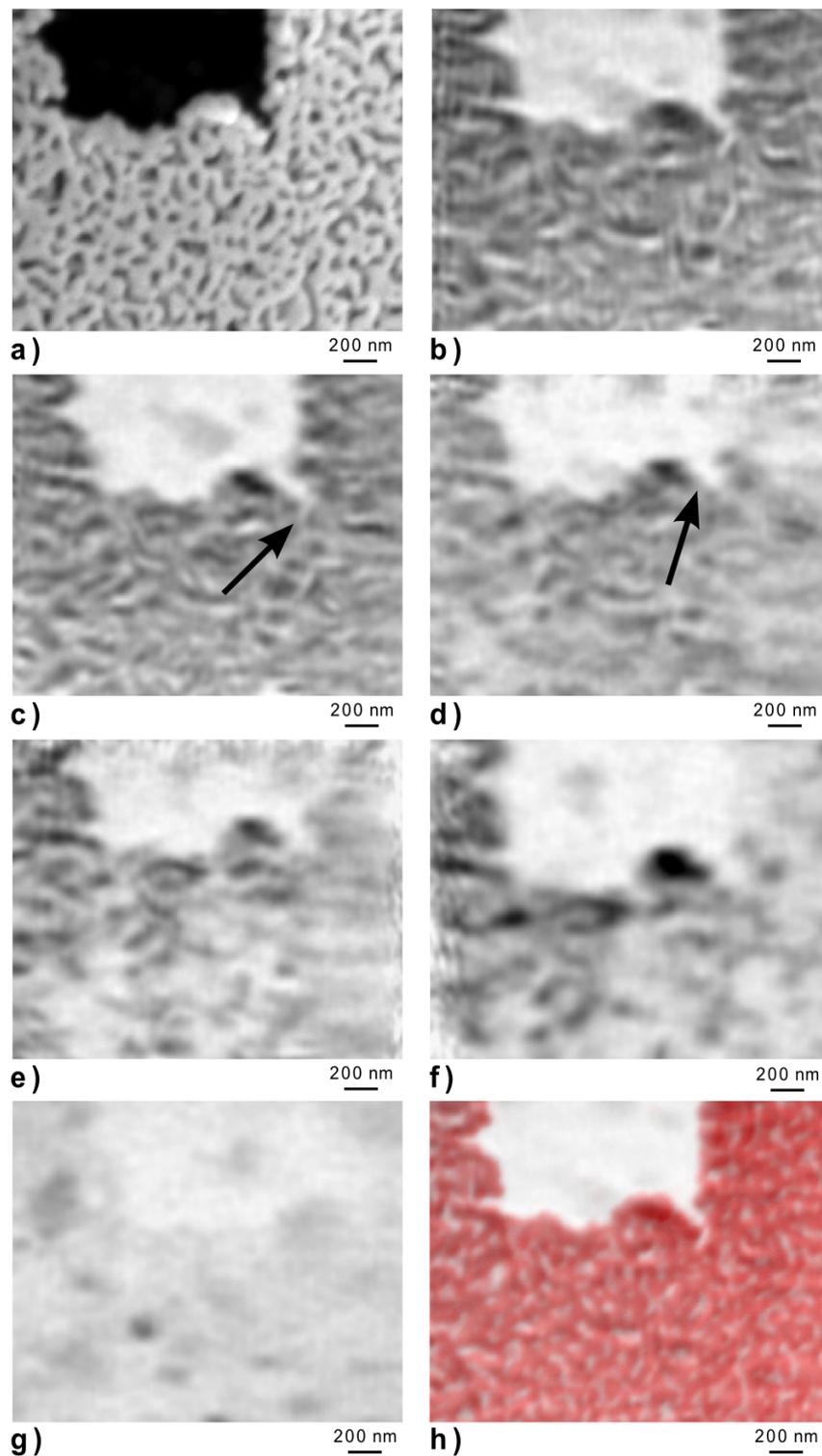
Figure 11.1: Np-Au on a Si_3N_4 membrane studied by SEM and ptychography. Ptychography measurements were carried out at different annealing steps using a flow of 3 ml/min synthetic air (20 % O_2/N_2). a) *Ex situ* SEM image under vacuum conditions using SE contrast before the thermal annealing, b) phase contrast image of the same area applying ptychography at RT, c) phase contrast image during annealing at a power of 59 mW (approximately 60 °C), d) phase contrast image during annealing at a power of 130 mW (approximately 250 °C), e) phase contrast image during annealing at a power of 194 mW (approximately 500 °C), f) phase contrast image during annealing at a power of 270 mW (> 600 °C), g) phase contrast image during annealing at a power of 315 mW (approximately 660 °C), h) inverted and colorized SEM image (red) overlaid with the ptychography reconstruction b). Reprinted from [229], reproduced with permission.
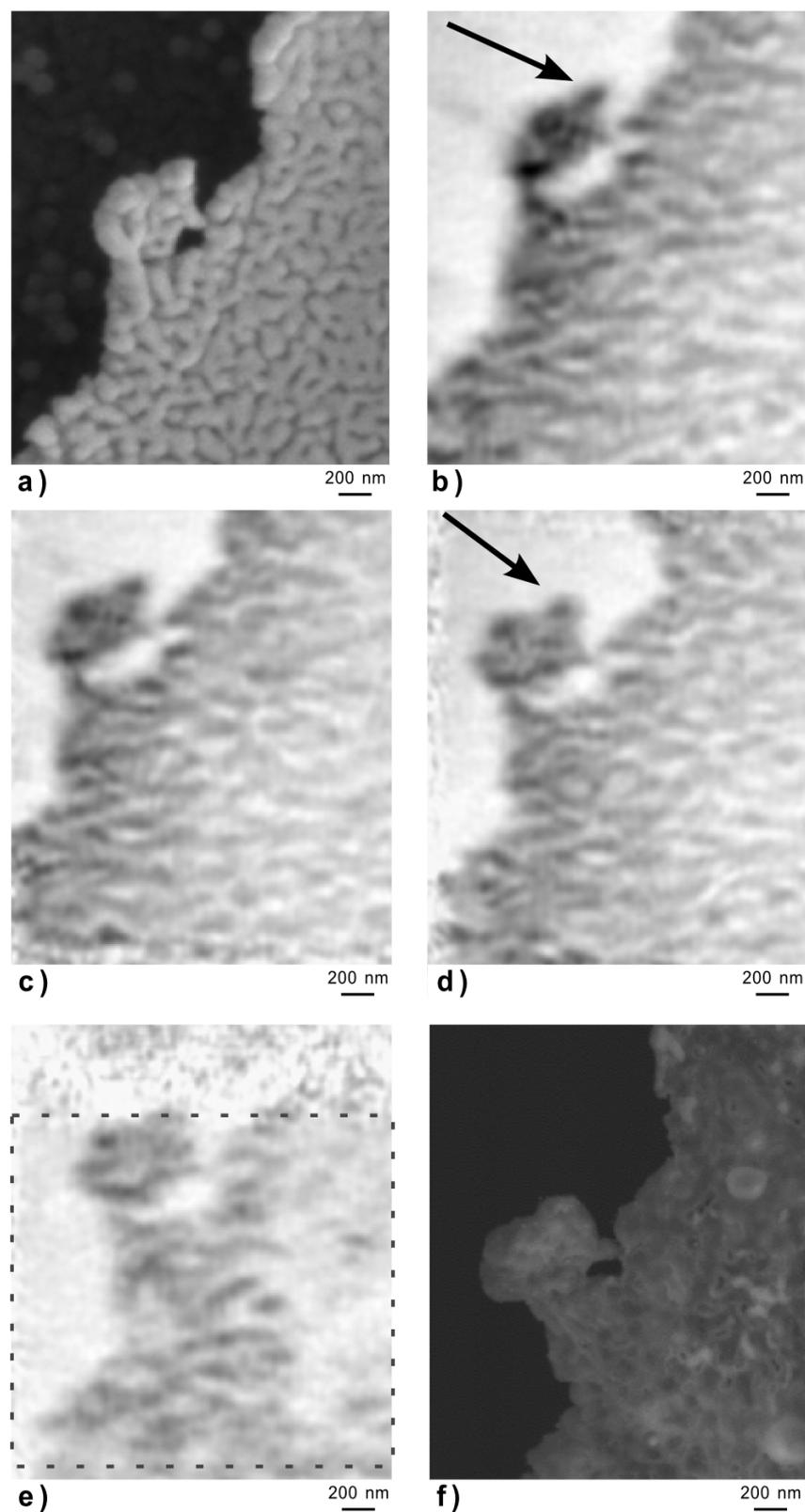
Figure 11.2: CeO$_2$/np-Au on a Si$_3$N$_4$ membrane studied by SEM and ptychography. Ptychography measurements were carried out at different annealing steps using a flow of 3 ml/min synthetic air (20 % O$_2$/N$_2$). a) *Ex situ* SEM image under vacuum conditions using SE contrast before the thermal annealing, b) phase contrast image of the same area applying ptychography at RT, c) phase contrast image during annealing at a power of 24 mW (approximately 30 °C), d) phase contrast image during annealing at a power of 65 mW (approximately 60 °C), e) phase contrast image during annealing at a power of 107 mW (< 250 °C) indicating the field of view by a rectangle, f) *ex situ* SEM image under vacuum conditions using SE contrast after thermal treatment. Reprinted from [229], reproduced with permission.

11.2.2.3 Technical Results Obtained during Annealing in 20 % O$_2$/N$_2$ and Determination of the Spatial Resolution

The spatial resolution of ptychography measurements can be estimated by comparing the reconstructed images to reference images. Additionally, algorithms closely related to the reconstruction algorithm can be used for determination. In the following, this analysis, which was carried out by Maria Scholz (DESY), is briefly described and the corresponding resolution of the first *in situ* measurements of np-Au in 20 % O$_2$/N$_2$ is discussed together with parameters influencing the spatial resolution of *in situ* ptychography.

Ptychography is based on the coherent scattering caused by the probed object. However, parasitic scattering, which does not result from the object itself, might be present and can thus degrade image quality. Therefore, the (e)PIE algorithm [126] used for image reconstruction, was further optimized by introduction of additional degrees of freedom for a background intensity map. This accounts for parasitic scattering contributions in the diffraction patterns, which might result from the microscope itself, but also from the experimental setup and the *in situ* cell. The Kapton® foil itself, which is used as a window material for the *in situ* cell, did not show significant scattering in the SAXS regime, which was used for the image acquisition.

The spatial resolution of the image can be either derived by evaluating the scattering signal with respect to the q-range [263], or by a Fourier Ring Correlation (FRC) [264]. Both attempts are shown to derive further information about the spatial resolution obtained by *in situ* ptychography. The reconstructed image is based on numerous diffraction patterns, *e. g.* 1681 for the images presented in Fig. 10.5, Fig. 11.1 and Fig. 11.2, but single scattering signals are very weak with respect to the direct beam. A model far-field diffraction pattern is depicted in Fig. 11.3a, showing the diffraction pattern from one of the patterns used for the reconstruction of Fig. 11.1b in linear scale. Fig. 11.3b depicts the diffraction patterns averaged over all 1681 diffraction patterns, and c) shows the azimuthal average count rate revealing that photons were also scattered up to the edge of the detector. The weak scattering intensity in Fig. 11.3a shows that considerations concerning the resolution based on the observed scattering intensity cannot be performed on one single diffraction pattern. Instead, the averaged scattering intensity depicted in Fig. 11.3b shows that strong scattering can be observed in the q-range signals corresponding to 20-30 nm spatial resolution, which is also highlighted in panel c.

Albeit, the high resolution proposed by the scattering intensity cannot be observed in the reconstructions. Therefore, a FRC [264] was performed. The FRC algorithm requires an initial division of the ptychographic data into two parts, such that either the odd or the even scan points were used for two separate reconstructions. Afterwards, the Fourier components of both reconstructed images are correlated and summed over each ring corresponding to a certain q-value. The resulting FRC for the data is plotted in Fig. 11.4. Also plotted are the so-called 1-bit and

1/2-bit threshold curves. According to Van Heel [264], the crossing of 1-bit or 1/2-bit threshold curve can be used to obtain the spatial resolution. As marked in the figure, the observed crossings correspond to a spatial resolution of 38 nm and 45 nm, respectively.

The lower spatial resolution determined by FRC, in comparison to that expected by the scattering intensity, might be explained by incompletely coherent scattering, which would lead to a non-fully consistent reconstruction with artifacts. Such parasitic scattering can, to some extend, be accounted for by adding a background to the algorithm. However, the signal to noise ratio seemed to be insufficient to further improve the resolution. Nevertheless, the images agreed well with SEM images and a resolution of approximately ≤ 35 nm was expected from comparison with those, which goes along with the resolution determined by FRC.
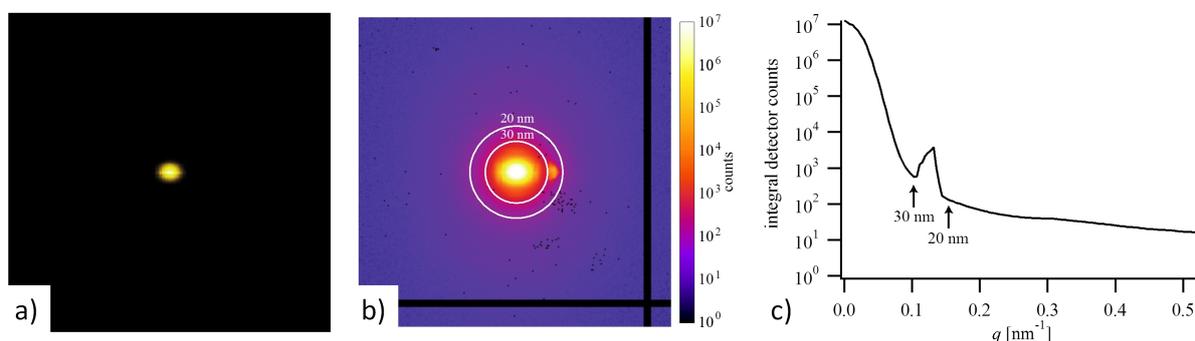
Figure 11.3: a) Far-field diffraction pattern from Fig. 11.1b in linear scale, b) diffraction patterns averaged over all 1681 diffraction patterns, c) the azimuthal average count rate as a function of the momentum transfer q. The black lines on the right and on the bottom in b) show areas between different parts of the detector, where no X-rays could be detected, additionally, some "dead" pixels can be observed as black spots. The white circles indicate q-values corresponding to 20 and 30 nm respectively, which is also shown in c) by the appearance of most scattering intensity for this q-range.
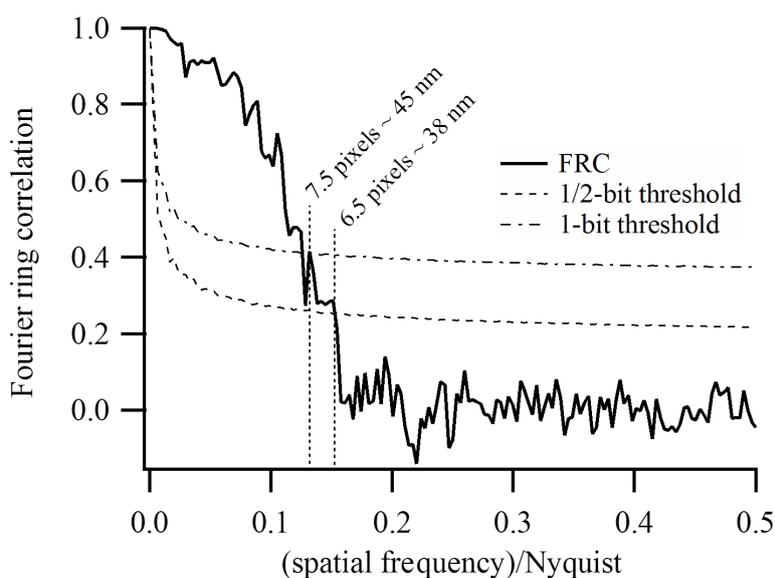
Figure 11.4: FRC of the ptychogram from Fig. 11.1b), where the 1/2-bit and 1-bit thresholds point to a spatial resolution of 38 and 45 nm, respectively. Reprinted from [229], reproduced with permission.

11.2.3 Conclusion – First Application of the Cell during *In Situ* Hard X-ray Ptychography

The good agreement of the SEM images and the phase contrast images obtained by *in situ* ptychography is obvious for both studied samples np-Au and CeO_2/np-Au. Although 3D materials were studied, for thin materials like the np-Au, the projected image results in sufficient contrast to gain insight into the structure of the studied np-Au based samples. The spatial resolution of approximately 40 nm, which was obtained in this experiment, is already comparable to resolutions obtained by full-field microscopy techniques [106] and better by the factor of 4, than the one reached in previously reported *in situ* ptychography studies [132]. In addition to the higher resolution obtained here, the cell used in the present work shows benefits during experimental use: it is completely gas tight (due to a closed cell approach with X-ray transparent windows) and the heated area is smaller, which is why no additional cooling is required. Last but not least offers the small size and light weight that the whole cell can be positioned on a piezo stage used for accurate sample positioning during ptychographic data acquisition, which facilitates the experimental setup. Moreover, the cell offers the unique possibility to perform *ex situ* EM and *in situ* ptychography on the same sample, which will also be presented in the following sections. This possibility enables complementary studies which combine the benefits of both techniques, namely high resolution imaging under model conditions using EM and the possibility for real *in situ* application using ptychography. A more detailed conclusion on the annealing of the np-Au system under different atmospheres will be presented in section 11.3.3 and an evaluation of *in situ* ptychography as a tool for studying heterogeneous catalyst *in situ* will be presented in section 14.

11.3 Annealing of np-Au under Different Atmospheres

In a next study, the annealing behavior of 100 nm thick np-Au was studied up to temperatures of 800 °C by complementary *in situ* (E)TEM and *in situ* ptychography under different atmospheres, pressures and with/without ceria coating. Furthermore, an improved *in situ* setup allowing for the direct determination of the temperature and a spatial resolution around 20 nm is presented. Finally, the same sample areas were studied by electron microscopy before and after the treatment during *in situ* ptychography investigation.

11.3.1 Experimental

11.3.1.1 Sample Preparation

Both samples, np-Au and CeO_2/np-Au, were prepared in the very same way as described in section 11.2.1.1. However, instead of a stabilizing Al frame, an Au frame was prepared by FIB. This enables, in contrast to the previously used Al frames which degraded at approximately $660\,°C$, a treatment at higher temperatures. Furthermore, an additional difference due to the various thermal expansion coefficients is avoided which minimizes problems due to different expansions during the heating experiments.

Hexagonal shaped Au frames of approximately $L \times W \times H = 25\,\mu m \times 15\,\mu m \times 500\,nm$ for pure np-Au and quadratic Au frames $L \times W \times H = 13\,\mu m \times 13\,\mu m \times 500\,nm$ for CeO_2/np-Au were used to stabilize the sample. The frames were fixed on the np-Au and CeO_2/np-Au samples by deposition of platinum on the outside of the frame. Afterwards, the sample was milled out and fixed on a Protochips E-Chip^{TM} by platinum deposition on the outside. In this way, both a np-Au and a CeO_2/np-Au sample were deposited on a single E-Chip^{TM}. By this procedure, it is ensured that both samples observe the same conditions during *in situ* treatment. FIB milling was performed by Dr. Torsten Scherer at the KNMF (located at the INT at KIT) using a Zeiss Auriga 60 or a FEI Strata dual beam FIB system. *Ex situ* SEM imaging was performed using the above mentioned FIB microscopes with a SE in-lens detector at $5\,keV$.

In parallel to the FIB prepared samples, another set of np-Au samples was prepared by drop-casting of an ethanolic dispersion of np-Au on a copper TEM grid with lacey carbon film as well as on a Protochips E-Chip^{TM}.

11.3.1.2 Electron Microscopy

Annealing studies were either performed via conventional heating in a TEM using a) a Gatan 652 Inconel heating holder (for the np-Au sample on the TEM grid) or b) by the Protochips Aduro heating holder. Transmission electron microscopy measurements were performed on three different microscopes.

- a Tecnai T20 G2 operating at $200\,kV$ and in Bright Field (BF) mode (drop-casted pure np-Au sample on a lacey carbon film coated copper grid)

- a FEI Titan 80-300 aberration corrected electron microscope operated at $300\,kV$ acquiring STEM by a Fischione model 3000 HAADF-STEM detector using the Protochips heating

holder for annealing studies (FIB prepared CeO$_2$/np-Au sample on a E-Chip^{TM}); Electron Energy Loss Spectroscopy (EELS) analysis was performed at 200 °C to avoid any contamination on the sample using a Gatan Tridiem imaging filter

- a FEI Titan E Cell 80-300 aberration corrected electron microscope operated at 300 kV with a pressure of 3.2 mbar O$_2$ acquiring images in STEM and BF mode using the Protochips heating holder (drop-casted pure np-Au sample on a E-Chip^{TM})

11.3.1.3 *In Situ* Ptychography

In situ X-ray ptychography measurements were carried out with the cell described in section 10.1, which enabled measuring under controlled atmosphere and temperature. A flow of 3 ml/min of 20% O$_2$/He was used to control the atmosphere. The samples were heated using the Joule heating possibility of the E-Chip^{TM}. Different temperature steps were used and the sample was kept at each step for approximately 90 minutes during performing ptychographic acquisitions. The temperature was directly measured by IR thermography (*c. f.* section 11.3.1.4). Measurements were performed at the cSAXS beamline of the Swiss Light Source (SLS) and image reconstruction was preformed by Dr. Ana Diaz (SLS, PSI).

The X-ray beam was defined using a coherently illuminated Fresnel zone plate made of Au [265] with a diameter of 170 μm and an outer-most zone width of 60 nm, corresponding to a focal length of 47.03 mm at the applied energy (5.72 keV). A flux of 2.7×10^8 photons/s was estimated. The samples were placed at a distance of 350 μm downstream the focus, such that the illumination on the sample had a diameter of about 1.3 μm. Ptychographic scans were recorded by scanning the sample over a field of view of $2 \times 2 \, \mu m^2$ in a grid of about 400 points which followed a Fermat spiral [266] with an average step size of 100 nm. At each scanning position diffraction patterns of 0.2 s exposure time were recorded with a Pilatus 2M detector with 172 μm pixel size [267] placed at 7.255 m downstream the specimen. The total duration of a scan was about 215 s, taking into account overhead time in between acquisitions. The scans were repeated at two detector positions in order to record intensities at missing regions of the detector due to module gaps. Such pairs of scans were repeated at 4 different positions covering a total field of view of $3.5 \times 3.5 \, \mu m^2$ with an overlapping region of 0.5 μm in between. For each pair of scans an estimated flux density of 8.6×10^9 photons/s μm^2 was irradiated on the samples, from which the surface dose deposited on the specimen could be described by Howells *et al.* [268]. For an assumed relative density of 30 % for the np-Au samples [269], an estimated dose of 3.8×10^8 Gy was applied on the specimen. The ptychographic image reconstructions were performed using 1000 iterations of the difference map algorithm [122] followed by 100 iterations of a maximum likelihood optimization used as a refinement step [270]. All 8 scans recorded

for each sample and for each temperature step were fed simultaneously into a ptychographic reconstruction in which a single object was reconstructed while refining a different probe for each scan. This idea has been introduced by Dierolf [123] and Guizar-Sicairos *et al.* [271] to avoid that the illumination probe changes during a ptychographic scan while benefiting from the robustness of reconstructing the entire region of interest in the same ptychographic reconstruction. All reconstructions were done using a region of the detector of 600×600 pixels containing the diffraction patterns, which corresponded to a reconstructed pixel size in the images of 15.2 nm. The resolution was estimated from a dataset on a CeO_2/np-Au sample acquired at room temperature. For this purpose two reconstructions of two pairs of scans acquired at two different positions, reconstructing for each pair a common object with two different illumination probes, were performed. Afterwards, the Fourier ring correlation of the two objects at the overlapping area, which had a total extension of $0.5 \times 2\,\mu m^2$, was computed and compared with a threshold corresponding to the 1-bit criterion [264], obtaining an estimated resolution of 20 nm. The reconstructed images were post-processed to remove a ramp and an offset which are intrinsic degrees of freedom in ptychographic reconstructions [272]. Because of the very small areas of air, which are typically used as a reference for constant phase [272], methods developed previously could not be applied for the phase ramp removal. Instead an approach in which the ramp was removed visually by checking different ramps in steps of 0.02, which corresponds to an error between pixels at both extremes of the image of $0.02 \times 2\pi = 0.12$ rad, was applied. For the phase offset correction, the largest area without sample in the images was used.

11.3.1.4 Infrared Thermography

IR thermography to determine the temperature during *in situ* ptychography was performed using an ImageIR® 8300 camera from InfraTec equipped with a macro objective M=1.0 x with a field of view of 9.6×7.7 mm and a pixel size of 15 μm. The spatial resolution was further improved down to approximately 5 μm using intermediate rings in addition to the objective lens. The obtained thermal emission data were calibrated to the Si_3N_4 membrane by setting the emissivity ϵ to 0.9 [158]. The resulting temperature for the membrane can then be assumed to be identical for the samples, as the samples were expected to be in good thermal contact to the membrane.

11.3.2 Results and Discussion

11.3.2.1 Combination of *In Situ* X-ray Microscopy using Ptychography and IR Thermography for Temperature Measurement

In order to demonstrate the improved capabilities of the *in situ* cell, results on both the temperature measurement and *in situ* ptychography are reported. As the temperature of the sample is very important during the measurements, IR thermography was used directly during annealing treatment to determine the temperature just prior to the acquisition of *in situ* ptychography datasets. A typical IR thermography image with a spatial resolution better than 10 μm is shown in Fig. 11.5, with the sample compartments being located in the middle. For determining the temperature during *in situ* ptychographic measurements with Kapton® foil as window material, the temperature measurement was calibrated by measuring empty chips beforehand. In this way the influence of the temperature determination through the 25 μm thick Kapton® foil could be estimated. Fig. 11.5a shows the measured temperature from the front with and without a Kapton® foil, in contrast to the temperature measured from the back of the cell. A difference of approximately 10 % between the measurement with and without foil could be detected as it is visible in Fig. 11.5a. Hence, during *in situ* measurements on the sample used during ptychography, the temperature estimated by the IR camera behind the Kapton® foil was corrected by an extra 10% of the measured temperature. The thermogram in Fig. 11.5a, which corresponds to the sample presented in Fig. 11.6 at 250 °C, shows that the sample seems to be at slightly higher temperature. As the emissivity chosen for temperature determination was set to the emissivity of the Si_3N_4 membrane, the higher temperature is probably due to the different emissivity of the sample and the membrane.
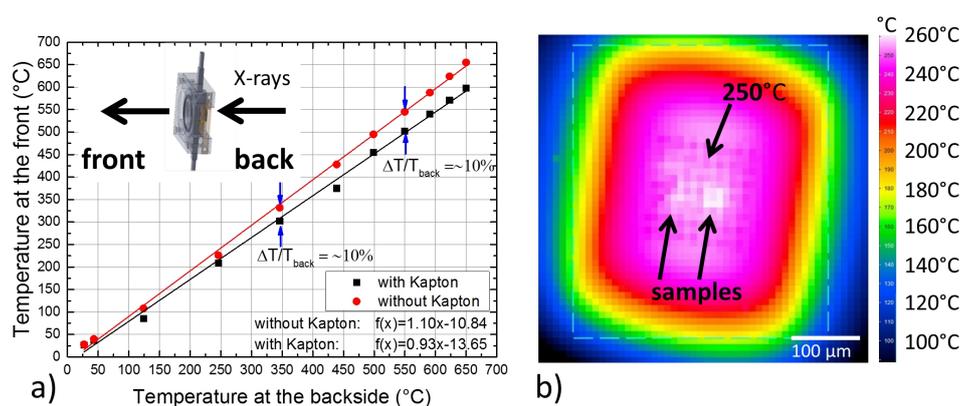
Figure 11.5: a) IR thermography measurement with (through) and without Kapton® foil in comparison to the temperature determined at the backside of the chip. b) IR thermography measurement of the E-Chip™ in the *in situ* ptychography cell at 250 °C (arrow pointing to the Si_3N_4 membrane) through the Kapton® foil.

Fig. 11.6a – d shows some examples of ptychographic images in comparison to EM images. The good agreement between SEM measurements under vacuum conditions before the annealing treatment, the *in situ* ptychography measurements at atmospheric pressure and elevated temperature during annealing and the STEM measurements after the annealing treatment is clearly visible. Fig. 11.6e shows a FRC plot, which was derived to determine the spatial resolution [264]. The intersection with the 1-bit threshold is at 0.746 and with a pixel size of 15.2 nm, a spatial resolution of 20 nm is obtained, which improved the previously obtained resolution by a factor of 2 (*c. f.* section 11.2.3).

In this study, the temperature measurement was performed under the same conditions applied during *in situ* ptychography which enables a precise knowledge of the temperature during the image acquisition. By the use of IR thermography with a spatial resolution $<10\,\mu$m, not only the average temperature of the heated area can be determined, like it is usually done with a temperature sensor [246, 252], but by imaging the heated area it can also be accounted for temperature inhomogeneities, which can occur when catalysts are studied during reactions. In contrast to indirect temperature determination of the application of pre-calibrated heating chips in vacuum [261], the direct measurement of the temperature allows to determine the temperature in a gas atmosphere as well, in which a calibration performed in vacuum would not be valid any more. The good agreement of electron microscopy and the high spatial resolution derived by *in situ* ptychography clearly underline the potential of *in situ* ptychography bridging the gap between high resolution imaging under model conditions in electron microscopy and realistic conditions.
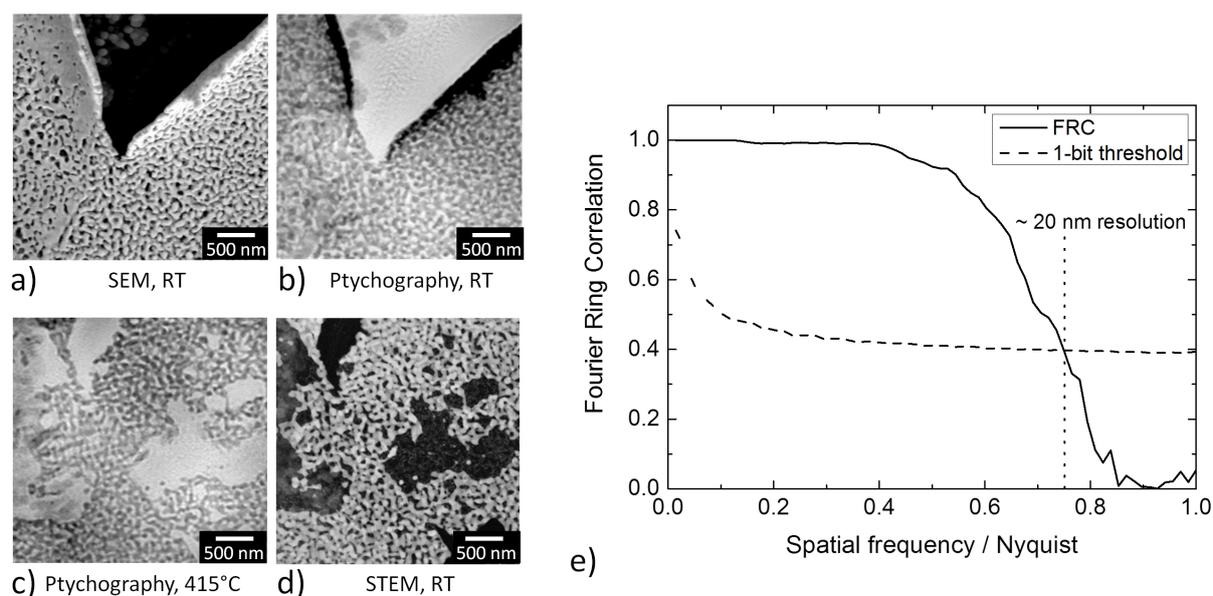
Figure 11.6: a) SEM image of the CeO_2/np-Au sample at RT under vacuum conditions before the annealing treatment, b) ptychographic image of the same sample acquired at RT under atmospheric pressure and c) at 415 °C, d) STEM image of the same sample under vacuum conditions at room temperature acquired after the annealing treatment. e) FRC for the ptychogram shown in panel b) to estimate the resolution of the ptychographic images at RT under atmospheric pressure.

11.3.2.2 Annealing of np-Au under Different Atmospheres and Pressures

To study the annealing behavior of np-Au at elevated temperatures under vacuum conditions, *in situ* heating was performed during TEM from RT up to 800 °C. A sample dispersed in ethanol was prepared on a copper TEM grid by drop-casting and heated to the desired temperature in 100 °C intervals. Overview bright field TEM images of the sample at different temperatures (RT to 800 °C) are presented in Fig. 11.7a – f. Due to the thickness of the sample, only the corner region was electron transparent. However, at 300 °C a few changes, like a contraction of material (marked by a red arrow in Fig. 11.7b), could be detected in the top region. Hardly any differences could be observed until 600 °C (Fig. 11.7d). Only at 700 °C (Fig. 11.7e) first changes became visible in the thick material, *i. e.* some material loss or migration. At 700 °C, the material loss occurred only once, whereas it continued steadily after the temperature increase to 800 °C (Fig. 11.7e). Where the material was no longer visible, a weak residue was left behind and thick areas were formed at the same time at different positions, indicating a coarsening behavior of the sample. Similar observations were also made for areas which were not probed with the electron beam during annealing, which excludes an influence of the electron beam on the observed behavior. EDX and EELS analysis of an area with a similar material loss, studied on a sample on a Si_3N_4 membrane, revealed the presence of Si, N and O, but excluded any trace of Au.
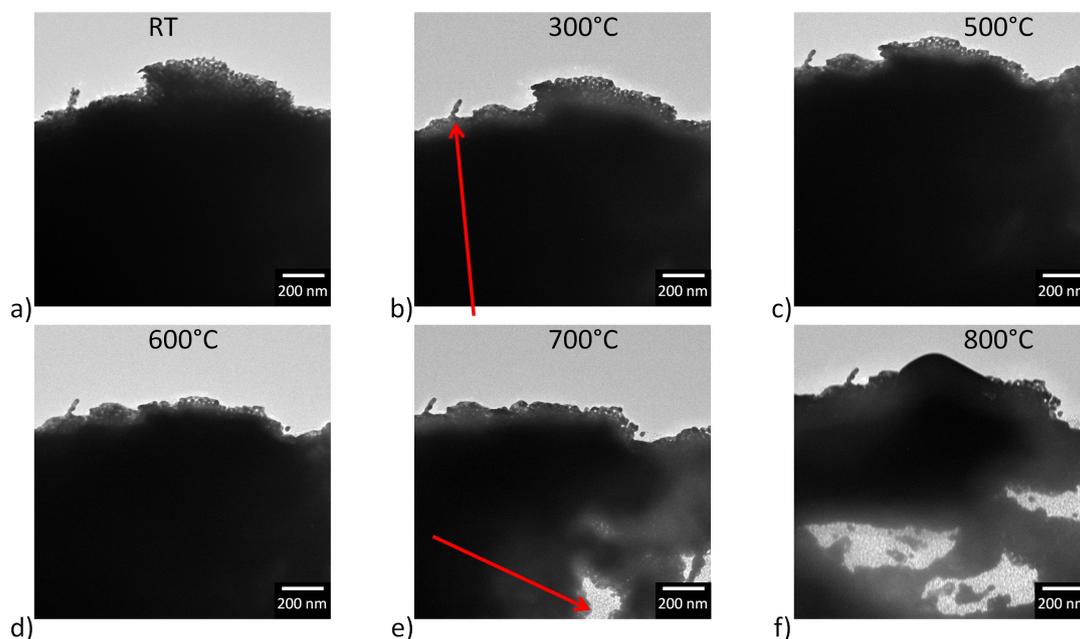
Figure 11.7: BF-TEM images during annealing of a pure np-Au flake drop casted on a copper TEM grid covered by lacey carbon film. Annealing studies were performed in vacuum. Only the corners of the flake were thin enough to be nearly electron transparent. The annealing for the temperature steps 25, 300, 500, 600, 700, 800 °C is depicted from a) – f). At a temperature of 700 °C presented in panel e), the first changes in the dark, thick area could be seen, which changed constantly at 800 °C as depicted in panel f).

In Fig. 11.8, a zoom into the top region of the area studied in Fig. 11.7 is presented in different magnifications (top to bottom), which shows that only slight changes, like a contraction of the ligaments, can be observed at temperatures of 200 and 300 °C (marked by red arrows in Fig. 11.8b and c).
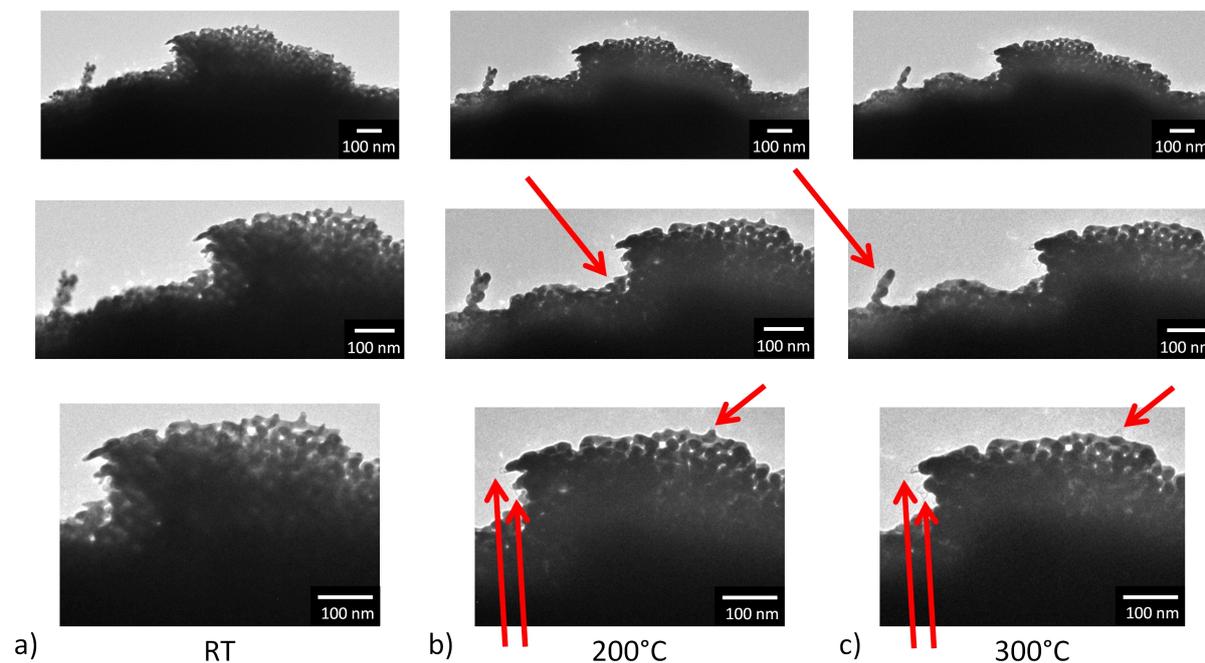
Figure 11.8: BF-TEM images of the top region in presented in Fig. 11.8 showing the porous structure at the corner of the studied flake at different temperatures. TEM images are shown at a) RT, b) 200 °C and c) 300 °C respectively with different magnifications (top to the bottom). Already at those relatively low temperatures, slight changes of the sample occurred. At 100 °C no changes were observed with respect to the measurement at RT.

In the next step, *in situ* annealing was carried out in the ETEM on a np-Au sample prepared by drop casting of dispersed flakes on a Protochips E-Chip^{TM} in an atmosphere of 3.2 mbar of O_2. This allowed studying the influence of an oxygen containing atmosphere. Selected images are presented in Fig 11.9. By drop-casting, the flakes could not be placed on the thin Si_3N_4 windows of the E-Chip^{TM} but were located on thicker parts of the SiC membrane (approximately 100-200 nm) which results in a higher background signal for the TEM images than if they were on the approximately 50 nm thick Si_3N_4 membrane. Some flakes deposited on the thicker part of the heated membrane were studied during annealing, but in comparison to the flake studied in vacuum they were smaller and showed bigger pores and ligaments. Similar to previous measurements in vacuum, the sample was heated in 100 °C intervals and no changes could be observed up to 200 °C. Between 200 °C and 300 °C changes could be detected in the sample, which can be both seen in the overview image Fig. 11.9a in HAADF-STEM contrast, as well as in the image showing the top right flake in higher magnification, which is depicted in BF-TEM contrast Fig. 11.9b. Both the overview and the magnified image show that the flakes

starts to coarsen when they were heated to 300 °C, which goes along with a collapse of some ligaments (indicated by the red arrows) and an increase in thickness. The latter becomes especially visible in the HAADF-STEM images, as the transparency of the material got less and the contrast changed (thicker areas got darker) which can be explained by a sintering behavior. In contrast to measurements in vacuum, no material loss was observed (also at higher temperatures up to 900 °C, not shown here), but the sample showed a coarsening behavior as also reported under air in literature [241, 245–247, 254, 255, 273].
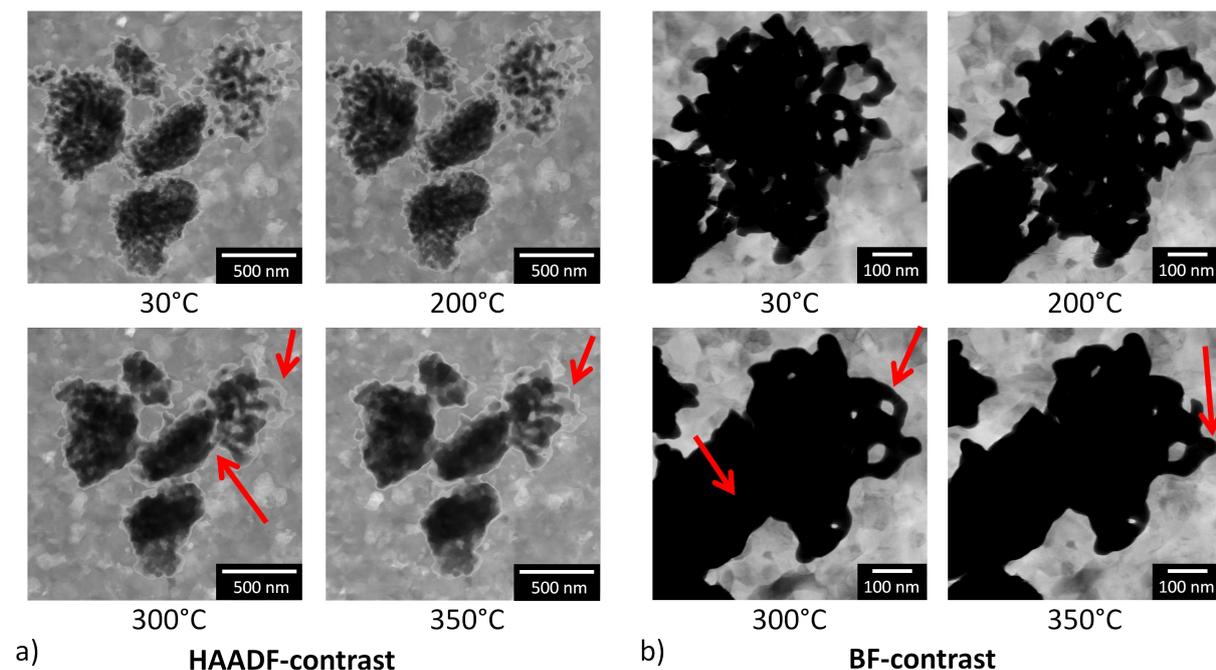
Figure 11.9: ETEM study of the *in situ* annealing of np-Au drop-casted on a E-Chip^{TM}. Annealing treatment was performed at different temperatures in an atmosphere of 3.2 mbar of O_2. a) Shows overview images on the studied flakes by HAADF-STEM images, whereas b) depicts a zoom into the top right flake by BF-TEM images.

Additionally to the measurements performed under model conditions in the TEM, complementary measurements were performed during *in situ* ptychography to unravel the influence of pressure and oxygen at ambient pressure. The sample was prepared by FIB micromanipulation and placed on a E-Chip^{TM} which was heated in the *in situ* ptychography cell at atmospheric pressure with a flow of 3 ml/min of 20% O_2/He; the temperature was controlled by IR thermography (see Fig. 11.5). The phase contrast images from the ptychographic measurements at a constant energy of 5.72 keV are presented in Fig. 11.10 and changes with respect to the previous image at lower temperature are marked with red arrows. Despite attempting to monitor the same area of interest during the annealing treatment, a slight shift in sample position is visible, due to a sample drift with increasing temperature and only manual position correction. At a temperature of approximately 300 °C, depicted in Fig. 11.10c, the first changes (indicated by red arrows) could be observed, which showed slight material loss or movement, similar to

this observed during heating in vacuum. With increasing temperature the loss increased, but a coarsening behavior similar to the one observed in oxygen during ETEM could not be found. This is also shown by quantitative comparison of the ligament diameter before and after the annealing treatment, which is depicted in Fig. 11.11. Here, the ligament diameter was determined by manually determining the diameter between connecting knots in the ligaments [250]. Before the annealing, evaluation was performed on the SEM images, whereas after annealing, TEM images were used for evaluation. Ptychography images could not be used because a pixel size of 15 nm was used during reconstruction of the images. The size distribution shows that similar diameters before (black bars) and after (red bars) the annealing were determined, revealing that no coarsening occurred. To be able to compare the very local studies performed by electron microscopy with those performed during *in situ* ptychography, a smaller field of view from the ptychographic reconstructions is presented in Fig. 11.12 as well.
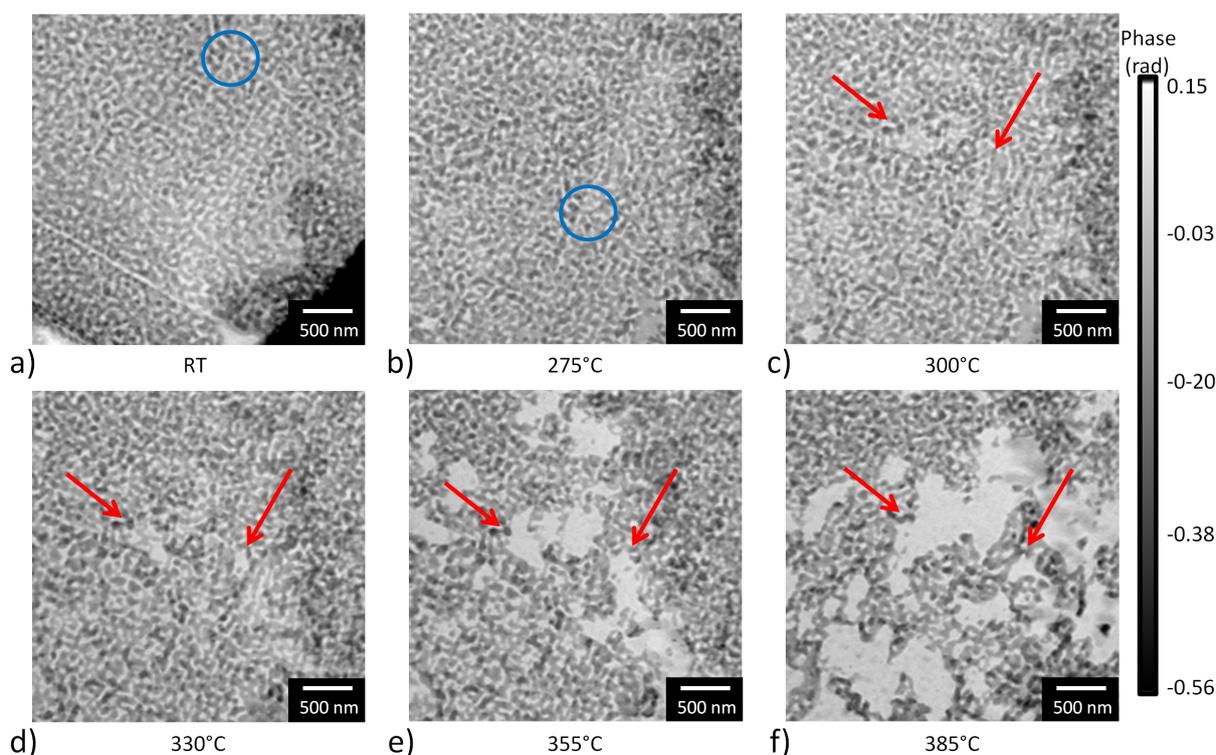
Figure 11.10: Phase contrast images of np-Au at different temperatures performed in the *in situ* cell for X-ray ptychography at the cSAXS beamline at SLS using a constant energy of 5.72 keV and a flow of 3 ml/min 20% O_2/He. a) – f) show the images recorded at 25, 275, 300, 330, 355, 385 °C respectively. Red arrows indicate changes with respect to the previous image at lower temperature, while blue circles show the same position inside the images.
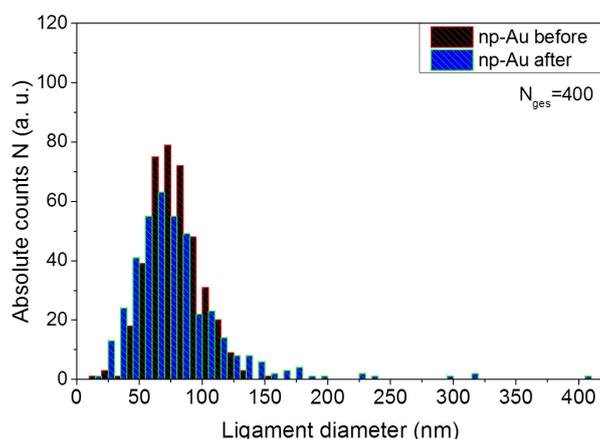
Figure 11.11: Ligament diameter distribution of np-Au before and after the annealing treatment performed during *in situ* ptychography. The mode ligament diameter is around 75 nm before (black bars) and after (blue bars) annealing, showing that no coarsening occurred.
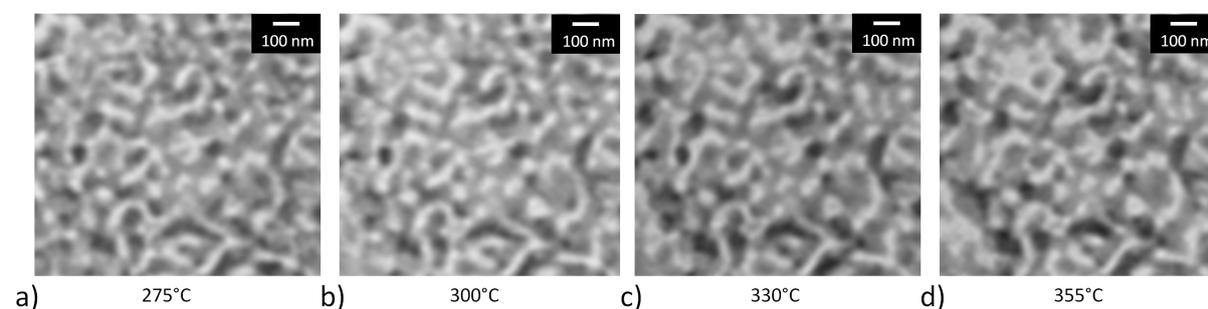
Figure 11.12: Magnified parts of the bottom left part of the phase contrast images presented in Fig. 11.10. a) – d) show the images recorded at 275, 300, 330, 355 °C respectively.

To get quantitative information on the material loss, the normalized grayscale values corresponding to the phase shift of X-rays after propagation through the sample have been calculated between 275 – 355 °C, which is plotted in Fig. 11.13. Since the phase shift depends on the thickness of the material, the change in grayscale values can be related to changes in the material's thickness. In Fig. 11.13a, the area where the material loss was studied is marked by a red box. It becomes obvious that the area in the center of the red box becomes slightly brighter with increasing temperature which goes along with a higher grayscale value. For quantitative information, the grayscale value measured in a 200×200 nm big box located in the center of the red box, was divided by the grayscale value obtained from the non-changing area marked by the blue box. Fig. 11.13b shows that the mean grayscale value, which presents the average grayscale value measured in the center of the red box, increased. However, this is only true assuming that no changes in the area used for calibration occur. This could only be determined approximately because no absolute calibration could be performed due to the application of the manual phase correction. Therefore, the consideration of the grayscale values should only be taken as an additional information.
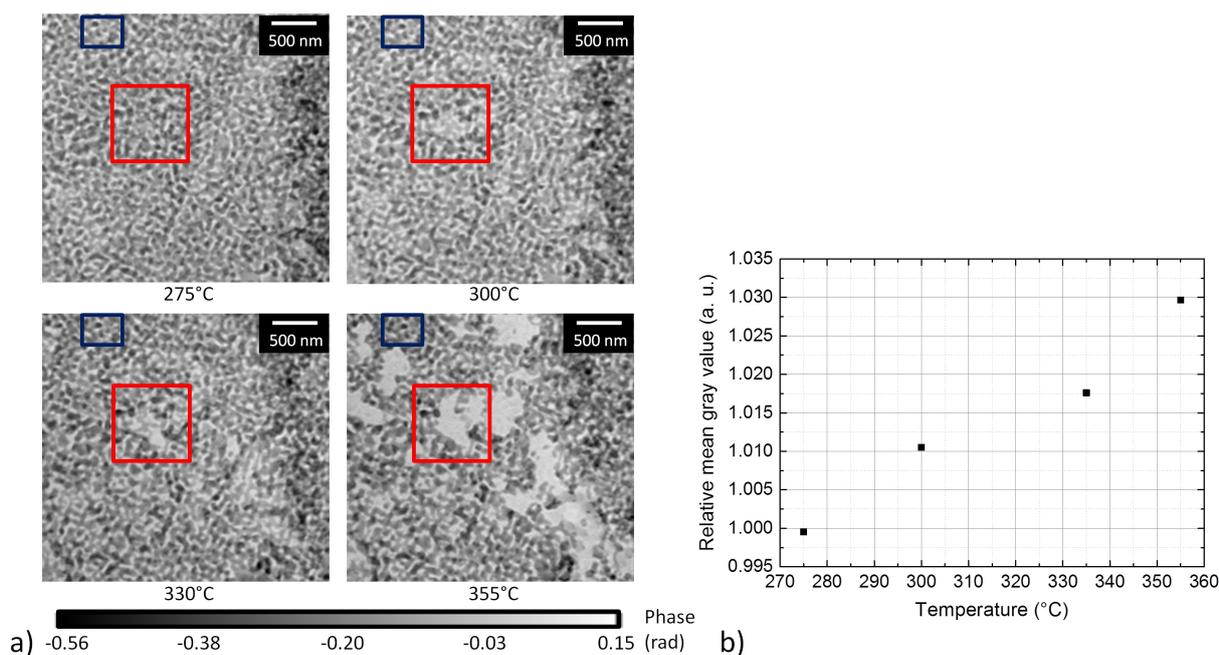
Figure 11.13: a) Selected phase contrast images derived from magnified parts of the bottom left part of the phase contrast images presented in Fig. 11.10 for 275, 300, 330, 355 °C respectively. The area where the loss starts to be visible is marked by a red box, while the visibly non-changing area is marked by a blue box. b) Plot of the relative mean grayscale values with respect to temperature. The grayscale values were normalized by correcting the grayscale values measured in the center of the red box by the ones measured in the blue box.

The results presented for the annealing of np-Au in different atmospheres show that during annealing of np-Au in vacuum and in 20% O_2/He a material loss or migration was observed, in contrast to measurements in 20% O_2/N_2 (compare section 11.2 and [229]) or pure O_2 in the mbar regime. Taking the high X-ray dose for the measurements performed in 20% O_2/He into account, the differences might be explained by beam damage. However, the loss was also observed in areas which were not probed by the X-ray beam, as determined by TEM after the ptychography treatment (*c. f.* section 11.3.2.3). In contrast to previous studies in literature [252, 253] it could be shown that np-Au samples started to change in vacuum when temperatures above 700 °C were applied. At these high temperatures, a material loss as well as sintering were observed. Interestingly, the loss observed during *in situ* ptychography in 20% O_2/He at ambient pressure started at much lower temperatures than under vacuum conditions, but at a comparable temperature to the onset of coarsening during ETEM analysis in oxygen atmosphere. These new findings indicate that the atmosphere strongly influences the coarsening behavior and the underlying mechanisms. Furthermore, it shows that measurements at ambient pressure are possible when techniques like *in situ* ptychography are applied, which are necessary to study realistic processes.

11.3.2.3 Stabilization of np-Au by Supported CeO$_2$ – Annealing of CeO$_2$/np-Au under Different Atmospheres and Pressures

Next, the influence of deposition of a CeO$_2$ layer on the np-Au surface was studied. Often such an additional layer has a stabilization effect [260, 274]. For this purpose, a sample was studied under vacuum conditions during *in situ* annealing in TEM and at atmospheric pressure during *in situ* ptychography in 20% O$_2$/He to compare the behavior under model conditions inside the TEM with realistic conditions. Both samples were prepared by FIB micromanipulation like the np-Au samples used for ptychography in section 11.3.2.2. Furthermore, the CeO$_2$/np-Au sample studied during *in situ* ptychography was placed next to the np-Au so that differences in temperature or atmosphere between the CeO$_2$-stabilized and the unstabilized np-Au can be excluded. The phase contrast images from CeO$_2$/np-Au during the ptychographic measurements at the same temperatures like np-Au applying a constant energy of 5.72 keV are presented in Fig. 11.14 and changes with respect to the previous image at lower temperature are marked with red arrows, while blue circles indicate the same position in the images.
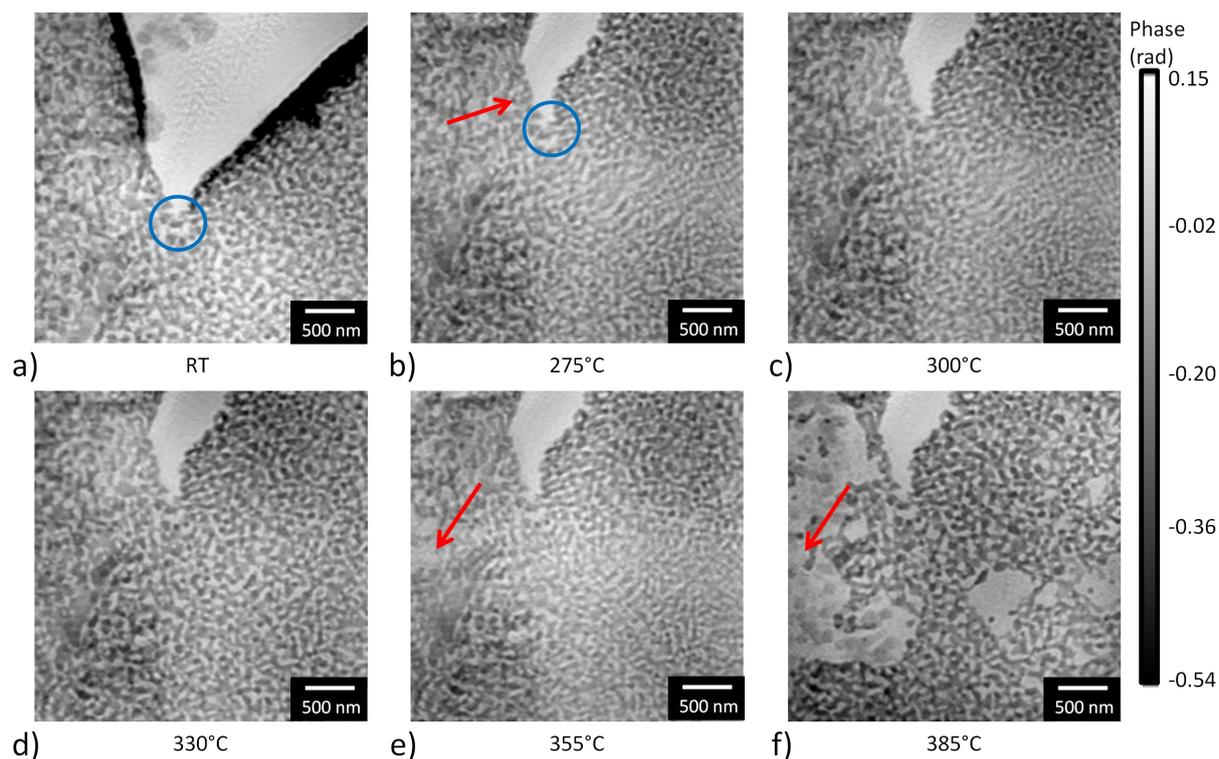
Figure 11.14: Phase contrast images of the CeO$_2$/np-Au sample at different temperatures performed in the *in situ* cell at the cSAXS beamline at SLS using a constant energy of 5.72 keV and a flow of 3 ml/min 20% O$_2$/He. a) – f) show the images recorded at 25, 275, 300, 330, 355, 385 °C respectively. The blue circles indicate the same position in the images, while red arrows highlight changes compared to the previous image.

Besides the marked changes, Fig. 11.14 shows that the sample seemed to move so that apart from a different field of view, the crack in the center had a slightly different shape at higher temperature than at the original RT measurement, which can be seen as well in the image at 275 °C. In fact, this movement already occurred at a temperature around 50 °C (not shown here) and might be explained by a loss of stress, induced by translation due to enhanced temperature. A magnified part of the top right area from 300 – 385 °C is depicted in Fig. 11.15.
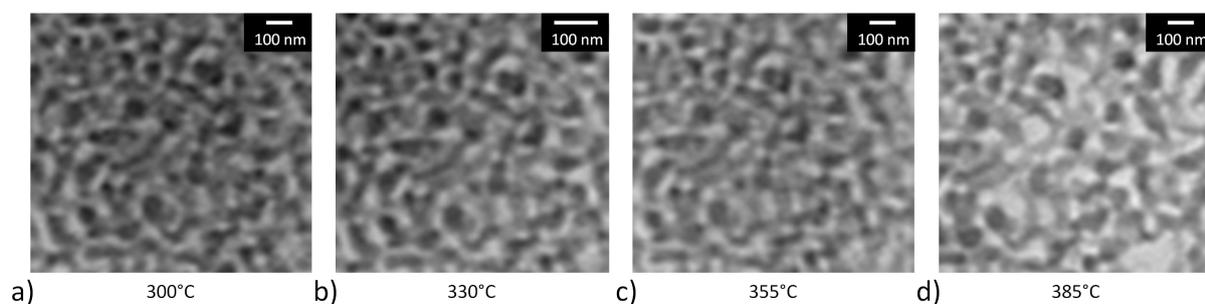

Figure 11.15: Magnified parts of the top right part of the phase contrast images presented in Fig. 11.10. a) – d) show the images recorded at 300, 330, 355, 385 °C respectively.
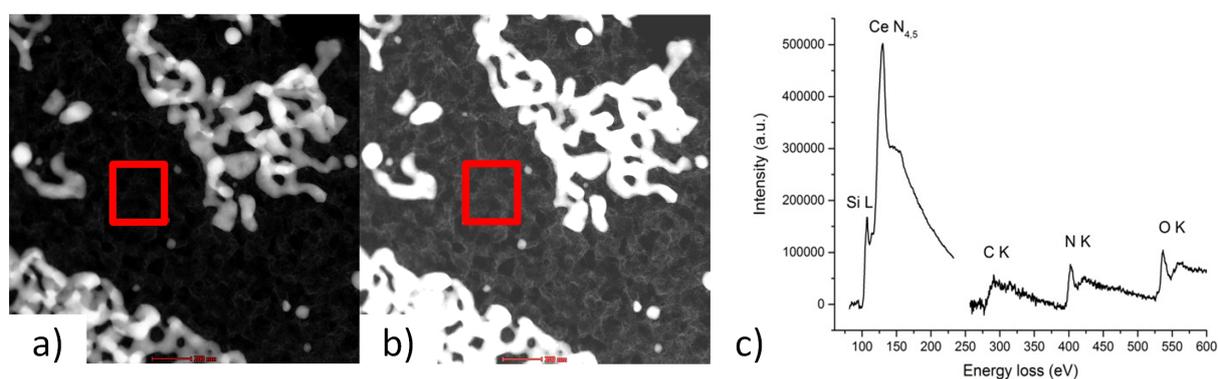
Figure 11.16: STEM-HAADF images of the CeO_2/np-Au sample showing the area of the EELS measurement (red box) and the EELS spectrum performed after annealing during *in situ* ptychography. a) STEM-HAADF image with normal contrast to show the position for the EELS measurement with respect to the remaining np-Au (bright material), b) STEM-HAADF image with increased contrast to visualize the remaining residue, c) EELS spectrum of the selected area marked by the red box in a) and b), revealing the presence of Si, Ce, C, N, and O.

Comparably to the unmodified pure np-Au sample a material loss or migration could be detected. Once the gold ligaments severed, a weak residue was observed. This residue can be attributed to CeO_2 containing material for the stabilized sample, as it becomes visible by the EELS analysis shown in Fig. 11.16, which was performed on an area where a material loss and a remaining residue was observed. EELS analysis revealed the presence of Si, Ce, slight amounts of C, N and O. Whereas the small amounts of C can be explained by impurities caused by the FIB process, the presence of Si and N can be related to the Si_3N_4 membrane, on which the sample is deposited. Finally, Ce and O can be explained by the CeO_2 particles used for stabilization.

A coarsening could not be found, as indicated by the distribution of the ligament diameter before and after the annealing depicted in Fig. 11.17 and the magnified part of the phase contrast images shown in Fig. 11.15. By comparing the onset temperature at which the loss appeared, it becomes obvious that changes occur first on the pure np-Au sample around 300 °C (compare Fig. 11.10) whereas the first changes for the CeO₂/np-Au sample started around 355 °C. This indicates a stabilization due to CeO_2 by about 50 °C. Furthermore, it shows that the observed effect of material loss or migration is independent of the stabilizing oxide, but the process starts at a slightly higher temperature.
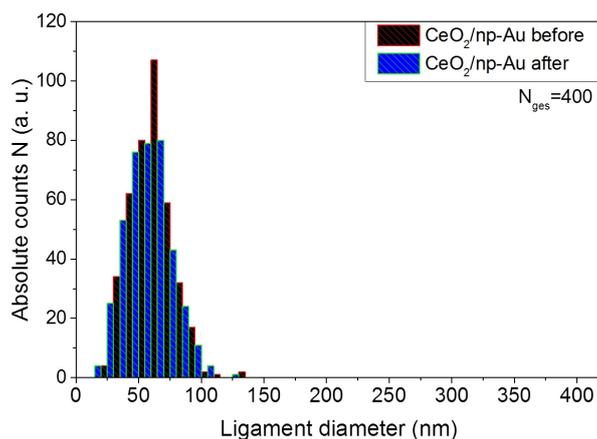
Figure 11.17: Ligament diameter distribution of CeO_2/np-Au before and after the annealing treatment performed during *in situ* ptychography. The mode ligament diameter is around 65 nm before (black bars) and after (blue bars) annealing, showing that no coarsening occurred. In contrast to the pure np-Au sample, the size distribution is narrower, as visible by comparison with Fig. 11.11.

To study the annealing behavior of the stabilized sample under vacuum conditions, *in situ* heating was performed during TEM in a conventional microscope (vacuum conditions around the sample). Model STEM images for the annealing of CeO_2/np-Au on a Protochips E-Chip™ at 840 °C are given in Fig. 11.18. Note that the bright area on the bottom left corner of the Fig. 11.18a – d has not been there before annealing treatment, but might result from redeposition as the electron beam was kept in the lower left corner. Comparably to the previous experiment of the unstabilized sample in vacuum, a material loss or migration could be observed. At lower temperatures, no changes could be seen. Evaluating the onset of changes (*e. g.* material loss) in the unstabilized material compared to the stabilized np-Au gives an indication for the stabilizing effect of the CeO_2 in vacuum. For the pure np-Au sample, the onset started at 700 °C (see Fig. 11.7), but continued steadily at 800 °C. In contrast, the onset started at 840 °C for the CeO_2/np-Au sample annealed in vacuum and continued at this temperature (see Fig. 11.14). The stabilization effect in vacuum is therefore comparable to the stabilizing effect in O_2/He under atmospheric pressure, where the onset of material loss or migration was shifted to about 50 °C higher temperatures.
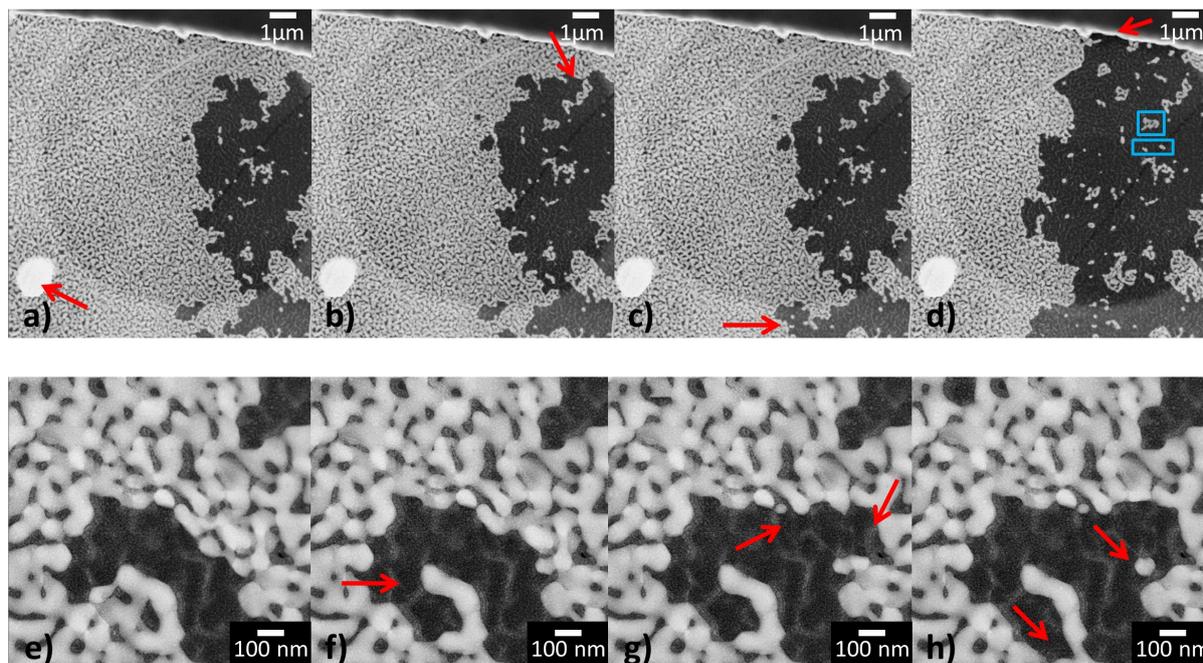
Figure 11.18: STEM images on low resolution (top, 10000x magnified) and higher resolution (bottom, 57000 x magnified) at 840 °C in vacuum. a) Represents the sample after being heated at 840 °C for 11 minutes, b) and c) after 12 minutes, and d) after 33 minutes. e) –h) were recorded within one minute directly after reaching 840 °C, indicating that material loss started immediately. Red arrows indicate exemplary areas where changes occurred in comparison to the image before. Additionally, in d) blue boxes indicate the area for the zoomed-in regions from Fig. 11.19.

Apart from the material loss or migration on larger length scale, some changes happened on a smaller length scale as well. Examples for such changes are given in Fig. 11.19 and seem to result from contractions of the gold ligaments which are similar to the expected coarsening due to ligament pinch-off [256, 275] (Fig. 11.19a) or sintering (Fig. 11.19b) of the np-Au samples. The positions of the studied areas are marked with blue boxes in Fig. 11.18d. Interestingly, the material loss started at one area and continued outgoing from this area, as it becomes visible by comparing Fig. 11.18a – d and e – f. Fig. 11.18e indicates that not only very small ligaments pinch off, but also some neighboring ligaments severe, whereas others stay stable and break off later (Fig. 11.18h). Additionally, Fig. 11.18f – h show at the top of the area where the loss occurs, that parts of the ligament can pinch off, while small single, isolated particles remain, like it is visible in Fig. 11.18g and h, which would be expected to be unstable at elevated temperatures.

a)   b)
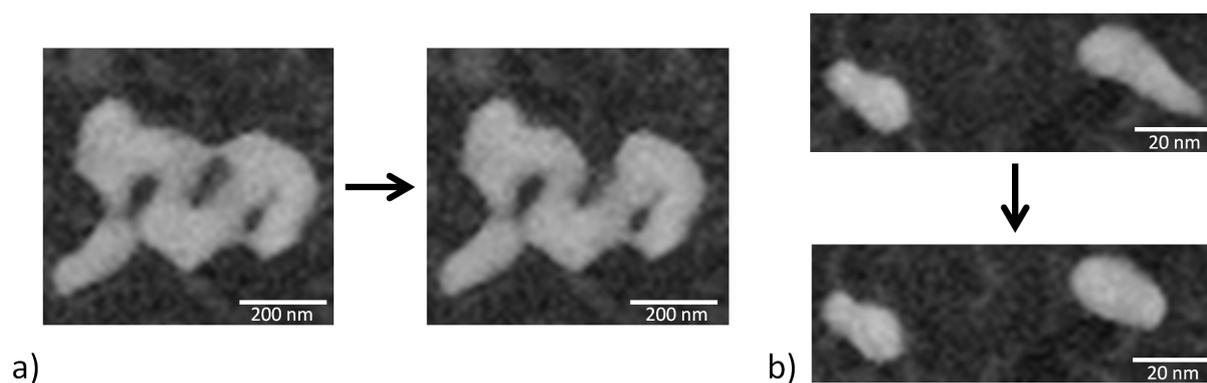
Figure 11.19: Zoom into regions (indicated by blue boxes in Fig. 11.18d) in the STEM images on the top row of Fig. 11.18. The images are acquired at different times after the first changes, which is symbolized by a black arrow. While the first images of a) and b) represent the structure derived after 11 minutes at 840 °C, the change to the second image occurred after 33 minutes for a) and after 25 minutes for b).

In Fig. 11.20 a and b, two comparisons of SEM images of the CeO_2/np-Au sample used for *in situ* ptychography, before the annealing (left images) and after annealing (right images) are shown. The depicted area shows a position, which was not imaged by ptychography, indicating that potential interaction of the sample by the X-ray beam did not significantly influence the behavior resulting in a material loss. Comparing Fig. 11.20a and b reveals that at the marked position (red arrows) next to a cut prepared by Ga ion milling, a part of the gold ligaments pinched off, while some areas of the sample stayed the same like they were before. However, some areas also changed their structure and the original ligaments cannot be recognized anymore, which might be explained by slight coarsening or restructuring. Additionally to the obvious material loss or migration on the bottom right corner of Fig. 11.20b, the remaining ligaments seem to be of the same size (*c. f.* Fig. 11.17), as far as conclusions can be drawn on the comparison of SEM and STEM images. In contrast, it seems as if the sample showed a contraction, like it was observed in Fig. 11.8 as well, corresponding to images shown by Kuwano-Natakami *et al.* [252]. Those contractions suggest that the gold tends to be mobile at annealing temperature, but the ligament seems to be hindered from usual coarsening, which seems to be the case for the annealing treatment in vacuum and in O_2/He.
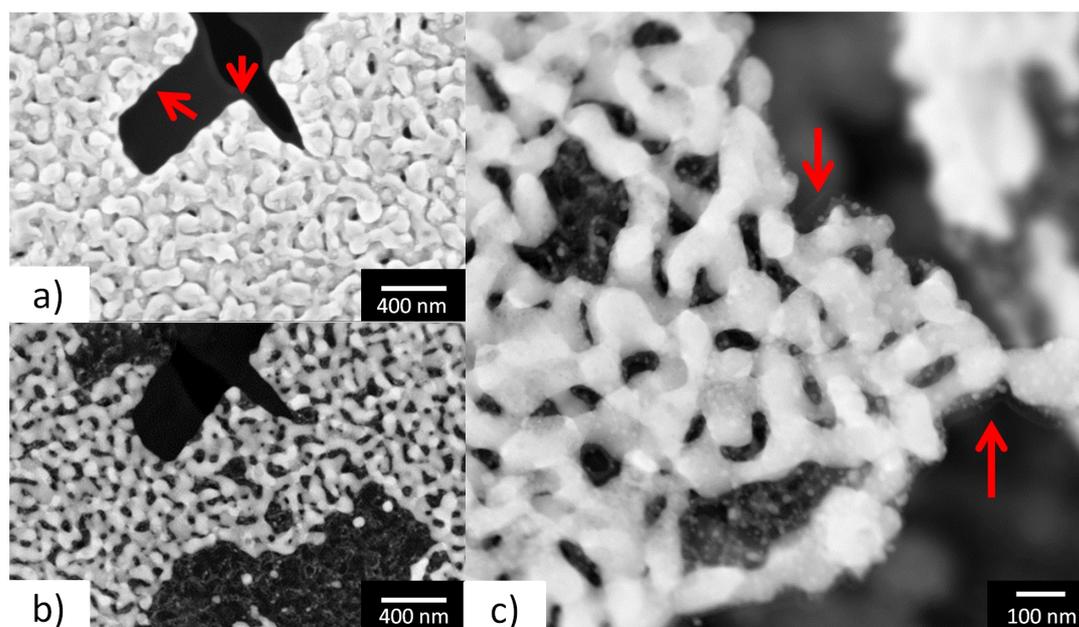
Figure 11.20: a) SEM image of the FIB prepared CeO_2/np-Au sample before the annealing with red arrows as markers for comparison, b) STEM-HAADF image of the prepared CeO_2/np-Au sample after the annealing at the same area from a), c) STEM-HAADF image of the prepared CeO_2/np-Au sample after the annealing at another area showing the contraction of the gold ligaments.

Coarsening is usually described as surface atom diffusion at temperatures below the melting point [241, 245, 247, 254, 256] and recent studies report on facilitated coarsening due to oxygen adsorption at temperatures >200 °C [245] compared to gases like Ar or CO. According to Peale and Cooper [276], the presence of adsorbed gas molecules promotes the generation of gold adatoms and edge vacancies, which facilitates surface diffusion under gas atmospheres compared to vacuum conditions. The lower activation barrier for surface diffusion than for volume diffusion can therefore facilitate coarsening and might explain the observed differences between the studied atmospheres (see the results obtained for np-Au in vacuum, oxygen and O_2/He, reported before). It shows that different mechanisms might be dominant for different atmospheres and can also be linked to the discussion about the underlying mechanisms for sintering of nanomaterials in general. For the sintering of nanoparticles different mechanisms like particle migration and coalescence, implying mobility of the material, as well as Ostwald ripening, implying mobile species or adatom migration, are discussed [15]. Those mechanisms could be transferred to the coarsening of nanoporous materials as well.

Coarsening was found to be prevented or delayed by surface contaminations [277] and Olson *et al.* [278] found an increased apparent activation energy for the surface diffusion for contaminated surfaces. If the surface atom diffusion pathway was blocked, the sample could be stabilized, like it was also seen by adsorption of CO molecules [245] or by formation of Au–O bonds [251]. Therefore, the observed stabilization of the material in the presented study might be caused by a hindered formation of adatoms or vacancies at step edges of the surface, either

due to vacuum or due to interaction with the surrounding gas molecules. However, changes in the material can be observed also in vacuum (compare Fig. 11.7), which points to the existence of additional mechanisms, *e. g.* comparable to Ostwald ripening, which implies migration of adatoms or mobile species [15].

Reaching a high temperature some loss or rearrangement of the gold ligaments was observed. Various reasons may be considered for this such as a) surface tension driven viscous flow above the melting point [248], b) sublimation of the material or c) mechanical loss, *e. g.* by stress. For TEM measurements high temperatures of $T_{reached,TEM} = 800$ °C were reached, which could possibly lead to sublimation as the vapor pressure is reached around 800 °C for 10^{-8} mbar [279]. However, for *in situ* ptychography, temperatures far away from the melting point, even for nanoparticulated materials [280], were reached ($T_{reached} = 375$ °C vs. $T_{melting,bulk} = 1064$ °C). From mechanical tests it is known that np-Au undergoes a ductile brittle transition due to microstructural changes [281] and that stress enhancement is observed at defects [282]. Additionally, according to Kahng *et al.* [283], in a narrow ligament-strength distribution a rupture of the weakest ligament can initiate a catastrophic failure of the material. Nevertheless, ruptures usually occur at defect sites which decrease during annealing as a result of the coarsening [282]. Therefore, at this stage the reasons for the material loss cannot be explained by the obtained results, but the different behavior observed in the various atmospheres show that different mechanisms might be involved during annealing of np-Au.

Furthermore, it could be shown by the combination of ETEM and *in situ* ptychography that pressure differences between the mbar and 1 bar regime in the present study did not influence the onset of the changes due to annealing. Similar temperature ranges were obtained for the annealing in O_2 in the mbar regime and in O_2/He or O_2/N_2 [229] at ambient pressure. However, when the samples were annealed in vacuum, which leads to a different surface coverage, the onset of changes differed at lot compared to the measurements in oxygen containing atmosphere. While the temperature was measured locally by IR thermography during the *in situ* ptychography experiments, the temperature was controlled by a thermocouple in the TEM heating holder (Gatan Inconel® heating holder) or by external calibration (Protochips E-Chip™) during the TEM experiments. As the temperature ranges are similar for the stabilized and unstabilized sample in vacuum or in oxygen containing atmosphere respectively, it can be assumed that problems in temperature determination could be minimized. Furthermore, due to similar temperature ranges for the differently prepared samples (FIB micromanipulation or drop-casting), influences due to of FIB preparation and possible contamination caused due to Ga ion milling and Pt deposition can also be neglected. Therefore, the behavior of the samples studied in different atmospheres is related to the different atmospheres. The results show that studies on the coarsening behavior of np-Au have to be performed under realistic conditions in order to draw conclusions on the underlying mechanisms, as the coarsening behavior is different.

11.3.3 Conclusions and Outlook – Annealing of np-Au under Different Atmospheres

Combined (E)TEM and *in situ* X-ray ptychography were used to study the thermal annealing of np-Au. This allows exploiting in the best way the complementary nature of the techniques with more realistic reaction conditions in case of X-ray microscopy and higher spatial resolution by (E)TEM. For the first time, the temperature applied during *in situ* ptychography was determined directly under *in situ* conditions using IR thermography, enabling a precise control of the temperature, which is particularly important when varying the gas atmosphere [229]. Strikingly, *in situ* hard X-ray ptychography under real conditions showed a uniquely high spatial resolution of about 20 nm which demonstrates its potential also for studying other functional nanoscale materials in future during temperature treatment [132, 229].

The present study demonstrates that annealing of np-Au based samples was strongly dependent on the gas atmosphere and the architecture of the nanoporous materials: Np-Au was found to be stable up to 700-800 °C in vacuum, above, a material loss or migration occurred. In contrast, coarsening was observed in oxygen atmosphere around 200-300 °C in the mbar regime and in O_2/N_2 atmosphere. Notably, a similar material loss to that observed in vacuum at ca. 800 °C was already found in O_2/He around 300 °C. The results obtained in this study therefore indicate that the coarsening behavior is strongly dependent on the atmosphere and points to additional coarsening mechanisms than only surface diffusion. This effect is similar to the different growth mechanisms of nanoparticles, like particle migration, coalescence or Ostwald ripening that also depend strongly on the support, contaminants/structural promoters and the gas atmosphere. Finally, it could be shown that np-Au and CeO_2/np-Au show a comparable behavior in the different atmospheres, but a stabilization was reached by CeO_2 indicated by the onset of changes at higher temperatures.

Hence, the use of the complementary techniques X-ray ptychography and TEM was obligatory to examine the annealing of np-Au under realistic conditions. *In situ* imaging with a high resolution under realistic conditions (ambient pressure) could be obtained by ptychography, whereas TEM under model conditions in contrast enabled to get information on the scale below 20 nm. Due to the results obtained in the performed experiments, future studies on the annealing of np-Au based samples should be performed under *in situ* conditions under different atmospheres and at ambient pressure to understand the underlying coarsening mechanisms. Furthermore, as a 3D material is used, tomographic studies would be beneficial and could also reveal the influence of the thickness of the probed material. In addition to X-ray based studies, which are suited for the *in situ* examination under ambient pressure of thicker samples, complementary EM studies should be carried out to retrieve information on the atomic scale.

Specifically, the application of a cylindrically shaped np-Au sample would be of interest. This would allow a study by *in situ* ptychography on the thicker base area and by TEM on the thin top. In this case, sample preparation should be performed by careful FIB milling from a "bulk" np-Au material. In particular, two identical samples containing an approximately $10\,\mu$m thick base area, which decreases continuously to reach an approximately $100\,$nm thick top, could be studied by complementary tomographic *in situ* ptychography and ETEM tomography on the base and the top, respectively. In this way, the best combination of tomographic studies could be performed, using model conditions during TEM on a thin sample under reduced pressure, and realistic conditions with lower resolution studied by *in situ* ptychography.

12 Redox Treatment of a CuO/ZnO/Al$_2$O$_3$@ZSM–5 Catalyst

When using bifunctional core-shell catalysts detailed information on the structure and stability of the core-shell interface is crucial for the catalytic application. Here, a study on the stability of a CuO/ZnO/Al$_2$O$_3$@ZSM–5 core-shell material, which is attractive for direct synthesis of dimethyl ether, is presented. The catalyst consists of a 80 – 100 μm CuO/ZnO/Al$_2$O$_3$ core and a zeolite shell of about 5 μm thickness. The stability during reductive activation, as well as during reoxidation was studied hierarchically by complementary ETEM, SEM and *in situ* ptychography. The core-shell interface was found to be stable during reducing and oxidizing treatment at 250 °C, although changes on the approximately 10 nm scale occurred due to reduction/reoxidation of the copper species in the core material, as observed by ETEM. At 350 °C, the core material and parts of the shell showed a restructuring on the micrometer scale, as indicated by *in situ* ptychography. However, the crucial core-shell interface required for full bifunctionality remained stable.

12.1 Introduction to CuO/ZnO/Al$_2$O$_3$@ZSM–5

Core-shell materials have attracted a lot of attention in heterogeneous catalysis due to their unique structure and catalytic behavior [5, 11, 284, 285]. These materials range from small particles on the nanometer scale [284, 285] to hierarchically-designed core-shell composites on the micrometer [5, 11] and even millimeter scale [142]. Core-shell catalysts can be subdivided into three groups, each showing specific functions of the core and shell materials, respectively.

- Bimetallic core-shell nanoparticles, in which the core-shell design improves the catalytic activity by modifying the catalyst surface [11, 284]

- Core-shell catalysts containing a catalyst core and a porous, inert shell which encapsulates the active core material and prevents sintering or coking [138, 286]

- Core-shell particles containing two catalytically active materials, allowing the performance of two-step reactions in close vicinity and therefore the performance of single stage processes [13, 26, 142, 287–289]

In the latter case, also physical mixtures [290–292] could be used. However, the bifunctional core-shell design allows exploiting a synergistic effect due to hierarchical ordering of the active sites in the core and the shell. *I. e.* products formed at the core are forced to diffuse through the shell, which itself catalyzes the conversion into the final product. Since the intermediate

product formed at the core is constantly being removed, the equilibrium of the first reaction can be shifted to the product side [13, 27] and even the selectivity can be enhanced [142, 288, 289]. The bifunctional functionality has been used for a number of processes including the selective formation of branched hydrocarbons in Fischer Tropsch processes [137], selective hydrogen formation from decomposition of formic acid [139], selective oxidation [138], hydrogen peroxide synthesis [286] or for direct production of dimethyl ether (DME) [12, 13, 26, 27, 287–289, 293, 294]. DME is a high value platform chemical which can be further processed into a wide range of products, but it is especially regarded as a promising clean fuel, due to its low soot, CO and NO$_x$ emissions as well as its safe storage possibilities [25]. DME can be synthesized from various feedstocks like natural gas, coal or crude oil via the production of synthesis gas, but the production of synthesis gas via gasification of biomass as a renewable energy source is especially attractive [295]. From synthesis gas, DME can be formed indirectly via methanol synthesis followed by dehydration [25], or "directly" in single stage approach [291].

$$CO + 2H_2 \longrightarrow CH_3OH \quad \Delta_f H^{\circ}_{298} = -90.4 \; kJ/mol \tag{12.1}$$

$$CO_2 + 3H_2 \longrightarrow CH_3OH + H_2O \quad \Delta_f H^{\circ}_{298} = -49.4 \; kJ/mol \tag{12.2}$$

$$2CH_3OH \longleftrightarrow CH_3OH + H_2O \quad \Delta_f H^{\circ}_{298} = -23.0 \; kJ/mol \tag{12.3}$$
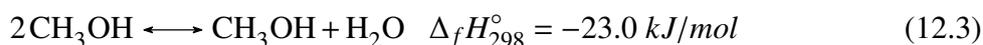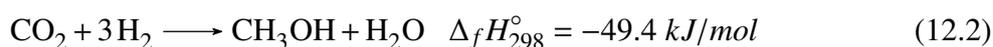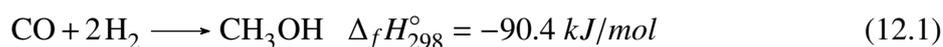
Bifunctional catalysts are particularly used for the one stage process, implying the functionality to form methanol (*c. f.* Eq. 12.1 and 12.2) by one catalyst and to dehydrate it subsequently (*c. f.* Eq. 12.3) by another one [290, 292, 296, 297]. Such core-shell catalyst usually contain a methanol synthesis CuO/ZnO/Al₂O₃ catalyst as a core, and a dehydrating acidic shell such as a zeolite, *e. g.* ZSM-5 [12, 142] or silicoaluminophosphates [287]. Due to the strong dependence of activity and selectivity on the catalyst structure, it is important that the core-shell interface remains stable, even under reaction conditions, or reducing conditions required for catalyst activation. To assess the stability of the catalyst, a hierarchical *in situ* imaging approach is required on all length scales to uncover the specific functional catalytic properties: from the atomic scale (1 Å to 5 nm), to the interfaces on a meso scale (20-500 nm), and the full structure of the particles on the micrometer scale [2, 19, 23, 24, 298]. Several techniques have been developed during the past years. On the one hand X-ray microscopy with XAS, XRD and XRF contrast has been found to give information on the micro and submicrometer scale [299], even under tomographic *in situ* [88] and quasi *in situ* conditions [196, 300]. On the other hand electron microscopy and electron tomography have been developed for gaining insight on the atomic level. *In situ* studies become possible either by using differentially pumped microscopes [15] or closed cells [50], but are still constrained. Although the spatial resolution with hard X-rays is limited, they offer a higher penetration depth and allow imaging under more realistic reaction

conditions [32, 82, 103, 108]. Due to the complementarity of these techniques [51, 104, 301], a combination of both electron and X-ray microscopy appears to be beneficial. In particular, developments in hard X-ray ptychography [118, 130, 131] have improved the resolution of X-ray microscopy and made it attractive for *in situ* studies.

Here the potential to investigate the stability and the structure of a core-shell catalyst for direct synthesis of DME is shown by applying complementary *in situ* ptychography and ETEM. The core consists of a $CuO/ZnO/Al_2O_3$ methanol catalyst encapsulated within a shell of ZSM-5. It is known that the CuO/ZnO system is dynamic under reaction conditions and upon reduction [29, 30, 302], which may influence the stability of the core-shell catalyst. The complementary nature of both methods was exploited for studying the catalyst stability under model conditions in the ETEM, while the sample was examined under more realistic conditions at ambient pressure and on a thicker sample using *in situ* ptychography.

12.2 Experimental

12.2.1 Sample Preparation

Preparation of the catalyst   The sample preparation was performed by Michael Klumpp (University of Erlangen-Nürnberg), following the procedure described in ref. [13]. First, a commercial $CuO/ZnO/Al_2O_3$ methanol catalyst was ground and sieved to a size of 80-100 μm. The shell was synthesized *via* the 2-step hydrothermal synthesis approach of *in situ* silicate-1 seeding followed by secondary growth of a H-ZSM-5 zeolite shell. The as-prepared sample was subsequently calcined and $CuO/ZnO/Al_2O_3$@ZSM–5 core-shell particles with a shell thickness of approximately 5 μm were obtained and further processed.

Preparation for SEM, ETEM and *In Situ* Ptychography   The calcined core-shell catalyst grains were embedded between two silicon wafers using M-bond 610 (Agar Scientific) as a resin. After drying at 100 °C for 24 hours, the sample was polished to obtain a thin section. This section was fixed between two aperture TEM grids made of molybdenum and thinned down further by using argon milling. An approximately 100 nm thick sample was directly used for ETEM imaging. For *in situ* ptychography, an approximately 300–400 nm thick sample (prepared as described above) was transferred into a FIB microscope to be further processed.

FIB micromanipulation was used to cut a piece of 10×17 μm^2 , containing the core-shell interface. This piece was then transferred to a Protochips E-Chip$^{\text{TM}}$ [261] and fixed by platinum deposition. For FIB micromanipulation, a FEI Helios EBS3 dual beam microscope located at DTU at the CEN was used, operated by Dr. Zoltan I. Balogh (DTU).

12.2.2 Techniques

12.2.2.1 Electron Microscopy

SEM images were collected on a) polished cross-sections of the embedded catalyst grains (M-bond 610) and b) the as-prepared *in situ* ptychography samples. Images were obtained using BSE contrast with the FEI Helios EBS3 dual beam microscope located at DTU-CEN and operated at 5 kV. EDX mapping was performed at 5 kV using an EDAX SD Apollo 10 Pegasus System with a resolution of 131 eV. After the *in situ* ptychography, BSE-SEM images were recorded using a Zeiss Auriga 60 dual beam FIB system at the KNMF, located at the INT, KIT. EDX mapping was performed at 5 kV using an EDAX Octane Super System with a resolution of 129 eV.

TEM was performed for comparison between phase contrast images obtained by *in situ* ptychography, using a Tecnai T20 G^2 operating at 200 kV in Bright Field (BF) mode. For *in situ* studies under redox conditions, environmental TEM was performed using a FEI Titan E-Cell 80-300 ST TEM aberration corrected electron microscope operated at 300 kV. STEM images were acquired by a Fischione model 3000 HAADF-STEM detector. EELS analysis was performed using a Gatan Tridiem imaging filter. For reduction, H$_2$ at a pressure of 1.1 mbar was applied and the sample was heated up to 250 °C using a heating rate of 10 °C/min. For reoxidation, the sample was kept at 250 °C, evacuated and O$_2$ was inserted until a pressure of 3.2 mbar was reached. TEM measurements were performed at DTU-CEN.

12.2.2.2 *In Situ* Ptychography

In situ ptychography was performed starting with the core-shell interface region of the calcined catalyst mounted on a Protochips E-Chip$^{\text{TM}}$ [261]. For *in situ* X-ray ptychography, the dedicated *in situ* cell (see section 10.1) was used which enables heating and a controlled gas atmosphere. A flow of 3 ml/min of 4 % H$_2$/He was used for reduction, whereas 3 ml/min of 20 % O$_2$/N$_2$ was used for reoxidation. The samples were heated using the resistive heating possibility of the E-Chip$^{\text{TM}}$. For the different temperature steps, the temperature was determined by IR thermography and heating rates of approximately 10 °C/min were applied. Before

the gas atmosphere was changed, the temperature was decreased first to avoid sudden temperature changes due to different thermal conductivity of the gases. However, short temperature spikes could not be ruled out completely. *In situ* ptychography measurements were performed at the P06 nanoprobe endstation of the high brillance synchrotron radiation source PETRA III at DESY, Hamburg, using a photon energy around the Cu K edge: 8.920 keV, 8.980 keV and 9.032 keV. The beam was focused using a coherently illuminated double-sided Fresnel zone plate [130] made of iridium with a diameter of 150 μm and an outer-most zone width of 25 nm, corresponding to a focal length of about 27 mm at this energy. The samples were placed at a distance of about 60 μm downstream from the focus, such that the illumination on the sample had a diameter of about 260 nm. Ptychographic scans were recorded by scanning the sample over a field of view of 5×5 μm^2 in a grid of 60×60 steps with a step size of 80 nm. At each scanning position diffraction patterns of 0.5 s exposure time were recorded with a EIGER X 4M detector with 75 μm pixels size placed at 2.1 m downstream the specimen. Including motor movements, the total duration of one scan was about 45 minutes. The algorithm used for reconstruction is based on the (e)PIE algorithm presented by Maiden and Rodenburg [126] and the reconstruction and determination of the spatial resolution was performed by Juliane Reinhardt (DESY). Cropping the diffraction patterns to 256×256 pixels led to a pixel size in the reconstructed images of approximately 15 nm. To estimate the spatial resolution, a Fourier Ring Correlation (FRC) analysis [264] was performed. As a common procedure, the ptychographic dataset was split up into two with each set containing every second scan point. Afterwards, the ptychographic reconstruction was performed for each of these half datasets. Before correlating the phase reconstruction, a Kaiser-Bessel window function with a window size equal to 1 was applied to the images in order to reduce artifacts caused by errorneous high frequencies resulting from the edges of the limited field of view of the reconstructions. The FRC results in an upper limit for the spatial resolution of about 28 nm (*c. f.* Fig. 12.9).

12.3 Results and Discussion

12.3.1 Electron Microscopy

The core-shell particles were first studied in the as-prepared state by *ex situ* electron microscopy. A cross section SEM image in BSE-contrast is shown in Fig. 12.1a, with two magnified parts of the image in panel b and c. In Fig. 12.1a, the general core-shell structure is clearly visible, revealing a shell with approximately 5 μm thickness, with a core diameter of around 70 μm. Apart from the evident core-shell structure, the shell around the particle varies in appearance or integrity, from a continuous well connected structure (blue box in Fig. 12.1a and magnified in

c), to a more fractured appearance (violet box in Fig. 12.1a, magnified in b). The latter areas are expected to be problematic in maintaining bifunctionality, as methanol could escape from the core without being dehydrated to DME. The well connected core-shell interface is therefore a desirable feature. Due to the application of BSE contrast, which is especially sensitive to changes in the atomic number (Z) of a material, the inhomogeneous nature of the core can be observed, revealing irregularly distributed high Z-material as well as large pores (up to 5 µm). Fig. 12.2 shows STEM-HAADF images the core-shell interface of a well intergrown part. In particular panel b shows that the shell is intergrown with the core material, revealing a complete coverage of needle shaped core material by the zeolite shell.
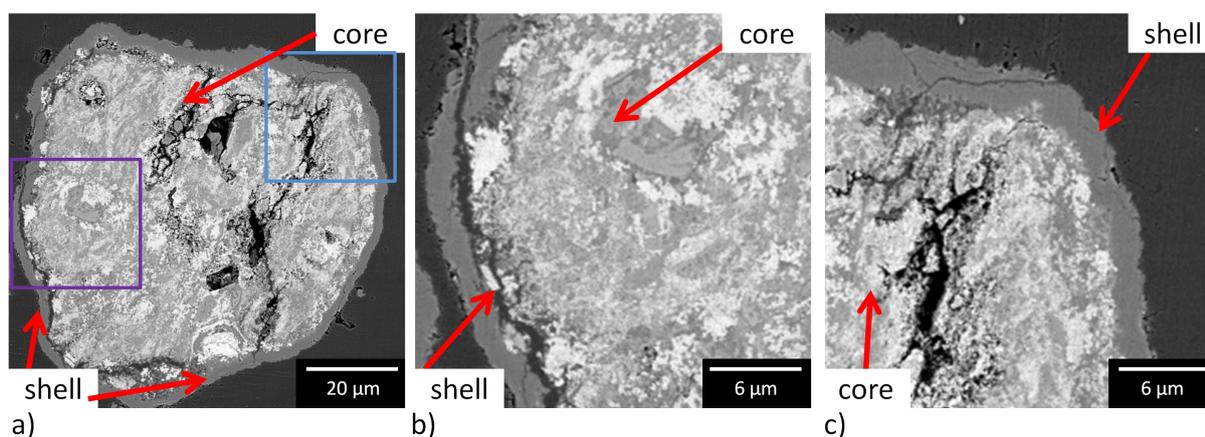
Figure 12.1: SEM images of a cross section recorded at 5 kV in BSE contrast revealing the core-shell structure of the as-prepared catalyst material. a) overview image, b) zoom into the violet marked area in panel a) revealing a non-connected part of the shell, c) zoom into the blue marked area in panel a) revealing the stable connection of the core and the shell.
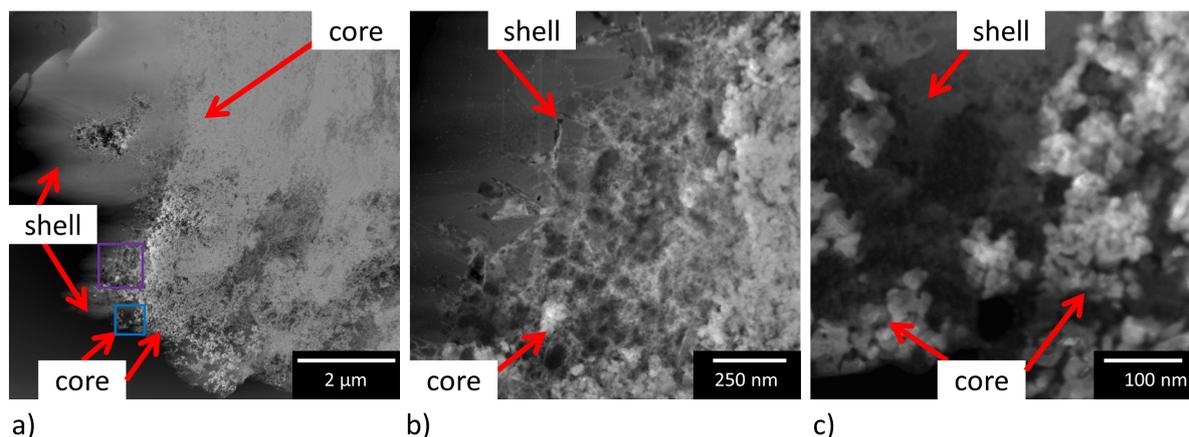
Figure 12.2: STEM-HAADF images of the core-shell interface of a thin section of the catalyst grain, revealing the stable connection of the core and the shell on the a) micrometer and b) and c) nanometer length scale; b) shows the area of the violet box and c) the area inside the blue box presented in panel a).

To study the stability of the core-shell interface during activation under model gas conditions, an approximately 100 nm thick core-shell interface, as depicted in Fig. 12.2, was studied during reduction (H_2, 1.1 mbar) and during reoxidation (O_2, 3.2 mbar) with ETEM. Redox treatments were conducted at 250 °C. Fig. 12.3 shows three STEM-HAADF images from the core shell interface (top) and corresponding EELS spectra on the core area (bottom). In the top row the interface between the bright core on the right and the darker shell on the left of the images is visible. Fig. 12.3b shows a darker area in the center of the image compared to the as-prepared and reoxidized sample depicted Fig. 12.3a or c, respectively. This observation is in agreement with the expected shrinkage of CuO particles on reduction to metallic Cu [29]. Upon reoxidation the particle size apparently increased again, revealing a brighter center of the image, although the Cu containing phases appear less defined. Notably, the core-shell interface remained unchanged during redox treatment. In addition to the imaging during redox treatment, EELS analysis was performed to determine the oxidation state of the sample in a qualitative manner, due to limitations in sample thickness. The decrease in the characteristic Cu $L_{2,3}$ edges for CuO from Fig. 12.3a to b indicates successful reduction of the sample by treatment in H_2. Reoxidation was indicated by an expected increase in the white line intensity (Fig. 12.3c).
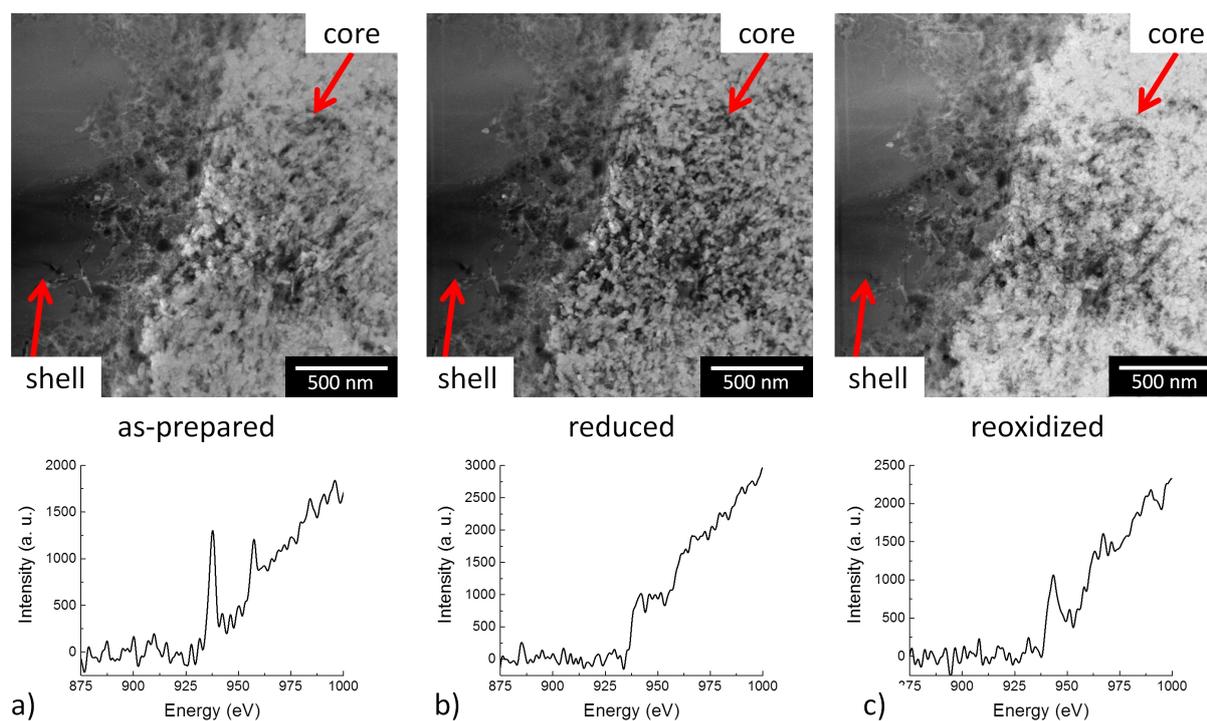
Figure 12.3: a) STEM images and EELS spectra: a) as-prepared catalyst studied at RT in H_2 by ETEM, b) catalyst under reducing conditions at 250 °C in 1.1 mbar of H_2, c) catalyst under oxidizing conditions at 250 °C in 3.2 mbar of O_2.

Fig. 12.4 shows the core-shell interface region during the same treatment at higher spatial resolution. Changes with respect to the image under previous conditions are highlighted by red arrows. In accordance with the behavior observed in Fig. 12.3, the Cu containing core particles became more separated and defined with longer interparticle distances on the nanometer scale during reduction, possibly due to the volume decrease of Cu particles formed from CuO. After reoxidation, the area occupied by Cu containing material increased again, the interparticle pores between the particles decreased and the particles became less defined. This indicates restructuring by oxidation and associated volume increase of the 5 to 20 nm particles. Despite these apparent changes in the core structure, the core-shell interface on the 500 nm to 1 μm length scale once more remained stable and the shell area did not show significant differences on this length scale. This might be explained by the thermal stability of the zeolite and the inertness to redox conditions. In addition, the porosity of the core material may allow changes in the core region on the 10 nm length scale without affecting the shell. However, it should be noted, that real core@shell particles with a spherical shape may behave differently than the slice of the core-shell interface studied here, which resulted from the sample preparation procedure. Therefore, further studies using the whole 3D particle non-invasively should be performed, which is not feasible by *in situ* electron microscopy.
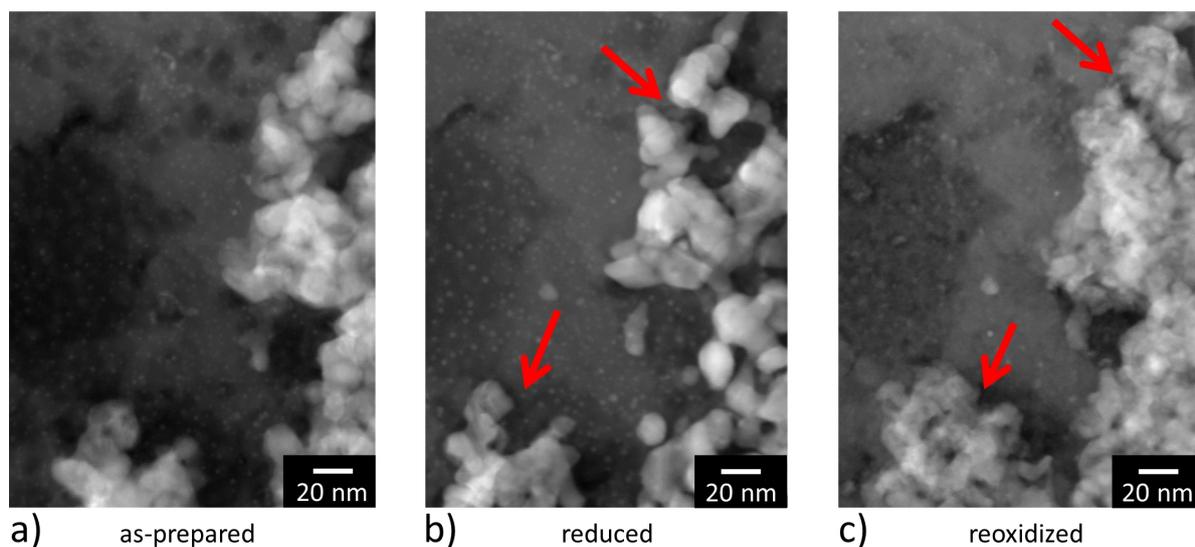
Figure 12.4: STEM images: a) as-prepared catalyst studied at RT in H$_2$ by ETEM, b) catalyst under reducing conditions at 250 °C in 1.1 mbar of H$_2$, c) catalyst under oxidizing conditions at 250 °C in 3.2 mbar of O$_2$.

12.3.2 *In Situ* Ptychography

To extend the hierarchical approach of catalyst characterization and to follow reductive activation, a core-shell interface was additionally studied during the corresponding redox treatments under ambient pressure using *in situ* ptychography. Thanks to the higher penetration depth of hard X-rays, a thicker sample (approximately 300 to 400 nm) could be used. Before and after the treatment, BSE-SEM images were acquired to provide correlative information. Phase contrast images obtained during *in situ* ptychography at different temperatures, along with inverted BSE-SEM images under vacuum conditions before and after *in situ* treatment are depicted in Fig. 12.5. Changes with respect to the previous image are highlighted by black arrows, while blue arrows are used to mark the same positions in the sample. The sample itself was placed on a E-Chip^{TM}, which contains electron transparent "holes" only covered by an approximately 50 nm thick Si_3N_4 membrane. The studied interface was placed on top of one of these holes, which can be seen in the ptychographic images by the round scheme above the blue arrow, indicating the border of the hole.

According to the series of phase contrast images gained by ptychography the catalyst remained unchanged up to 250 °C in both reducing and oxidizing atmosphere. Although previous TEM analysis showed small changes in the core material, they cannot be resolved by *in situ* ptychography at the current resolution limit, but support the ETEM results on the 100 nm thick sample. However, when the temperature was increased to 350 °C, *in situ* ptychography revealed visible changes in the core material, as highlighted by black arrows. Upon moving from reducing to oxidizing atmosphere at 350 °C, further changes seem to occur, including visible darkening of certain areas and a possible migration of material (blue arrow). Some reconstruction artifacts were also observed at the right edge of the frame, which produce an "out of focus appearance". It should be noted that the image quality is somewhat limited compared to electron microscopy, although images were recorded at 350 °C and at ambient pressure. However, this should be balanced against the possibility to obtain images at more realistic environmental conditions than it is possible in conventional ETEM and particularly on a sample which is thicker and therefore more closely resembles a volume of the actual catalyst.

Complementary SEM and SEM-EDX analysis revealed changes within the core and the shell material, as indicated in Fig. 12.6 and Fig. 12.7. Fig. 12.6a and b show the BSE-SEM images before and after *in situ* ptychography. Blue horizontal lines, as well as light blue and red arrows, indicate the same sample positions before and after treatment. Fig. 12.7 shows the BSE-SEM image after the treatment and the EDX maps for Cu, Al, Si and Pt.

By comparison of Fig. 12.6a and b with Fig. 12.7b, it can be seen that the Cu containing material of the core could be localized at a different position after the treatment. Furthermore, the bright "dots" distributed all over the BSE-SEM image after the treatment could be related to platinum, as shown in Fig. 12.7d. In fact, the platinum used for fixation of the sample on the Protochips E-Chip$^{\text{TM}}$, was unstable during the reaction treatment and was therefore deposited in the neighboring area.
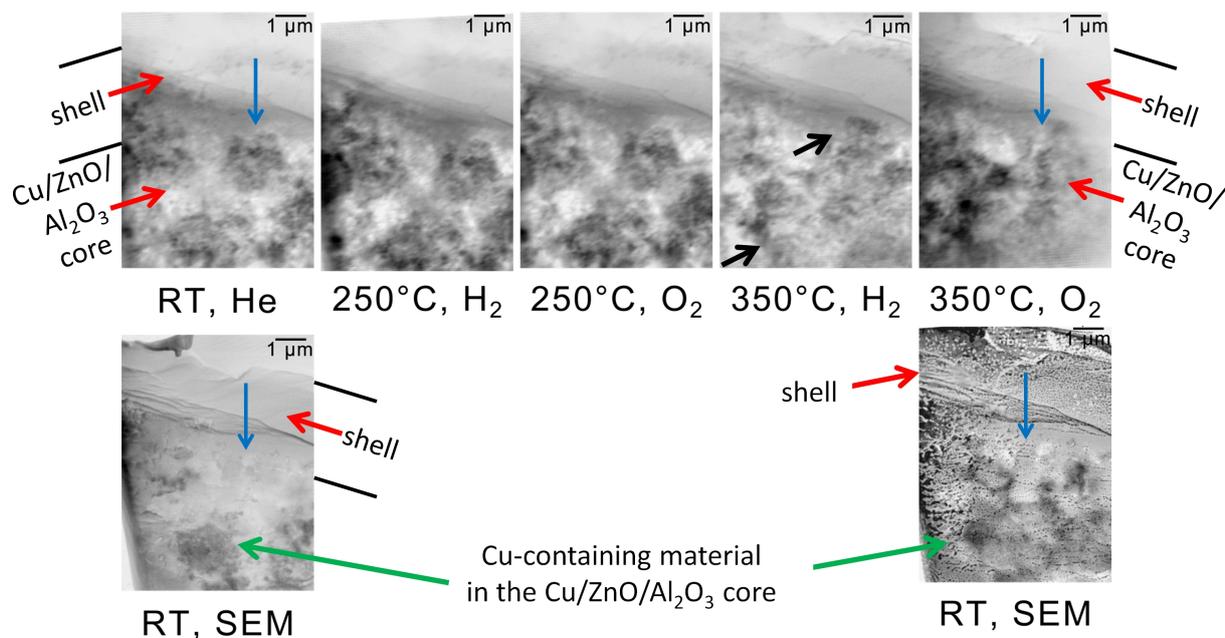
Figure 12.5: Top: Phase contrast images obtained by *in situ* ptychography under different gas atmospheres and at different temperatures. Black arrows indicate changes, while blue arrows mark the same position on the sample. Bottom: Inverted BSE-SEM images showing material with a high atomic number as darker areas. The BSE-SEM images were recorded *ex situ* before and after the *in situ* ptychography treatment of the sample.
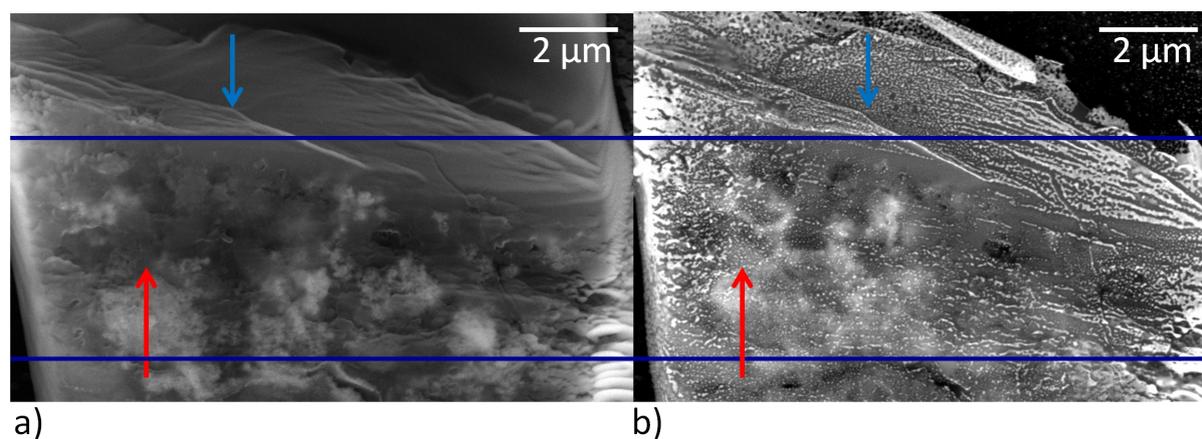
Figure 12.6: BSE-SEM image a) before and b) after the *in situ* ptychography treatment with arrows pointing to the same positions and lines for orientation.

a) BSE-SEM image   b)   Cu   c)   Al   d)   Si   e)   Pt
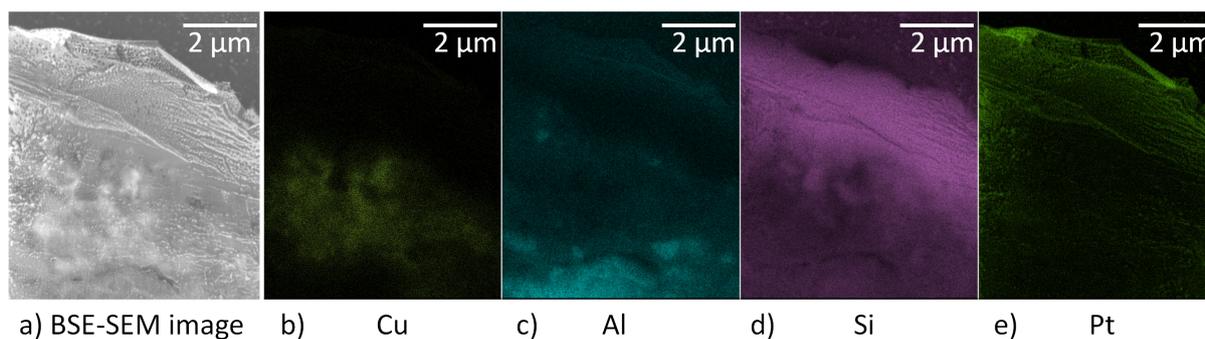
Figure 12.7: a) BSE-SEM image of the sample after the *in situ* treatment and EDX maps for b) Cu, c) Al, d) Si and e) Pt.

By SEM-EDX analysis (Fig. 12.7), it was confirmed that the dark areas indicated by green arrows in Fig. 12.5 contained Cu. As expected from STEM studies, this material should be reduced during H_2 treatment and subsequently reoxidized under O_2, but as indicated in Fig. 12.4, the changes were only visible on a small length scale. However, here under ambient pressure using a thicker sample, a change on micrometer length scale was observed. This can be either related to the pressure, the sample thickness, or the higher temperature applied in comparison to the treatment in the ETEM. By comparing the phase contrast images in the top row of Fig. 12.5 showing the electron density along the transmitted sample volume with the inverted BSE-SEM images depicted in the bottom row of Fig. 12.5 (or Figure 12.6), it is evident that the different contrast mechanisms from BSE-SEM and ptychography reveal complementary information on both the bulk material and the surface, respectively. With ptychography, changes unrelated to Cu containing areas in the core were observed. The blue arrow points to an area with a high electron density in the ptychographic images, while this area is not clearly visible in the BSE-SEM images. Therefore, it cannot be related to a high Z-species, but might result from thicker or more densely packed material. With the application of complementary EDX analysis, this part of the sample could be attributed to Si (Fig. 12.7). In fact, the observed changes in this material mean that during *in situ* treatment at 350 °C not only the Cu containing material is affected but also other regions of the core-shell structure. In this case, parts of the Si containing shell seemed to be changed. However, as depicted in Fig. 12.5 and Fig. 12.6, the overall core shell interface itself remained stable, which is critical to maintaining catalyst bifunctionality.

The obtained results therefore suggest a behavior schematically shown in Fig. 12.8 which may be further elaborated by future studies. At 250 °C changes mainly occur on the nanometer scale, as observed by TEM and in agreement with earlier work in literature [29, 30, 302]. According to the ETEM and X-ray microscopy results this does not visibly influence the mesoscopic structure and only increases the interparticle distances on the nm scale.
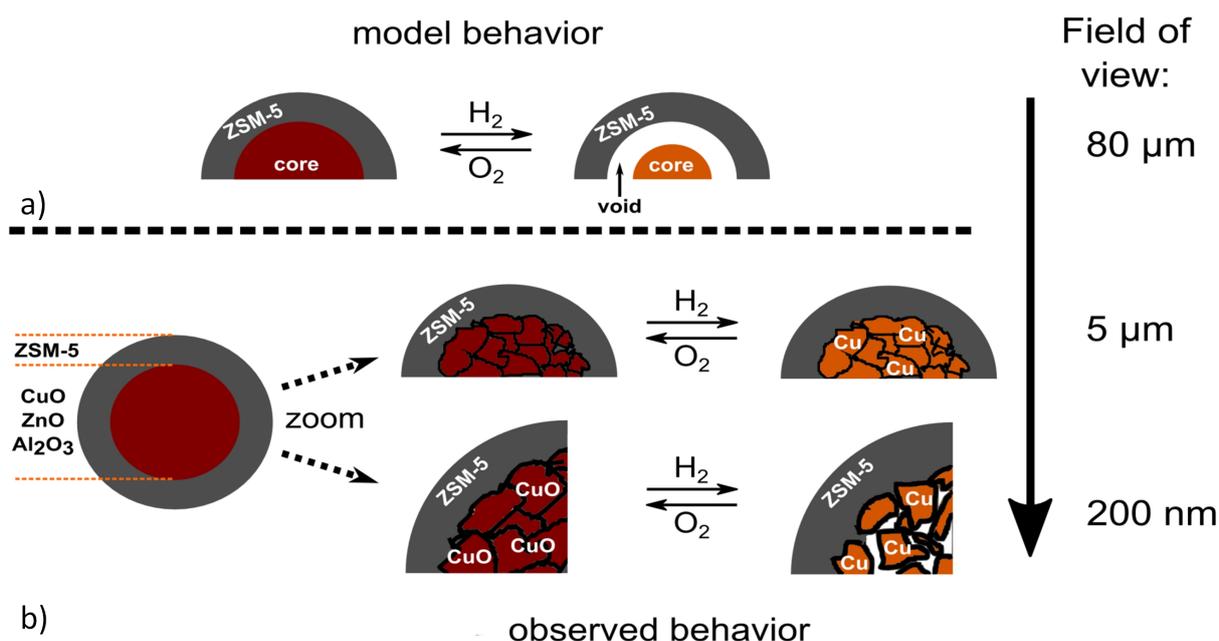
Figure 12.8: Model of the hierarchically designed core shell particle showing a) the shrinkage of the core assuming a simple model consisting of a CuO core and a zeolite shell; b) the observed behavior of the catalyst on the macro, meso and nano scale.

Under these conditions the bifunctional catalyst remains fully intact on the μm scale. However, at 350 °C changes which influenced the mesoscopic structure of the catalyst were also observed. This might be related to more extensive volume changes caused by reduction/reoxidation or even sintering of the Cu/ZnO particles. Although the overall core-shell interface still remained unaffected on the μm scale, as illustrated in Fig. 12.8b. These first changes indicate that the temperature applied might be critical to the catalyst macrostructure and that reductive activation of the catalyst should be performed carefully at low temperatures. This information is crucial for hybrid catalysts as it will influence the surface reactions that take place on the Cu nanoparticles in the core and the heat/mass transport effects which play a role on the micrometer scale, *i. e.* diffusion and reaction in the acidic zeolite [2, 8, 10].

The present study indicates the importance of studying hierarchically designed bifunctional catalysts at different length scales *in situ* and the potential value of complementary electron microscopy and hard X-ray ptychography. Although the complementarity of X-ray and electron microscopy has often been discussed [2, 24, 32, 51, 102, 298], the methods were only rarely applied to study the same catalytic system [23] or even the same catalyst samples [229, 301]. In particular, complementary *in situ* studies on the same catalytic systems are missing, since this requires the design of special *in situ* cells and careful sample preparation. Nevertheless, *in situ* or quasi *in situ* studies are important to draw more solid conclusions, as the statistics would be limited in multi-scale approaches based on *ex situ* studies [196]. While ETEM can give information on the structural changes on the nanoscale, SEM and X-ray microscopy can probe larger areas. SEM is more surface sensitive and in combination with backscattering contrast

strongly sensitive to the atomic number. Ptychography on the other hand offers information on the electron density along the transmitted beam path through the sample, similar to TEM.

To estimate the spatial resolution, a Fourier Ring Correlation (FRC) analysis was performed [264], which is depicted in Fig. 12.9. The intersection of the FRC with the 1/2-bit threshold curve indicates a spatial resolution of 28 nm. For such thick samples, the resolution obtained by ptychography is similar to the one obtained by TEM, but is seems as if a higher contrast can be achieved by ptychography (*c. f.* Fig. 12.10). Hard X-ray ptychography furthermore allows combination with resonant measurements to provide chemical contrast [58, 128].
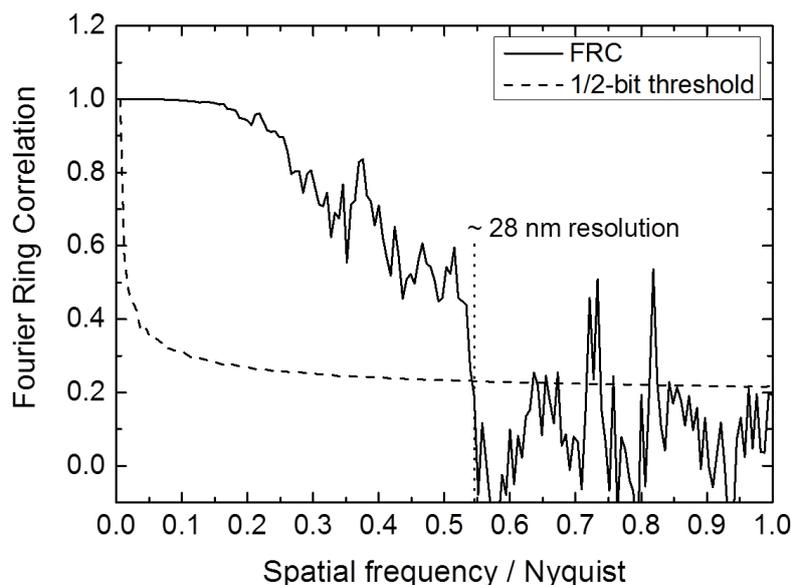
Figure 12.9: FRC plot to estimate the spatial resolution derived by *in situ* ptychography at RT while probing with a photon energy of 9032 eV.

Fig. 12.10 shows a BF-TEM image and phase contrast images obtained by *in situ* ptychography at different energies. The core-shell interface of a different sample was studied, but the samples were prepared identically and obtained from the same thin section of the catalyst grain. The phase contrast images are shown for different energies below, on and above the Cu *K*-edge, to relate to a Cu sensitivity. However, by visual evaluation, no differences, apart from a reconstruction artifact (shown by the blue box) at 25 °C at 9032 eV, could be detected.

Alternatively to the combination of *in situ* ptychography with resonant measurements, as depicted in Fig. 12.4, TEM analysis offers information with high resolution, which can also be combined with spectroscopy (EDX or EELS) and diffraction (Selected Angle Electron Diffraction, SAED). Nevertheless, for 3D samples studied by 2D transmission imaging, it has to be taken into account that only projections of the electron density are obtained, which requires the need for non-invasive tomographic studies to obtain 3D information [91, 124, 299, 303].
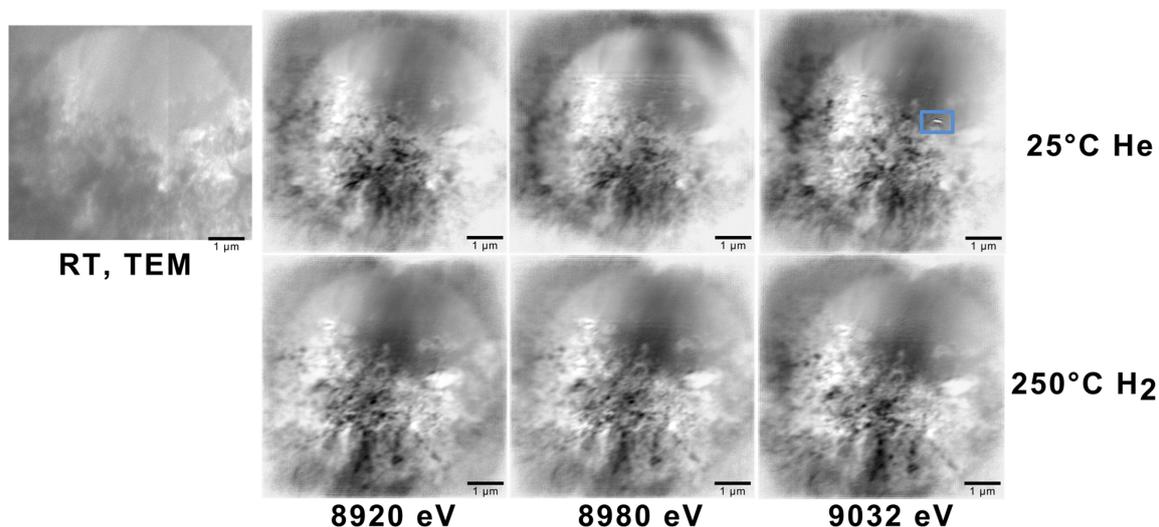
Figure 12.10: Comparison of a TEM image of the core-shell interface of the studied catalyst studied at RT under vacuum conditions before the *in situ* treatment with the phase contrast images recorded at 25 °C in He and 250 °C in H$_2$ atmosphere. The phase contrast images are depicted at 25 °C in the top row and at 250 °C in the bottom row, using a photon energy of 8920 eV before the Cu *K*-edge, 8980 eV around the edge and 9032 eV above the edge. An area showing a reconstruction artifact in the measurement at 25 °C in He at 9032 eV is shown by a blue box.

The combination of these approaches, *i. e. in situ* hard X-ray ptychography and ETEM analysis, allows complementary information to be obtained on hierarchically designed structures, which should further be combined with *in situ* tomographic imaging [88] for a holistic understanding of the overall structure. The multi-scale *in situ* imaging approach pioneered here for assessing the stability of structure-dependent materials such as hierarchically designed core-shell catalysts should be furthered, as it will also be excellently suited for investigating related questions: for example the stability of nanoparticles in fluidized bed reactors [22, 140, 148], the structure and homogeneity of shell impregnated catalysts [304], structural and compositional changes in bifunctional Fischer-Tropsch catalysts [143] and other core-shell catalysts [305, 306]. In all these examples, the structure and stability of the catalyst is critically related to the function and a hierarchical *in situ* characterization at various length scales and under steadily more realistic conditions is expected to become more important in the near future.

12.4 Conclusion

In the present work, the complementary use of *in situ* hard X-ray ptychography and electron microscopy was evaluated to study the stability of a core-shell catalyst in a hierarchical manner at different length scales. Both activation in hydrogen atmosphere and reoxidation under synthetic air were selected as model conditions for this first case study. ETEM for a thin section of the catalyst under reduced pressure revealed a stable core-shell interface at 250 °C, although reduction of the Cu containing core material led to a shrinkage of the particles on the nanometer scale. Complementary *in situ* ptychography allowed studying the system not only under model conditions, but also at atmospheric pressure and on a thicker sample. Whereas at 250 °C the core-shell interface was found to be stable, further heating to 350 °C indicated microscopic changes on the micrometer scale. According to complementary SEM-EDX analysis, not only the Cu containing core material was affected by the treatment, but also parts of the shell material were rearranged. Despite strong changes in the core material, the overall core-shell interface of the catalyst remained stable, which is critical to maintain the bifunctional operation of such catalysts.

The results obtained in this study support that complementary information from electron microscopy and X-ray microscopy can be used to study working catalytic systems, covering different length scales and different pressure regimes. *In situ* ptychography with better than 30 nm spatial resolution can now start to bridge the gap between high-resolution TEM under idealized conditions and hard X-ray imaging techniques under more realistic conditions, although simpler sample preparation and improved *in situ* cells are still areas which require further development. In future, such studies should be performed non-destructively on sections and complete core-shell particles by tomography to fully support the so-called product design of catalysts in chemical engineering.

13 Design of an Improved *In Situ* Cell for Ptychography

The results presented in the previous chapters were obtained with the *in situ* cell developed by Ass. Prof. Dr. Christian Damsgaard in collaboration with KIT and DTU. However, this cell design is not perfectly suited for studying catalytic reactions. In particular, the gas volume of approximately $500\,mm^3$ is considerably too big to carry out sensitive measurements on sample amounts in the nanogram range. In addition, its bulky layout compared to a thin TEM heating chip does not allow for parallel recording of fluorescence radiation. Therefore, a more compact cell suitable for following the conversion of reactants during catalytic reactions and for sufficient XRF contrast was developed at KIT with a considerable smaller gas volume of approximately $1\,mm^3$. Furthermore, the small dimensions of the cell also show the potential to obtain 3D images by tilting the sample. Within this work however, only preliminary tests have been carried out on this cell.

13.1 Design of the Cell

A schematic drawing and a photograph of the cell are given in Fig. 13.1. Similar to the cell presented in section 10.1, the new cell is composed of a cell body with a TEM compatible heating chip (green label) and features both integrated gas (red label) and electrical (purple label) connections. The electrical contact is obtained by placing a circuit board on top of the chip. The latter is built of a $25\,\mu m$ thick Kapton® foil with electrical contacts made of $12\,\mu m$ thick Cu, covered by $4\,\mu m$ Ni and $0.5\,\mu m$ Au. Additionally, balls made of Au (diameter $\times$ height $= 50\,\mu m \times 15\,\mu m$) are placed in the center of the contacts. For insulation, another Kapton® foil is added on top, which is used as a X-ray window. A second Kapton® foil is glued on the bottom of the plate for sealing of the cell. Mechanical stability is achieved by embedding the shown stack between a bottom and a top plate of $1.9\,mm$ and $1.0\,mm$ thickness respectively. The cell can be conveniently mounted on X-ray microscopy stages with a pin (diameter $= 3\,mm$) at the top plate. X-rays can reach the sample within the cell body through holes in the bottom (center) and top (slit) plate since the sealing Kapton® foils are highly transparent towards hard X-rays. As labeled in Fig. 13.1b, the slit in the top plate is also intended to enable the detection of fluorescence radiation.
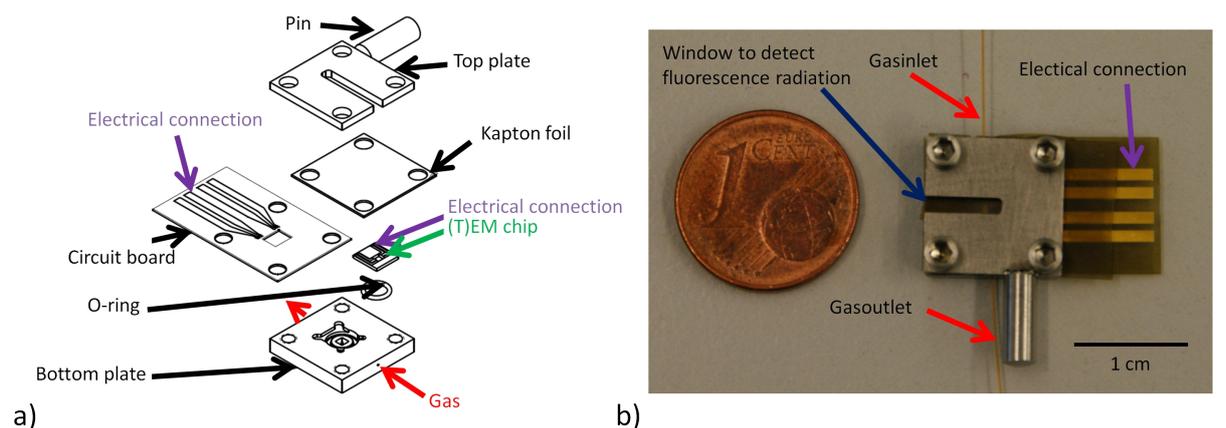
Figure 13.1: a) Schematic drawing (explosion) of the new cell, b) photograph of the mounted cell without connecting the circuit board to the power supply.

Before a series of measurements, the cell has to be prepared in the following way: the sample is placed on the backside of the heating chips, *i. e.* on the backside of the electrical contacts. Subsequently, the chip is put on top of an O-ring with the backside facing the bottom of the cell and the circuit board is placed on top of it, together with the other Kapton® foil and the top plate for closing. A detailed design of the bottom plate, fabricated by 3D printing (Layerwise, Leuven) of stainless steel, is presented in Fig. 13.2. Besides the X-ray window in the center, in particular the embedded gas channels can be seen. The achieved gas volume above the sample is approximately $1\,\mathrm{mm}^3$. The size of the gas channels (ID = $250\,\mu\mathrm{m}$) was chosen as small as possible within limitations of the fabrication process. Both inlet and outlet channel are split, as depicted in Fig. 13.2a, into two symmetric channels which are both bent, as shown in Fig. 13.2b. In this way the gas flow is directed onto the sample.
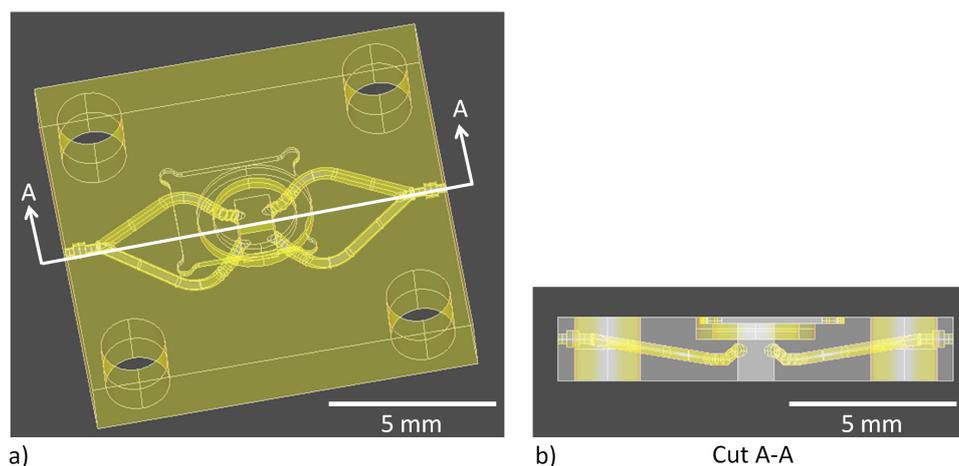
Figure 13.2: Schematic drawings of the bottom plate highlighting the channel geometry. a) View diagonally from above facing the bottom of the cell and b) cut away along line A-A.

The main two advantages of this new cell design are the smaller gas volume and the smaller overall size. The latter enables easier positioning of the cell within the X-ray microscopes since the smaller size enables using optical microscopes providing a higher magnification. A novelty compared to the DTU cell is the fluorescence radiation window which will not only allow to acquire fluorescence maps and ptychographic data simultaneously, but will also further simplify the sample alignment. Furthermore, the cell has the potential to be tilted to perform tomographic studies.

13.2 Preliminary Tests

In this work, the principle applicability of the presented cell is demonstrated by evaluating its heating capability. The temperature within the cell is again controlled by resistive heating. In contrast to the Protochips E-Chips$^{\text{TM}}$ described in section 10.1, the new chips based on heating chips from DENSsolutions (Delft, Netherlands) apply 4 probe heating [307], not 2 probe heating (*c. f.* the four contact pads in Fig. 13.3a). An optical micrograph of a DENSsolutions compatible heating chip is presented in Fig. 13.3a. The central spiral shaped heater (red box) is designed to enable uniform heating within the covered area [92, 308]. The four contact pads enable a precise measurement of the resistance of the heater geometry (4-point measurement), in parallel to resistive heating. Thus, potentially a direct evaluation of the temperature via the thermoresistive effect can be obtained. The heating inside the cell was evaluated by applying different heating powers via a Keithley 6220 DC power supply connected to the circuit board and a simultaneous temperature measurement with IR thermography. An exemplary thermogram, recorded at a heating power of 51.5 mW, is depicted in Fig. 13.3b. It can be clearly seen that above the heater geometry (depicted circle) and thus the sample area, a uniform temperature distribution (average temperature of 236 °C) is achieved. In Fig. 13.3c, the obtained average temperatures within this area are plotted versus the applied heating powers. Clearly, a linear relationship is observed. In the future, convenient control of the temperature within the cell is therefore possible without additional IR thermography by using the obtained relationship between temperature and heating power. This is also better suited for the application as a standard *in situ* cell at synchrotron radiation sources.
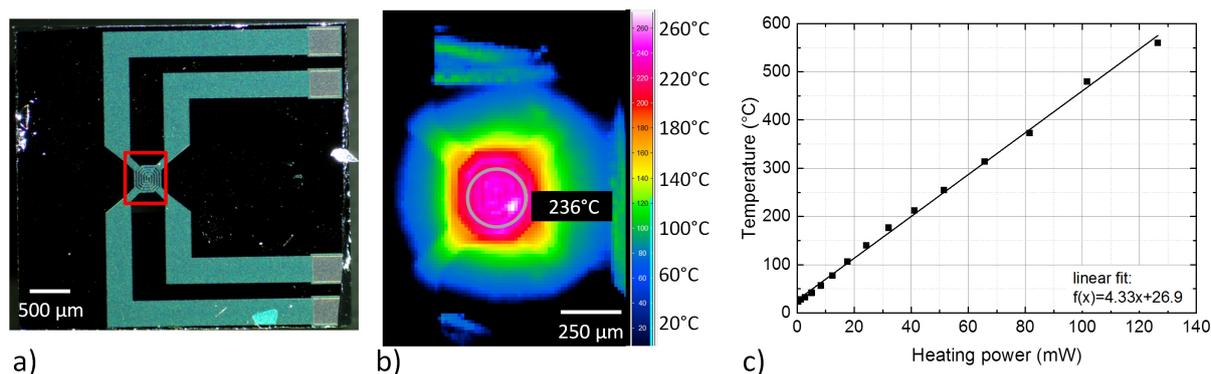
Figure 13.3: a) Optical micrograph of the DENSsolutions based TEM heating chips [92, 308], b) IR thermogram of the heated area of the cell recorded during application of a heating power of 51.5 mW, c) IR thermography based calibration of the temperature dependent on the heating power.

For further evaluation of the cell, the tightness has to be examined by measuring different gas flows either through bypass or through the cell. Yet, the connection of the capillaries to the gas inlet and outlet, which is realized by glueing the capillaries on the outside, has not been optimized so far. Eventually, X-ray microscopy studies have to be carried out to finally evaluate the capability of the cell, in particular its stability and the influence of the new Kapton® window on the image quality. However, due to the similarity to the cell built at DTU in a collaboration, major problems with respect to the application in microscopy are not expected.

It is expected that the considerable reduction of the gas volume will enable probing the catalytic conversion within the presented cell. In the future, the gas volume could potentially be further reduced by developing a closed chip similar to those used for closed cell TEM approaches [50] or STXM [108]. This would be advantageous for determinations of catalytic activity, but sample preparation by FIB micromanipulation would be significantly more difficult with a closed chip.

14 Conclusions and Outlook – *In Situ* Ptychography

In the previous chapters, different aspects required to further improve *in situ* microscopy techniques on the length scale of 20 – 500 nm were highlighted by the demonstration of the application of *in situ* hard X-ray ptychography. This technique is especially promising to study the meso scale of catalysts under realistic conditions, allowing information about transport processes and hierarchically structured catalysts. In the following section, the different aspects highlighted in the context of this work are summarized and considerations for future improvements are discussed.

14.1 Technical Achievements

Development of *In Situ* Cells The results presented above show the applicability of hard X-ray ptychography for studying heterogeneous catalysts under *in situ* conditions. Two different cells based on TEM heating chips were presented, which differ mostly by their size. Both cells were successfully electrically connected to TEM heating chips. These chips, made for electron microscopy at controllable temperature, enable resistive heating inside the *in situ* ptychography cell and allow for complementary electron microscopy measurements. The *in situ* setup was developed in the framework of a BMBF-funded project for development of user infrastructure for the X-ray microscopy beamline P06 at PETRA III. Hence, it will be available for future users in Hamburg.

The big cell built in a joint collaboration between KIT and DTU was extensively studied during *in situ* thermal annealing of Au nanoparticles, np-Au and CuO/ZnO/Al$_2$O$_3$@ZSM–5, while the smaller one developed at KIT has only been used for preliminary tests so far. However, the small one promises to be applicable for on-line detection of reactants and to follow the catalytic conversion. These possibilities have to be confirmed in future tests and first *in situ* ptychography measurements have to be performed. Furthermore, this small cell has the potential to be used for tomographic investigations by tilting the cell under different tilting angles instead of rotating it for 3D image acquisition.

For future studies, the focus should be put on the development of cells with an even smaller gas volume. These can be realized by closed cell approaches similar to ETEM and will facilitate on-line detection of reactants as well as widen the maximal tilting angle for 3D imaging. In addition, cells allowing for 3D image acquisition by rotation should be developed, such that tomographic *in situ* ptychography studies will become available. These will enable non-invasive studies of the 3D structure of catalysts on the meso scale under *in situ* conditions, which is highly desirable for bridging TEM tomography under model conditions with X-ray tomography on the micrometer scale under more realistic conditions.

Combination with IR Thermography   Aside from the developments of the two cells, it was shown that IR thermography can be applied to both cells. It can be used for temperature determination in a gas environment through a Kapton® foil and it works without preliminary calibration of the chip. Furthermore, it allows for spatially resolved temperature measurements under reaction conditions, which is crucial when exothermic reactions are studied [40, 72].

Spatial Resolution during *In Situ* Ptychography   With the first *in situ* cell a spatial resolution up to 20 nm could be achieved during *in situ* ptychography measurements on 100 nm thick np-Au. This resolution was significantly better than the highest one reported for *in situ* ptychography in literature [132]. Moreover, a similar resolution like the one obtained by TEM could be achieved for a 300-400 nm thick $CuO/ZnO/Al_2O_3$@ZSM–5 section, but with a higher and different contrast. Due to the application of a lensless technique based on the interaction with the coherent beam, even higher spatial resolutions should be possible in future. To achieve this, the signal-to-noise ratio has to be improved, *i. e.* by reduction of parasitic scattering from the environment, but also by a more stable sample environment un-affected by vibrations, which can be obtained *e. g.* by active damping solutions. Therefore, apart from the increase of brilliance in fourth generation synchrotron radiation sources, like MAX IV [226] or the planned PETRA IV [225], an improvement on the X-ray microscopes themselves and on the cells used for *in situ* studies can lead to higher spatial resolution.

Resonant Ptychography   Hard X-ray ptychography offers the possibility to be combined with fluorescence contrast by STXM, and with XAS by resonant ptychography. However, the latter remains challenging. In this work, no further information could be obtained from visible comparisons of phase contrast images obtained at different energies. Nevertheless, literature studies [58, 128, 129] show that chemical contrast can be achieved. In future attempts, resonant *in situ* ptychography should therefore be used on real catalyst samples.

Complementary Hard X-ray Ptychography and Electron Microscopy   The complementary use of hard X-ray ptychography and EM was presented in this work by highlighting the good agreement of samples studied with both techniques by performing EM images before and after *in situ* ptychography. Furthermore, the different contrast mechanisms were discussed. For future studies, this complementary character should be exploited even more, *i. e.* by improvement of the transfer of the sample from one microscope to the other under inert conditions.

14.2 Catalytic Systems

The application of *in situ* hard X-ray ptychography was demonstrated on different catalytic systems, for which a spatial resolution of 10 nm to 1 μm is relevant. The annealing of np-Au based catalysts, in particular of np-Au and CeO_2/np-Au, was studied in different atmospheres and pressures. Therefore the complementary approaches of *in situ* ptychography and EM were used. It could be shown that the coarsening of np-Au strongly depends on the atmosphere and annealing conditions, whereas the pressure did not seem to affect the behavior. The studies highlighted that *in situ* microscopic studies under realistic conditions are crucial to draw conclusions on the growth mechanisms of np-Au based catalysts.

Furthermore, a bifunctional $CuO/ZnO/Al_2O_3$@ZSM–5 catalyst was examined to study the stability of the core-shell interface during redox treatment. The complementary approach of electron microscopy and *in situ* ptychography showed that the catalyst structure remained unchanged at 250 °C, although changes on the nano scale occurred in the core, as observed by ETEM. At higher temperature changes even on the micro scale could be detected, while the overall stability of the core-shell catalyst remained, which is crucial for catalytic applications. By the combination of both methods, different pressure ranges could be covered and *in situ* ptychography offered the study during more realistic conditions, although the resolution was lower. Therefore, this work revealed the necessity for the application of complementary techniques. It furthermore showed the potential for such hierarchically performed studies of heterogeneous catalysts under real conditions, which will also be interesting for other heterogeneous catalysts [22, 140, 143, 148, 304–306].

Nevertheless, the samples studied in the this work were 3D samples, which were studied in transmission geometry resulting in a projected image. Therefore, the images show the electron density of the sample along the complete path probed by the X-ray beam. For a more reliable reconstruction of thick 3D materials, structure determination can only be performed reliably by tomographic data acquisition [303, 309, 310]. For *in situ* ptychography, however, this is not going to be possible until the necessary infrastructure for such experiments has been further developed. Despite these drawbacks, for thin samples like they were used in the study of np-Au based

catalysts, the projected image results in sufficient contrast and gives insight into the structure of the studied np-Au based samples. Also for the thicker $CuO/ZnO/Al_2O_3$@ZSM–5 samples, sufficient contrast and a similar resolution to TEM could be obtained by *in situ* ptychography. However, one of the advantages of hard X-ray ptychography in contrast to TEM is the high penetration depth of X-rays, which will be a benefit for future 3D experiments and allows probing of more realistic samples.

To conclude, the application of *in situ* hard X-ray ptychography demonstrates the potential of this technique for applications in catalysis and material science. Furthermore, it shows that such *in situ* cells are attractive tools for a hard X-ray microscopy beamline, since these cells can be now applied by other users from different scientific fields. These can include catalysis, energy storage materials or other functional solid materials, where hierarchically designed samples play an important role. Characterization on these materials will therefore allow studying the structure and stability and the obtained knowledge can be used for optimization processes, *e. g.* by modeling and experimental improvement of the materials.

Part IV

Final Remarks and Outlook

15 Overall Conclusions and Outlook

In this work both complementary characterization techniques and hierarchical imaging approaches were further developed and applied to *in situ* characterization of heterogeneous catalysts. For this purpose, novel reactors specifically designed and optimized for complementary approaches were developed and tested. The presented experimental results obtained with these reactors already demonstrate the benefits of these complementary *in situ* techniques compared to standard *ex situ* methods, to develop an actual understanding of chemical reactions within a reactor. The results pave the way to a better understanding of heterogenous catalysts under realistic conditions and will help to establish these techniques within the synchrotron radiation community such that in the future also other experimentalists can use them conveniently. In fact, the presented reactors were developed in the framework of projects dedicated to the implementation of a user interface at the P06 beamline at PETRA III. Hence, the reactors will be available for other users in future. The work was divided into two different topics and size ranges: a) The structure of catalysts in a reactor was studied with complementary characterization techniques on the micrometer scale. For this purpose, a special silicon-based gas phase microreactor was used and further optimized. b) For the investigation on the nano and meso scale, special cells suitable for complementary hard X-ray *in situ* microscopy, especially ptychography, and electron microscopy, were developed and evaluated. Both approaches were treated independently from each other. However, the importance of correlating these techniques was highlighted.

Gas Phase Microreactor The design and application of a silicon-based gas phase microreactor, especially the improvements obtained by the introduction of a second generation of this reactor, were presented. In particular, a second generation of microreactors was developed to overcome the poor temperature homogeneity along the catalytic bed and the high temperature instability (evolution of diffraction signals above 500 °C) of the first generation. For this purpose, in this second generation the heater geometry was better adjusted to the geometry of the cell. The improved temperature homogeneity within the catalyst bed of 8 mm length was verified within a series of IR thermography measurements. Besides the original microreactor composition where the silicon reactor was sealed with borosilicate glass, an additional reactor completely composed of silicon was developed to solve the high temperature instability which originated from the borosilicate glass.

The applicability of the developed cells for correlative *in situ* characterization was demonstrated within several experiments using various characterization techniques. In particular, the application of XAS and XRD revealed the distortion free application of the reactor for both techniques, which was studied in comparison to conventional capillary reactors. For XAS, it was tested on a 2.5 wt.% Rh-2.5 wt.% Pd/γ-Al$_2$O$_3$ sample, while for XRD, a LaB$_6$ sample and a

5 wt. % Pt/γ-Al$_2$O$_3$ catalyst were studied. Additionally, Raman spectroscopy and Raman spectromicroscopy on H$_2$PtCl$_6$ and PtO$_2$ were performed to show the compatibility of the Si-glass microreactor with Raman spectroscopy. Furthermore, the cells are also compatible with IR thermography which enables spatially resolved monitoring of the temperature within the cell. In this way, temperature gradients during the CPO of methane could be analyzed. Finally, on-line gas analysis by mass spectrometry at the outlet of the reactor allowed correlation of the spectroscopic results with the catalytic reaction process.

The reactor was used to study the ignition and extinction of the CPO of methane, using a 4 wt.% Pt/γ-Al$_2$O$_3$ catalyst. Similar results to those presented in literature in conventional reactors were obtained. In particular, a gradient in oxidation state and temperature could be observed during ignition and extinction, which moved along the catalytic bed with changing temperature, as observed in conventional reactors. Additionally, the microreactor has a strong potential for application during transient reaction conditions as shown during the SCR of NO$_x$ by NH$_3$ over Cu-zeolites. The fast heating and cooling capabilities, which microreactors exhibit intrinsically due to their low heat capacity, were exploited for the first *operando* QEXAFS study during the transient temperature conditions of a New European Driving Cycle. The latter requires high heating and cooling rates (300 °C/min) and is therefore limited to special engine test benches, which do not allow simultaneous *in situ* spectroscopic characterization. The required heating and cooling rates could be provided by the reactor. Both the N$_2$ partial pressure as well as the coordination number of Cu followed the temperature ramps. These results highlight the unique possibilities of such microreactors for the application during transient reaction conditions.

In future, the reactor will help, due to its unique capabilities for studying transient effects, to gain a deeper understanding of other catalytic reactions, such as the CO or hydrocarbon oxidation during driving cycles. With its unique heating and cooling capabilities, it especially has a strong potential for application in exhaust gas catalysis, supporting the development of better catalysts to reduce air pollution. Further improvement of the reactor will help to increase the image quality, which will be necessary for future applications in X-ray microscopy. In particular, for future generations of the reactor, the X-ray window which is used to obtain a higher transmission of X-rays, should cover the whole catalytic bed and the temperature sensor should be shifted in position, such that it is placed directly next to the catalyst bed, instead of on top of it. Both actions will facilitate spatially resolved measurements on the very end of the catalytic bed. Moreover, different materials like aluminium oxynitride or pyrolytic graphite could be considered as reactor materials. Furthermore, due to the modular design of the setup, other microreactors optimized for different spectroscopic or scattering techniques, can be developed and used inside the present setup. The latter aspect is especially beneficial, since the present setup is user-friendly and, due to its small size, facilitates measurements at various beamlines.

Combination of Electron Microscopy and X-ray Microscopy   The second topic studied in this work is the complementary application of X-ray microscopy, especially ptychography, and electron microscopy. In this work, two cells available for *in situ* ptychography are presented. They build a good basis for a future *in situ* platform for users at the P06 hard X-ray microscopy beamline at PETRA III. One cell was fabricated at DTU and intensively studied in the context of this work; the other cell was developed at KIT and only preliminary tests were performed so far. The cell built at DTU exhibits a bigger gas volume, such that it is not possible to follow catalytic conversion during the treatment. Additionally, the relatively big dimensions did not allow recording X-ray fluorescence data in parallel to ptychographic data acquisition. Both drawbacks were addressed in the new cell designed at KIT. Both cells presented based on similar ones in electron microscopy. They are significantly smaller, lighter and gas tight, in contrast to previously used cells in literature, which facilitates experimental application and also enables working with hazardous gases.

A benchmark of the quality of ptychographic imaging is the obtained spatial resolution. Already in the first proof of principle measurements performed on 50 nm gold nanoparticles, a spatial resolution below 100 nm could be achieved. In later experiments using an optimized measurement setup, the resolution could be further improved to approximately 40 nm on nanoporous gold, outmatching the previously best spatial resolution for *in situ* ptychography of 100 to 200 nm reported in literature so far. Nevertheless, in a later experiment even 20 nm resolution was obtained on nanoporous gold-based catalysts. For a 300-400 nm thick $CuO/ZnO/Al_2O_3@ZSM–5$ section, a comparable resolution, but at the same time a higher contrast compared to TEM measurements, was achieved. In future, the resolution can even be further enhanced by improving the signal-to-noise ratio, *e. g.* by reduction of parasitic scattering from the environment, an active damping mechanism inside the microscope improving the mechanical stability of the sample environment and reducing vibrations, and by an increase of brilliance of the synchrotron radiation sources and therefore an increase of the coherent beam fraction. The latter aspect is considered in new fourth generation synchrotron radiation facilities, *e. g.* PETRA IV, MAX IV, SLS 2, or Sirius.

Within this work it was also demonstrated that the cell enables spatially resolved temperature monitoring, carried out by IR thermography directly under *in situ* conditions. On one hand this enables a precise control of the temperature, which is particularly important when the samples are studied inside certain gas atmospheres, but on the other hand it also offers to monitor temperature variations across the studied catalyst, which can be encountered in exothermic reactions. The acquisition of ptychographic measurements around an absorption edge during *in situ* treatment was also tested in this work, but by visible comparison no differences were observed. Although, the combination of XAS and ptychography is of great importance and previous studies in literature showed the potential for ptychography with chemical contrast. Therefore, the

combination of both methods should be furthered, which mainly requires an optimization of the algorithms. The unique possibility to perform complementary EM and X-ray microscopy on the same sample is obtained since both cells are based on TEM heating chips. Both chips can be used inside the TEM before and after *in situ* ptychography, allowing studying the same sample under different pressure regimes. Furthermore, by combination of SEM with secondary electron contrast and *in situ* ptychography also thicker samples can be studied allowing complementary contrast mechanisms, by either probing more the bulk material or the surface. The good agreement of *in situ* ptychography with the EM of the sample studied before and after *in situ* ptychography treatment was also shown in the context of this work. Therefore, the possibility for the application of complementary techniques and the potential for hierarchically performed studies of heterogeneous catalysts was presented. Since this will also be interesting for other heterogeneous catalysts, such as for hierarchically designed core-shell catalysts, further studies on hierarchically designed catalysts, which requires correlative characterization on different length scales, should be performed in future.

Both, complementary (E)TEM and *in situ* hard X-ray ptychography were used to study the thermal annealing of nanoporous-Au and CeO_2/nanoporous-Au in different gas atmospheres. Measurements were performed in vacuum inside the TEM, under O_2 atmosphere of reduced pressure in the ETEM and under O_2/He and O_2/N_2 by *in situ* ptychography. The study demonstrated that annealing of nanoporous-Au based samples is strongly dependent on the gas atmosphere. In vacuum, nanoporous-Au was stable up to 700-800 °C, but showed a material loss or migration afterwards. Contrarily, around 200-300 °C a coarsening was observed in an O_2 atmosphere in the mbar regime and in O_2/N_2 atmosphere at ambient pressure. However, around 300 °C in O_2/He a similar material loss to the one observed in vacuum at approximately 800 °C was observed. Due to the strong dependency on the gas atmosphere and the observed material loss or migration, the results point out that besides surface diffusion also other mechanisms must contribute to coarsening. This is similar to discussions on the growth mechanisms of nanoparticles, *i. e.* particle migration, coalescence or Ostwald ripening. They also depend on the support or the gas atmosphere. Finally, nanoporous-Au and CeO_2/nanoporous-Au showed a comparable behavior in the different atmospheres, but CeO_2/np-Au was stabilized, as indicated by the onset of changes at higher temperatures.

To understand the underlying coarsening mechanisms, further studies on the annealing of such nanoporous-Au based catalysts should be conducted in future, especially under *in situ* conditions and different gas atmospheres. Thereby, microscopic studies on the atomic structure should be conducted by ETEM under model conditions, while similarly prepared samples should be studied under ambient pressure by *in situ* ptychography. Complementarily, also spectroscopic and scattering techniques could be used to investigate the atomic scale under realistic conditions. Additionally, the 3D nanoporous-Au was only probed during annealing in 2D ge-

ometry, which requests extension to tomographic studies. These should ideally be combined with probing a "bulk" sample by X-ray tomography and a thin material by electron tomography to get further knowledge on the behavior according to the size of the network.

In addition to the thin nanoporous-Au based catalysts, *in situ* ptychography was applied to study a thicker sample of a bifunctional $CuO/ZnO/Al_2O_3$@ZSM–5 core-shell catalyst. Complementary knowledge was obtained by ETEM studies. By this combination, the core-shell interface of the catalyst could be studied in a hierarchical manner at different length scales. The studies were performed during activation in hydrogen atmosphere and reoxidation under synthetic air, which were applied as model conditions. For a thin sample under reduced pressure in the ETEM, a stable core-shell interface was obtained at 250 °C, although a shrinkage of the Cu containing particles in the core material was caused by reduction. This took place only on the nanometer scale by increased interparticle distances. By *in situ* ptychography, the system could not only be studied under model conditions, but also under atmospheric pressure and on a thicker sample. In agreement with the results obtained by ETEM at 250 °C the core-shell material was found to be stable, a temperature increase to 350 °C however led to microscopic changes on the µm scale. These did not only affect the Cu containing core material but also parts of the shell, as indicated by SEM-EDX analysis. Albeit the overall core-shell interface remained stable, which is required to maintain the bifunctional operation of the catalyst. However, all studies were performed on thin slices cut from the whole 3D particle, which may have influenced the behavior. Therefore, further studies on full 3D particles should be carried out by tomography. Due to the dimensions of the particle, this is only possible by X-ray tomography.

To conclude, *in situ* ptychography with spatial resolutions down to 20 to 30 nm paves the way to bridge the gap between high-resolution TEM under idealized conditions and hard X-ray imaging techniques under more realistic conditions and on more realistic samples. Apart from the presented example of the $CuO/ZnO/Al_2O_3$@ZSM–5 catalyst, such a multi-scale imaging approach will also be interesting for other catalyst systems. For example, it can be used to investigate the structure and connectivity of shell impregnated catalysts, the stability of particles in fluidized bed reactors or to study compositional or structural changes of bifunctional catalysts under reaction conditions, like in the Fischer-Tropsch reaction.

Further improvements of the *in situ* cells are required in order to make high-resolution tomographic imaging possible and to reduce requirements on the sample preparation. Additionally, since both *in situ* cells are available for users at the P06 beamline of PETRA III, it is beneficial if further characterization tools become available on-site. Therefore, the development and access to the Nanolab at DESY will be advantageous. Moreover, the installation of a TEM and a glove box would be important with respect to transferring the sample studied by *in situ* ptychography to the TEM under inert conditions. For future experiments the improvement in brilliance of synchrotron radiation sources and active damping mechanisms on the microscopes could po-

tentially allow studying samples with a spatial resolution about 1 to 2 nm. This even has the potential for studying supported metal nanoparticles and bridge to the catalytic application in fixed-bed reactors, which would open the door for studies of typical catalysts used in exhaust gas aftertreatment systems.

General Conclusions and Outlook   The presented techniques and *in situ* cells were developed and optimized independently from each other, but they can be used in a complementary manner. For example, first the microscale can be studied by spatially resolved measurements in the gas phase microreactor, which enables a combination of several characterization techniques. Questions which arise on the catalyst particles themselves, *e. g.* their stability or rearrangement, can then be studied by *in situ* ptychography and ETEM. By this approach, the full length scales from the nano scale to the micro scale (*c. f.* Fig. 1.1) can be covered, which paves the way towards a better understanding of catalytic reactions and ultimately to the systematic development of new and better catalysts.

Bibliography

[1] I. Chorkendorff, J. W. Niemantsverdriet, *Concepts of Modern Catalysis and Kinetics*, Wiley–VCH, Weinheim, **2007**.

[2] J.-D. Grunwaldt, J. B. Wagner, R. E. Dunin-Borkowski, Imaging Catalysts at work. A hierarchical approach from the macro- to the meso- and nano-scale, *ChemCatChem* **2013**, *5*, 62–80.

[3] J. Anton, D. Cahatterjee, G. A. Frey, Marcus, T. Jocob, V. M. Janardhanan, P. Kaghazchi, R. J. Kee, F. J. Keil, L. Kunz, L. Maier, J. Mantzaras, K. Reuter, J. R. Rostrup-Nielsen, V. Schmeißer, S. Tischer, M. Weibel, H. Zhu, *Modeling and simulation of heterogeneous catalytic reactions*, (Ed.: O. Deutschmann), John Wiley & Sons, Weinheim, **2012**.

[4] R. Güttel, T. Turek, Improvement of Fischer–Tropsch synthesis through structuring on different scales, *Energy Technol.* **2016**, *4*, 44–54.

[5] W. Schwieger, M. Klumpp, Präparationsprinzipien mikroposöser Materialien: Vom building block zum hierarchisch aufgebauten porösen System, *Chem. Ing. Tech.* **2016**.

[6] R. Gani, K. Dam-Johansen, *Chemical Product Design: Towards a Perspective through Case Studies*, Vol. 23, (Ed.: K. M. Ng), Elsevier, Amsterdam, Oxford, **2006**.

[7] A. Vantomme, A. Leonard, Z.-Y. Yuan, B.-L. Su, Self–formation of hierarchical micro–meso–macroporous structures: generation of the new concept "Hierarchical Catalysis", *Colloids Surf., A* **2007**, *300*, 70–78.

[8] S. Matera, K. Reuter, When atomic-scale resolution is not enough: spatial effects on in situ model catalyst studies, *J. Catal.* **2012**, *295*, 261–268.

[9] M. Klumpp, L. Zeng, S. A. Al-Thabaiti, A. P. Weber, W. Schwieger, Building concept inspired by rasperries: From microporous zeolite nanocrystals to hierarchical porous assemblies, *Microporous Mesoporous Mater.* **2016**, *229*, 155–156.

[10] R. Güttel, Structuring of reactors and catalysts on multiple scales: potential and limitations for Fischer-Tropsch synthesis, *Chem. Ing. Tech.* **2015**, *87*, 694–701.

[11] F. Zaera, Nanostructured materials for applications in heterogeneous catalysis, *Chem. Soc. Rev.* **2013**, *42*, 2746–2762.

[12] X.-Y. Yang, S. Sun, J.-J. Ding, Y. Zhang, M.-M. Zhang, C. Gao, J. Bao, Preparation, structure and performance of $CuO-ZnO-Al_2O_3$/HZSM-5 core–shell bifunctional catalysts for one-step synthesis of dimethyl ether from CO_2 + H_2, *Acta Phys.-Chim. Sin.* **2012**, *28*, 1957–1963.

[13] W. Ding, M. Klumpp, S. Lee, S. Reuß, S. A. Al-Thabaiti, P. Pfeifer, W. Schwieger, R. Dittmeyer, Simulation of one-stage dimethyl ether synthesis over a core-shell catalyst, *Chem. Ing. Tech.* **2015**, *87*, 702–712.

[14] W. C. Ketchie, Y.-L. Fang, M. S. Wong, M. Murayama, R. J. Davis, Influence of gold particle size on the aqueous-phase oxidation of carbon monoxide and glycerol, *J. Catal.* **2007**, *250*, 94–101.

[15] T. W. Hansen, A. T. Delariva, S. R. Challa, A. K. Datye, Sintering of catalytic nanoparticles: particle migration or Ostwald ripening?, *Acc. Chem. Res.* **2013**, *46*, 1720–1730.

[16] M. Haruta, S. Tsubota, T. Kobayashi, H. Kageyama, M. J. Genet, B. Delmon, Low-temperature oxidation of CO over gold supported on TiO_2, α-Fe_2O_3, and Co_3O_4, *J. Catal.* **1993**, *144*, 175–192.

[17] J.-D. Grunwaldt, C. Kiener, C. Wogerbauer, A. Baiker, Preparation of supported gold catalysts for low-temperature CO oxidation via "size-controlled" gold colloids, *J. Catal.* **1999**, *181*, 223–232.

[18] P. L. Hansen, J. B. Wagner, S. Helveg, J. R. Rostrup-Nielsen, B. S. Clausen, H. Topsøe, Atom-resolved imaging of dynamic shape changes in supported copper nanocrystals, *Science* **2002**, *295*, 2053–2055.

[19] B. M. Weckhuysen, Chemical imaging of spatial heterogeneities in catalytic solids at different length and time scales, *Angew. Chem. Int. Ed.* **2009**, *48*, 4910–4943.

[20] A. P. Merkle, J. Gelb, A. Orchowski, J. Fuchs, X-ray microscopy: the cornerstone for correlative characterization methods in materials research and life science, *Microsc. Microanal.* **2014**, *20*, 986–987.

[21] A. M. Beale, S. D. M. Jacques, B. M. Weckhuysen, Chemical imaging of catalytic solids with synchrotron radiation, *Chem. Soc. Rev.* **2010**, *39*, 4656–4672.

[22] S. Kalirai, U. Boesenberg, G. Falkenberg, F. Meirer, B. M. Weckhuysen, X-ray fluorescence tomography of aged fluid-catalytic-cracking catalyst particles reveals insight into metal deposition processes, *ChemCatChem* **2015**, *7*, 3674–3682.

[23] F. Basile, P. Benito, S. Bugani, W. De Nolf, G. Fornasari, K. Janssens, L. Morselli, E. Scavetta, D. Tonelli, A. Vaccari, Combined use of synchrotron-radiation-based imaging techniques for the characterization of structured catalysts, *Adv. Funct. Mater.* **2010**, *20*, 4117–4126.

[24] J.-D. Grunwaldt, C. G. Schroer, Hard and soft X-ray microscopy and tomography in catalysis: bridging the different time and length scales, *Chem. Soc. Rev.* **2010**, *39*, 4741–4753.

[25] Z. Azizi, M. Rezaeimanesh, T. Tohidian, M. R. Rahimpour, Dimethyl ether: A review of technologies and production challenges, *Chem. Eng. Process* **2014**, *82*, 150–172.

[26] R. Nie, H. Lei, S. Pan, L. Wang, J. Fei, Z. Hou, Core–shell structured CuO–ZnO@H-ZSM-5 catalysts for CO hydrogenation to dimethyl ether, *Fuel* **2012**, *96*, 419–425.

[27] Y. Wang, W. Wang, Y. Chen, J. Ma, J. Zheng, R. Li, Core–shell catalyst CuO–ZnO–Al$_2$O$_3$@Al$_2$O$_3$ for dimethyl ether synthesis from syngas, *Chem. Lett.* **2013**, *42*, 335–337.

[28] M. Behrens, F. Studt, I. Kasatkin, S. Kühl, M. Hävecker, F. Abild-Pedersen, S. Zander, F. Girgsdies, P. Kurr, B.-L. Kniep, et al., The active site of methanol synthesis over Cu/ZnO/Al$_2$O$_3$ industrial catalysts, *Science* **2012**, *336*, 893–897.

[29] C. Holse, C. F. Elkjaer, A. Nierhoff, J. Sehested, I. Chorkendorff, S. Helveg, J. H. Nielsen, Dynamic behavior of CuZn nanoparticles under oxidizing and reducing conditions, *J. Phys. Chem. C* **2015**, *119*, 2804–2812.

[30] J.-D. Grunwaldt, A. M. Molenbroek, N. Y. Topsøe, H. Topsøe, B. S. Clausen, In situ investigations of structural changes in Cu/ZnO catalysts, *J. Catal.* **2000**, *194*, 452–460.

[31] M. A. Bañares, Operando methodology: combination of in situ spectroscopy and simultaneous activity measurements under catalytic reaction conditions, *Catal. Today* **2005**, *100*, 71–77.

[32] F. M. F. de Groot, E. de Smit, M. M. van Schooneveld, L. R. Aramburo, B. M. Weckhuysen, In-situ scanning transmission X-ray microscopy of catalytic solids and related nanomaterials, *ChemPhysChem* **2010**, *11*, 951–962.

[33] J. Singh, C. Lamberti, J. A. van Bokhoven, Advanced X-ray absorption and emission spectroscopy: in situ catalytic studies, *Chem. Soc. Rev.* **2010**, *39*, 4754–4766.

[34] H. Topsøe, Developments in operando studies and in situ characterization of heterogeneous catalysts, *J. Catal.* **2003**, *216*, 155–164.

[35] B. M. Weckhuysen, Snapshots of a working catalyst: possibilities and limitations of in situ spectroscopy in the field of heterogeneous catalysis, *Chem. Commun.* **2002**, *2*, 97–110.

[36] B. M. Weckhuysen, *In-situ spectroscopy of catalysts*, American Scientific Publishers, Valencia, California, **2004**.

[37] J.-D. Grunwaldt, A. Baiker, Axial variation of the oxidation state of Pt-Rh/Al$_2$O$_3$ during partial methane oxidation in a fixed-bed reactor: An in situ X-ray absorption spectroscopy study, *Catal. Lett.* **2005**, *99*, 5–12.

[38] J. Stötzel, R. Frahm, B. Kimmerle, M. Nachtegaal, J.-D. Grunwaldt, Oscillatory behavior during the catalytic partial oxidation of methane: following dynamic structural changes of palladium using the QEXAFS technique, *J. Phys. Chem. C* **2012**, *116*, 599–609.

[39] A. Urakawa, Trends and advances in operando methodology, *Curr. Opin. Chem. Eng.* **2016**, *12*, 31–36.

[40] A. M. Gänzler, M. Casapu, A. Boubnov, O. Müller, S. Conrad, H. Lichtenberg, R. Frahm, J.-D. Grunwaldt, Operando spatially and time-resolved X-ray absorption spectroscopy and infrared thermography during oscillatory CO oxidation, *J. Catal.* **2015**, *328*, 216–224.

[41] S. R. Challa, A. T. Delariva, T. W. Hansen, S. Helveg, J. Sehested, P. L. Hansen, F. Garzon, A. K. Datye, Relating rates of catalyst sintering to the disappearance of individual nanoparticles during Ostwald ripening, *J. Am. Chem. Soc.* **2011**, *133*, 20672–20675.

[42] F. C. Meunier, The design and testing of kinetically-appropriate operando spectroscopic cells for investigating heterogeneous catalytic reactions, *Chem. Soc. Rev.* **2010**, *39*, 4602–4614.

[43] M. A. Vuurman, I. E. Wachs, In situ Raman spectroscopy of alumina-supported metal oxide catalysts, *J. Phys. Chem.* **1992**, *96*, 5008–5016.

[44] I. E. Wachs, J.-M. Jehng, G. Deo, B. M. Weckhuysen, V. V. Guliants, J. B. Benziger, In situ Raman spectroscopy studies of bulk and surface metal oxide phases during oxidation reactions, *Catal. Today* **1996**, *32*, 47–55.

[45] X. Gao, J.-M. Jehng, I. E. Wachs, In situ UV–vis–NIR diffuse reflectance and Raman spectroscopic studies of propane oxidation over ZrO$_2$-supported vanadium oxide catalysts, *J. Catal.* **2002**, *209*, 43–50.

[46] M. Bañares, M. Martınez-Huerta, X. Gao, J. Fierro, I. Wachs, Dynamic behavior of supported vanadia catalysts in the selective oxidation of ethane: In situ Raman, UV–Vis DRS and reactivity studies, *Catal. Today* **2000**, *61*, 295–301.

[47] A. Boubnov, A. Gänzler, S. Conrad, M. Casapu, J.-D. Grunwaldt, Oscillatory CO oxidation over Pt/Al₂O₃ catalysts studied by in situ XAS and DRIFTS, *Top. Catal.* **2013**, *56*, 333–338.

[48] J. M. Thomas, J.-C. Hernandez-Garrido, Probing solid catalysts under operating conditions: electrons or X-rays?, *Angew. Chem. Int. Ed.* **2009**, *48*, 3904–3907.

[49] J.-D. Grunwaldt, B. Kimmerle, A. Baiker, P. Boye, C. G. Schroer, P. Glatzel, C. N. Borca, F. Beckmann, Catalysts at work: From integral to spatially resolved X-ray absorption spectroscopy, *Catal. Today* **2009**, *145*, 267–278.

[50] J. F. Creemer, S. Helveg, G. H. Hoveling, S. Ullmann, A. M. Molenbroek, P. M. Sarro, H. W. Zandbergen, Atomic-scale electron microscopy at ambient pressure, *Ultramicroscopy* **2008**, *108*, 993–998.

[51] J. M. Thomas, C. Ducati, R. Leary, P. A. Midgley, Some turning points in the chemical electron microscopic study of heterogeneous catalysts, *ChemCatChem* **2013**, *5*, 2560–2579.

[52] B. S. Clausen, G. Steffensen, B. Fabius, J. Villadsen, R. Feidenhansl, H. Topsøe, In situ cell for combined XRD and online catalysis tests – studies of Cu-based water gas shift and methanol synthesis, *J. Catal.* **1991**, *132*, 524–535.

[53] A. I. Frenkel, J. A. Rodriguez, J. G. Chen, Synchrotron techniques for in situ catalytic studies: capabilities, challenges, and opportunities, *ACS Catal.* **2012**, *2*, 2269–2280.

[54] Y. Iwasawa, *X-ray absorption fine structure for catalysts and surfaces*, Vol. 2, World Scientific, Singapore, **1996**.

[55] G. Sankar, P. A. Wright, S. Natarajan, J. M. Thomas, G. N. Greaves, A. J. Dent, B. R. Dobson, C. A. Ramsdale, R. H. Jones, Combined QuEXAFS-XRD – A new technique in high-temperature materials chemistry – an illustrative in-situ study of the zinc oxide-enhanced solid-state production of codierite from a precursor zeolite, *J. Phys. Chem.* **1993**, *97*, 9550–9554.

[56] B. Clausen, L. Gråbæk, G. Steffensen, P. Hansen, H. Topsøe, A combined QEXAFS/XRD method for on-line, in situ studies of catalysts: examples of dynamic measurements of Cu-based methanol catalysts, *Catal. Lett.* **1993**, *20*, 23–36.

[57] J.-D. Grunwaldt, B. S. Clausen, Combining XRD and EXAFS with on-line catalytic studies for in situ characterization of catalysts, *Top. Catal.* **2002**, *18*, 37–43.

[58] M. Beckers, T. Senkbeil, T. Gorniak, M. Reese, K. Giewekemeyer, S.-C. Gleber, T. Salditt, A. Rosenhahn, Chemical contrast in soft X-ray ptychography, *Phys. Rev. Lett.* **2011**, *107*, 208101.

[59] S. Price, K. Ignatyev, K. Geraki, M. Basham, J. Filik, N. Vo, P. Witte, A. Beale, J. Mosselmans, Chemical imaging of single catalyst particles with scanning μ-XANES-CT and μ-XRF-CT, *Phys. Chem. Chem. Phys.* **2015**, *17*, 521–529.

[60] A. Urakawa, A. Baiker, Space-resolved profiling relevant in heterogeneous catalysis, *Top. Catal.* **2009**, *52*, 1312–1322.

[61] K. Morgan, J. Touitou, J.-S. Choi, C. Coney, C. Hardacre, J. A. Pihl, C. E. Stere, M.-Y. Kim, C. Stewart, A. Goguet, W. P. Partridge, Evolution and enabling capabilities of spatially resolved techniques for the characterization of heterogeneously catalyzed reactions, *ACS Catal.* **2016**, *6*, 1356–1381.

[62] A. Zellner, R. Suntz, O. Deutschmann, In-situ-Untersuchungen katalytischer NO-Reduktion in einem optisch zugänglichen Strömungskanal, *Chem. Ing. Tech.* **2014**, *86*, 538–543.

[63] R. Horn, K. Williams, N. Degenstein, L. Schmidt, Syngas by catalytic partial oxidation of methane on rhodium: Mechanistic conclusions from spatially resolved measurements and numerical simulations, *J. Catal.* **2006**, *242*, 92–102.

[64] C. Diehm, O. Deutschmann, Hydrogen production by catalytic partial oxidation of methane over staged Pd/Rh coated monoliths: Spatially resolved concentration and temperature profiles, *Int. J. Hydrogen Energ.* **2014**, *39*, 17998 – 18004.

[65] A. Zellner, R. Suntz, O. Deutschmann, Two-dimensional spatial resolution of concentration profiles in catalytic reactors by planar laser-induced fluorescence: NO reduction over diesel oxidation catalysts, *Angew. Chem. Int. Ed.* **2015**, *54*, 2653–2655.

[66] F. Moates, M. Somani, J. Annamalai, J. Richardson, D. Luss, R. Willson, Infrared thermographic screening of combinatorial libraries of heterogeneous catalysts, *Ind. Eng. Chem. Res.* **1996**, *35*, 4801–4803.

[67] R. B. Biniwale, H. Yamashiro, M. Ichikawa, In-situ infrared thermographic analysis during dehydrogenationof cyclohexane over carbon-supported Pt catalysts using spray-pulsed reactor, *Catal. Lett.* **2005**, *102*, 23–31.

[68] P. Pawlicki, R. Schmitz, Spatial effects on supported catalysts, *Chem. Eng. Prog.* **1987**, *83*, 40–45.

[69] L. G. van de Water, J. A. Bergwerff, G. Leliveld, B. M. Weckhuysen, K. P. de Jong, Insights into the preparation of supported catalysts: A spatially resolved Raman and UV-Vis spectroscopic study into the drying process of CoMo/γ-Al$_2$O$_3$ catalyst bodies, *J. Phys. Chem. B* **2005**, *109*, 14513–14522.

[70] E. Stavitski, B. M. Weckhuysen, Infrared and Raman imaging of heterogeneous catalysts, *Chem. Soc. Rev.* **2010**, *39*, 4615–4625.

[71] E. Stavitski, M. H. Kox, I. Swart, F. M. de Groot, B. M. Weckhuysen, In situ synchrotron-based IR microspectroscopy to study catalytic reactions in zeolite crystals, *Angew. Chem. Int. Ed.* **2008**, *47*, 3543–3547.

[72] S. Hannemann, J.-D. Grunwaldt, B. Kimmerle, A. Baiker, P. Boye, C. Schroer, Axial changes of catalyst structure and temperature in a fixed-bed microreactor during noble metal catalysed partial oxidation of methane, *Top. Catal.* **2009**, *52*, 1360–1370.

[73] S. Srinivas, A. Dhingra, H. Im, E. Gulari, A scalable silicon microreactor for preferential CO oxidation: performance comparison with a tubular packed-bed microreactor, *Appl. Catal., A.* **2004**, *274*, 285–293.

[74] R. Lødeng, E. Bjørgum, B. C. Enger, J. L. Eilertsen, A. Holmen, B. Krogh, I. A. Bøe, M. Rønnekleiv, E. Rytter, A fixed-bed reactor study of catalytic partial oxidation over Rh/Al$_2$O$_3$: an indication of a direct pathway to CO, *Top. Catal.* **2011**, *54*, 873–880.

[75] K. Heitnes, S. Lindberg, O. Rokstad, A. Holmen, Catalytic partial oxidation of methane to synthesis gas, *Catal. Today* **1995**, *24*, 211–216.

[76] F. Basile, G. Fornasari, F. Trifiro, A. Vaccari, Partial oxidation of methane: Effect of reaction parameters and catalyst composition on the thermal profile and heat distribution, *Catal. Today* **2001**, *64*, 21–30.

[77] B. S. Clausen, H. Topsøe, Application of combined X-ray diffraction and absorption techniques, *Adv. Catal.* **1998**, *42*, 315–344.

[78] S. D. Jacques, M. Di Michiel, A. M. Beale, T. Sochi, M. G. O'Brien, L. Espinosa-Alonso, B. M. Weckhuysen, P. Barnes, Dynamic X-ray diffraction computed tomography reveals real-time insight into catalyst active phase evolution, *Angew. Chem. Int. Ed.* **2011**, *50*, 10148–10152.

[79] S. Rabe, M. Nachtegaal, F. Vogel, Catalytic partial oxidation of methane to synthesis gas over a ruthenium catalyst: the role of the oxidation state, *Phys. Chem. Chem. Phys.* **2007**, *9*, 1461–1468.

[80] J. Kinney, Q. Johnson, M. C. Nichols, U. Bonse, R. Nusshardt, Elemental and chemical-state imaging using synchrotron radiation, *Appl. Opt.* **1986**, *25*, 4583–4585.

[81] J.-D. Grunwaldt, S. Hannemann, C. G. Schroer, A. Baiker, 2D-mapping of the catalyst structure inside a catalytic microreactor at work: Partial oxidation of methane over Rh/Al$_2$O$_3$, *J. Phys. Chem. B* **2006**, *110*, 8674–8680.

[82] R. Falcone, C. Jacobsen, J. Kirz, S. Marchesini, D. Shapiro, J. Spence, New directions in X-ray microscopy, *Contemp. Phys.* **2011**, *52*, 293–318.

[83] S. Hannemann, J.-D. Grunwaldt, N. van Vegten, A. Baiker, P. Boye, C. G. Schroer, Distinct spatial changes of the catalyst structure inside a fixed-bed microreactor during the partial oxidation of methane over Rh/Al$_2$O$_3$, *Catal. Today* **2007**, *126*, 54–63.

[84] B. Kimmerle, J.-D. Grunwaldt, A. Baiker, P. Glatzel, P. Boye, S. Stephan, C. G. Schroer, Visualizing a catalyst at work during the ignition of the catalytic partial oxidation of methane, *J. Phys.Chem. C* **2009**, *113*, 3037–3040.

[85] D. E. Doronkin, M. Casapu, T. Günter, O. Müller, R. Frahm, J.-D. Grunwaldt, Operando spatially- and time-resolved XAS study on zeolite catalysts for selective catalytic reduction of NO$_x$ by NH$_3$, *J. Phys. Chem. C* **2014**, *118*, 10204–10212.

[86] T. Hyakutake, W. van Beek, A. Urakawa, Unravelling the nature, evolution and spatial gradients of active species and active sites in the catalyst bed of unpromoted and K/Ba-promoted Cu/Al$_2$O$_3$ during CO$_2$ capture-reduction, *J. Mater. Chem. A* **2016**.

[87] C. Schroer, M. Kuhlmann, T. Günzler, B. Lengeler, M. Richwin, B. Griesebock, D. Lützenkirchen-Hecht, R. Frahm, E. Ziegler, A. Mashayekhi, D. R. Haeffner, J.-D. Grunwaldt, A. Baiker, Mapping the chemical states of an element inside a sample using tomographic x-ray absorption spectroscopy, *Appl. Phys. Lett.* **2003**, *82*, 3360–3362.

[88] S. W. Price, K. Geraki, K. Ignatyev, P. T. Witte, A. M. Beale, J. F. W. Mosselmans, In situ microfocus chemical computed tomography of the composition of a single catalyst particle during hydrogenation of nitrobenzene in the liquid phase, *Angew. Chem. Int. Ed.* **2015**, *54*, 9886–9889.

[89] G. Hofmann, A. Rochet, E. Ogel, M. Casapu, S. Ritter, M. Ogurreck, J.-D. Grunwaldt, Aging of a Pt/Al$_2$O$_3$ exhaust gas catalyst monitored by quasi in situ X-ray micro computed tomography, *RSC Adv.* **2015**, *5*, 6893–6905.

[90] A. M. Beale, S. D. M. Jacques, J. A. Bergwerff, P. Barnes, B. M. Weckhuysen, Tomographic energy dispersive diffraction imaging as a tool to profile in three dimensions the distribution and composition of metal oxide species in catalyst bodies, *Angew. Chem. Int. Ed.* **2007**, *46*, 8832–8835.

[91] J. C. da Silva, K. Mader, M. Holler, D. Haberthuer, A. Diaz, M. Guizar-Sicairos, W.-C. Cheng, Y. Shu, J. Raabe, A. Menzel, J. A. van Bokhoven, Assessment of the 3D pore structure and individual components of preshaped catalyst bodies by X-ray imaging, *ChemCatChem* **2015**, *7*, 413–416.

[92] J. F. Creemer, S. Helveg, P. J. Kooyman, A. M. Molenbroek, H. W. Zandbergen, P. M. Sarro, A MEMS reactor for atomic-scale microscopy of nanomaterials under industrially relevant conditions, *J. Microelectromech. Sys.* **2010**, *19*, 254–264.

[93] T. W. Hansen, J. B. Wagner, R. E. Dunin-Borkowski, Aberration corrected and monochromated environmental transmission electron microscopy: challenges and prospects for materials science, *Mater. Sci. Technol.* **2010**, *26*, 1338–1344.

[94] T. W. Hansen, J. B. Wagner, Environmental transmission electron microscopy in an aberration-corrected environment, *Microsc. Microanal.* **2012**, *18*, 684–690.

[95] J. B. Wagner, F. Cavalca, C. D. Damsgaard, L. D. L. Duchstein, T. W. Hansen, Exploring the environmental transmission electron microscope, *Micron* **2012**, *43*, 1169–1175.

[96] P. L. Gai, E. D. Boyes, S. Helveg, P. L. Hansen, S. Giorgio, C. R. Henry, Atomic-resolution environmental transmission electron microscopy for probing gas–solid reactions in heterogeneous catalysis, *MRS Bull.* **2007**, *32*, 1044–1050.

[97] H. Yoshida, Y. Kuwauchi, J. R. Jinschek, K. Sun, S. Tanaka, M. Kohyama, S. Shimada, M. Haruta, S. Takeda, Visualizing gas molecules interacting with supported nanoparticulate catalysts at reaction conditions, *Science* **2012**, *335*, 317–319.

[98] S. B. Simonsen, S. Dahl, E. Johnson, S. Helveg, Ceria-catalyzed soot oxidation studied by environmental transmission electron microscopy, *J. Catal.* **2008**, *255*, 1–5.

[99] R. Sharma, Z. Iqbal, In situ observations of carbon nanotube formation using environmental transmission electron microscopy, *Appl. Phys. Lett.* **2004**, *84*, 990–992.

[100] R. F. Egerton, P. Li, M. Malac, Radiation damage in the TEM and SEM, *Micron* **2004**, *35*, 399–409.

[101] A. D. Benavidez, L. Kovarik, A. Genc, N. Agrawal, E. M. Larsson, T. W. Hansen, A. M. Karim, A. K. Datye, Environmental transmission electron microscopy study of the origins of anomalous particle size distributions in supported metal catalysts, *ACS Catal.* **2012**, *2*, 2349–2356.

[102] I. L. C. Buurmans, B. M. Weckhuysen, Heterogeneities of individual catalyst particles in space and time as monitored by spectroscopy, *Nat. Chem.* **2012**, *4*, 873–886.

[103] K. H. Cats, I. D. Gonzalez-Jimenez, Y. Liu, J. Nelson, D. van Campen, F. Meirer, A. M. J. van der Eerden, F. M. F. de Groot, J. C. Andrews, B. M. Weckhuysen, X-ray nanoscopy of cobalt Fischer-Tropsch catalysts at work, *Chem. Commun.* **2013**, *49*, 4622–4624.

[104] E. A. Stach, Y. Li, S. Zhao, A. Gamalski, D. Zakharov, R. Tappero, K. Chen-Wiegart, J. Thieme, U. Jung, A. Elsen, Characterizing working catalysts with correlated electron and photon probes, *Microsc. Microanal.* **2015**, *21*, 563–564.

[105] Y. S. Chu, J. M. Yi, F. De Carlo, Q. Shen, W.-K. Lee, H. J. Wu, C. L. Wang, J. Y. Wang, C. J. Liu, C. H. Wang, S. R. Wu, C. C. Chien, Y. Hwu, A. Tkachuk, W. Yun, M. Feser, K. S. Liang, C. S. Yang, J. H. Je, G. Margaritondo, Hard-X-ray microscopy with Fresnel zone plates reaches 40 nm Rayleigh resolution, *Appl. Phys. Lett.* **2008**, *92*, 103119.

[106] A. M. Kiss, W. M. Harris, A. Nakajo, S. Wang, J. Vila-Comamala, A. Deriy, W. K. S. Chiu, In situ heater design for nanoscale synchrotron-based full-field transmission X-ray microscopy, *Microsc. Microanal.* **2015**, *21*, 290–297.

[107] I. J. Drake, T. C. N. Liu, M. Gilles, T. Tyliszczak, A. L. D. Kilcoyne, D. K. Shuh, R. A. Mathies, A. T. Bell, An in situ cell for characterization of solids by soft X-ray absorption, *Rev. Sci. Instrum.* **2004**, *75*, 3242–3247.

[108] E. de Smit, I. Swart, J. F. Creemer, G. H. Hoveling, M. K. Gilles, T. Tyliszczak, J. Kooyman, Patricia, H. W. Zandbergen, C. Morin, M. Weckhuysen, Bert, F. M. F. de Groot, Nanoscale chemical imaging of a working catalyst by scanning transmission X-ray microscopy, *Nature* **2008**, *456*, 222–225.

[109] Y. Suzuki, F. Uchida, X-ray focusing with elliptic Kirkpatrick-Baez mirror system, *Jpn. J. Appl. Phys.* **1991**, *30*, 1127–1130.

[110] A. Ruhlandt, T. Liese, V. Radisch, S. P. Krüger, M. Osterhoff, K. Giewekemeyer, H. U. Krebs, T. Salditt, A combined Kirkpatrick-Baez mirror and multilayer lens for sub-10 nm X-ray focusing, *AIP Adv.* **2012**, *2*, 12175.

[111] H. G. Oltman, The focusing of short electromagnetic waves by means of the Fresnel half-period zone plate, *Phys. Rev.* **1953**, *92*, 1093.

[112] J. Camus, F. Girard, R. Clark, Fresnel zone plate generation, *Appl. Opt.* **1967**, *6*, 1433.

[113] S. Suehiro, H. Miyaji, H. Hayashi, Refractive lens for X-ray focus, *Nature* **1991**, *352*, 385–386.

[114] A. Snigirev, V. Kohn, I. Snigireva, B. Lengeler, A compound refractive lens for focusing high-energy X-rays, *Nature* **1996**, *384*, 49–51.

[115] B. Lengeler, C. G. Schroer, M. Richwin, J. Tummler, M. Drakopoulos, A. Snigirev, I. Snigireva, A microscope for hard X-rays based on parabolic compound refractive lenses, *Appl. Phys. Lett.* **1999**, *74*, 3924–3926.

[116] S. P. Krüger, H. Neubauer, M. Bartels, S. Kalbfleisch, K. Giewekemeyer, P. J. Wilbrandt, M. Sprung, T. Salditt, Sub-10 nm beam confinement by X-ray waveguides: design, fabrication and characterization of optical properties, *J. Synch. Rad.* **2012**, *19*, 227–236.

[117] I. D. Gonzalez-Jimenez, K. Cats, T. Davidian, M. Ruitenbeek, F. Meirer, Y. Liu, J. Nelson, J. C. Andrews, P. Pianetta, F. M. F. de Groot, B. M. Weckhuysen, Hard X-ray nanotomography of catalytic solids at work, *Angew. Chem. Int. Ed.* **2012**, *51*, 11986–11990.

[118] C. G. Schroer, P. Boye, J. M. Feldkamp, J. Patommel, A. Schropp, D. Samberg, S. Stephan, M. Burghammer, S. Schoder, C. Riekel, B. Lengeler, G. Falkenberg, G. Wellenreuther, M. Kuhlmann, R. Frahm, D. Lutzenkirchen-Hecht, W. H. Schroeder, Hard X-ray microscopy with elemental, chemical, and structural contrast, *Acta. Phys. Pol. A* **2010**, *117*, 357–368.

[119] A. J. Morgan, M. Prasciolu, A. Andrejczuk, J. Krzywinski, A. Meents, D. Pennicard, H. Graafsma, A. Barty, R. J. Bean, M. Barthelmess, D. Oberthuer, O. Yefanov, A. Aquila, H. N. Chapman, S. Bajt, High numerical aperture multilayer Laue lenses, *Sci. Rep.* **2015**, *5*, 09892.

[120] M. Stampanoni, A. Menzel, B. Watts, K. S. Mader, O. Bunk, Coherent X-ray imaging: bridging the gap between atomic and micro-scale investigations, *Chimia* **2014**, *68*, 66–72.

[121] J. N. Clark, M. Trigo, T. Henighan, R. Harder, B. Abbey, T. Katayama, M. Kozina, E. Dufresne, H. Wen, D. Walko, Y. Li, X. Huang, I. Robinson, D. Reis, Lensless imaging of nano-and meso-scale dynamics with X-rays, *Microsc. Microanal.* **2015**, *21*, 2165–2166.

[122] P. Thibault, M. Dierolf, A. Menzel, O. Bunk, C. David, F. Pfeiffer, High–resolution scanning X–ray diffraction microscopy, *Science* **2008**, *321*, 379–382.

[123] M. Dierolf, Dissertation, Technical University of Munich, **2015**.

[124] M. Dierolf, A. Menzel, P. Thibault, P. Schneider, C. M. Kewish, R. Wepf, O. Bunk, F. Pfeiffer, Ptychographic X-ray computed tomography at the nanoscale, *Nature* **2010**, *467*, 436–439.

[125] A. M. Maiden, M. J. Humphry, F. Zhang, J. M. Rodenburg, Superresolution imaging via ptychography, *J. Opt. Soc. Am. A. Opt. Image Sci. Vis.* **2011**, *28*, 604–612.

[126] A. M. Maiden, J. M. Rodenburg, An improved ptychographical phase retrieval algorithm for diffractive imaging, *Ultramicroscopy* **2009**, *109*, 1256–1262.

[127] J. M. Rodenburg, H. M. L. Faulkner, A phase retrieval algorithm for shifting illumination, *Appl. Phys. Lett.* **2004**, *85*, 4795–4797.

[128] R. Hoppe, J. Reinhardt, G. Hofmann, J. Patommel, J.-D. Grunwaldt, C. D. Damsgaard, G. Wellenreuther, G. Falkenberg, C. G. Schroer, High-resolution chemical imaging of gold nanoparticles using hard X-ray ptychography, *Appl. Phys. Lett.* **2013**, *102*, 203104.

[129] D. A. Shapiro, Y.-S. Yu, T. Tyliszczak, J. Cabana, R. Celestre, W. Chao, K. Kaznatcheev, A. L. D. Kilcoyne, F. Maia, S. Marchesini, Y. S. Meng, T. Warwick, L. L. Yang, H. A. Padmore, Chemical composition mapping with nanometre resolution by soft X-ray microscopy, *Nature Photon.* **2014**, *8*, 765–769.

[130] J. Vila-Comamala, A. Diaz, M. Guizar-Sicairos, A. Mantion, C. M. Kewish, A. Menzel, O. Bunk, C. David, Characterization of high–resolution diffractive X-ray optics by ptychographic coherent diffractive imaging, *Opt. Express* **2011**, *19*, 21333–21344.

[131] A. Schropp, R. Hoppe, J. Patommel, D. Samberg, F. Seiboth, S. Stephan, G. Wellenreuther, G. Falkenberg, C. G. Schroer, Hard X-ray scanning microscopy with coherent radiation: Beyond the resolution of conventional X-ray microscopes, *Appl. Phys. Lett.* **2012**, *100*, 253112.

[132] K. Høydalsvik, J. B. Floystad, T. Zhao, M. Esmaeili, A. Diaz, J. W. Andreasen, R. H. Mathiesen, M. Ronning, D. W. Breiby, In situ X-ray ptychography imaging of high-temperature CO_2 acceptor particle agglomerates, *Appl. Phys. Lett.* **2014**, *104*, 241909.

[133] M. Esmaeili, J. B. Floystad, A. Diaz, K. Hoydalsvik, M. Guizar-Sicairos, J. W. Andreasen, D. W. Breiby, Ptychographic X-ray tomography of silk fiber hydration, *Macromolecules* **2013**, *46*, 434–439.

[134] J. Bo Floystad, E. T. B. Skjonsfjell, M. Guizar-Sicairos, K. Hoydalsvik, J. He, J. W. Andreasen, Z. Zhang, D. W. Breiby, Quantitative 3D X-ray imaging of densification, delamination and fracture in a micro-composite under compression, *Adv. Eng. Mater.* **2015**, *17*, 545–553.

[135] A. Ulvestad, A. Singer, H.-M. Cho, J. N. Clark, R. Harder, J. Maser, Y. S. Meng, O. G. Shpyrko, Single particle nanomechanics in operando batteries via lensless strain mapping, *Nano Lett.* **2014**, *14*, 5123–5127.

[136] J. N. Clark, J. Ihli, A. S. Schenk, Y.-Y. Kim, A. N. Kulak, J. M. Campbell, G. Nisbet, F. C. Meldrum, I. K. Robinson, Three-dimensional imaging of dislocation propagation during crystal growth and dissolution, *Nat. Mater.* **2015**, *14*, 780–784.

[137] J. Bao, J. He, Y. Zhang, Y. Yoneyama, N. Tsubaki, A core/shell catalyst produces a spatially confined effect and shape selectivity in a consecutive reaction, *Angew. Chem. Int. Ed.* **2008**, *47*, 353–356.

[138] L. Xu, P. Hog-gen, W. Haihong, L. Chen, L. Yueming, W. Peng, Core-shell-structured titanosilicate as a robust catalyst for cyclohexanone ammoximation, *ACS Catal.* **2013**, *3*, 103–110.

[139] Y. Huang, X. Zhou, M. Yin, C. Liu, W. Xing, Novel PdAu@Au/C core–shell catalyst: Superior activity and selectivity in formic acid decomposition for hydrogen generation, *Chem. Mater.* **2010**, *22*, 5122–5128.

[140] F. Meirer, S. Kalirai, D. Morris, S. Soparawalla, Y. Liu, G. Mesu, J. C. Andrews, B. M. Weckhuysen, Life and death of a single catalytic cracking particle, *Sci. Adv.* **2015**, *1*, e1400199.

[141] F. Meirer, S. Kalirai, J. N. Weker, Y. Liu, J. Andrews, B. Weckhuysen, Agglutination of single catalyst particles during fluid catalytic cracking as observed by X-ray nanotomography, *Chem. Commun.* **2015**, *51*, 8097–8100.

[142] G. Yang, N. Tsubaki, J. Shamoto, Y. Yoneyama, Y. Zhang, Confinement effect and synergistic function of H-ZSM-5/Cu-ZnO-Al$_2$O$_3$ capsule catalyst for one-step controlled synthesis, *J. Am. Chem. Soc.* **2010**, *132*, 8129–8136.

[143] N. Kruse, A. G. Machoke, W. Schwieger, R. Güttel, Nanostructured encapsulated catalysts for combination of Fischer–Tropsch synthesis and hydroprocessing, *ChemCatChem* **2015**, *7*, 1018–1022.

[144] R. F. Egerton, *Physical Principles of Electron Micrsocopy: An Introduction to TEM, SEM and AEM*, Springer, Cham, **2005**.

[145] P. J. Potts, *A Handbook of Silicate Rock Analysis*, Blackie and Son, Glasgow, London, **1987**.

[146] S. J. B. Reed, *Electron micro probe analysis and scattering electron microscopy in geology*, Cambridge University Press, New York, **1996**.

[147] L. A. Giannuzzi, *Introduction to Focused Ion Beams: Instrumentation, Theory, Techniques and Practice*, (Ed.: L. A. Giannuzzi), Springer Science & Business Media, New York, **2006**.

[148] D. A. M. de Winter, F. Meirer, B. M. Weckhuysen, FIB-SEM tomography probes the mesoscale pore space of an individual catalytic cracking particle, *ACS Catal.* **2016**, *6*, 3158–3167.

[149] B. Fultz, J. M. Howe, *Transmission Electron Microscopy and Diffractometry of Materials*, Springer Science & Business Media, Berlin, Heidelberg, **2012**.

[150] R. F. Egerton, *Electron Energy-Loss Spectroscopy in the Electron Microscope*, Springer Science & Business Media, New York, **2011**.

[151] J. Als-Nielsen, D. McMorrow, *Elements of Modern X-ray Physics*, John Wiley & Sons, Chichester, West Sussex, **2011**.

[152] K. Wille, Synchrotron radiation sources, *Rep. Prog. Phys.* **1991**, *54*, 1005–1067.

[153] G. Bunker, *Introduction to XAFS: A Pracical Guide to X-ray Absorption Fine Structure Spectroscopy*, Cambridge University Press, Cambridge, **2010**.

[154] R. Frahm, M. Nachtegaal, J. Stötzel, M. Harfouche, J. A. van Bokhoven, J.-D. Grunwaldt, The dedicated QEXAFS facility at the SLS: Performance and scientific opportunities, *AIP Conf. Proc.* **2010**, *1234*, 251–255.

[155] J. H. Gross, *Mass Spectrometry: A Textbook*, Springer Science & Business Media, Berlin, Heidelberg, **2011**.

[156] J. Barker, *Mass Spectrometry: Analytical Chemistry by Open Learning*, (Ed.: D. J. Ando), John Wiley & Sons, Chichester, West Sussex, **1999**.

[157] P. Childs, J. Greenwood, C. Long, Review of temperature measurement, *Rev. Sci. Instrum.* **2000**, *71*, 2959–2978.

[158] N. M. Ravindra, S. Abedrabbo, W. Chen, F. M. Tong, A. K. Nanda, A. C. Speranza, Temperature-dependent emissivity of silicon-related materials and structures, *IEEE T. Semiconduct. M.* **1998**, *11*, 30–39.

[159] J. W. Niemantsverdriet, *Spectroscopy in Catalysis*, John Wiley & Sons, Weinheim, **2007**.

[160] X. Liu, B. Unal, K. F. Jensen, Heterogeneous catalysis with continuous flow microreactors, *Catal. Sci. Tech.* **2012**, *2*, 2134–2138.

[161] W. Ehrfeld, V. Hessel, L. H., *Microreactors: New Technology for Modern Chemistry*, Wiley VCH, Weinheim, **2000**.

[162] E. Klemm, H. Döring, A. Geisselmann, S. Schirrmeister, Microstructured reactors in heterogenous catalysis, *Chem. Eng. Technol.* **2007**, *30*, 1615–1621.

[163] K. Jähnisch, V. Hessel, H. Lowe, M. Baerns, Chemistry in microstructured reactors, *Angew. Chem. Int. Ed.* **2004**, *43*, 406–446.

[164] W. Wibel, A. Wenka, J. J. Brandner, R. Dittmeyer, Measuring and modeling the residence time distribution of gas flows in multichannel microreactors, *Chem. Eng. J.* **2013**, *227*, 203–214.

[165] K. F. Jensen, Microreaction engineering – is small better?, *Chem. Eng. Sci.* **2001**, *56*, 293–303.

[166] T. R. Henriksen, J. L. Olsen, P. Vesborg, I. Chorkendorff, O. Hansen, Highly sensitive silicon microreactor for catalyst testing, *Rev. Sci. Instrum.* **2009**, *80*, 124101.

[167] J.-D. Grunwaldt, B. Kimmerle, S. Hannemann, A. Baiker, P. Boye, C. G. Schroer, Parallel structural screening of solid materials, *J. Mater. Chem.* **2007**, *17*, 2603–2606.

[168] E. Gross, X.-Z. Shu, S. Alayoglu, H. A. Bechtel, M. C. Martin, F. D. Toste, G. A. Somorjai, In situ IR and X-ray high spatial-resolution microspectroscopy measurements of multistep organic transformation in flow microreactor catalyzed by Au nanoclusters, *J. Am. Chem. Soc.* **2014**, *136*, 3624–3629.

[169] R. M. Tiggelaar, P. van Male, J. W. Berenschot, J. G. E. Gardeniers, R. E. Oosterbroek, M. de Croon, J. C. Schouten, A. van den Berg, M. C. Elwenspoek, Fabrication of a high–temperature microreactor with integrated heater and sensor patterns on an ultrathin silicon membrane, *Sens. Actuators A-Phys.* **2005**, *119*, 196–205.

[170] A. Urakawa, F. Trachsel, P. R. von Rohr, A. Baiker, On-chip Raman analysis of heterogeneous catalytic reaction in supercritical CO_2: phase behaviour monitoring and activity profiling, *Analyst* **2008**, *133*, 1352–1354.

[171] R. Srinivasan, I. M. Hsing, P. E. Berger, K. F. Jensen, S. L. Firebaugh, M. A. Schmidt, M. P. Harold, J. J. Lerou, J. F. Ryley, Micromachined reactors for catalytic partial oxidation reactions, *AIChE J.* **1997**, *43*, 3059–3069.

[172] L. Kiwi-Minsker, A. Renken, Microstructured reactors for catalytic reactions, *Catal. Today* **2005**, *110*, 2–14.

[173] J. Vandenbergh, T. Tura, E. Baeten, T. Junkers, Polymer end group modifications and polymer conjugations via "Click" chemistry employing microreactor technology, *J. Polym. Sci. A Polym. Chem.* **2014**, *52*, 1263–1274.

[174] J. Yue, J. C. Schouten, T. A. Nijhuis, Integration of microreactors with spectroscopic detection for online reaction monitoring and catalyst characterization, *Ind. Eng. Chem. Res.* **2012**, *51*, 14583–14609.

[175] G. Sankar, E. Cao, A. Gavriilidis, A microstructured reactor based in situ cell for the study of catalysts by X-ay absorption spectroscopy under operating conditions, *Catal. Today* **2007**, *125*, 24–28.

[176] C. K. C. Tan, W. N. Delgass, C. D. Baertsch, Spatially resolved in situ FTIR analysis of CO adsorption and reaction on Pt/SiO_2 in a silicon microreactor, *Appl. Cat., B.* **2009**, *93*, 66–74.

[177] F. Dionigi, P. C. K. Vesborg, T. Pedersen, O. Hansen, S. Dahl, A. Xiong, K. Maeda, K. Domen, I. Chorkendorff, Gas phase photocatalytic water splitting with $Rh_{2-y}Cr_yO_3$/GaN:ZnO in small μ-reactors, *Energy. Environ. Sci.* **2011**, *4*, 2937–2942.

[178] F. Dionigi, M. G. Nielsen, T. Pedersen, O. Hansen, I. Chorkendorff, P. C. K. Vesborg, A transparent Pyrex μ-reactor for combined in situ optical characterization and photocatalytic reactivity measurements, *Rev. Sci. Instrum.* **2013**, *84*, 103910.

[179] D. Ferri, M. A. Newton, M. Di Michiel, G. L. Chiarello, S. Yoon, Y. Lu, J. Andrieux, Revealing the dynamic structure of complex solid catalysts using modulated excitation X-ray diffraction, *Angew. Chem. Int. Ed.* **2014**, *53*, 8890–8894.

[180] A. Urakawa, W. Van Beek, M. Monrabal-Capilla, J. R. Galán-Mascarós, L. Palin, M. Milanesio, Combined, modulation enhanced X-ray powder diffraction and Raman spectroscopic study of structural transitions in the spin crossover material [Fe(Htrz)$_2$(trz)](BF$_4$), *J. Phys. Chem. C* **2010**, *115*, 1323–1329.

[181] J.-D. Grunwaldt, M. Caravati, S. Hannemann, A. Baiker, X-ray absorption spectroscopy under reaction conditions: suitability of different reaction cells for combined catalyst characterization and time-resolved studies, *Phys. Chem. Chem. Phys.* **2004**, *6*, 3037–3047.

[182] A. Bansode, G. Guilera, V. Cuartero, L. Simonelli, M. Avila, A. Urakawa, Performance and characteristics of a high pressure, high temperature capillary cell with facile construction for operando X-ray absorption spectroscopy, *Rev. Sci. Instrum.* **2014**, *85*, 8.

[183] J. Yue, F. H. Falke, J. C. Schouten, T. A. Nijhuis, Microreactors with integrated UV/Vis spectroscopic detection for online process analysis under segmented flow, *Lab Chip* **2013**, *13*, 4855–4863.

[184] T. Beuvier, E. A. C. Panduro, P. Kwaśniewski, S. Marre, C. Lecoutre, Y. Garrabos, C. Aymonier, B. Calvignac, A. Gibaud, Implementation of in situ SAXS/WAXS characterization into silicon/glass microreactors, *Lab Chip* **2015**, *15*, 2002–2008.

[185] J. Kehres, T. Pedersen, Pedersen, F. Masini, J. W. Andreasen, M. M. Nielsen, A. Diaz, J. H. Nielsen, O. Hansen, I. Chorkendorff, Novel micro-reactor flow cell for investigation of model catalysts using in situ grazing-incidence X-ray scattering, *J. Synch. Rad.* **2016**, *23*, 455–463.

[186] R. M. Tiggelaar, J. G. E. Gardeniers, A. van den Berg, Silicon–based microreactors as research tools in chemistry, *Chim. Oggi Chem. Today* **2006**, *24*, 52–54.

[187] F. Priolo, T. Gregorkiewicz, M. Galli, T. F. Krauss, Silicon nanostructures for photonics and photovoltaics, *Nature* **2014**, *9*, 19–32.

[188] M. Soltani, J. Lin, R. A. Forties, J. T. Inman, S. N. Saraf, R. M. Fulbright, M. Lipson, M. D. Wang, Nanophotonic trapping for precise manipulation of biomolecular arrays, *Nat. Nanotechn.* **2014**, *9*, 448–452.

[189] R. M. Tiggelaar, P. W. H. Loeters, P. van Male, R. E. Oosterbroek, J. G. E. Gardeniers, M. de Croon, J. C. Schouten, M. C. Elwenspoek, A. van den Berg, Thermal and mechanical analysis of a microreactor for high temperature catalytic gas phase reactions, *Sensors and Actuators A - Physical* **2004**, *112*, 267–277.

[190] M.-H. Kiang, O. Solgaard, R. S. Muller, K. Y. Lau, Silicon-micromachined micromirrors with integrated high-precision actuators for external-cavity semiconductor lasers, *IEEE Photon. Technol. Lett.* **1996**, *8*, 95–97.

[191] E. Cao, S. Firth, P. F. McMillan, A. Gavriilidis, Application of microfabricated reactors for operando Raman studies of catalytic oxidation of methanol to formaldehyde on silver, *Catal. Today* **2007**, *126*, 119–126.

[192] E. Cao, M. Sankar, S. Firth, K. F. Lam, D. Bethell, D. K. Knight, G. J. Hutchings, P. F. McMillan, A. Gavriilidis, Reaction and Raman spectroscopic studies of alcohol oxidation on gold-palladium catalysts in microstructured reactors, *Chem. Eng. J.* **2011**, *167*, 734–743.

[193] S. H. Ahn, I. Choi, O. J. Kwon, J. J. Kim, Hydrogen production through the fuel processing of liquefied natural gas with silicon-based micro-reactors, *Chem. Eng. J.* **2014**, *247*, 9–15.

[194] M. Roumanie, C. Pijolat, V. Meille, C. De Bellefon, P. Pouteau, C. Delattre, Deposition of Pt-catalyst in a micro-channel of a silicon reactor: Application to gas micro-TAS working at high temperature, *Sens. Actuator B Chem.* **2006**, *118*, 297–304.

[195] S.-M. Hwang, O. J. Kwon, S. H. Ahn, J. J. Kim, Silicon-based micro-reactor for preferential CO oxidation, *Chem. Eng. J.* **2009**, *146*, 105–111.

[196] G. H. Hofmann, Dissertation, Karlsruhe Institute of Technology, **2015**.

[197] S. Baier, A. Rochet, G. Hofmann, M. Kraut, J.-D. Grunwaldt, Lithographically fabricated silicon microreactor for in situ characterization of heterogeneous catalysts - Enabling correlative characterization techniques, *Rev. Sci. Instrum.* **2015**, *86*, 065101.

[198] D. E. Doronkin, S. Baier, T. Sheppard, F. Benzi, J.-D. Grunwaldt, Lithographically fabricated silicon microreactor for operando QEXAFS studies in exhaust gas catalysis during simulation of a standard driving cycle, *J. Phys.: Conf. Ser.* **2016**, *712*, 012030.

[199] G. Wallis, D. I. Pomerantz, Field assisted glass metal sealing, *J. Appl. Phys.* **1969**, *40*, 3946–3949.

[200] A. Plößl, G. Kräuter, Wafer direct bonding: tailoring adhesion between brittle materials, *Mat. Sci. Eng. R.* **1999**, *25*, 1–88.

[201] http://psec.uchicago.edu/glass/borofloat_33_e.pdf for the product data sheet (03.02.2015).

[202] J. S. Evans, Negative thermal expansion materials, *Dalton Trans.* **1999**, *19*, 3317–3326.

[203] S. Conrad, Diplomarbeit, Karlsruhe Insitutute of Technology, **2011**.

[204] K. Robinson, S. Ye, Y. Yap, S. T. Kolaczkowski, Application of a methodology to assess the performance of a full-scale diesel oxidation catalyst during cold and hot start NEDC drive cycles, *Chem. Eng. Res. Des.* **2013**, *91*, 1292–1306.

[205] A. P. N. V. Hammersley, FIT2D: An Introduction and Overview, ESRF Internal Report, **1997**.

[206] S. Baier, A. Rochet, G. Hofmann, J.-D. Kraut, M.and Grunwaldt, Lithographically fabricated silicon microreactor for in situ characterization of heterogeneous catalysts - Enabling correlative characterization techniques, supplementary material http://dx.doi.org/10.1063/1421775, **2015**.

[207] B. Ravel, M. Newville, Athena, Artemis, Hephaestus: data analysis for X-ray absorption spectroscopy using Ifeffit, *J. Synch. Rad.* **2005**, *12*, 537–541.

[208] A. Rack, T. Weitkamp, S. B. Trabelsi, P. Modregger, A. Cecilia, T. d. S. Rolo, T. Rack, D. Haas, R. Simon, R. Heldele, M. Schulz, B. Mayzel, A. N. Danilewsky, T. Waterstradt, W. Diete, H. Riesemeier, B. R. Mueller, T. Baumbach, The micro-imaging station of the TopoTomo beamline at the ANKA synchrotron light source, *Nucl. Instrum. Methods Phys. Res. B* **2009**, *267*, 1978–1988.

[209] O. Müller, J. Stötzel, D. Lützenkirchen-Hecht, R. Frahm, Gridded ionization chambers for time resolved X-ray absorption spectroscopy **2013**, *425*, 092010.

[210] H. Swanson, E. Tatge, Standard X-ray diffraction powder patterns I, *National Bureau of Standards (U.S.)* **1953**, 1–95.

[211] B. Shelimov, J. F. Lambert, M. Che, B. Didillon, Initial steps of the alumina-supported platinum catalyst preparation: a molecular study by Pt-195 NMR, UV-visible, EXAFS, and Raman spectroscopy, *J. Catal.* **1999**, *185*, 462–478.

[212] J. R. McBride, G. W. Graham, C. R. Peters, W. H. Weber, Growth and characterization of reactively sputtered thin-film platinum oxides, *J. Appl. Phys.* **1991**, *69*, 1596–1604.

[213] G. W. Graham, W. H. Weber, J. R. McBride, C. R. Peters, Raman investigation of simple and complexe oxides of platinum, *J. Raman Spectrosc.* **1991**, *22*, 1–9.

[214] K. Otto, W. H. Weber, G. W. Graham, J. Z. Shyu, Identification of dispersed platinum on γ-Alumina by laser-Raman spectroscopy, *Appl. Surf. Sci.* **1989**, *37*, 250–257.

[215] J.-D. Grunwaldt, M. Beier, B. Kimmerle, A. Baiker, M. Nachtegaal, B. Griesebock, D. Lutzenkirchen-Hecht, J. Stötzel, R. Frahm, Structural changes of noble metal catalysts during ignition and extinction of the partial oxidation of methane studied by advanced QEXAFS techniques, *Phys. Chem. Chem. Phys.* **2009**, *11*, 8779–8789.

[216] B. Kimmerle, A. Baiker, J.-D. Grunwaldt, Oscillatory behaviour of catalytic properties, structure and temperature during the catalytic partial oxidation of methane on Pd/Al$_2$O$_3$, *Phys. Chem. Chem. Phys.* **2010**, *12*, 2288–2291.

[217] B. C. Enger, R. Lodeng, A. Holmen, A review of catalytic partial oxidation of methane to synthesis gas with emphasis on reaction mechanisms over transition metal catalysts, *Appl.Catal., A.* **2008**, *346*, 1–27.

[218] S. Siegel, H. R. Hoekstra, B. S. Tani, The crystal structure of β-platinum dioxide, *J. Inorg. Nucl. Chem.* **1969**, *31*, 3803–3807.

[219] P. D. Maycock, Thermal conductivity of silicon, germanium, III-V compound and III-V alloys, *Solid-State Electron.* **1967**, *10*, 161–168.

[220] R. W. Powell, C. Y. Ho, P. E. Liley, Thermal conductivity of selected materials, National Standard Reference Data Series – National Bureau of Standards – 8, **1966**.

[221] W. Weisweiler, R. Wunsch, Simulation of a driving cycle in laboratory: an approach for testing catalysts suitable for automotive exhaust NO$_x$ abatement under lean conditions, *Chem. Eng. Process.* **1998**, *37*, 229 – 232.

[222] S. Brandenberger, O. Kröcher, A. Tissler, R. Althoff, The state of the art in selective catalytic reduction of NO$_x$ by ammonia using metal-exchanged zeolite catalysts, *Catal. Rev.* **2008**, *50*, 492–531.

[223] T. Günter, H. W. Carvalho, D. E. Doronkin, T. Sheppard, P. Glatzel, A. J. Atkins, J. Rudolph, C. R. Jacob, M. Casapu, J.-D. Grunwaldt, Structural snapshots of the SCR reaction mechanism on Cu-SSZ-13, *Chem. Commun.* **2015**, *51*, 9227–9230.

[224] G. Bagnasco, Improving the selectivity of NH$_3$ TPD measurements, *J. Catal.* **1996**, *159*, 249–252.

[225] http://www.desy.de/forschung/anlagen__projekte/petra_iv/index_ger.html (31.05.2016).

[226] https://www.maxlab.lu.se/node/1055 (31.05.2016).

[227] http://www.esrf.eu/files/live/sites/www/files/events/conferences/XXII ESLS /Ehrlichman-ESLS_XXII-1.pdf (31.05.2016).

[228] http://www.lnls.cnpem.br/sirius/ (31.05.2016).

[229] S. Baier, C. D. Damsgaard, M. Scholz, F. Benzi, A. Rochet, R. Hoppe, T. Scherer, J. Shi, A. Wittstock, B. Weinhausen, J. B. Wagner, C. G. Schroer, J.-D. Grunwaldt, In situ ptychography of heterogeneous catalysts using hard X-rays: high resolution imaging at ambient pressure and elevated temperature, *Microsc. Microanal.* **2016**, *22*, 178–188.

[230] L. F. Allard, A. Borisevich, W. Deng, R. Si, M. Flytzani-Stephanopoulos, S. H. Overbury, Evolution of gold structure during thermal treatment of Au/FeO$_x$ catalysts revealed by aberration-corrected electron microscopy, *J. Electron Microsc.* **2009**, *58*, 199–212.

[231] S. B. Simonsen, K. Agersted, K. V. Hansen, T. Jacobsen, J. B. Wagner, T. W. Hansen, L. T. Kuhn, Environmental TEM study of the dynamic nanoscaled morphology of NiO/YSZ during reduction, *Appl. Catal., A.* **2015**, *489*, 147–154.

[232] http://www.protochips.com/products/fusion (31.05.12016).

[233] A. Wittstock, M. Bäumer, Catalysis by unsupported skeletal gold catalysts, *Acc. Chem. Res.* **2014**, *47*, 731–739.

[234] V. Zielasek, B. Jürgens, C. Schulz, J. Biener, M. M. Biener, A. V. Hamza, M. Bäumer, Gold catalysts: Nanoporous gold foams, *Angew. Chem. Int. Ed.* **2006**, *45*, 8241–8244.

[235] T. Fujita, P. Guan, K. McKenna, X. Lang, A. Hirata, L. Zhang, T. Tokunaga, S. Arai, Y. Yamamoto, N. Tanaka, Y. Ishikawa, N. Asao, Y. Yamamoto, J. Erlebacher, M. Chen, Atomic origins of the high catalytic activity of nanoporous gold, *Nat. Mater.* **2012**, *11*, 775–780.

[236] J. A. Rodriguez, S. Ma, P. Liu, J. Hrbek, J. Evans, M. Perez, Activity of CeO$_x$ and TiO$_x$ nanoparticles grown on Au(111) in the water-gas shift reaction, *Science* **2007**, *318*, 1757–1760.

[237] A. Wittstock, V. Zielasek, J. Biener, C. M. Friend, M. Bäumer, Nanoporous gold catalysts for selective gas–phase oxidative coupling of methanol at low temperature, *Science* **2010**, *327*, 319–322.

[238] Y. Iizuka, A. Kawamoto, K. Akita, M. Date, S. Tsubota, M. Okumura, M. Haruta, Effect of impurity and pretreatment conditions on the catalytic activity of Au powder for CO oxidation, *Catal. Lett.* **2004**, *97*, 203–208.

[239] L. Y. Chen, X. Y. Lang, T. Fujita, M. W. Chen, Nanoporous gold for enzyme-free electrochemical glucose sensors, *Scr. Mater.* **2011**, *65*, 17–20.

[240] D. Hung, Z. Liu, Y. W. Hao, P. C. Searson, Fabrication of 3-D ordered nanoporous gold for chemical sensors, *Abstr. Pap. Am. Chem. Soc.* **2005**, *230*, U1113–U1114.

[241] C. A. R. Chapman, H. Chen, M. Stamou, J. Biener, M. M. Biener, P. J. Lein, E. Seker, Nanoporous gold as a neural interface coating: effects of topography, surface chemistry, and feature size, *ACS Appl. Mater. Interfaces* **2015**, *7*, 7093–7100.

[242] L. V. Moskaleva, S. Röhe, A. Wittstock, V. Zielasek, T. Klüner, K. M. Neyman, M. Bäumer, Silver residues as a possible key to a remarkable oxidative catalytic activity of nanoporous gold, *Phys. Chem. Chem. Phys.* **2011**, *13*, 4529–4539.

[243] A. Wittstock, B. Neumann, A. Schäfer, K. Dumbuya, C. Kübel, M. M. Biener, V. Zielasek, H.-P. Steinrück, J. M. Gottfried, J. Biener, A. Hamza, M. Bäumer, Nanoporous Au: an unsupported pure gold catalyst?, *J. Phys. Chem. C* **2009**, *113*, 5593–5600.

[244] A. J. Forty, P. Durkin, A micromorphological study of the dissolution of silver-gold alloys in nitric acid, *Philos. Mag. A* **1980**, *42*, 295–318.

[245] A. Y. Chen, S. S. Shi, F. Liu, Y. Wang, X. Li, J. F. Gu, X. F. Xie, Effect of annealing atmosphere on the thermal coarsening of nanoporous gold films, *Appl. Surf. Sci.* **2015**, *355*, 133–138.

[246] L. Schade, S. Franzka, M. Mathieu, M. M. Biener, J. Biener, N. Hartmann, Photothermal laser microsintering of nanoporous gold, *Langmuir* **2014**, *30*, 7190–7197.

[247] J. Wang, R. Xia, J. Zhu, Y. Ding, X. Zhang, Y. Chen, Effect of thermal coarsening on the thermal conductivity of nanoporous gold, *J. Mater. Sci.* **2012**, *47*, 5013–5018.

[248] C. A. R. Chapman, L. Wang, J. Biener, E. Seker, M. M. Biener, M. J. Matthews, Engineering on-chip nanoporous gold material libraries via precision photothermal treatment, *Nanoscale* **2015**.

[249] Y.-C. K. Chen-Wiegart, S. Wang, Y. S. Chu, W. Liu, I. McNulty, P. W. Voorhees, D. C. Dunand, Structural evolution of nanoporous gold during thermal coarsening, *Acta Mater.* **2012**, *60*, 4972–4981.

[250] Z. Li, S. Zhou, H. Li, W. Si, Y. Ding, Determination of ligament size distribution of nanoporous gold by scanning electron microscopy and image analysis, *J. Nanosci. Nanotechnol.* **2009**, *9*, 1651–1654.

[251] J. Biener, A. Wittstock, M. M. Biener, T. Nowitzki, A. V. Hamza, M. Bäumer, Effect of surface chemistry on the stability of gold nanostructures, *Langmuir* **2010**, *26*, 13736–13740.

[252] S. Kuwano-Nakatani, T. Fujita, K. Uchisawa, D. Umetsu, Y. Kase, Y. Kowata, K. Chiba, T. Tokunaga, S. Arai, Y. Yamamoto, N. Tanaka, M. Chen, Environment-sensitive thermal coarsening of nanoporous gold, *Mater. Trans.* **2015**, *56*, 468–472.

[253] Y. Sun, S. A. Burger, T. J. Balk, Controlled ligament coarsening in nanoporous gold by annealing in vacuum versus nitrogen, *Philos. Mag.* **2014**, *94*, 1001–1011.

[254] Y.-C. K. Chen-Wiegart, J. S. Cronin, Q. Yuan, K. J. Yakal-Kremski, S. A. Barnett, J. Wang, 3D Non-destructive morphological analysis of a solid oxide fuel cell anode using full-field X-ray nano-tomography, *J. Power Sources* **2012**, *218*, 348–351.

[255] E. Seker, J. T. Gaskins, H. Bart-Smith, J. Zhu, M. L. Reed, G. Zangari, R. Kelly, M. R. Begley, The effects of post-fabrication annealing on the mechanical properties of free-standing nanoporous gold structures, *Acta Mater.* **2007**, *55*, 4593–4602.

[256] J. Erlebacher, Mechanism of coarsening and bubble formation in high-genus nanoporous metals, *Phys. Rev. Lett.* **2011**, *106*, 225504.

[257] M. Hakamada, M. Mabuchi, Thermal coarsening of nanoporous gold: Melting or recrystallization, *J. Mater. Res.* **2009**, *24*, 301–304.

[258] K. Kolluri, M. J. Demkowicz, Coarsening by network restructuring in model nanoporous gold, *Acta Mater.* **2011**, *59*, 7645–7653.

[259] M. P. Klein, B. W. Jacobs, M. D. Ong, S. J. Fares, D. B. Robinson, V. Stavila, G. J. Wagner, I. Arslan, Three-dimensional pore evolution of nanoporous metal particles for energy storage, *J. Am. Chem. Soc.* **2011**, *133*, 9144–9147.

[260] J. Shi, A. Schaefer, A. Wichmann, M. M. Murshed, T. M. Gesing, A. Wittstock, M. Bäumer, Nanoporous gold-supported ceria for the watergas shift reaction: UHV inspired design for applied catalysis, *J. Phys. Chem. C* **2014**, *118*, 29270–29277.

[261] L. F. Allard, M. Flytzani-Stephanopoulos, S. H. Overbury, A novel heating technology for ultra-high resolution imaging in electron microscopes, *Micros. Today* **2009**, *17*, 50–55.

[262] S. Baier, A. Wittstock, C. D. Damsgaard, A. Diaz, J. Reinhardt, F. Benzi, J. Shi, T. Scherer, D. Wang, C. Kübel, C. G. Schroer, J.-D. Grunwaldt, Influence of gas atmosphere and ceria layers on the stability of nanoporous gold studied by environmental electron microscopy and *in situ* ptychography, *RSC Adv.* **2016**, *DOI: C6RA12853J*.

[263] A. Schropp, C. G. Schroer, Dose requirements for resolving a given feature in an object by coherent x-ray diffraction imaging, *New J. Phys.* **2010**, *12*, 035016.

[264] M. van Heel, M. Schatz, Fourier shell correlation threshold criteria, *J. Struct. Biol.* **2005**, *151*, 250–262.

[265] S. Gorelick, J. Vila-Comamala, V. A. Guzenko, R. Barrett, M. Salomé, C. David, High-efficiency Fresnel zone plates for hard X-rays by 100 keV e-beam lithography and electroplating, *J. Synch. Rad.* **2011**, *18*, 442–446.

[266] X. Huang, H. Yan, R. Harder, Y. Hwu, I. K. Robinson, Y. S. Chu, Optimization of overlap uniformness for ptychography, *Opt. Express* **2014**, *22*, 12634–12644.

[267] B. Henrich, A. Bergamaschi, C. Broennimann, R. Dinapoli, E. Eikenberry, I. Johnson, M. Kobas, P. Kraft, A. Mozzanica, B. Schmitt, PILATUS: A single photon counting pixel detector for X-ray applications, *Nucl. Instrum. Methods Phys. Res., Sect. A* **2009**, *607*, 247–249.

[268] M. R. Howells, T. Beetz, H. N. Chapman, C. Cui, J. Holton, C. Jacobsen, J. Kirz, E. Lima, S. Marchesini, H. Miao, D. A. Shapiro, J. C. H. Spence, D. Starodube, An assessment of the resolution limitation due to radiation-damage in x-ray diffraction microscopy, *J. Electron Spectrosc. Relat. Phenom.* **2009**, *170*, 4–12.

[269] A. M. Hodge, J. R. Hayes, J. A. Caro, J. Biener, A. V. Hamza, Characterization and mechanical behavior of nanoporous gold, *Adv. Eng. Mater.* **2006**, *8*, 853–857.

[270] P. Thibault, M. Guizar-Sicairos, Maximum–likelihood refinement for coherent diffractive imaging, *New J. Phys.* **2012**, *14*, 063004.

[271] M. Guizar-Sicairos, I. Johnson, A. Diaz, M. Holler, P. Karvinen, H.-C. Stadler, R. Dinapoli, O. Bunk, A. Menzel, High-throughput ptychography using Eiger: scanning X-ray nano-imaging of extended regions, *Opt. Express* **2014**, *22*, 14859–14870.

[272] M. Guizar-Sicairos, A. Diaz, M. Holler, M. S. Lucas, A. Menzel, R. A. Wepf, O. Bunk, Phase tomography from X-ray coherent diffractive imaging projections, *Opt. Express* **2011**, *19*, 21345–21357.

[273] T. S. Dorofeeva, E. Seker, Electrically tunable pore morphology in nanoporous gold thin films, *Nano Res.* **2015**, *8*, 2188–2198.

[274] A. Wichmann, A. Wittstock, K. Frank, M. M. Biener, B. Neumann, L. Madler, J. Biener, A. Rosenauer, M. Bäumer, Maximizing activity and stability by turning gold catalysis upside down: oxide particles on nanoporous gold, *ChemCatChem* **2013**, *5*, 2037–2043.

[275] R. N. Viswanath, V. A. Chirayath, R. Rajaraman, G. Amarendra, C. S. Sundar, Ligament coarsening in nanoporous gold: insights from positron annihilation study, *Appl. Phys. Lett.* **2013**, *102*, 253101.

[276] D. R. Peale, B. H. Cooper, Adsorbate-promoted mass-flow on the gold (111) surface obserced by scanning tunneling microscopy, *J. Vac. Sci. Technol. A* **1992**, *10*, 2210–2215.

[277] F. Kertis, J. Snyder, L. Govada, S. Khurshid, N. Chayen, J. Erlebacher, Structure/processing relationships in the fabrication of nanoporous gold, *Jom* **2010**, *62*, 50–56.

[278] D. L. Olson, J. M. Blakely, H. R. Patil, Influence of contaminants on surface self-diffusion coefficient of gold, *Scr. Metall.* **1972**, *6*, 229–240.

[279] R. E. Honig, D. A. Kramer, Vapor pressure data for the solid and liquid elements, *RCA Rev.* **1969**, *30*, 285–305.

[280] G. Schmid, B. Corain, Nanoparticulated gold: Syntheses, structures, electronics, and reactivities, *Eur. J. Inorg. Chem.* **2003**, *2003*, 3081–3098.

[281] R. Li, K. Sieradzki, Ductile-brittle transition in random porous Au, *Phys. Rev. Lett.* **1992**, *68*, 1168–1171.

[282] J. Biener, A. M. Hodge, A. V. Hamza, Microscopic failure behavior of nanoporous gold, *Appl. Phys. Lett.* **2005**, *87*, 121908.

[283] B. Kahng, G. G. Batrouni, S. Redner, L. de Arcangelis, H. J. Herrmann, Electrical breakdown in a fuse network with random, continuously distributed breaking strengths, *Phys. Rev. B* **1988**, *37*, 7625–7637.

[284] M. Sankar, N. Dimitratos, P. J. Midziak, P. P. Wells, C. J. Kiely, G. J. Huthings, Designing bimetallic catalysts for a green and sustainable future, *Chem. Soc. Rev.* **2012**, *41*, 8099–8139.

[285] C.-J. Zhong, M. M. Maye, Core-shell assembled nanoparticles as catalysts, *Adv. Mater.* **2001**, *13*, 1507–1511.

[286] H. Lee, S. Kim, D. W. Lee, K. Y. Lee, Direct synthesis of hydrogen peroxide from hydrogen and oxygen over a Pd core-silica shell Catalyst, *Catal. Commun.* **2011**, *12*, 968–971.

[287] R. Phienluphon, K. Pinkaew, G. Yang, J. Li, Q. Wei, Y. Yoneyama, T. Vitidsant, N. Tsubaki, Designing core (Cu/ZnO/Al$_2$O$_3$)–shell (SAPO-11) zeolite capsule catalyst with a facile physical way for dimethyl ether direct synthesis from syngas, *Chem. Eng. J.* **2015**, *270*, 605–611.

[288] K. Pinkaew, G. Yang, T. Vitidsant, Y. Jin, C. Zeng, Y. Yoneyama, N. Tsubaki, A new core–shell-like capsule catalyst with SAPO-46 zeolite shell encapsulated Cr/ZnO for the controlled tandem synthesis of dimethyl ether from syngas, *Fuel* **2013**, *111*, 727–732.

[289] Y. Wang, W. Wang, Y. Chen, J. Ma, R. Li, Synthesis of dimethyl ether from syngas over core–shell structure catalyst CuO–ZnO–Al$_2$O$_3$@SiO$_2$–Al$_2$O$_3$, *Chem. Eng. J.* **2014**, *250*, 248–256.

[290] J. Abu-Dahrieh, D. Rooney, A. Goguet, Y. Saih, Activity and deactivation studies for direct dimethyl ether synthesis using CuO–ZnO–Al$_2$O$_3$ with NH$_4$ZSM-5, HZSM-5 or γ-Al$_2$O$_3$, *Chem. Eng. J.* **2012**, *203*, 201–211.

[291] R. Ahmad, D. Schrempp, S. Behrens, J. Sauer, M. Döring, U. Arnold, Zeolite-based bifuctional catalysts for the single step synthesis of dimethyl ether from CO-rich synthesis gas, *Fuel Process. Technol.* **2014**, *121*, 38–46.

[292] S. Allahyari, M. Haghighi, A. Ebadi, H. Qavam Saeedi, Direct conversion of syngas to DME over CuO–ZnO–Al$_2$O$_3$/HZSM-5 nanocatalyst synthesized via ultrasound-assisted co-precipitation method: New insights into the role of gas injection, *Int. J. Energy Res.* **2014**, *38*, 2030–2043.

[293] J. Li, X. Pan, X. Bao, Direct conversion of syngas into hydrocarbons over a core–shell Cr-Zn@SiO$_2$@SAPO-34 catalyst, *Chinese J. Catal.* **2015**, *36*, 1131–1135.

[294] Q. Li, C. Xin, P. Lian, The synthesis and application of CuO-ZnO/HZSM-5 catalyst with core-shell structure, *Pet. Sci. Technol.* **2012**, *30*, 2187–2195.

[295] N. Dahmen, E. Henrich, E. Dinjus, F. Weirich, The bioliq® bioslurry gasification process for the production of biosynfuels, organic chemicals, and energy, *Energy Sustain. Soc.* **2012**, *2*, 1–44.

[296] Q. Ge, Y. Huang, F. Qiu, S. Li, Bifunctional catalysts for conversion of synthesis gas to dimethyl ether, *Appl. Catal., A.* **1998**, *167*, 23–30.

[297] P. S. Prasad, J. W. Bae, S.-H. Kang, Y.-J. Lee, K.-W. Jun, Single-step synthesis of DME from syngas on Cu–ZnO–Al$_2$O$_3$/zeolite bifunctional catalysts: the superiority of ferrierite over the other zeolites, *Fuel Process. Technol.* **2008**, *89*, 1281–1286.

[298] J. C. Andrews, B. M. Weckhuysen, Hard X-ray spectroscopic nano-imaging of hierarchical functional materials at work, *ChemPhysChem* **2013**, *14*, 3655–3666.

[299] F. Meirer, J. Cabana, Y. Liu, A. Mehta, J. Andrews, P. Pianetta, Three-dimensional imaging of chemical phase transformations on the nanoscale with full-field transmission X-ray Microscopy, *J. Synch. Rad.* **2011**, *18*, 773–781.

[300] H. Markötter, I. Manke, P. Krüger, T. Arlt, J. Huasmann, M. Klages, C. Riesemeier, H Hartnig, J. Scholta, J. Banhart, Investigation of 3D water transport paths in gas diffusion layers by combined in-situ synchrotron X-ray radiography and tomography, *Electrochem. Commun.* **2011**, *13*, 1001–1004.

[301] Y. Li, D. Zakharov, S. Zhao, R. Tappero, U. Jung, A. Elsen, P. Baumann, R. G. Nuzzo, E. A. Stach, A. I. Frenkel, Complex structural dynamics of nanocatalysts revealed in operando conditions by correlated imaging and spectroscopy probes, *Nat. Commun.* **2015**, *6*, 7583.

[302] J. W. Andreasen, F. B. Rasmussen, S. Helveg, A. Molenbroek, K. Stahl, M. M. Nielsen, R. Feidenhans'l, Activation of a Cu/ZnO catalyst for methanol synthesis, *J. Appl. Crystallogr.* **2006**, *39*, 209–221.

[303] M. Holler, A. Diaz, M. Guizar-Sicairos, P. Karvinen, E. Farm, E. Harkonen, M. Ritala, A. Menzel, J. Raabe, O. Bunk, X-ray ptychographic computed tomography at 16 nm isotropic 3D resolution, *Sci. Rep.* **2014**, *4*, 3857.

[304] J.-D. Grunwaldt, A. I. Frenkel, Synchrotron studies of catalysts: from XAFS to QEXAFS and beyond, *Synchrotron Radiat. News* **2009**, *22*, 2–4.

[305] H. C. Lee, Y. Potapova, D. Lee, A core-shell structured, metal-ceramic composite-supported Ru catalyst for methane steam reforming, *J. Power Sources* **2012**, *216*, 256–260.

[306] X. Li, L. Yao, Y. Song, S. Liu, J. Zhao, W. Ji, C. T. Au, Core-shell structured microcapsular-like Ru@SiO$_2$ reactor for efficient generation of Co$_x$-free hydrogen through ammonia decomposition, *Chem. Commun.* **2010**, *46*, 5298–5300.

[307] http://www.denssolutions.com/producst/heating (31.05.2016).

[308] M. A. van Huis, N. P. Young, G. Pandraud, J. F. Creemer, D. Vanmaekelbergh, A. I. Kirkland, H. W. Zandbergen, Atomic imaging of phase transitions and morphology transformations in nanocrystals, *Adv. Mater.* **2009**, *21*, 4992–4995.

[309] M. Holler, J. Raabe, A. Diaz, M. Guizar-Sicairos, C. Quitmann, A. Menzel, O. Bunk, An instrument for 3D X-ray nano-imaging, *Rev. Sci. Instrum.* **2012**, *83*, 073703.

[310] A. M. Maiden, M. J. Humphry, J. M. Rodenburg, Ptychographic transmission microscopy in three dimensions using a multi-slice approach, *J. Opt. Soc. Am. A. Opt. Image Sci. Vis.* **2012**, *29*, 1606–1614.

Appendix

List of Abbreviations

Abbreviation	Name
AES	Auger Electron Spectroscopy
ANKA	Angströmquelle Karlsruhe (synchrotron in Karlsruhe)
BF	Bright Field
BMBF	Bundesministerium für Bildung und Forschung (Federal Ministry of Education and Research)
BSE	Back Scattered Electrons
CDI	Coherent Diffractive Imaging
CEN	Center for Electron Nanoscopy (at DTU)
CPO	Catalytic Partial Oxidation
CT	Computed Tomography
DESY	Deutsches Elektronen Synchrotron (synchrotron radiation facility in Hamburg operating PETRA III, FLASH etc.)
DF	Dark Field
DME	Dimethyl Ether
DOC	Diesel Oxidation Catalyst
DTU	Technical University of Denmark
DRIE	Deep Reactive Ion Etching
DRIFTS	Diffuse Reflectance Infrared Fourier Transform Spectroscopy
EDX	Energy Dispersive X-ray Spectroscopy
EELS	Electron Energy Loss Spectroscopy
EM	Electron Microscopy
ESRF	European Synchrotron Radiation Facility (synchrotron radiation facility in Grenoble)
EXAFS	Extended X-ray Absorption Fine Structure
FIB	Focused Ion Beam
FT	Fourier Transform
FRC	Fourier Ring Correlation
FWHM	Full Width Half Maximum
GC	Gas Chromatography
GHSV	Gas Hour Space Velocity
HAADF	High-Angle Annular Dark-Field
ID	Inner Diameter
IR	Infrared
INT	Institute for Nanotechnology
KIT	Karlsruhe Institute of Technology
KNMF	Karlsruhe Nano Micro Facility
LCF	Linear Combination Fitting

Abbreviation	Name
MS	Mass Spectrometry
NEDC	New European Driving Cycle
OD	Outer Diameter
PETRA III	Synchrotron radiation source in Hamburg operated by DESY
PSI	Paul-Scherrer-Institute, Villigen, Switzerland
QEXAFS	Quick Extended X-ray Absorption Fine Structure
RT	Room Temperature (25 °C)
SAXS	Small Angle X-ray Scattering
SCR	Selective Catalytic Reduction
SE	Secondary Electrons
SEM	Scanning Electron Microscopy
SLS	Swiss Light Source (synchrotron radiation source in Villigen, operated by PSI)
STEM	Scanning Transmission Electron Microscopy
TEM	Transmission Electron Microscopy
UV-vis	Ultraviolet and visible light
WAXS	Wide Angle X-ray Scattering
wt.%	Weight percent
XANES	X-ray Absorption Near-Edge Structure
XAS	X-ray Absorption Spectroscopy
XRD	X-Ray Diffraction
XRF	X-Ray Fluorescence

List of Symbols

Notation	Name
Å	Angström
cm	Centimeter
Δ	Difference
E	Energy
ϵ	Emissivity
M	Molar mass
m	Meter
m	Mass
mm	Millimeter
μm	Micrometer
μl	Microliter
nm	Nanometer
k	Wave vector
q	Momentrum transfer
T_{melt}	Melting Temperature
T_{boil}	Boiling Temperature
χ	EXAFS function
z	Charge

Curriculum Vitae

Personal Information

Name   Sina, Maria Baier

Education

12.2012 – 07.2016   **PhD Student**

Karlsruhe Institute of Technology (KIT), Institute for Chemical Technology and Polymer Chemistry, supervisor: Prof. Dr. Jan-Dierk Grunwaldt

09.2015 – 10.2015   **Guest Scientist**

Technical University of Denmark (DTU), Center for Electron Nanoscopy, supervisor: Ass. Prof. Dr. Christian D. Damsgaard

04.2010 – 08.2012   **M. Sc. Chemistry**

Philipps-Universität Marburg

01.2012 – 08.2012   **Master Thesis**

Goethe-Universität Frankfurt, supervisor: Prof. Dr. Gerhard Brey

05.2012 – 08.2012   **Guest Master Student**

Universitet Uppsala, Sweden, supervisor: Prof. Dr. Valentin Troll

04.2007 – 03.2010   **B. Sc. Chemistry**

Philipps-Universität Marburg

08.1997 – 07.2007   **A levels**

Marienschule Fulda, secondary school

Experience

12.2012 – present   **Research Assistant**

Karlsruhe Institute of Technology (KIT), Institute for Chemical Technology and Polymer Chemistry

List of Publications

Publications related to this thesis

2016   **Stability of a bifunctional Cu-based core@zeolite catalyst under redox conditions studied by ETEM and *in situ* ptychography**, S. Baier, C. D. Damsgaard, M. Klumpp, Z. Balogh, J. Reinhardt, T. Kasama, T. Sheppard, F. Benzi, J. B. Wagner, W. Schwieger, C. G. Schroer, J.-D. Grunwaldt, submitted for publication.

Results from this publication are presented in chapter 12.

2016   **Influence of gas atmosphere and ceria layers on the stability of nanoporous gold studied by environmental electron microscopy and *in situ* ptychography**, S. Baier, A. Wittstock, C. D. Damsgaard, A. Diaz, J. Reinhardt, F. Benzi, J. Shi, T. Scherer, D. Wang, C. Kübel, C. G. Schroer, J.-D. Grunwaldt, *RSC Adv.*, in press, DOI: 10.1039/C6RA12853J.

Results from this publication are presented in chapter 11; reproduced with permission.

2016   **Lithographically fabricated silicon microreactor for operando QEXAFS studies in exhaust gas catalysis during simulation of a standard driving cycle**, D. E. Doronkin, S. Baier, T. Sheppard, F. Benzi, *J. Phys.: Conf. Ser.*, Vol. 712, pp. 012030 (2016).

Results from this publication are presented in chapter 7.1; reproduced with permission.

2016   ***In situ* ptychography of heterogeneous catalysts enabling high resolution imaging at ambient pressure and temperature**, S. Baier, C. D. Damsgaard, M. Scholz, F. Benzi, A. Rochet, R. Hoppe, T. Scherer, J. Shi, A. Wittstock, B. Weinhausen, J. B. Wagner, C. S. Schroer, J.-D. Grunwaldt, *Microsc. Microanal.*, Vol 22, pp. 178–188 (2016).

Results from this publication are presented in chapter 11; reproduced with permission.

2015   **Lithographic silicon microreactor for *in situ* characterization in heterogeneous catalysis – enabling correlative characterization techniques,** S. Baier, A. Rochet, G. Hofmann, M. Kraut, J.-D. Grunwaldt, *Rev. Sci. Instr.*, Vol. 86, pp. 065101 (2015).

Results from this publication are presented in chapter 4.1, 5 and 6.1; reproduced with permission of AIP Publishing.

Further publications

2016   **A microfluidic device for the investigation of rapid gold nanoparticle formation in continuous turbulent flow**, G. Hofmann, G. Tofighi, G. Rinke, S. Baier, A. Ewinger, A. Urban, A. Wenka, S. Heideker, A. Jahn, R. Dittmeyer, J.-D. Grunwaldt, *J. Phys.: Conf. Ser.*, Vol. 712, pp. 012072 (2016).

2015   **Electrochemically synthesized Pt/Al$_2$O$_3$ oxidation catalysts**, D. E. Doronkin, A. B. Kuriganova, I. N. Leontyev, S. Baier, H. Lichtenberg, N. V. Smirnova, J.-D. Grunwaldt, *Catal. Lett.*, Vol. 146, pp. 452–463 (2015).

2015   **Continuous catalytic hydrodeoxygenation of guaiacol over Pt/SiO$_2$ and Pt/H-MFI90**, M. Hellinger, S. Baier, P. M. Mortensen, W. Kleist, A. D. Jensen, J.-D. Grunwaldt, *Catalysts*, Vol. 5, pp. 1152–1166 (2015).

2015   **Solvent influence on the hydrodeoxygenation of guaiacol over Pt/SiO$_2$ and Pt/H-MFI90 catalysts**, M. Hellinger, H. W. P. Carvalho, S. Baier, L. Gharnati, J.-D. Grunwaldt, *Chem. Ing. Tech.*, Vol. 87, pp. 1771–1780 (2015).

2015   **Catalytic hydrodeoxygenation of guaiacol over platinum supported on metal oxides and zeolites**, M. Hellinger, H. W. P. Carvalho, S. Baier, D. Wang, W. Kleist, J.-D. Grunwaldt, *Appl. Catal. A*, Vol. 490, pp. 181–192 (2015).

2014   **Ageing effects on exhaust gas catalysts: microscopic changes captured by X-ray tomography**, G. Hofmann, A. Rochet, S. Baier, M. Casapu, S. Ritter, F. Wilde, M. Ogurreck, F. Beckmann, J.-D. Grunwaldt, *J. Phys.: Conf. Ser.*, Vol. 499, pp. 012017 (2014).

Oral Presentations

2016   **Studying a bifunctional Cu/ZnO-zeolite catalyst for direct production of dimethyl ether with *in situ* ptychography and ETEM**, S. Baier, C. D. Damsgaard, J. Reinhardt, M. Klumpp, F. Benzi, M. Scholz, T. Sheppard, Z. Balogh, T. Kasama, J. B. Wagner, W. Schwieger, C. G. Schroer, J.-D. Grunwaldt, Nordic Symposium on Catalysis, Lund, Sweden, 14.-16.06.2016.

2015   **Lithographically fabricated silicon microreactor for *in situ* characterization of heterogeneous catalysts**, S. Baier, D. E. Doronkin, A. Rochet, G. Hofmann, T. Sheppard, F. Benzi, J.-D. Grunwaldt, XAFS16, Karlsruhe, Germany, 23.-28.08.2015.

2015   ***In situ* ptychography during the annealing treatment of heterogeneous nanoporous gold catalysts**, S. Baier, C. D. Damsgaard, A. Rochet, M. Scholz, A. Wittstock, C. G. Schroer, J.-D. Grunwaldt, OperandoV, Deauville, France, 17.-21.05.2015.

2015   **Application of X-ray microscopy and ptychography in heterogeneous catalysis**, S. Baier, A. Rochet, J.-D. Grunwaldt, DESY Photon Science Users'Meeting, Hamburg, Germany, 29-30.01.2015 (invited).

Poster Presentations

2016 **Studying a bifunctional Cu/ZnO-zeolite catalyst for direct production of dimethyl ether with *in situ* ptychography and ETEM**, S. Baier, C. D. Damsgaard, J. Reinhardt, M. Klumpp, F. Benzi, M. Scholz, T. Sheppard, Z. Balogh, T. Kasama, J. B. Wagner, W. Schwieger, C. G. Schroer, J.-D. Grunwaldt, DESY Photon Science Users' Meeting, Germany, 28.-29.01.2016.

2015 ***In situ* ptychography during the annealing treatment of nanoporous gold catalysts**, S. Baier, C. D. Damsgaard, F. Benzi, A. Rochet, M. Scholz, R. Hoppe, T. Scherer, J. Shi, A. Wittstock, M. Bäumer, C. G Schroer, J.-D. Grunwaldt, XAFS16, Karlsruhe, Germany, 23.-28.08.2015.

2014 **The catalytic partial oxidation of methane over noble metal catalysts: spatially resolved study in a microreactor**, S. Baier, A. Rochet, G. Hofmann, J.-D. Grunwaldt, Deutsche Tagung für Forschung mit Synchrotronstrahlung (SNI), Bonn, Germany, 20.-22.09.2014.

2013 **Importance of spatial resolution in catalytic reactors: gradients in the catalyst structure during the partial oxidation of methane**, A. Rochet, G. Hofmann, S. Baier, J.-D. Grunwaldt, Bunsen Tagung, Karlsruhe, Germany, 09-11.05.2013.

2013 **Gradients in the catalyst structure along a catalytic microreactor during the partial oxidation of methane**, A. Rochet, G. Hofmann, S. Baier, J.-D. Grunwaldt, E-MRS 2013 Spring Meeting, Strasbourg, France, 27-31.05.2013.

Eidesstattliche Erklärung

Hiermit versichere ich, die vorliegende Doktorarbeit selbstständig angefertigt und keine anderen als die von mir angegebenen Quellen und Hilfsmittel verwendet, sowie wörtliche und sinngemäße Zitate als solche gekennzeichnet zu haben. Weiterhin habe ich die Satzung des Karlsruher Instituts für Technologie (KIT) zur Sicherung guter wissenschaftlicher Praxis in der gültigen Fassung beachtet. Die Arbeit wurde in gleicher oder anderer Form keiner anderen Prüfungsbehörde zur Erlangung eines akademischen Grades vorgelegt. Die elektronische Version der Arbeit stimmt mit der schriftlichen überein und die Primärdaten sind beim Institut gesichert.

Karlsruhe, den